Anion exchange in green rust : the chloride, sulphate and carbonate binary and ternary systems

Myriam Agnel

UNIVERSITÉ D'ORLÉANS

ÉCOLE DOCTORALE ÉNERGIE - MATERIAUX - SCIENCES DE LA TERRE ET DE L'UNIVERS

Institut des Sciences de la Terre d'Orléans

THÈSE présentée par :

Myriam Agnel

soutenue le : **11 décembre 2020**

pour obtenir le grade de : **Docteur de l'Université d'Orléans**

Discipline / Spécialité : Sciences de la Terre

Doctoral thesis in Geosciences

Échanges anioniques binaires et ternaires pour le système chlore, sulfate et carbonate dans les rouilles vertes

THÈSE dirigée par/Supervised by :

TOURNASSAT Christophe	Professeur, Université d'Orléans
GRANGEON Sylvain	Chercheur, BRGM

RAPPORTEURS/REVIEWERS :

COURTIN-NOMADE Alexandra	Professeur, Université Paris-Saclay
TERTRE Emmanuel	Professeur, Université de Poitiers

JURY :

ISAURE Marie-Pierre	Maître de conférences, Université de Pau
LE FORESTIER Lydie	Maître de conférences, Université d'Orléans
MOTELICA-HEINO Mikael	Professeur, Université d'Orléans – Président du jury
ROBINET Jean-Charles	Chef de service, ANDRA

ACKNOWLEDGEMENTS

Voici un petit mot pour remercier celles et ceux qui ont participé à mon aventure *thésesque* et pour signer la fin de ma quête en Orléanais.

Tout d'abord, merci à la région Centre-Val de Loire pour le financement de ma thèse et aux différents projets comme l'ANR Nacre pour le financement de matériels ou déplacements professionnels.

Merci beaucoup, beaucoup ?, beaucoup ! à Christophe Tournassat & Sylvain Grangeon pour tellement de choses que je crois que je n'en finirai pas. Merci pour avoir osé me prendre en stage puis en thèse malgré ma faible connaissance initiale du sujet et des techniques (en espérant avoir retenu quelques éléments), pour leur patience, leur aide, leurs corrections, leurs blagues & contrepétries.

Je remercie également tous les membres du jury d'avoir accepté d'examiner ce travail.

Merci aux deux équipes qui m'ont acceuillies à Orléans, SVP/MG2 au BRGM et l'équipe milieux poreux à l'ISTO. Un merci particulier pour leur aide ou pour m'avoir inculqué un peu de leur savoir à Francis, Nicolas, Mathieu, Adeline, Stéphanie, Valérie & Prescillia. A nouveau, une mention spéciale pour ceux qui sont venus m'épauler en synchrotron (même jusqu'à la toute fin de cette thèse) : Sylvain, Christophe, Francis, Nicolas & Hervé de Coco. J'ai survécu grâce aux Dinosaurus !

I switch to English for a bit: thank you very much & merci (with a American accent) to Ian Bourg for welcoming me in his team and teaching me how to do molecular dynamic simulations. Thank you to all his team members and especially Tom Underwood, Bastien Will & Anne-Laure, Ayumi Koishi and Xiaohan Li for their help and some very nice gatherings to try various types of food. Dziękuję (sorry if the translation is bad...) to Dawid Szymanowski for going on trip with us to discover the US (and some food, food is very important!).

Cette thèse en bonne partie expérimentale et analytique n'aurait pas pu aussi bien marcher sans l'aide des ces personnes à qui je dis un grand merci :

— Clémence, Benoit & surtout Stéphane. Merci pour tout et, en particulier, pour toutes ces bouteilles changées (d'azote) à l'autre bout du BRGM,

— Élodie, Céline & Thibault pour m'avoir donné accès tant de fois à HPLC !

— Nicolas Maubec et la DRX,

— Fabienne Warmont pour le MET,

— Marjorie Roulet pour l'ATG,

— Guillaume Wille & Mollud Alleki pour la préparation et les analyses d'échantillons en microsonde.

Je remercie Erik Elkaïm & François Fauth pour leur aide et leurs apports lors des expériences en synchotron.

Merci à Fabienne Trolard et Guilhem Bourrié pour m'avoir conté la fabuleuse histoire des fougérites lors de l'Euroclay. Un deuxième merci particulier à Fabienne pour m'avoir acceuillie et m'avoir montré comment chasser la Fougérite (et les châtaignes).

Pour tous mes co-bureaux (dans l'ordre historique), merci à Romain, Cherif, Florian, Tom and Chris, Saideep & Clément (confinement oblige...) ; qui ont réussi à me supporter malgré mes idées farfelues de trouver tous les départements français et les éléments du tableau périodique grâce à leur nombre , to debate about Brexit & French-English relationship, ou bien de leur apprendre quelques mots de français.

Le merci le plus 'étrange' de cette thèse mais pas des moindres, car sans elle, je n'aurais pas pu travailler sur ce sujet si particulier... Elle a eu ses hauts et ses bas, ses fuites, et elle a fait pêter les plombs (électriques) plusieurs fois... Elle aura usé plusieurs pompes et 'bu' des dizaines de bouteille (plutôt des centaines car en moyenne 3 bouteilles par semaines sur 3 ans, ça fait 468 bouteilles...). Je lui ai tenu la main de nombreuses fois mais ça n'aura pas suffit comme thérapie.

Longue vie & prosperité à Georgette :

Georgette Glovebox of house MBraun UNIlab Pro, First of Her Name, the Anoxic, Savior of PhD, Protector of Fougerite, Breaker of Electrostatic Bonds and Mother of Green Rusts

Merci à elle ! (Un petit merci à la boite à gants du G2 qui m'aura dépanné sur la fin.)

Un grand merci à mes amis qui m'ont soutenu pendant cette aventure et désolée d'avoir décaler/annuler quelques parties de JDR à cause de la rédaction : Amélie, Bryan, Clara & Élodie ; Samantha ; Boris ; Sissi ; et Maxime & Sarah ! Un merci aux fournisseurs officiels de St Nectaire pendant la thèse et surtout pendant la rédaction (même pendant le confinement !) : Seb & Léontine ! On s'en serait pas sorti sans vos "petits" fromages. Un très grand merci à Morgan & Estelle qui nous auront suivis et soutenus pendant toute l'aventure Orléanaise ! Bon courage pour la suite ;) J'en profite également pour remercier ma belle-famille : Marina & Pierre, Frédérique & Régis et Madeleine & Mignon, pour leur soutien sans faille et nous avoir donné tant de légumes du jardin.

Le dernier immense merci (ou l'avant dernier ?) revient à Clément, qui a été là dès le début, qui est devenu mon mari nordique entre temps, qui m'a plus que supportée pendant le confinement, qui m'a soutenu, qui a gentiment accepter de relire des parties de cette thèse et qui sera là jusqu'à la fin ! ♡

Merci :)

CONTENTS

LIST OF FIGURES

LIST OF TABLES

CHAPTER I

INTRODUCTION

I.1 Green rust & Fougerite - Definition

Green rust is a layered double hydroxide (LDH) that contains Fe^{2+} and Fe^{3+} and which is found both in engineered and natural environments (Trolard and Bourrié, 2008; Vodyanitskii and Shoba, 2015; Usman et al., 2018; Bhave and Shejwalkar, 2018). Fougerite, the naturally-occurring form of green rust, has been identified in several natural settings such as hydromorphic soils and river streams (Trolard et al., 1996; Abdelmoula et al., 1998; Trolard et al., 2007; Trolard and Bourrié, 2008; Christiansen et al., 2009). In the following "Fougerite" will be used to refer specifically to the mineral [1], while "green rust" will be used both to refer to synthetic samples and to discuss properties that are common to fougerite and synthetic samples.

The structure of LDHs is composed of a stacking of brucite-like layers (Figure I.1), i.e. layers of edge-sharing $M_{Oct}O_6$ octahedra (M_{Oct} = Al, Mg, Fe, ...), separated from each other by an interlayer space. These layers are positively charged due to isomorphic substitutions of trivalent cations by divalent cations, e.g. Mg^{2+} with Al^{3+}. The general layer structural formula is:

$$[(M^{2+}_{Oct,1-x}M^{3+}_{Oct,x})(OH)_2]^{x+}$$

where x is the stoichiometry of the trivalent cation. The $x+$ positive layer charge is counterbalanced by hydrated anions, which are located in the interlayer space. These interlayer anions are often readily exchangeable with surrounding aqueous anions. Because of their ion exchange properties, layered structure, variable charge density, and high specific surface area, LDH are often described as clay-like

1. Nomenclature details: fougerite, the natural form of green rust has been identified and recognized by the International Mineralogical Association (IMA). Fougerite was spelled this way in English by Trolard (2006); Trolard et al. (2007); Trolard and Bourrié (2008), but the IMA registered it as "Fougèrite". The original English spelling, fougerite, will be used in this work.

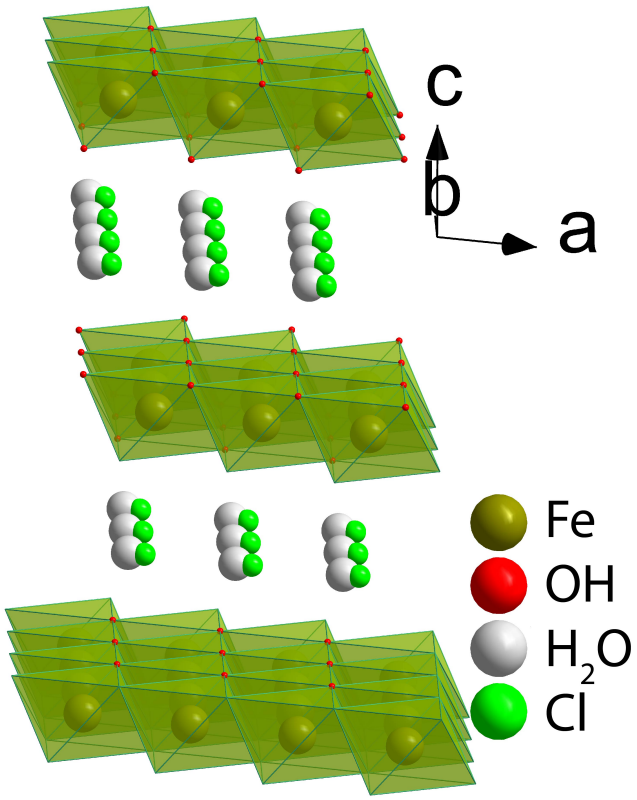

Figure I.1 – Representation of green rust structure with chloride anions in the interlayer (structure obtained from the cif file given in Trolard et al. (2007), occupancy of interlayer atoms not representative).

materials. However, the sign of their layer charge is opposite to that of clay minerals such as smectites. For this reason, LDH are referred to as "anionic clays" (Forano et al., 2006). Fougerite is one of the rare cases of LDH in which the two main cations in the layer are cations of the same chemical element, iron, but in different oxidation states.

I.2 Discovery of green rust & fougerite

In 1905, bluish-green horizons were described in hydromorphic soils (Vysostskii, 1905, 1999). They rapidly turned ocherous on contact with air. It was hypothesized that this phenomenon was due to the presence of mixed Fe(II)-Fe(III) minerals in these soils.

Later, corrosion sciences focused on the elucidation of rust formation, its mineralogic composition and oxidation pathways. (Deiss and Schikorr, 1928; Krause, 1928; Hüttig and Möldner, 1931; Schikorr, 1933). Studies tried to elucidate the nature of a green phase forming during iron oxidation processes

under certain conditions. Girard and Chaudron (1935) synthesized this phase but they identified it as hydrated magnetite ($Fe_3O_4 \cdot nH_2O$). The second synthesis method and characterisation was made by Keller (1948); Feitknecht and Keller (1950). They gave a structural formula of $4\,Fe(OH)_2$,$FeOCl \cdot nH_2O$, which was close to the real structural formula of green rust, as identified later. First X-ray diffraction (XRD) powder photographs of synthetic green rust allowed then for a better understanding of its structure, and for the distinction between green rust I, which contains anions or planar negatively-charged molecules in its interlayer (OH^-, Cl^-, ${CO_3}^{2-}$, etc.), and green rust II, which contains anions in tetrahedral coordination to O/OH (${SO_4}^{2-}$, ${SeO_4}^{2-}$, Keller (1948); Bernal et al. (1959); Etter and Dinnebier (2014).

Green rust was identified in artificial environments, inside iron pipes (Stampfl, 1969), and analyzed as carbonate green rust with a structure similar to that of the pyroaurite group (Ingram and Taylor, 1967; Allmann, 1968). Taylor (1980) argued that green rust may form in natural environments because of the greenish colours often encountered in wet soils and sediments, and because of the rapidity with which this colour changes on exposure to oxygen. However, an identification in natural environments was lacking. Green rust was later identified in ochre sludge, i.e. a natural soil-like environment by Koch and Mørup (1991). Finally, fougerite was identified by Trolard et al. (1996) in a gleysol near Fougères, Brittany, France, as a natural occurring form of green rust. This mineral was fully described in Trolard et al. (2007). The structural formula of the fougerite sample described in this study was: $(Fe^{2+}Mg^{2+})_6Fe_2^{3+}(OH)_{18} \cdot 4H_2O$ This mineral was recognized as "Fougèrite" by the International Mineralogical Association with the reference IMA2003-057. A group was created for fougerite containing three minerals: fougerite (IMA2003-057), trébeurdenite (IMA2012-s.p) and mössbaurerite (IMA2012-049) (Mills et al., 2012). Fougerite contains Mg^{2+}, but other isomorphic substitutions by other cations have been reported in polluted environments such as in Zn- (Johnson et al., 2014) or Ni-bearing green rust (Zegeye et al., 2012).

I.3 Natural occurrences

I.3.1 Fougerite in gleysols

Gleysol - Definition, profile, development and occurrence

Gleysols are soils saturated with groundwater for long enough periods to develop a characteristic "gleyic colour pattern" due to humidity and Fe^{2+} content. This gleyic colour pattern is characterized

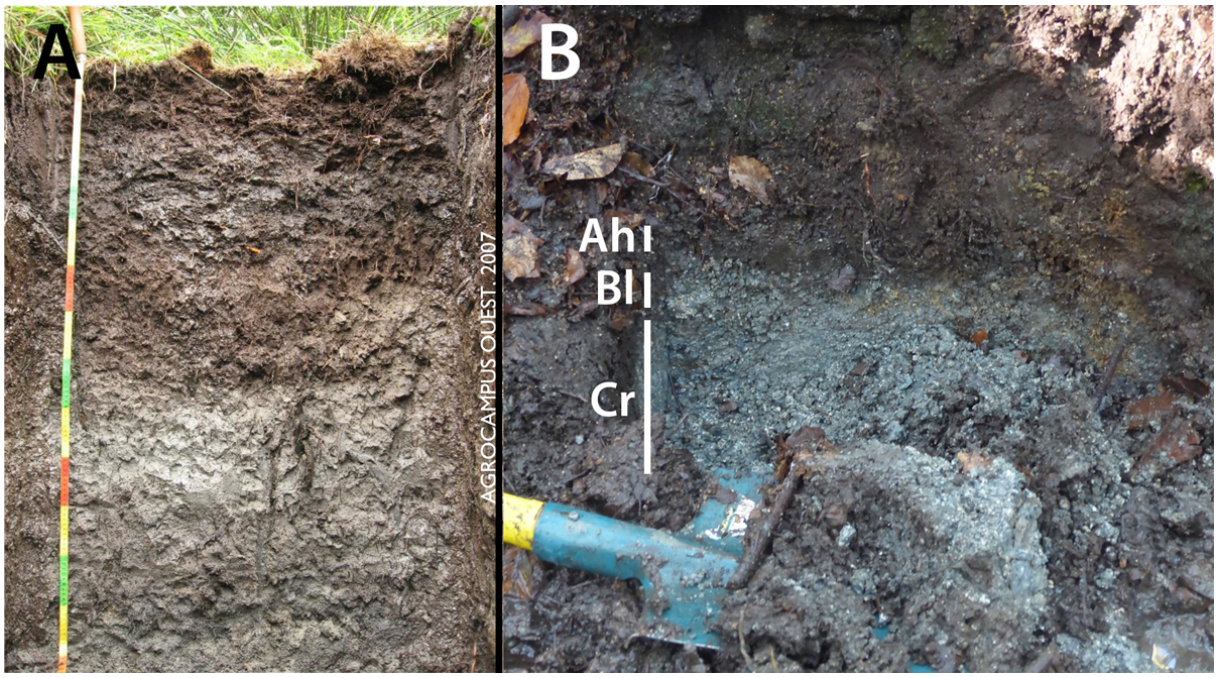

Figure I.2 – Profile of gleysols from Ménéac (Morbihan, France; A, GIS SOL (2019)) and Fougères (Ille-et-Vilaine, France, B, ©Myriam Agnel). Succession of horizons characteristic to gleysols are visible on B (abbreviation from World Reference Base for Soil Resources, WRB): A- Upper mineral horizon, mainly with humus; h-Accumulation/Illuviation of humus; Bl - oxidation horizon; Cr - reduction horizon (Bl/Cr are diagnostic horizon of gleysol).

with > 90 % of reductomorphic colours (reddish, brownish or yellowish colours in the upper soil layer(s), in combination with greyish/bluish colours deeper in the soil) and > 5 % mottles. Parent materials are a wide range of unconsolidated materials, mainly fluvial, marine and lacustrine sediments. They can be found in depression areas and low landscape positions with shallow groundwater (Blume et al., 2010).

A common horizon sequence is the succession, from surface to depth, of a humus-rich, an oxidation, and a reduction horizon (Ah/Bl/Cr sequence – Figure I.2). The Ah horizon is not affected by groundwater, whereas the Bl horizon is identified by its orange-light brown colours that is due to oxidation (oxidation horizon). The Bl horizon is present only when soil is not permanently flooded up to the Ah horizon. The permanently wet Cr horizon exhibits greyish, greyish-green and bluish black colours (reduction horizon).

Gleysols develop under the influence of oxygen-poor groundwater. Water only travels slowly because of endorheic depressions, which retain water, or loomy-clayey floodplains. The development of gleysols is thus intrinsically linked to presence and seasonal variation of the groundwater table depth. The nature and thickness of the different horizons is also dependent on the rock composition, the oxygen concentration, as well as the presence of salts, nutrients or organic matter.

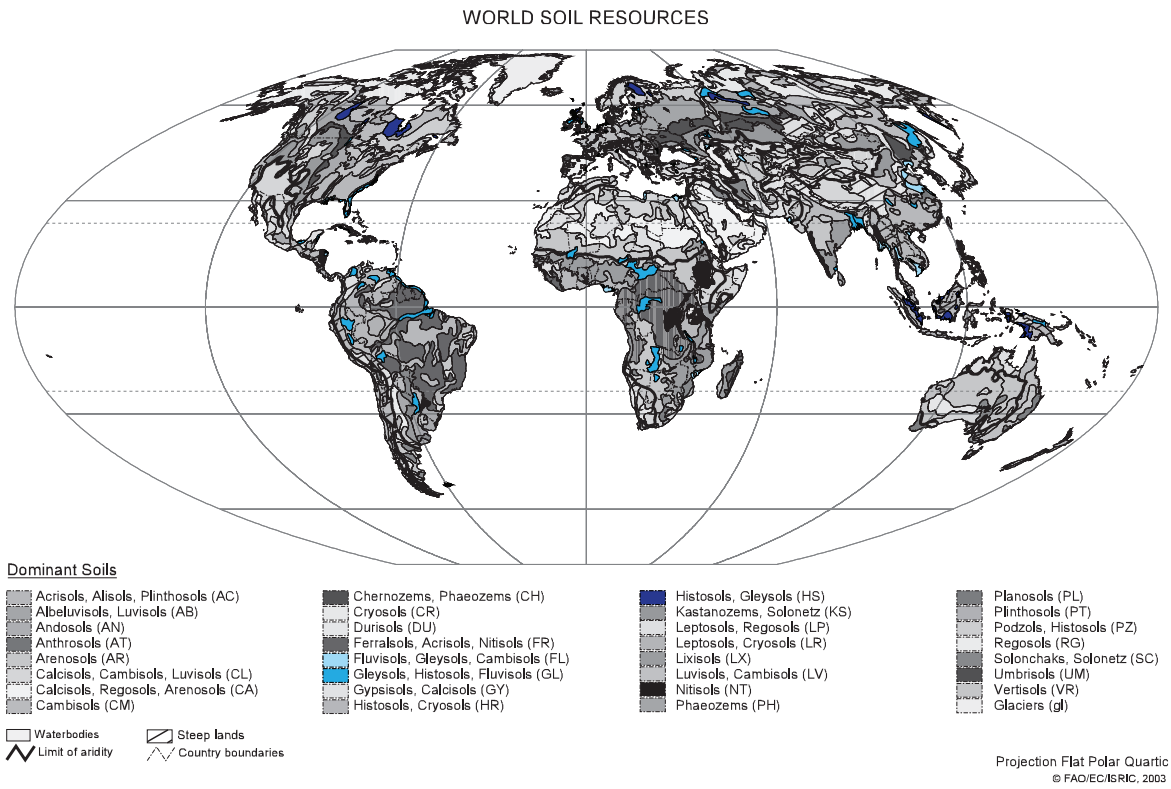

Figure I.3 – Soil map of the world. Modified from FAO (1971) to highlight (in blue) where gleysols are present. Colours for other dominant soils have been converted to shades of grey.

Gleysols are widely distributed over the world and represent 720 million hectares world-wide, i.e. 5.4 % of world's land surface according to the World Reference Base for Soil Resources (WRB) and the food and agricultural organization of the united nations (FAO; Figure I.3, FAO (1971)). Gleysols are present on 1.8 % of the surface of the metropolitan French territory (GIS SOL, 2019). They can be found under nearly all climates where the groundwater table is high. Gleysols specific properties vary depending on surrounding rocks and soils. The largest extent of gleysols is in sub-arctic areas of Siberia, northern Canada and Alaska, and in humid temperate and subtropical lowlands, *e.g.* in China and Bangladesh. An estimated 200 million hectares of gleysols can be found in the tropics, mainly in the Amazon region, equatorial Africa and the coastal swamps of Southeast Asia (FAO, 1971).

Formation mechanism of fougerite

Fougerite formation is intrinsically linked to its stability, which depends on reduction–oxidation (redox) conditions. Seasonality plays a major role in controlling fougerite formation, since it influences redox conditions (Feder et al., 2005; Trolard et al., 2007; Trolard and Bourrié, 2008; Vodyanitskii and Shoba, 2015). The water table level, the amount of rainfall, and the diffusion of O_2 are the most

important parameters that control the redox state, especially iron speciation, in gleysols. Reductive conditions are visible with the colour change of minerals to green, blue or black.

The cycle of precipitation/dissolution of iron phases in gleysols was described as follows (Feder et al., 2005; Vodyanitskii and Shoba, 2015):

1. During the driest period, fougerite is completely oxidized to Fe(III) oxides (ferrihydrite, lepidocrocite, goethite or magnetite, Figure I.4).
2. When reducing conditions appear, such as in the autumn in temperate climates or during the wet season in tropical climates, soil conditions become anoxic due to water saturation and the presence of fresh organic matter that limits the activity of dissolved O_2. Iron oxides undergo reductive dissolution, releasing Fe^{2+} in the solution.
3. Oxygen seeps in soils during rainfall, and Fe^{2+} thus oxidizes to Fe^{3+}. Fe^{2+}, Fe^{3+} and Mg^{2+} co-precipitate to form fougerite, with a variable iron content. Because of seasonnal rainfall heterogeneities, formation and dissolution of fougerite are varying depending on anoxic and oxic periods.
4. The cycle starts again during the next dry season.

This cycle is abiotic, however, bacteria are suspected to play a role in bioreduction of iron oxides in soils (Ona-Nguema et al., 2002; Zegeye et al., 2005; Trolard and Bourrié, 2008). Fougerite with ferrihydrite is a key intermediate in the pathways of iron oxides formation (Figure I.4, Trolard et al. (2007)). If the oxidation is slow and not too important, fougerite forms, but a faster oxidation leads to ferrihydrite. Because of its reactivity towards oxygen and its capacity to transform to other Fe (oxyhydr)oxides or to form from other Fe (oxyhydr)oxides, fougerite plays an important role in the iron cycle, as well as in the magnesium cycle and other trace elements (Co, Cr, Mn, Ni and Zn, Trolard and Bourrié (2008)), and also in anions cycling (nitrogen, sulphur, chlorine, inorganic carbon), because of their adsorption in fougerite interlayer (Rennert et al., 2012).

I.3.2 Other occurrences

Fougerite is often present in gleysols but it has been identified in other natural and artificial environments, such as mine drainage in south Wales (Bearcock et al., 2006; Johnson et al., 2014); buried lacustrine deposits in Ohio, United-States (Weatherington-rice and Bigham, 2006); groundwater in Sweden (Christiansen et al., 2009); mofette formation sites (volcanic structures that diffuse gas, such as CO_2) in Czech Republic (Rennert et al., 2012); and in the water column of a ferruginous lake in Indonesia (Zegeye et al., 2012). Trébeurdenite and Mössbauerite were sampled from marine

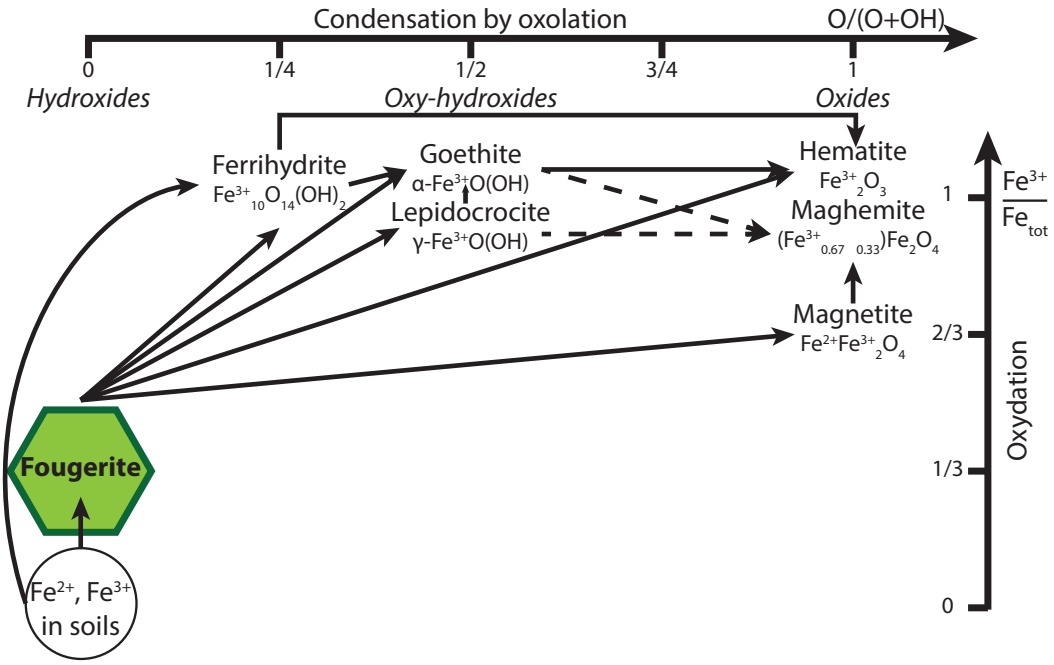

Figure I.4 – Location of fougerite in the formation pathways of Fe oxides. x-axis: molar ratio O/(O+OH), increasing condensation by oxylation from left to right. y-axis: molar ratio of Fe^{3+}/Fe_{total}, increasing oxidation from the bottom to the top. Fougerite and ferrihydrite appear as key intermediate phases (reproduced and modified from Trolard et al. (2007), structural formulas taken from IMA database on RRUFF website).

environments, beaches of nothern Brittany and the bay of Mont-Saint-Michel, Brittany and Normandy, France (Génin et al., 2012, 2014). They were differentiated from fougerite with the help of Mössbauer analysis.

The presence of green rust was hypothesized next to alkaline hydrothermal vents in the Hadean ocean, and models were developed in which green rust could have played a role in the emergence of life (Russell, 2018; Duval et al., 2019). Green rust could also have had a major role in the iron cycle of Precambrian oceans before the Great Oxidation Event, 2.3-2.4 billion years ago (Koeksoy et al., 2019; Halevy et al., 2017; Luo et al., 2016; Gumsley et al., 2017; Ossa et al., 2019).

I.4 Synthesis of green rust

Following the pioneering green rust synthesis methods developed by Girard and Chaudron (1935) and Keller (1948), many synthesis procedures have been developed, including inorganic and biological methods (Bhave and Shejwalkar, 2018). A widespread method is the coprecipitation synthesis (Cuttler et al., 1990; Géhin et al., 2002). Ferrous and ferric salts are mixed in stoichiometric quantities. The pH of the solution is raised slowly to a value of 7 with addition of sodium or potassium hydroxide under stirring, allowing green rust to precipitate. The molar ratio between ferrous and ferric salts

controls the final Fe^{2+} to Fe^{3} ratio in green rust. Another method is the oxidation of ferrous salt (Drissi et al., 1994; Génin et al., 1996, 1998). This salt is mixed with sodium hydroxide. This process precipitates ferrous hydroxide. This hydroxide is mixed with sodium chloride, sodium sulphate or sodium carbonate and stirred under normal atmospheric conditions, thus forming green rust by (partial) oxidation. The oxidation can also be done with sodium nitrite (Hansen et al., 1994). Several other methods were used such as electrochemical methods (Legrand et al., 2001; Moreno et al., 2007), remineralization of ferric oxides (Usman et al., 2012), or reduction of iron oxides nanoparticles (Jones et al., 2015). These methods can also help incorporating other cations through substitutions in the layers, such as zinc (coprecipitation method, Tamaura et al. (1984)), cobalt (Hadi et al., 2014), uranium, or technetium (electrochemical method, Roh et al. (2000)). Finally, sulphate green rust has been synthesized also using bacteria (*Shewanella putrefaciens*, *Klebsiella mobilis*, etc.), by bioreduction of lepidocrocite (Ona-Nguema et al., 2002), ferrihydrite (Kukkadapu et al., 2004), γ-FeOOH (Zegeye et al., 2005), magnetite (Etique et al., 2016), or indirect oxidation of Fe(II) (Etique et al., 2014a; Etique, 2014). These biologically-induced syntheses helped understanding the possible processes of formation of fougerite in soils.

I.5 Green rust & Fougerite - Composition and structure

I.5.1 Chemical composition

Green rust structural formula is Trolard and Bourrié (2008):

$$[Fe^{2+}_{1-x}Fe^{3+}_{x}(OH)_2]^{+x}[\frac{x}{n}A^{-n}\cdot mH_2O]^{-x} \tag{I.1}$$

where A is the interlayer anion, with charge $-n$, and with $\frac{1}{4} \leq x \leq \frac{1}{3}$. Green rusts can substitute Fe(II) or Fe(III) for other di- or trivalent cations in the metal hydroxide layers (Rives, 2001).

Fougerite structural formula is (Trolard et al., 2007):

$$[Fe^{2+}_{1-x}Fe^{3+}_{x}Mg^{2+}_{y}(OH)_{2+2y}]^{+x}[\frac{x}{n}A^{-n}\cdot mH_2O]^{-x} \tag{I.2}$$

where A is the interlayer anion, with charge $-n$, and with $\frac{1}{4} \leq \frac{x}{2+y} \leq \frac{1}{3}$ and $m \leq (1-x+y)$. The structural formula of trébeurdenite is (Génin et al., 2012):

$$Fe^{2+}_{2}Fe^{3+}_{4}O_2(OH)_{10}CO_3\cdot 3H_2O \tag{I.3}$$

The structural formula of mössbauerite is (Génin et al., 2012, 2014):

$$Fe_6^{3+}O_4(OH)_8CO_3 \cdot 3H_2O \tag{I.4}$$

According to a comparison of pure synthetic samples with increasing x from 0.33 to 1, the structural parameters and structure of trébeurdenite and mössbauerite are close to those of fougerite (Ruby et al., 2010a; Génin et al., 2012). For fougerite, x does not exceed $\frac{1}{3}$ because of long range order of Fe^{3+}. Fe^{3+} sites are surrounded by six Fe^{2+} sites (Génin et al., 2005). If Fe^{3+} content exceeds $x = \frac{1}{3}$, fougerite transformation into other iron oxides is generally observed (Bourrié et al., 2004; Génin and Ruby, 2008; Trolard and Bourrié, 2008). The presence of mixed valence iron cations in green rust and fougerite allow them to take part in redox processes impacting iron minerals and other species (Figure I.4, Trolard and Bourrié (2008)).

I.5.2 Structure

Some examples of hypothetical or actual structures of green rusts containing different interlayer anions or molecules are presented in Table I.1.

Table I.1 – Composition and structural parameters of some green rusts and fougerite depending on the interlayer anion (Me^{tot} - Stoichiometry of all the cations in the layer, copreci. - coprecipitation method, L-to-L. dist. - Layer-to-layer distance). References: 1-Génin et al. (2001), 2-Refait et al. (1998), 3-Aissa et al. (2006), 4-Simon et al. (2003) and 5-Trolard et al. (2007).

Sample		Green rust			Fougerite
Anion	OH^-	Cl^-	CO_3^{2-}	SO_4^{2-}	OH^-
Fe^{3+}/Me_{tot}	-	0.25-0.31	1/3	1/3	1/4
$a = b$ (Å)	≈3.2	3.19	3.18	3.20	3.13
L-to-L. dist. (Å)	≈7.5	7.95	7.57	11.01	7.52-7.95
Crystal size (nm)	-	-	-	60	400-500
Reference	(1)	(2)	(3)	(4)	(5)
Synthesis	Never*	Oxidation	Copreci.	Oxidation	Natural

* - To our knowledge, hydroxy-green rust has never been synthetized, data derived from the structure of a green rust containing Cl^-, see Génin et al. (2001).

I.5.3 Specific surface area, surface charge and anion exchange capacity

The specific surface area (SSA) is the size of the surface area per unit of mass (in $m^2 \cdot g^{-1}$), which depends on the size of the particles (small particles have large specific surface area), and of the shape of the particles. Because of their layered structure, green rust and fougerite exhibit a very high total specific surface area, for example, 492 $m^2 \cdot g^{-1}$ for a fougerite with a crystal diameter of 500 nm

(Table I.1). Smaller SSA values are commonly reported in the literature (47 $m^2 \cdot g^{-1}$ Williams and Scherer (2001) or 21.6 $m^2 \cdot g^{-1}$ Rogers et al. (2014) for a carbonate green rust and 26.6 $m^2 \cdot g^{-1}$ for a sulphate green rust (Mitsunobu et al., 2009)). Similarly to what was described for swelling clays such as smectite (Tournassat et al., 2015), these values, obtained with gas adsorption methods, are representative of the external surface area of the particles, and not of the total surface area that includes internal surfaces bordering the interlayer spaces. Reported SSA values are thus dependent on the average number of stacked layers in one particle. The total SSA of green rust and fougerite is comparable to the highest SSA values reported for natural compounds, calculated based on crystallographic and particle size considerations, such as smectite (750 – 800 $m^2 \cdot g^{-1}$), hydrous ferric oxide (740 $m^2 \cdot g^{-1}$), and vernadite (most common Mn oxide; 750 $m^2 \cdot g^{-1}$, Tonkin et al. (2004)). However, the internal SSA can only be accessed by water molecules and other compounds depending on their size and their affinity for the layered mineral (Rives, 2001).

Surface charge in green rust and fougerite arises from the excess of charge of Fe^{3+} compared to Fe^{2+}. Fe^{2+} can also be substituted with other cations during the synthesis of green rust or the formation of fougerite (Figure I.5), for example Mg (Trolard et al., 2007), Zn (Johnson et al., 2014) or Ni (Zegeye et al., 2012) in fougerite, or Ni, Al, Mg or Co in green rust (Refait and Génin, 1993; Refait et al., 2001, 2002; Ruby et al., 2008, 2010b; Hadi et al., 2014). A substitution with a trivalent cation (e.g. Al^{3+}) also leads to an increase of the surface charge. These charges are compensated by interlayer anions. Interlayer anions are often used to differentiate and classify green rusts (chloride green rust, sulphate green rust, etc., Table I.1), as if they were intrinsically part of the structure. However, these anions can be possibly exchanged without altering the layer structure.

Equation I.1 shows that the amount of anion per unit mass is directly linked to the proportion of substitutions with Fe^{3+} or trivalent cations in the layer. This property is quantified by the Anion Exchange Capacity (AEC), which is expressed as moles of negative charge per unit weight of mineral (mol_c/100 kg). Any change in layer Fe^{3+}, for example by oxidation, has a direct impact on the layer charge and so, on the anion content in the interlayer. AEC in LDH is commonly mentioned to be high (2 – 4 $mol_c \cdot kg^{-1}$, Taviot-Guého et al. (2018)). In cationic clays , the cation exchange capacity (CEC), is usually proportional to the structural layer charge. An exception is seen in micas (including illite, muscovite, etc.), in which K^+ interlayer ions are not exchangeable. Consequently, the AEC quantification method based on the structural charge measurement does not enable to validate the exchangeable nature for the interlayer anions in green rusts.

I.6 Green rust & Fougerite - Reactivity

I.6.1 General considerations

The combination of small crystal size, presence of a interlayer space containing exchangeable anions, and presence of both Fe^{2+} and Fe^{3+} within the layer, makes that green rust can interact with solutes through a range of reactions that include Latta et al. (2015); Usman et al. (2018):

— Iron phase transformation by redox processes due to the presence of oxygen,

— Redox reactions with redox sensitive species in solution,

— Cationic substitutions in the octahedral layer,

— Specific adsorption as inner sphere complexes on edges (Figure I.5),

— Interlayer incorporation and anion exchange.

I.6.2 Redox reactions

Redox reactions in green rust lead to phase transformations (solid redox), or facilitate redox transformations of chemical species available in the solution (heterogeneous redox reaction). Studies of redox reactions of green rust with other species available in solution are numerous and most of them aim towards water decontamination applications such as for: nitrate - Hansen et al. (1994, 1996, 2001); Etique et al. (2014b); Refait et al. (2014); Guerbois et al. (2014); Grabb et al. (2017); selenium - Myneni et al. (2008); Hayashi et al. (2009); Holmes and Gu (2016); chromium - Williams and Scherer (2001); Rogers et al. (2014); Alidokht et al. (2016); Thomas et al. (2020); Zhao et al. (2021); copper, gold, mercury and silver - O'Loughlin et al. (2003b); uranium - O'Loughlin et al. (2003a); Latta et al. (2012); Sihn and In-Ho (2020); neptunium - Christiansen et al. (2011a); or organic compounds - Erbs et al. (1999); O'Loughlin and Burris (2004); Yin et al. (2017); Mangayayam et al. (2018); Ai et al. (2019, 2020); Han et al. (2020).

I.6.3 Sorption reactions

The term sorption regroups adsorption, absorption and exchange processes (McBride, 1994). A definition of adsorption is "the enrichment or release of dissolved gaseous ions or molecules at the surface of solids (the sorbent)" (Blume et al., 2010). The dissolved compound adheres to the surface of the solid. Ions, uncharged inorganic and organic molecules can be adsorbed. Absorption suggests that the chemical is taken up into the solid (coprecipitation processes can be considered in this way,

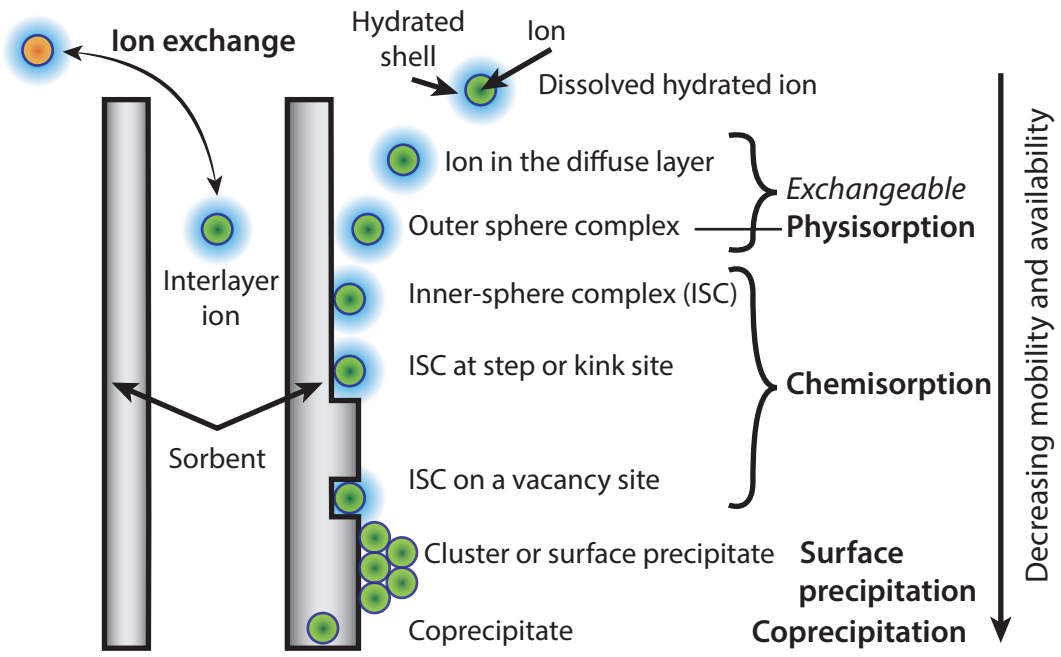

Figure I.5 – Sorption of ions on a layered mineral and its surfaces (Process in bold, modified from Blume et al. (2010) and Neumann (2012)). A more detailed view of ion exchange is available on Figure I.6.

Neumann (2012)). Ion exchange involves a replacement of one ion for another on the solid surface. The various interactions between an ion and a sorbent are diverse and represented in Figure I.5. Cationic substitutions in the octahedral layer, which can be considered as an absorption process, were observed for green rust during coprecipitation synthesis (magnesium - Refait et al. (2002); zinc - Ahmed et al. (2008) and aluminium - Ruby et al. (2008)). Two adsorption processes were observed in green rust: surface complexation and ion exchange.

Surface complexation

Surface complex formation implies the formation of coordinative bonds between metals and ligands at the surface (chemisorption) Neumann (2012). Ligands must displace one or more coordinated water molecules, forming a bond with atoms on the surface, usually with some covalent character (inner-sphere complex). Surface complexation on layered mineral occurs usually on the broken edge termination of the layer, which exhibit the presence of amphoteric surface functional groups. Examples of surface complexation on green rust can be found with arsenic (Randall et al., 2001; Wang et al., 2010; Perez, 2019; Perez et al., 2020), or antimony (Mitsunobu et al., 2009).

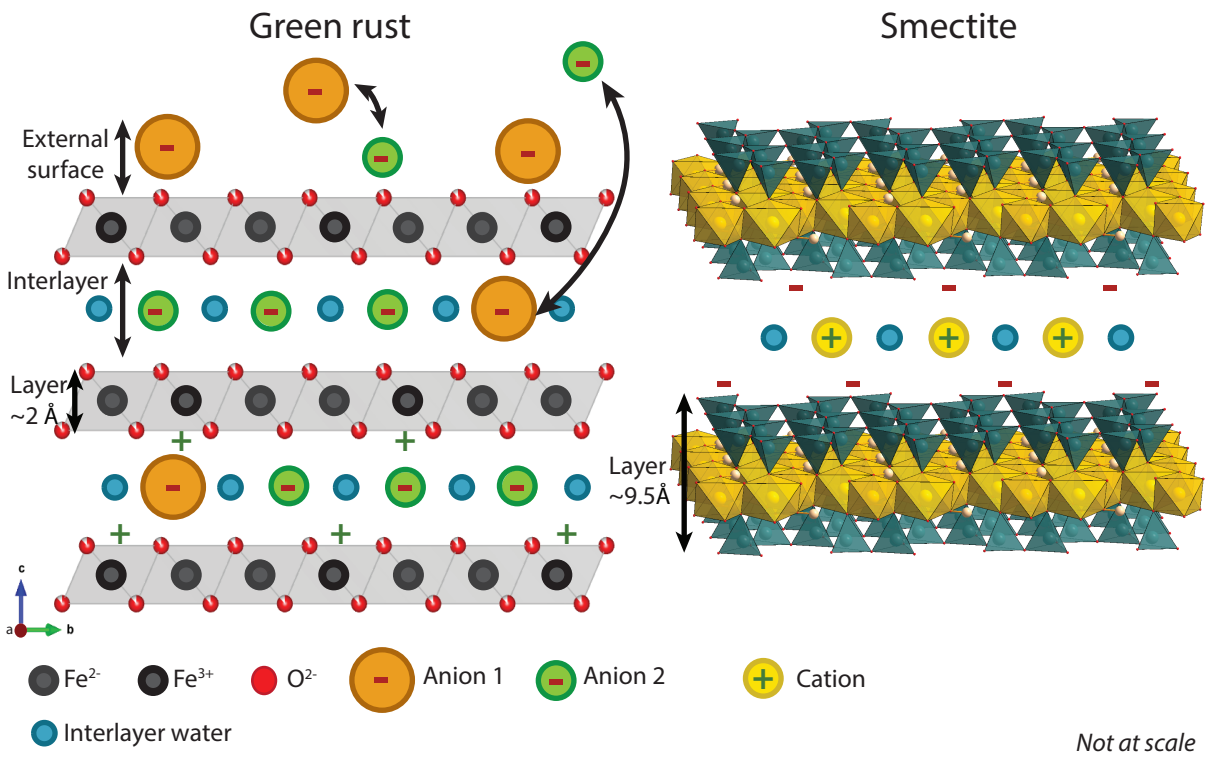

Figure I.6 – Schematic representation of green rust structure and ion exchange process (left figure), and comparison with the structure of a smectite (right figure; not at scale, chemistry or mechanism not quantified or real, smectite representation taken from Tournassat et al. (2015)).

Anion exchange

Ions can be attracted to surfaces with opposite charge, because of the presence of an electrostatic surface potential and the development of electrostatic forces (Figure I.6). In the absence of chemical bonding force, the main attractive interaction force is composed of long-range electrostatic bonds. Ions adsorbed on the surface with this mechanism usually remain hydrated and no sharing of electron between the adsorbed ion and the surface atoms occur. Because of the low energy of these bonds, ions can be exchanged with ions present in surrounding solution, hereby the name of exchanged ions.The ion exchange kinetics is often limited by the diffusion of each species from and to the surface (McBride, 1994). Ion exchange reactions with cationic clays are usually written in the formalism of chemical reactions using the ion exchange theory formalism. These reactions help quantifying the exchange using a thermodynamic formalism.

Anions present in the interlayer of green rusts can range from simple monovalent anions (*e.g.* Br^-, Cl^-, F^-, I^-, $NO_3{}^-$), divalent anions (*e.g.* $CO_3{}^{2-}$, $SO_4{}^{2-}$), trivalent anions ($PO_4{}^{3-}$), to complex organic

anions with various sizes (Latta et al., 2015; Usman et al., 2018).

It may be speculated that there is a degree of similarly between green rust properties and those of other LDH such as hydrotalcite (a Mg-Al LDH). Miyata (1983) worked on exchange isotherms with hydrotalcite and measured ion-exchange selectivity coefficients. Miyata established the following orders of affinity $OH^- > F^- > Cl^- > Br^- > NO_3^- > I^-$ for monovalent anions and $CO_3^{2-} > NYS^{2-} > SO_4^{2-}$ for divalent anions. The reported relative affinity of green rust for various common and inorganic anions are mostly based on the work of Miyata (1983) on hydrotalcite (Rives, 2001).

The applicability of these results was confirmed by Refait et al. (1997) with the study of green rust formation during corrosion processes. Refait et al. (1997) did not study directly anion exchange reactions, but characterized the affinity of green rust for certain anions (Cl^-, SO_4^{2-} and CO_3^{2-}) during its formation. The observed competition of SO_4^{2-} and CO_3^{2-} showed the preference of green rust surfaces for carbonate ions during the precipitation of green rust. Refait et al. (1997) explained that carbonate green rust is formed during corrosion processes in most cases, with the exception of sulphate green rust being produced during corrosion processes in seawater with the help of bacteria, which can be explained by the large ratio of sulphate over carbonate in sea water (≈ 23, Olowe et al. (1989); Génin et al. (1992); Genin et al. (1993); Millero et al. (2008)). They also showed that chloride green rust never formed, confirming the following affinity order between the three studied anions: $CO_3^{2-} > SO_4^{2-} > Cl^-$ in their experimental conditions.

Aiming to create reactive adsorbants for non-polar compounds, Ayala-Luis et al. (2010) studied the exchange between sulphate anions and carboxylates in green rust. Carboxylates with a number of carbon atoms higher than 9 replaced sulphate anions in the interlayer. The study of XRD patterns showed that the kinetics of exchange was faster for the longest alkyl chains in carboxylate anions (C14 or C16 - 14 or 16 carbon atoms), and the exchange was nearly complete in their experimental conditions with less than 2 % of remaining sulphate green rust. Incomplete exchange occurred for alkyl chain containing 9 or 12 carbon atoms, and no exchange was observed with C5 and C8 alkyl chains. The affinity for carboxylate anions increased with an increasing size of alkyl chains in carboxylate ions and with an increasing initial concentration of carboxylate. Mössbauer analyses confirmed that the Fe(II)/Fe(III) ratio was identical between the sulphate green rust and carboxylate green rust, and so the layer charge was not altered by the exchange reaction. They also studied the C12 carboxylate - sulphate exchange stoichiometry, and showed that around three C12 carboxylate ions replaced one

sulphate anion. This exchange stoichiometry was higher than the stoichiometry of two carboxylate ions for one sulphate anion which is expected based on the formal charge of the two anions. The authors hypothesized that the negative charge excess was compensated by the presence of additional cations in the interlayer and/or that external surfaces with the carboxylate groups protruded in the solution, forming hemimicelles (a micelle attached to a surface), and thus increasing the apparent exchange stoichiometry.

Perez et al. (2018) showed that an exchange between benzene sulphanate (BzS) with sulphate anions is possible, but this exchange was limited to about 18 % of intercalation of BzS (phase percentages from Rietveld refinement of XRD pattern). The exchange maintained the original symmetry of the sulphate green rust. However, the XRD patterns were recorded before and after the exchange so the mechanism of the ion exchange was only supposed after a careful investigation of the patterns. Each interlayer contained only one type of anion at the end, and the authors supposed a gliding along the (101) plane while the layer-to-layer distances increased with the presence of BzS (cell symmetry calculation using the McMaille method to confirm that the structure of the BzS green rust retained the original trigonal symmetry of sulphate green rust). Pair Distribution Function (PDF) analysis evidenced that the layer structure was not altered during the exchange. Additionally, they showed that 1,3-benzene disulfonate was not able to replace interlayer sulphate anions, probably because of the steric hindrances and electrostatic repulsion between this benzenic compound and green rust.

I.7 Objectives

The studies on ion exchange in green rusts previously mentioned showed that the exchange of different anions were possible under different chemical conditions. They partially confirmed the affinity order demonstrated by Miyata (1983) for hydrotalcite ($CO_3^{2-} > SO_4^{2-} > Cl^-$) during synthesis but also exchange experiments. In all those studies about anion exchange on green rust, the structure of green rust was often analyzed before and after the exchange. Structural modifications were not observed as the exchange proceeded. Other processes than ion exchange could have happened such as dissolution/recrystallization. The structural modifications occurring during the reaction should be followed *in situ* in order to assess the exchange mechanism.

Moreover, the quantification of the exchange was often incomplete (determination of the stoichiometry of the exchange, the AEC, or the affinity of green rust towards each anion). The order of

affinity was qualitatively observed and this order should be confirmed quantitatively with the determination of selectivity coefficients. Dedicated experiments must be conducted to determine parameters for reactivity models. Several thermodynamic models have been used to describe macroscopic variations in chemical composition of a phase such as pure phase equilibrium models, solid-solution models, or ion exchange models. It is interesting to determine which of these models is the most appropriate to describe anion exchange processes in green rust, because this determination would help to gain confidence in the extrapolation of green rust reactivity in various chemical conditions. Mechanism determination and reactivity quantification are complementary information that is necessary to build these models.

Once an anion is exchanged with another anion, it is also interesting to verify if it is possible to reverse the reaction. Hysteresis effects influence the reactivity of other layered materials such as clay minerals (Verburg and Baveye, 1994), so it might be possible this effect also affects green rust reactivity. It has been shown also that particle crystallinity and size may play a role on sorption mechanisms and parameters (Barthélémy et al., 2012; Caraballo et al., 2015; Johnson et al., 2015).

Consequently, the objective of this work was to develop a thermodynamic model for anion uptake in green rust that is grounded on molecular-scale foundations,and that takes into account the influence of particle size and stacking defects on the model parameters. The result and models would allow to have a better understanding of nutrient availability and cycling of trace element in gleysols (Sparks, 2001).

The chosen exchanged anions were chloride, sulphate and carbonate species. They were selected because of their quantitative importance in surficial waters and because of their simple aqueous speciation. The initial green rust material used in most studies contains these anions in the interlayer space, and sulphate and carbonate fougerite have also been reported in natural environments. Consequently, it is important to determine reliable thermodynamic models and parameters for the chosen anions.

This Ph.D. thesis manuscript is divided in five chapters, including the introduction. The theoretical background is detailed in chapter II. Chapter III describes the synthesis method of green rust samples, the analyses done to characterize the chemical composition and structure of studied samples, and the experiments carried out with these samples to study ion exchange processes. Chapter IV presents the

result of the samples characterization. Then, chapter V shows the results of ion exchange experiments with first, the determination of the mechanism using *in situ* XRD analyses and then, the results of batch exchange experiments and the modeling of ion exchange processes. A comparison with other materials and the applicability of this work is discussed at the end of chapter V. Finally, a conclusion summarizes the main results of this work and introduces some perspectives for future work.

CHAPTER II

THEORETICAL BACKGROUND

II.1 Mechanism - Anion exchange versus dissolution-precipitation processes

II.1.1 General note

Two different types of mechanisms can lead to an apparent ion exchange reaction: the first one is a 'simple' ion exchange mechanism in which an ion is replaced by another ion in the interlayer with breaking and formation of long-range electrostatic bonds of low energy (referred as 'ion exchange mechanism' or 'ion exchange process' in this work, Figure I.6, McBride (1994)). The second one follows a dissolution/recrystallization process of the entire particle. If the initial and the final structures of the layered mineral are observed alone following an exchange experiment, it can not be determined with certainty that one or the other mechanisms prevailed . In addition, ion exchange processes can proceed with various intermediate steps ranging from the coexistence of anions of different natures in the same interlayer, to segregation of particle containing only one type of interlayer anion, to interstratified structure in a single particle in which interlayers containing one type of anion alternates with interlayers containing another type of anion. Ion exchange processes have been reported for various LDH in Ay et al. (2007); Goh et al. (2009); Taviot-Guého et al. (2010); Dessalegne et al. (2016); Ma et al. (2017, 2018); Marty et al. (2018); Grangeon et al. (2020),as well as dissolution/recrystallization processes LDH (Radha et al., 2005; Wu et al., 2012; Zhang et al., 2012).

II.1.2 Interstratification

Paragraph based on Drits and Tchoubar (1990); Claret (2001); Ferrage (2004)

Interstratification corresponds to crystals built up from two-dimensional fragments having different structures and compositions (Drits and Tchoubar, 1990). For layered materials in particular, interstratification is defined as the presence of successive structural units (*e.g.* layers and interlayer spaces) having different structures, or compositions, or both. Selective modifications can occur on the composition or structure of the phase. Step by step, these modifications can change the composition or structure and lead to a different phase.

Interstratified crystal are usually described with two layered arrangements from two different phases but three layer arrangements or more have also been described. In the following, examples are given with two layered arrangements (layer type A and B), and interstratified crystals consist of a mixture of the two layer types. For example, if an interstratified crystal has only two different stacked layers, four types of neighboring layer succession can occur: AB, BA, AA or BB.

A probabilistic approach is necessary to describe an interstratified crystal. For example, it can be speculated that in a given direction, probability of finding a layer of a certain type depends on its nearest and previous neighbors. In this assumption, a Markov chains formalism was used in this work. Two sets of data are necessary to fully describe and model an interstratified phase, using Markovian probabilities:

— a chemical composition, which gives the various types of layers and the proportions or abundance of each type of layers (W). In our example, the abundance of layer type A is W_A and the abundance of layer type B is W_B,

— a stacking description, which depends on probabilities (P) of succession of each type of layer. The probabilities of succession rely on the composition of the interstratified mineral and its degree of ordering. The degree of ordering is characterized by a parameter, called Reichweite (R), which measures the range of interaction between layers (Jagodzinski, 1949). For example if R = 1, the type of layer at position n will have an influence on the next type of layer at position $n+1$. R = 0, 1, 2, 3 have been observed in natural samples.In our example case and with R < 2, the probability of having layer A followed by layer A is P_{AA}, and similarly, the probability of having layer A followed by layer B is P_{AB}, layer B followed by layer A P_{BA} and layer B followed by layer B P_{BB}.

Four equations are necessary to describe a system with two types of layer and R < 2:

$$\begin{cases} W_A + W_B = 1 \\ P_{AA} + P_{AB} = 1 \\ P_{BA} + P_{BB} = 1 \\ W_A \cdot P_{AB} = W_B \cdot P_{BA} \end{cases} \quad \text{(II.1)}$$

With these equations, only two independent parameters are necessary to describe the entire system: for example W_A and P_{AA}.

Three main groups of structures can be distinguished based on the layer stacking order (Figure II.1):

— R = 0 - Random degree of ordering: a layer at a given position has no influence on the composition of the neighboring layers. The only constraints are the abundance of each type of layer (Figure II.1-B) and $W_A = P_{AA}$ (Figure II.2). the knowledge of only one parameter is necessary to know each of the other parameters using equations II.1.

— R = 1 - Maximum Possible Degree of Ordering (MPDO): layers of the least abundant type can not follow each other (Figure II.1-A_1). For example, if layer B is the least abundant, $P_{BB} = 0$ and only one abundance is needed to calculate the other parameters in equation II.1 because $P_{AA} = 1 - \frac{1-W_A}{W_A}$ (Figure II.2). In case of $W_A = W_B = 0.5$ and $P_{AA} = P_{BB} = 0$, a superstructure appears (the succession can be ...ABABABAB... and the supercell becomes AB; Figure II.1-A_2). R = 1 − MPDO is a particular case of R = 1.

— Physical mixture: layers of different types are in different crystals (Figure II.1-C_2). However, if only XRD patterns are observed, this case can not be differentiated from the case in which layer types are completely segregated, *e.g.* all layers A follow each other and then, all layers B follow each other (Figure II.1-C_1). In both cases, P_{AA} is taken equal to 1 (Figure II.2).

Any type of interstratified crystals could exist as intermediates between these three end points. Because a maximum of two parameters are needed to describe an interstratified mineral with two types of layer, interstratified structures are usually plotted in a graph with W_A on the x-axis and P_{AA} on the y-axis (or W_B on the x-axis and P_{BB} on the y-axis, Figure II.2). The type of interstratified structure is given by the position of the studied interstratified mineral in this type of representation. W_A and P_{AA} can be determined by modeling XRD patterns. In this study, the software MLM2C was used to conduct the

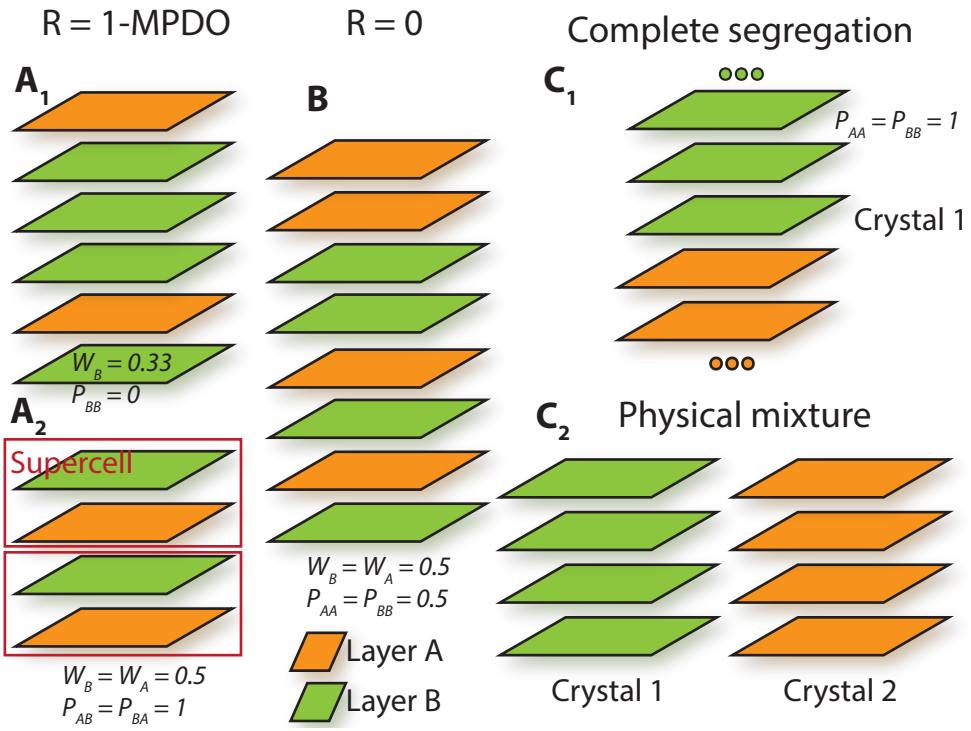

Figure II.1 – Some examples of structures of interstratified crystals. Orange and green trapezoid represents two different layers from different phases. A_1 and A_2 represent a case of R = 1 and more specifically R = 1 – MPDO and B for R = 0. C_1 represent a case of complete segregation. $C_2$is a physical mixtures. For C_1, "..." means that layers of the given colour are stacked below or above this representation.

modeling work (Plançon and Drits, 2000).

Interstratification has been shown to take place during ion exchange processes on cationic clays (Barer and Brummer, 1963; Inoue and Minato, 1979) and on LDH (Taviot-Guého et al., 2010; Marty et al., 2018). Natural LDH from the hydrotalcite-manasseite group and natural clays can also exhibit interstratified structures (Schmehl and Jackson, 1955; Drits et al., 1987; Rives, 2001; Claret et al., 2002).

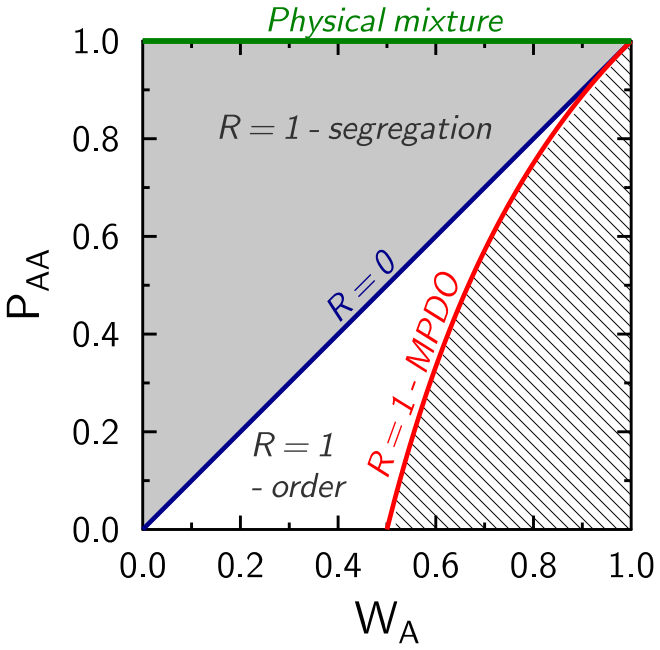

Figure II.2 – Junction probability diagram showing regions of R = 1-segregated and R = 1-ordered layer arrangements (modified from Bethke et al. (1986)). The location in this graph of other specific structures are also represented by lines such as R = 0, R = 1 – MPDO and physical mixture. No rational arrangements of layers can be found in the hatched area of the figure.

II.2 Reactivity models for anion exchange

Thermodynamic equilibrium models can be used to predict the chemical composition of solid as the function of the composition of the solution. For a layered mineral with variable interlayer compositions, it is possible to reproduce variations in mineral composition by (Tardy and Fritz, 1981):

— considering a set of separate mineral phases, and including in the models a large number of minerals of discrete compositions, each of them having a different solubility product value,

— considering a single solid solution phase, the composition of which changes gradually with the progress of a chemical reaction.

The two above approaches necessitate usually to use thermodynamic models that equilibrate the layer and interlayer composition with the equilibrium solution composition. However, ions in LDH can be possibly exchanged without changes of the layer composition. Ion exchange models have been developed to deal with the latest type of process.

II.2.1 Equilibria within an assemblage of pure phases

With this approach, chemical composition of layered minerals are considered to be fixed, and changes in their composition are reproduced with mixtures of different end-members. The equilibrium between the various species would be described by their composition and solubility product (McBride, 1994). This modeling approach is especially representative of a change from one end-member to another with a dissolution/recrystallisation process. However, it must be reminded that the capability of such a thermodynamic model to reproduce experimental data cannot demonstrate the mechanism at work. The exact mechanism must be confirmed with other analyses.

At specific chemical conditions, all the possible minerals with their composition and solubility product have to be known. Database have been developed for specific geochemical modeling codes such as Thermoddem with PHREEQC (Blanc et al., 2012; Parkhurst and Appelo, 2013), which make it possible to predict the presence (or not) of a phase and its quantity at certain chemical conditions if a thermodynamic equilibrium is reached.

Several solubility products for specific green rust compositions have been determined from data available in the literature with, for example, hydroxy-green rust in Bourrié et al. (1999), chloride green rust in Refait and Génin (1993), sulphate green rust in Davesne et al. (2010), and carbonate green rust in Drissi et al. (1995). In principle, it is thus possible to model exchange reactions by considering each of these green rust end-members in a phase assemblage model.

II.2.2 Ion exchange models

Ion exchange models were developed initially for clay minerals that exchange cations. So all equations developed for cation exchange modeling will be transposed for anion exchange on green rust. These equations are based on thermodynamic considerations and modeling results give only macroscopic information.

The general form of anion exchange reaction between A^{n-} and B^{m-} (n and m may be unequal) is (Sposito, 1981b; McBride, 1994):

$$n\,AX_{m(s)} + m\,C_nB_{(aq)} = m\,BX_{n(s)} + n\,C_mA_{(aq)} \tag{II.2}$$

where X and C respectively symbolise a positive exchange site and a cation, and m and n are ion charges. The subscripts (aq) and (s) mean "aqueous" and "surface". An example of an exchange equation between Cl^- and SO_4^{2-} on green rust surfaces is:

$$2\ \mathrm{G}r\mathrm{C}l + \mathrm{N}a_2\mathrm{SO}_4 = \mathrm{G}r_2\mathrm{SO}_4 + 2\ \mathrm{N}a\mathrm{C}l \tag{II.3}$$

where Gr is a cation exchange site.

The equilibrium constant for exchange equation II.3 is:

$$\mathrm{K}_{ex} = \frac{(\mathrm{G}r_2\mathrm{SO}_4)(\mathrm{N}a\mathrm{C}l)^2}{(\mathrm{G}r\mathrm{C}l)^2(\mathrm{N}a_2\mathrm{SO}_4)} \tag{II.4}$$

where values in round brackets are chemical activities. Equation II.4 can be simplified using the following relations $(\mathrm{N}a\mathrm{C}l) = (\mathrm{N}a^+)(\mathrm{C}l^-)$ and $(\mathrm{N}a_2\mathrm{SO}_4) = (\mathrm{N}a^+)^2(\mathrm{SO}_4^{2-})$. Electrolyte activities can be easily calculated with the Extended Debye-Hückel equation for ionic strength less than 10^{-1} mol$\cdot$ L^{-1} and Davies equation for ionic strength less than 0.5 mol$\cdot$L^{-1}) (Sposito, 1981b; McBride, 1994)). However, there are no unifying theory to describe the activity of exchange sites (Tournassat et al., 2011). In practice, selectivity coefficients, or exchange conditional constants, instead of true equilibrium constants, are determined to characterize ion exchange processes. Several conventions have been developed such as Vanselow, Gapon or Gaines & Thomas convention. The convention of Gaines & Thomas model is widely used in the literature to several mineral and phase types (Gaines and Thomas, 1953; Israëli et al., 2000; Tournassat et al., 2011). This convention is based on the assumption that the activity of adsorbed cations corresponds to the charge equivalent fraction E_i on the exchanger surface. According to this convention, the selectivity coefficient is:

$$\mathrm{K}_{ex,\mathrm{GT}} = \frac{(\mathrm{C}l^-)^2}{(\mathrm{SO}_4^{2-})} \cdot \frac{\mathrm{E}_{\mathrm{SO}_4}}{\mathrm{E}_{\mathrm{C}l}^2} = \mathrm{K}_{ex} \cdot \frac{\gamma^{\mathrm{GT}}_{\mathrm{G}r\mathrm{C}l}}{\gamma^{\mathrm{GT}}_{\mathrm{G}r_2\mathrm{SO}_4}} \tag{II.5}$$

where E is a site equivalent fraction:

$$\mathrm{E}_{\mathrm{C}l} = \frac{[\mathrm{G}r\mathrm{C}l]}{[\mathrm{G}r\mathrm{C}l] + 2[\mathrm{G}r_2\mathrm{SO}_4]} = \frac{(\mathrm{G}r\mathrm{C}l)}{\gamma_{\mathrm{G}r\mathrm{C}l}} \tag{II.6}$$

and

$$\mathrm{E}_{\mathrm{SO}_4} = \frac{[\mathrm{G}r_2\mathrm{SO}_4]}{[\mathrm{G}r\mathrm{C}l] + 2[\mathrm{G}r_2\mathrm{SO}_4]} = \frac{(\mathrm{G}r_2\mathrm{SO}_4)}{\gamma_{\mathrm{G}r_2\mathrm{SO}_4}} = 1 - \mathrm{E}_{\mathrm{C}l} \tag{II.7}$$

where γ is an activity coefficient. Anion exchange capacity (AEC) is given by

$$\mathrm{AEC} = [\mathrm{G}r\mathrm{C}l] + 2[\mathrm{G}r_2\mathrm{SO}_4] \tag{II.8}$$

$\frac{E_{Gr_2SO_4}}{E_{GrCl}}$ is deduced from measurements and $\frac{(Cl^-)^2}{(SO_4^{2-})}$ is inferred from measurements of total chloride and sulphate ion concentrations and activity ratios calculated with PHREEQC (a computer program for geochemical calculations, Parkhurst and Appelo (2013)). As a consequence, $K_{ex,GT}$ can be easily determined.

The Rothmund & Kornfeld convention makes it possible to describe ion exchange data when the affinity of the substance for a surface increases when the occupancy of this ions for the surface is increasing. This convention is also based on the ratio of equivalent fractions, but the ratio is augmented by an exponent (Bond, 1995). For example, the Rothmund & Kornfeld selectivity coefficient for the Cl-SO_4 exchange is:

$$K_{ex,RK} = \frac{(Cl^-)^2}{(SO_4^{2-})} \cdot \left(\frac{E_{SO_4}}{E_{Cl}^2}\right)^{\frac{1}{\beta}} \tag{II.9}$$

where β is an empirical positive-valued parameter. In this case, two parameters, β and $K_{ex,RK}$ must be determined with experiments.

The relationship between the Gaines & Thomas selectivity coefficient and the Rothmund & Kornfeld selectivity coefficient is :

$$K_{ex,GT} = K_{ex,RK}\left(\frac{(1-E_{SO_4})^2}{E_{SO_4}}\right)^{\frac{1}{\beta}-1} \tag{II.10}$$

The Rothmund & Kornfeld model is equivalent to the Gaines & Thomas thermodynamic convention in the case β = 1.

Examples of modeling ion exchange in LDH with these equations can be found in the litterature (Miyata, 1983; Israëli et al., 2000; Goh et al., 2009; Dessalegne et al., 2016; Marty et al., 2018; Everaert et al., 2019). To our knowledge, those models have not tested on exchange data obtained with green rust.

II.2.3 Solid solutions

A solid solution is a homogeneous mineral of variable composition, the end members of which do not necessarily have the same structure. In soils, the formation of solid solution may be responsible for the low solubility levels of trace elements such as zinc, for which pure phases are undersaturated (McBride, 1994). In the following, the principle of solid solution solubility modeling is taken from

McBride (1994). A mineral is composed of a trace metal cation, B, isomorphously substituted into a solid composed of metal cations, A, and anions, Y. The chemical formula of this mineral is $A_{1-x}B_xY$, where x can range from 0 to 1. AY and BY are the end members of the solid-solution and form a continuous series. Unlike ionic compounds of fixed composition, solid solutions do not have constant solubility products. Instead, solubility products K_{SO} of pure AY and BY have to be specified:

$$\begin{cases} K_{SO}^{AY} = \frac{(A)(Y)}{(AY)} \\ K_{SO}^{BY} = \frac{(B)(Y)}{(BY)} \end{cases} \tag{II.11}$$

with round brackets representing the activity of the species inside the brackets. At equilibrium, a reaction can described the distribution of A and B ions between the aqueous (aq) and solid (sl) phase by:

$$AY_{(sl)} + B_{(aq)} = BY_{(sl)} + A_{(aq)} \tag{II.12}$$

If the solid phase is homogeneous, the distribution coefficient D quantifies the degree to which cations A and B are incorporated into the solid with the following equation:

$$D = \frac{(BY)(A)}{(AY)(B)} = \frac{K_{SO}^{AY}}{K_{SO}^{BY}} \tag{II.13}$$

Ion exchange processes in fougerite has been modeled with this type of formalism considering all the elements present in the mineral in equilibrium equations (Parmar et al., 2001; Bourrié et al., 2004, 2019).

CHAPTER III

MATERIALS & METHODS

III.1 Necessity to avoid green rust contact with O_2 and CO_2

Green rusts and Fougerite contain a significant amount of Fe^{2+}, which can react with atmospheric dioxygen and transform into various iron (hydr)oxides (Ferrihydrite, Lepidocrocite, Goethite, etc.; Trolard and Bourrié (2008)). Therefore, minimizing contact with atmospheric O_2 at every experimental step is very important in order to avoid any phase transformation. LDH have also a high affinity for (bi)carbonate ions (Miyata, 1983), and gaseous CO_2 should also be regulated to avoid its dissolution into solution and its dissociation into bicarbonate and carbonate ions. Consequently, all synthesis steps and laboratory experiments (unless noted otherwise) were conducted in a glove box filled with a N_2 atmosphere (MBraun UNIlab Pro, Figure III.1). All solutions were prepared with O_2- and CO_2-free ultrapure water (resistivity of 18.2 MΩ.cm) and analytical grade salts. The glove box O_2 volumetric concentration was regularly monitored and did not exceed 0.1 Pa.

Figure III.1 – MBraun UNIlab Pro Glovebox used during this PhD thesis.

III.2 Synthesis of Co-GR

Synthetic samples were studied instead of natural samples for several reasons:

— a wide range of synthesis methods were available in the literature,

— synthesized samples had a higher level of purity,

— synthesis method allowed a fine-tuning of the structure and/or chemical composition. Especially, some of these methods allowed to include different types of isomorphic substitutions in the layer and to generate structural defects.

The synthesis method of Hadi et al. (2014) was chosen because it allowed for a fine-tuning of the size and amount of stacking defects. The drawback of the method was the partial substitution of Fe^{2+} by Co^{2+} in the layer. However, this was not considered to be a problem because (i) the crystallographic structure of the synthesized solids was almost identical to that of fougerite (see Chapter IV on Material Characterization), (ii) the layer charge was not influenced by the Fe^{2+} versus Co^{2+} substitution, and (iii) fougerite has never been observed as a pure Fe^{2+}/Fe^{3+} phase in natural environments because of isomorphic substitutions of Fe by foreign cations such as Mg, Ni, or Zn (Trolard et al., 2007; Zegeye et al., 2012; Johnson et al., 2014).

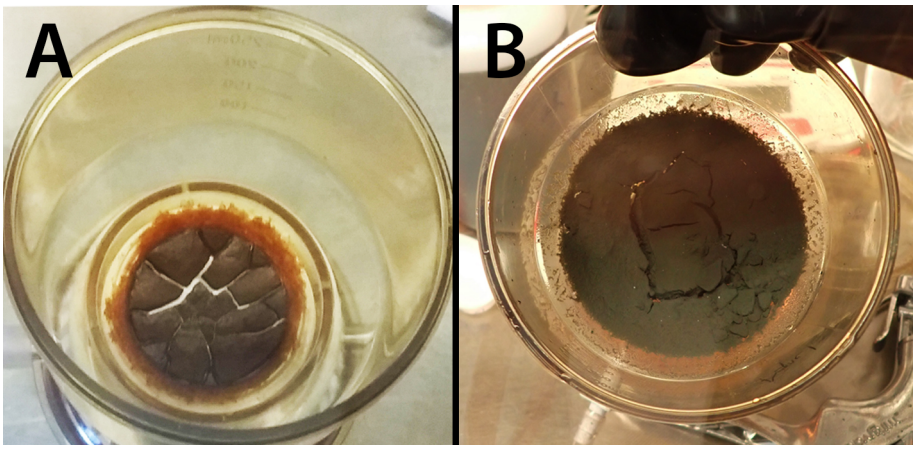

Figure III.2 – Various synthesized samples: A- a wet powder of nano-Co-GR and B- a wet powder of micro-Co-GR.

Green rust were synthetized by mixing a $FeCl_2$ solution (50 $g.L^{-1}$ or 394.5 $mmol \cdot L^{-1}$) with an hexamminecobalt(III) chloride solution (CoHex, 10 $g.L^{-1}$ or 37.4 $mmol \cdot L^{-1}$). Two samples were synthesized by varying the volume ratio of $FeCl_2$ to CoHex solutions so as to produce a turbostratic [1] and nanometric green rust, hereafter named nano-Co-GR(Cl) (Fe/Co = 0.12 in the initial solution, P1 sample in Hadi et al. (2014), Figure III.2 B), and a defect-free and micrometric green rust, hereafter named micro-Co-GR(Cl) (Fe/Co = 1.84 in the initial solution, P4 sample in Hadi et al. (2014), Figure III.2 C). The samples aged for three days before filtration of the dispersion (cut-off diameter: 0.22 µm). This synthesis method did not require external control on the pH, which reached green rust equilibrium pH as soon as the solid precipitated (pH range during synthesis for nano-Co-GR(Cl) = 8.3-8.6, and micro-Co-GR(Cl) = 8-8.2) (Hadi et al., 2014). No additional washing was done before the solid samples were dried for one day in order to minimize side reactions, including dissolution, that could have been induced by changes in chemical conditions, which always occur during washing procedures. Micro-Co-GR(Cl) displayed a dark green color but nano-Co-GR(Cl) was orange to dark orange (Figure III.2). Further characterization of the mineral were made to verify that their structure were close to that of green rust or fougerite, and to detect and quantify impurities such as iron oxides.

III.3 Chemical composition of Co-GR samples

The structural formula of the Co-GR was:

$$[Fe^{2+}_{1-x-y}Fe^{3+}_{x}Co^{2+}_{y}(OH)_2]^{+x} \cdot [\frac{x}{n}A^{-n} \cdot mH_2O]^{-x} \quad \text{(III.1)}$$

1. Turbostratism is defined by the systematic occurrence of random translations parallel to the layers and/or rotations about the normal direction to the layers between successive layers.

Figure III.3 – Cameca SX Five electron microprobe (Source: ISTO website).

where A^{-n} is an anion with a n charge.

III.3.1 Layer Structural Formula & Interlayer Anion Content - Electron Probe Micro-Analyzes (EPMA)

Electron probe micro-analyzes (EPMA) is an analytical tool used to determine the chemical composition of phases (or solid materials in general). In this work, the values of x and y (Equation III.1), which can vary between 0 and 1, were calculated from EPMA (Cameca SX Five electron microprobe, Figure III.3). Four samples were studied: Micro-Co-GR(Cl) and (SO_4) and Nano-Co-GR(Cl) and (SO_4). Co-GR(SO_4) were obtained after an ion exchange experiment with a 25 mmol$\cdot L^{-1}$ Na_2SO_4 solution on Co-GR(Cl) samples. Analyses were carried out on freeze-dried samples embedded in epoxy resin mounts (two weeks of embedding before hardening the epoxy resin in order to minimize the presence of N_2 bubbles). After polishing the epoxy resin mount, a 10 – 20 nm thick carbon layer was sputter-coated on the samples. Acceleration voltage was 15 kV, beam current was 10 nA, and beam width was 1 – 2 µm. Fe Kα and Co Kα were analyzed using a LiF (lithium floride) crystal, while Cl Kα and SO_4 Kα were analyzed with a large pentaerythritol and a pentaerythritol crystal, respectively. Pyrite, metallic Co, vanadinite, and celestite were used as standards for Fe, Co, Cl, and SO_4, respectively. Counting times were set to 30 s for all elements. Depending on the sample, the number of independent measurements ranged from 35 to 61.

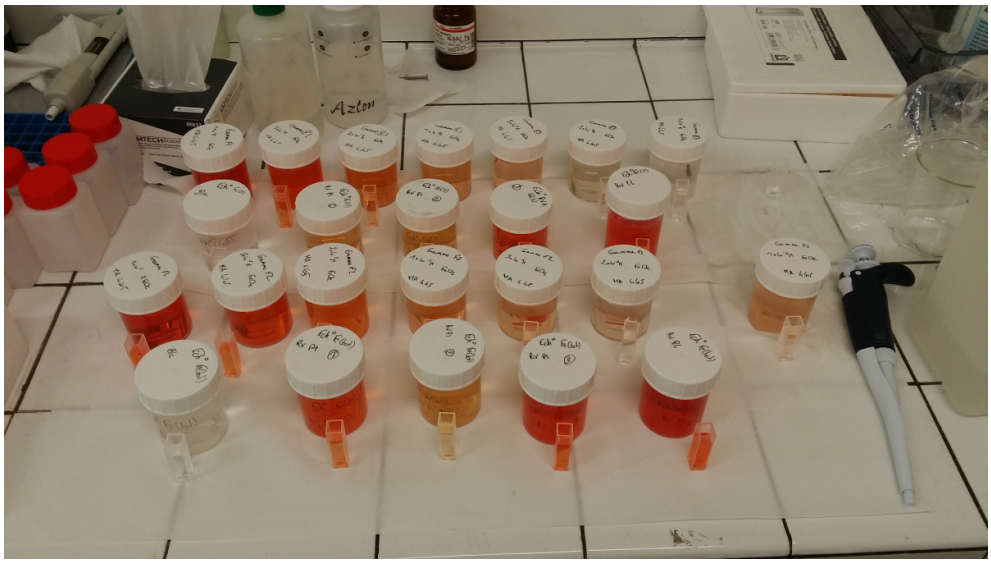

Figure III.4 – Samples with iron concentration quantified by spectrophotometry using the 1,10-phenanthroline method.

III.3.2 Iron content - 1,10-phenanthroline method

Total Fe content in Co-GR was cross-checked using a modified 1,10-phenanthroline method (Amonette and Templeton, 1998; Stucki, 1980; Stucki and Anderson, 1980), which was developed for iron speciation analysis in solid samples. The method proceeds in two steps: the measurement of Fe^{2+} content, and then the measurement of total Fe content after reduction of all Fe^{3+} present into Fe^{2+}. However, Vydra and Přibil (1959, 1960) have shown that Co(II)-phenanthroline complexes reduce Fe(III)-phenanthroline complexes. Therefore, when applied on samples containing Fe and Co, the Fe(II) value obtained during the first step represents, in fact, the Fe(II) content in the sample plus a part of Fe(III)-phenanthroline complexes that was reduced by Co(II)-phenanthroline complexes. Consequently, only the total Fe content (Fe(tot)) was taken into considerations.

The methodology used is described in Hadi et al. (2013) and modifications from Hadi et al. (2014) were followed. Preparations and analyses were done out of the glove box (Figure III.4). 20 to 25 mg of solids were dissolved in a 15 mL solution containing HNO_3 (10 %w) and 1,10-phenanthroline (10 %w) at 70 °C for 30 min. The reaction was stopped by adding 10 mL $B(OH)_3$ (10 %w). The resulting solutions were diluted to 100 mL with pure Mili-Q water. Then, 10 mL aliquots were reacted overnight with 100 mL of a solution containing citrate and hydroxyl ammonium (to reduce all of the Fe^{3+} to Fe^{2+}). Finally, solutions were analyzed by colorimetry, at 510 nm, in triplicate, and using a 50 Scan UV–Vis spectrometer (VARIAN). Iron concentrations were obtained with the use of a calibration curve where total Fe concentrations ranged from 0 (Pure Mili-Q water) to 100 $\mu mol \cdot L^{-1}$.

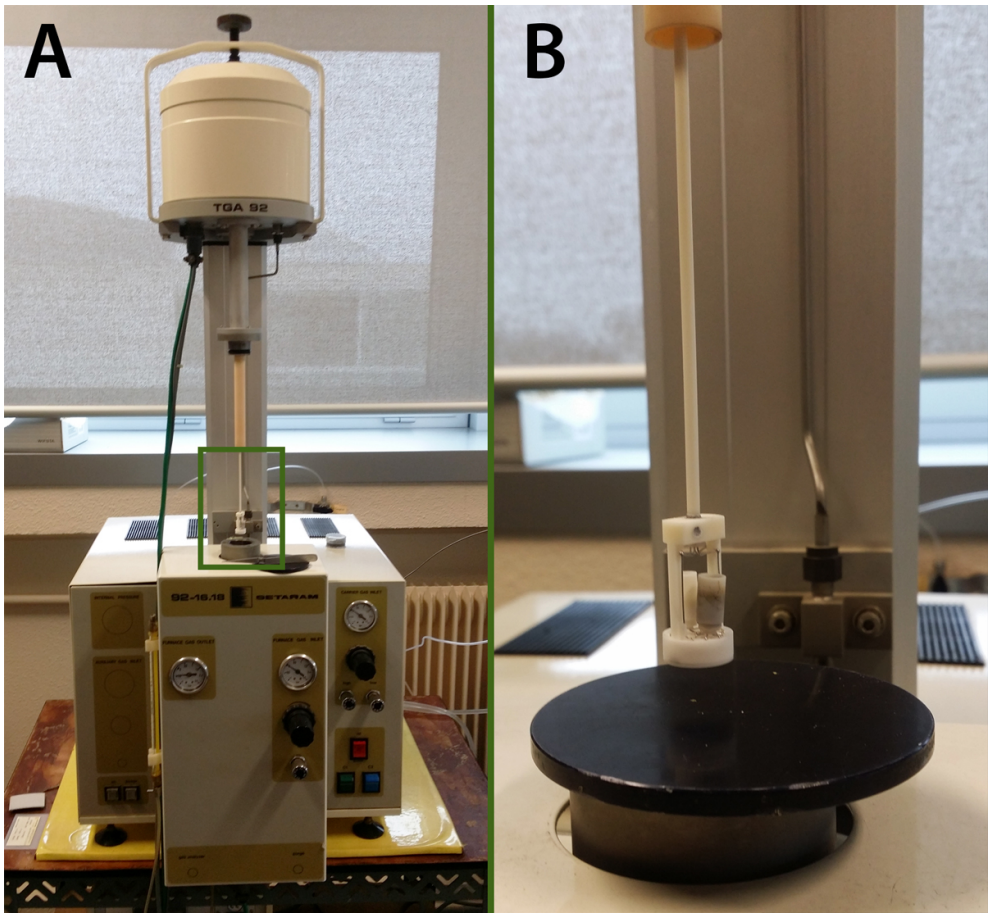

Figure III.5 – Setaram TGA 92-16.18 (A) with a zoom on the sample holder (B).

III.3.3 Water content - Thermogravimetric Analysis (TGA)

The water content (m) was determined with thermogravimetric analysis (TGA) and differential scanning calorimetry (DSC, Equation III.1). Samples were dried for one day in the glove box, before measurement on a Setaram TGA 92-16.18 under an Argon flux (Figure III.5). Approximately 50 mg of powder was heated from 20 °C to 500 °C at 1 °C $\cdot$ min^{-1}. Then, the temperature was maintained at 500 °C for 1 h before cooling.

The mass loss attributed to water vaporization during the TGA measurement (ΔTG) was linked to the value of m according to:

$$m = \frac{\mathrm{M_{GR}}}{\mathrm{M}_w} \times \frac{\Delta \mathrm{TG}}{m_{\mathrm{GR}}} \tag{III.2}$$

where $\mathrm{M_{GR}}$ is the molar mass of the anhydrous GR (i.e. considering m = 0), m_{GR} is the mass of the anhydrous sample, and M_w is the molar mass of water. Care was taken to avoid any contact with atmospheric O_2 and CO_2 during sample transportation and analysis.

III.4 Structure of studied samples - X-ray Diffraction (XRD)

III.4.1 Laboratory and synchrotron analysis

The X-Ray Diffraction pattern (XRD) of a single phase is composed of three main contributions: the interference function, the structure factor and the polarization function. The interference function depends on the geometry of the unit cell. This function is responsible for the number and positions of reflections on a XRD pattern. The structure factor depends on the distribution of the electronic density in the unit cell, which is dependent on the nature and position of the atoms in the unit cell. Its main influence on the XRD pattern of a 3D-ordered phase is the relative intensity of the diffraction maxima. Finally, the polarization function describes the polarization of X-rays after the interaction with the powder.
Non-reacted green rust samples were first characterized in the BRGM laboratory, and XRD patterns were acquired in continuous scan mode over the 4 – 80° 2θ Cu Kα range using a Brucker D8 diffractometer equipped with a Cu anode (λ Kα = 1.5418 Å) and a LynxEye XE detector. Total counting time was 6 h. Intensities were integrated every 0.04° 2θ Cu Kα. Samples were prepared in the glovebox and put in closed polyimide capillaries to be preserved from oxidation during the preparation and XRD measurements.

All other XRD patterns presented in the manuscript were measured at either beamline Crystal, Soleil synchrotron (X-ray wavelength λ was 0.4367 Å) or beamline MSPD, Alba synchrotron (λ was 0.8258 or 0.8266 Å). All polyimide capillaries were prepared in the glovebox and sealed in a glass jar for transportation from the BRGM laboratory to the synchrotron facilities.

Rietveld refinements were carried out on micro-Co-GR(Cl) with data measured at Alba synchrotron, using the Fullprof software (Rodriguez-Carvajal, 1990) with the structure models from fougerite and magnetite (Trolard et al., 2007; Wechsler et al., 1984). The quality of the data modeling was quantified using the R_p, R_{wp}, R_{exp}, and goodness-of-fit (GoF) parameters, where R_p is the unweighted residual error, R_{wp} is the weighted residual error, R_{exp} is the lowest R_{wp} that can be achieved as a result of statistical noise on the data, and GoF is the squared R_{wp} to R_{exp} ratio (Post and Bish, 1989):

$$\begin{cases} R_p = \frac{\sum |Y_{io} - Y_{ic}|}{\sum Y_{io}} \\ R_{wp} = \left[\frac{\sum w_i (Y_{io} - Y_{ic})^2}{\sum w_i Y_{io}^2} \right]^{0.5} \\ R_{exp} = \left[\frac{(N-P)}{\sum w_i Y_{io}^2} \right]^{0.5} \\ GoF = \frac{R_{wp}^2}{R_{exp}^2} \end{cases} \quad \text{(III.3)}$$

where Y_{io} and Y_{ic} are respectively observed and calculated intensities at a point i, w_i is the weight assigned each step intensity, N is the number of data points in the pattern and P is the number of parameters refined. Rietveld refinements were only applied to 3D-ordered structures. A dedicated software was used to refine defective structures (Plançon, 1981, 2002).

III.4.2 XRD & Pair distribution function (PDF)

Pair distribution function (PDF) data were calculated from X-ray patterns to isolate and quantify the short-range (lower than the layer-to-layer distance) order of atoms. High-energy X-ray scattering data were measured at beamline CRISTAL at the SOLEIL synchrotron (Paris, France; September 2017). Methods and instrumental set-up previously developed by Grangeon et al. (2017b,a) were used. The energy was 28 keV and the X-ray wavelength λ was 0.4367 Å. Powders were loaded into polyimide capillaries (Kapton). An XPad hybrid pixel detector collected data between 1.2 and 124.5° 2θ angular range with a total collection time of 30 min. Then, data were processed with the software FUSION (Ounsy et al., 2013) and Fourier transformed to X-ray pair distribution function (PDF) data with PDFgetX3 (Juhás et al., 2013).

PDF were also calculated with structural models to observe the influence of various parameters on the PDF results. For example, systematic random stacking disorder (turbostratism disorder) affects the PDF by cancelling out the contribution from atomic pairs formed from atoms located on distinct layers. To quantitatively assess this effect, two PDF were calculated with PDFgui (Farrow et al., 2007). The first one, which served as a model PDF for an ordered and micrometric green rust, was calculated using the fougerite structure model (Trolard et al., 2007), in which the number of water molecules and *a* and *b* lattice parameters were adjusted to match data acquired with a Rietveld refinement on X-ray patterns, and in which the occupancy of layer oxygen was set to 1. The second calculated PDF aimed at mimicking the PDF of a turbostratic and nanosized green rust. For this purpose, a structure model was created, in which a single fougerite sheet was isolated in a lattice cell with *a* and *b* dimensions identical to that of the ordered fougerite but with *c* dimension expended to 30 Å to cancel any correlations related to atoms located on distinct layers in the calculated PDF (up to 20 Å). Note that the relative

atomic coordinates of all atoms were corrected correspondingly, so that the layer structure remained unaffected by this operation. The drawback of using such a "supercell" approach was the significant lowering of the electronic density in the cell, ρ, compared to that of an actual turbostratic sample. This effect manifested itself in the calculated PDF with an underestimation of the slope at low r values, which is a function of ρ (Egami and Billinge, 2012a). However, this did not affect the position or the intensity of correlations, which could be compared safely to other calculated or experimental data. The size of crystallites was set to 50 Å using the "spdiameter" parameter from PDFgui. For both structures, the u_{11}, u_{22}, and u_{33} anisotropic displacement parameters of Fe were 0.01 Å and those of interlayer species were 0.1 Å. u_{11} and u_{22} of layer oxygen were also 0.01 Å, but u_{33} was set to 0.03 Å to match the experimental data. Such an increase in u_{33} of layer oxygen was also observed for several other layered phases such as manganese oxide (Zhu et al., 2012; Grangeon et al., 2017b), hydrated calcium aluminate (Marty et al., 2018), calcium silicate hydrate (Grangeon et al., 2017a) or poly-phase materials (Shi et al., 2014). This effect was possibly related to layer corrugation.

III.4.3 XRD models & Interstratification

The software developed by Plançon and Drits (2000) was used to model the effect of various interstratification types on XRD patterns. The instrumental parameters for MLM2C code were fixed to the instrumental parameters of MSPD beamline at Alba (Table III.1). The sample parameters such as μ^*, the mass absorption coefficient, and the sample density were fixed at 45 $g^{-1} \cdot cm^2$ (value for phyllosilicate,(Ferrage, 2004)) and 3000 $kg \cdot m^3$ respectively. The only fitted parameter was σ^*, the angle that corresponds to the standard deviation of a Gaussian function of crystal orientation in the powder. The more σ^* is important, the more particle are oriented in the powder. σ^* was fitted on the first pattern and then, it was kept fixed for all other patterns.

Table III.1 – Instrumental and sample parameters for modeling *00l* reflections with MLM2C code.

Parameter	
λ (Å)	0.82655
Divergent slit (°)	0.003
Goniometer radius (cm)	55
Sample length (beam size, cm)	0.1
Sample density ($kg \cdot m^3$)	3000
μ^* ($g^{-1} \cdot cm^2$)	45
σ^*	0.55

Two structural models were implemented for each layer type: one layer containing Cl^- in the interlayer (Gr-Cl), and one layer with ${CO_3}^{2-}$ in the interlayer (Gr-CO_3). In the structure model, the

occupancy of each atom was taken from the structural formula deduced from EPMA results (Table IV.1, see chapter IV). A stoichiometry of 2 Cl^- for 1 CO_3^{2-} was chosen in order to compensate for the charge difference between the two anions. Two water molecules were associated with Cl^- for Gr-Cl layers following TGA results (Table IV.3, see chapter IV). The stoichiometry of water molecules for Gr-CO_3 had to be fitted and results can be found in chapter V. The Debye-Waller factors (DWF) were fitted on the initial ($V/V_r = 0$, V/V_r is the pore volume) and last pattern ($V/V_r = 20.4$) for Gr-Cl and Gr-CO_3 layers respectively and this parameter was fixed for all the other patterns. The layer-to-layer distance d_{003} for each layer type was fitted at each pattern. The mean number of layer was fitted on the initial pattern and then, fixed for the other patterns. Intensities were normalized to the 006 reflection. These models also had 20 values of scattering-factor functions f for each atom (unit: electron, Waasmaier and Kirfel (1995)):

$$f(s) = \left(\sum_{i=0}^{4} a_i \exp(-b_i s^2) \right) + c \tag{III.4}$$

where $s = \frac{\sin\theta}{\lambda}$ from 0 to 0.95 $Å^{-1}$ with a step of 0.05 $Å^{-1}$, a_i, b_i and c are tabulated parameters from Waasmaier and Kirfel (1995).

Table III.2 – Structural model of the two layers used to model the interstratified XRD patterns with MLM2C (d_{003} - layer-to-layer distance, DWF - Debye-Waller Factor, fitted - this parameter was fitted for each file).

Layer type		Gr-Cl	Gr-CO_3
	d_{003} (Å)	fitted	fitted
position z (Å)	Fe and Co layer	0	0
	O layer	1 & -1	1 & -1
	Water	$d_{003}/2$ & $-d_{003}/2$	$d_{003}/2$ & $-d_{003}/2$
	Cl^- or CO_32- interlayer	$d_{003}/2$ & $-d_{003}/2$	$d_{003}/2$ & $-d_{003}/2$
DWF	Fe and Co layer	0.5	0.5
	O layer	0.5	0.5
	Water	1	3
	Cl^- interlayer	1	
	CO_3^{2-} interlayer		3
Occupation	Fe^{2+}	0.42	0.42
	Fe^{3+}	0.25	0.25
	Co^{2+}	0.33	0.33
	O layer	2	2
	Water	0.5	0.625
	Cl^- interlayer	0.25	
	CO_3^{2-} interlayer		0.125
	Mean number layers	40 (together)	

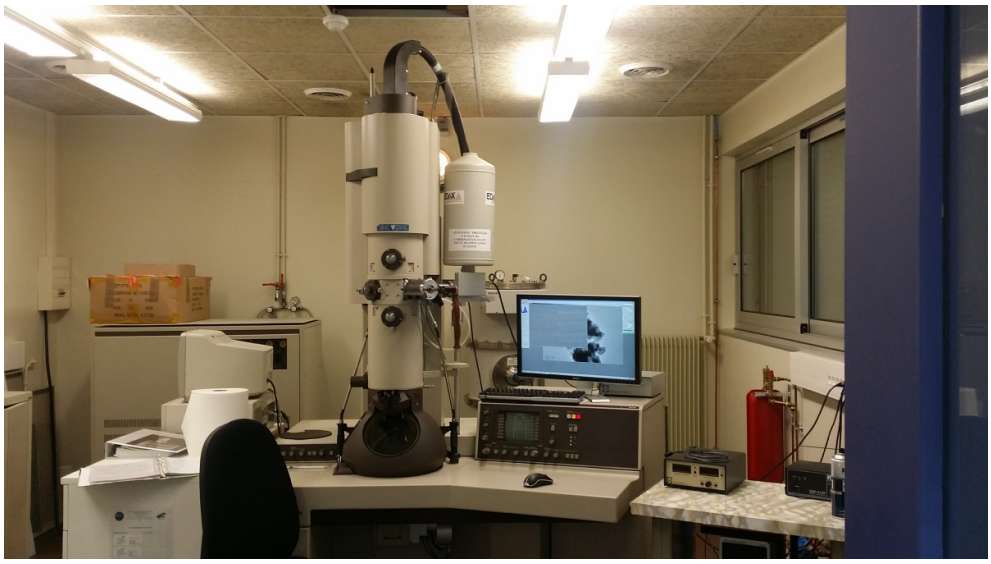

Figure III.6 – Philips CM20 transmission electron microscope.

III.5 Morphology of studied samples - Transmission Electron Microscopy (TEM)

Transmission electron microscopy (TEM) images allowed to have a high-definition image of the morphology and size of crystals. TEM samples were prepared according to two different methods. In the first method, solid powders were dispersed into ultrapure water using an ultrasonic bath and then deposited on lacey carbon films loaded on copper grids in the glovebox. In order to avoid oxidation, samples were preserved in a glovebox until the sample was put on the sample holder. The contact of the sample with air was minimized to less than 2 min. Samples were then directly inserted in the transmission electron microscope. In the second method, samples were embedded in Agar 100 resin and left for polymerization for 2 days in the dark. Then, 80 nm thick slices were prepared with an ultramicrotome (Reichert-Jung Ultra-cut E) equipped with a diamond knife. The slices were deposited on lacey carbon films loaded on copper grids. TEM data were acquired using a Philips CM20 operated at 200 kV (Figure III.6). Energy dispersive X-ray specta (EDX) were acquired with an EDAX EDX detector.

III.6 Anion exchange processes on studied samples

III.6.1 Mechanism determination - *in situ* XRD

Phase structure modifications such as dissolution and precipitation, modification of the interlayer distances, or interstratification was followed during sorption processes using *in situ* and time-resolved

XRD. Two sets of experiments were conducted at beamline MSPD (ALBA Synchrotron, Barcelona, Spain) to search for structural modifications in the case of long-range interactions modifications during the exchange, and possibly investigate the associated exchange mechanisms:

— Exchanges of chloride and sulphate ions on nano-Co-GR and micro-Co-GR (November 24-27 2017). The X-ray wavelength (λ) was 0.8258 Å (15 keV). A diffraction pattern was acquired every 15 s during the experiments.

— Exchanges of chloride ions, sulphate ions and carbonate species on micro-Co-GR (January 24-27 2020). λ was 0.8266 Å (15 keV). A diffraction pattern was acquired every 25 s during the experiments.

Experimental methods and equipment setup were similar for both sets of experiments and adapted from Grangeon et al. (2017b). In the N_2 atmosphere glovebox, glass marbles and then, sample powder were loaded in polyimide capillaries sealed at both extremities using a frit-in-a-ferrule system (Idex Health & Science) (Figure III.7 and III.8 A). Glass marbles were useful to avoid clogging the frit-in-a-ferrule system with the sample and to limit the amount of powder because the capillary was long (9 cm long capillary and ≈ 30 mg of sample powder). Samples were sealed in airtight containers in glovebox. Then, they were stored in another N_2 atmosphere glovebox at the synchrotron facility until being used for the experiments. At the beginning of each experiment, a capillary was connected on one-side to a peristaltic pump and to the other side to a sampling pot, using silicon tubing (Figure III.7 and III.8 B). The flow rate of the pump was $1-2\ mL\cdot h^{-1}$. X-ray diffraction patterns were collected with a Mythen detector. In a first step (equilibrium step), the Co-GR sample was hydrated by flowing a solution of 50 $mmol\cdot L^{-1}$ NaCl at pH 7-8. In a second step (exchange step), a solution containing Na_2SO_4, $NaHCO_3$ or Na_2CO_3 a binary mix of these salts was flowed through the capillary. In the following, the exact composition of the solutions will be specified for each experiment. All solutions were bubbled with N_2 during the experiments except the solutions containing $NaHCO_3$ or Na_2CO_3, which were prepared in a glovebox under N_2 and put in JM Bioconnect pillow bags (Figure III.8 C). The pillow bags avoided gas exchange with the atmosphere, and prevented O_2 dissolution and associated changes in solution composition. They were connected to the peristaltic pump and emptied themselves during the experiment without any gas entrance from the atmosphere.

Several hundreds of XRD patterns were acquired for each experiment, and were treated automatically using a custom-made Python code in order to extract peaks position, intensity, area, full width at half-maximum (FWHM) and crystallite size. The crystallite size was calculated using Scherrer's law

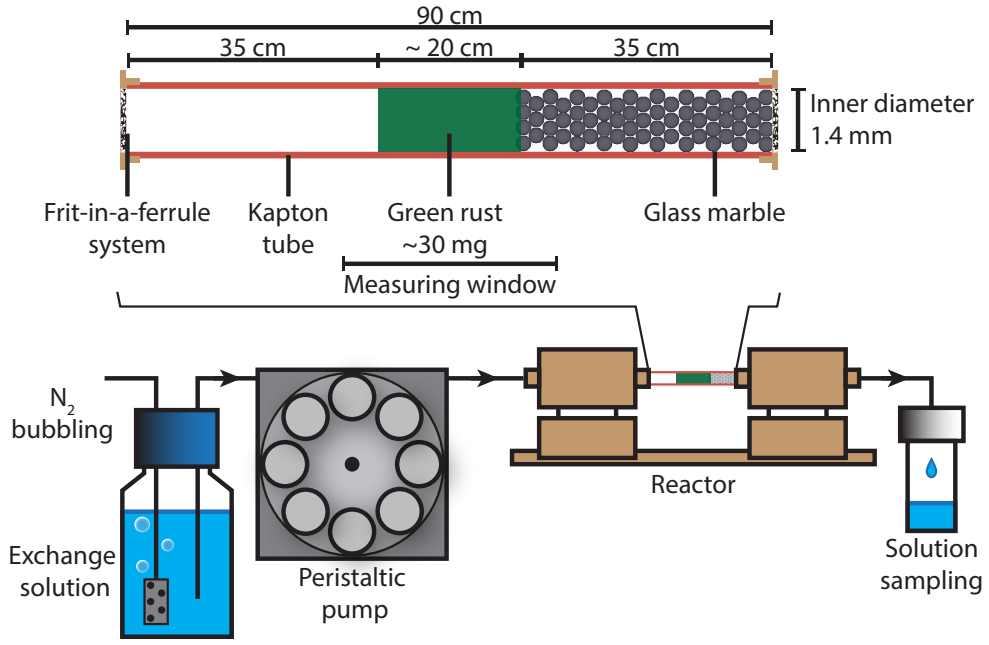

Figure III.7 – The experimental setup during sorption experiment at MSPD beamline (modified from Grangeon et al. (2017b))

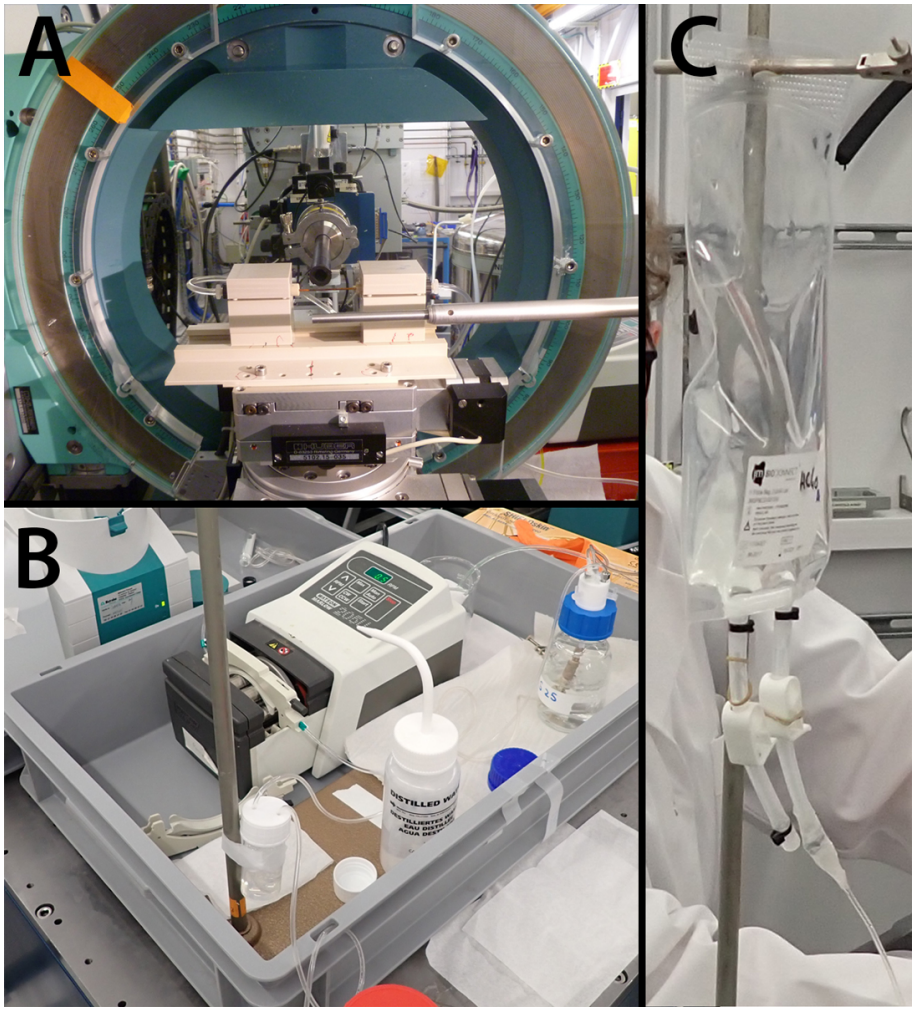

Figure III.8 – Pictures of experimental setup during sorption experiment at MSPD beamline: A- Reactor containing the capillary, B-Peristaltic pump and solutions, C- Pillow bag for solution containing $NaHCO_3$ or Na_2CO_3.

(Scherrer, 1918):

$$D = \frac{k\,\lambda}{FWMH\ cos(\theta)} \tag{III.5}$$

in which D is the crystallite size (Å), k is a shape constant (equal to 1), λ is the X-ray wavelength (Å), FWHM is the full width at half-maximum of the diffraction peak (rad) and θ is the Bragg angle (rad). FWHM were measured from a fit of the *00l* peak so the crystallite size was given along c^* *i.e.* perpendicular to the **a**-**b** plane.

III.6.2 Quantification - Wet chemistry experiments

Ion exchange experiments were carried out in order to, first, determine the stoichiometry of the exchange and the sample anion exchange capacity (AEC) , and second, quantify the exchange with thermodynamic parameters. Anion exchange were studied with chloride ions, sulphate ions and carbonate species (CO_3^{2-} and HCO_3^-) on micro-Co-GR. Chloride and sulphate ion exchange were also studied on nano-Co-GR to decipher the influence of crystal size and structural defects with a comparison to micro-Co-GR results. Tests were also made to observe the reversible nature of the exchange with carbonate species (Miyata, 1983; Costantino et al., 1998; Rives, 2001; Okamoto et al., 2006; Iyi and Sasaki, 2008). Chloride and sulphate ions are among the most abundant mineral anions in forest soils along with nitrate ions (Blume et al., 2010). Carbonate species are also usually found in soils and sorb strongly to LDH (Miyata, 1983).

The following steps were common to every set of batch experiments, experiments to determine exchange stoichiometries, AEC, and exchange selectivity coefficients. Stock solutions as well as a mixtures of these solutions were prepared so as to reach a constant Na^+ concentration of 50 $mmol \cdot L^{-1}$ and a pH value between 7 and 8. Green rust samples were dried for one day prior to experiments. During the preconditioning step, about 0.2 g of nano-Co-GR(Cl) or 0.5 g of micro-Co-GR(Cl) were equilibrated with 200 mL of a 50 $mmol \cdot L^{-1}$ NaCl solution for 30 min (Step E). Then, the solution and the solid were separated by filtration (cut-off diameter of 0.22 µm). The solid was rinsed with $30-40$ mL of O_2- and CO_2-free ultrapure water and then filtrated (Step R_1). During each of the following steps, except rinsing, the green rust sample was dispersed in the solutions during 30 min, which was sufficient to attain steady-state conditions based on *in situ* XRD measurements of exchange experiments. Experimental details can be found in appendix for each experiment (Tables S2, S3, S13, S14 and S15).

Table III.3 – Example of a batch exchange experiment method used with micro-Co-GR. Each step lasted 30 min except when direct filtration is written (Solutions specifications: Cl50 - 50 mmol·L^{-1} of NaCl, S2.4/Cl45 - 2.4 mmol·L^{-1} of Na_2SO_4 and 45 mmol·L^{-1} of NaCl, S15 - 15 mmol·L^{-1} of Na_2SO_4).

Step	Name	Solution specification
Equilibrium phase	E	200 mL Cl50
Rinsing 1	R_1	30-40 mL Milli-Q Water
		Direct Filtration
Exchange phase 1 - 1	1	20 mL S2.4
2	2	40 mL S2.4/Cl45
3	3	60 mL S2.4/Cl45
4	4	100 mL S2.4/Cl45
5	5	200 mL S2.4/Cl45
6	6	200 mL S2.4/Cl45
Rinsing 2	R_2	30-40 mL Milli-Q Water
		Direct Filtration
Exchange phase 2 - 1	7	200 mL S15
2	8	200 mL S15

Stoichiometry & AEC determination with total exchange experiments

The objective of this set of experiments was the characterization of the exchange stoichiometries between chloride and either sulphate or carbonate species. The second objective was the determination of the anion exchange capacity (AEC), with the measurement of the total amount of Cl^- released by the sample. Green rust samples were dispersed in a 25 mmol·L^{-1} Na_2SO_4, $NaHCO_3$ or Na_2CO_3 solutions and then filtrated. Two experiments were also done with a 50 mmol·L^{-1} Na_2CO_3 solution. Three to five successive dispersion-filtration steps were carried out.

Thermodynamic parameters - Partial exchange experiments

The objectives of this second set of experiments were to calculate surface equivalent fractions as a function of solution composition (Equation II.6 for example), and to calculate the corresponding ion exchange selectivity coefficients.

Green rust samples were dispersed in solutions containing a mix of NaCl and Na_2SO_4, $NaHCO_3$ or Na_2CO_3 with a total Na^+ concentration of 50 mmol·L^{-1} and then filtrated. Experiments were also done with a solution containing a mix of Na_2SO_4 and $NaHCO_3$ to study an ion exchange between SO_4^{2-} and CO_3^{2-}. Again, several dispersion-filtration steps were carried out at different chemistry conditions. All concentrations and volume values can be found in appendix for each experiment (Tables S2, S3, S13, S14 and S15). An detailed example of the experimental method can be found in Table III.3.

Experiments were modelled using PHREEQC (Parkhurst and Appelo, 2013). Measured concentrations of stock solutions and volumes added to the system were used as inputs in the model. Exchange stoichiometries and AEC were obtained from previous total exchange experiments. Selectivity coefficients for Gaines & Thomas or Rothmund & Kornfeld convention were then adjusted to fit data measured in the solutions after every step of the experiment. Model results also gave proportions of each anion on green rust surfaces (equivalent fraction).

Ionic concentration analysis

Cl^- and SO_4^{2-} concentrations of all solutions used for and obtained after chemistry experiments and synchrotron experiments were quantified by high-performance liquid chromatography (HPLC, Thermo Scientific Dionex ICS-3000). Concentrations of solutions used for the calibration of the HPLC ranged from 0.05 mg·L^{-1} to 50 mg·L^{-1} ($1.4\times10^{-3}-1.4$ mmol·L^{-1} for Cl^- and $5.2\times10^{-4}-0.52$ mmol·L^{-1} for SO_4^{2-}). Three calibration curves were calculated from the measurements of these standard solutions for the following concentration ranges: $0.05-0.5$, and $0.5-5$, $5-50$ mg$\cdot L^{-1}$. Solutions from the experiments were diluted so that the concentration fell in the range of calibration. Each measurement was made in duplicate. Solutions from the calibration, a standard solution (Ion Chromatography Anion Mix 14 from AccuStandard), and pure-water were analyzed several times during the analysis to verify the accuracy and precision of the equipment. Measurement uncertainties of measurements were obtained from the BRGM laboratories, and amounted to 6 % and 7.5 % for for Cl^- and SO_4^{2-} concentrations respectively.

For the exchange with carbonate species, alkalinity of each solution was measured once by automatic titration (Metrohm 905 Titrando and 800 Dosino) in the N_2 atmosphere glovebox just after sampling. Stock solutions containing carbonate species were analyzed before and after the experiment to make sure that concentrations did not change significantly due to CO_2 volatilising. Solutions were titrated down to pH 2.5 with a titrant solution of HCl at 0.05 mol$\cdot L^{-1}$ or 0.1 mol$\cdot L^{-1}$. Titrant solution was added automatically by the titrator in order to have a high ΔpH resolution, especially near the equivalence point. Data were interpreted with the Gran function plot method (Gran, 1952; Rounds and Wilde, 2012). The F_1 Gran function was calculated with:

$$F_1 = (V_0 + V_t) \times 10^{-pH} \tag{III.6}$$

with V_0 the initial volume of the sample and V_t the added volume of acid titrant. This function identifies the point at which all alkalinity has been titrated and hydronium ions begin to be in excess. A straight line was extrapolated from the data in the region beyond the bicarbonate equivalence point, its intersection with the x-axis gives V_{eq} ($F_1 = 0$ and $V_t = V_{eq}$). The bicarbonate equivalence point was given by the volume V_{eq}. Alkalinity (Alk) was given by (unit: $meq \cdot L^{-1}$):

$$Alk = \frac{V_{eq}}{V_0} \times C_t \tag{III.7}$$

with C_t the concentration of acid titrant.

pH, alkalinity and other ion concentrations (Na^+, Cl^- and SO_4^{2-} if needed) were used as input in a PHREEQC model to define the total carbon concentration and the speciation of carbonate species (CO_3^{2-}, HCO_3^-, $NaCO_3^-$, etc.). Uncertainty of measurement was estimated to be 5 %.

Uncertainty calculations

Two different type of calculations were made to assess the quality of the data (Danzer, 2007):

1. Experimental means and standard deviations were calculated when necessary if the number of data points was large enough. These values give an idea about the statistical distribution of the results of series of measurements,
2. Empirical uncertainties give an assumed probability distribution for the actual value, usually based on technical information and experience. For a single value, empirical uncertainty is calculated according to the law of error propagation as the combination of the errors for each measurement needed in calculating the said value.

For the empirical uncertainty, a measured value (y) was calculated from the list of n parameters p ($p_1, p_2, ..., p_n$) of which y is a function ($y = f(p_1, p_2, ..., p_n)$). The source of uncertainty and its value should be assigned and calculated for each parameter p. When this method was used, all parameters were considered independent. The uncertainty u of the measured value y is:

$$u(y(p_1, p_2, ..., p_n)) = \sqrt{\left(\frac{\partial y}{\partial p_1}\right)^2 \cdot (u(p_1))^2 + \left(\frac{\partial y}{\partial p_2}\right)^2 \cdot (u(p_2))^2 + \cdots + \left(\frac{\partial y}{\partial p_n}\right)^2 \cdot (u(p_n))^2} \tag{III.8}$$

with $u(p_i)$ the uncertainty of the p_i parameter.

The extended combined uncertainty $U(y)$ represents an interval that contains a (sufficiently) large part of the values of a series of measurements that could reasonably be attributed to the measured value:

$$U(y) = k \cdot u(y) \tag{III.9}$$

where k is the coverage factor, usually $k = 2$ or 3. For normally distributed measured values, $k = 2$ covers an interval in which 95.5 % of the values are found and $k = 3$ covers correspondingly 99.7 %. For this work, $k = 3$ was taken.

The confidence interval includes the estimated y and is given by:

$$unc(y) = y \pm U(y) \tag{III.10}$$

CHAPTER IV

MATERIAL CHARACTERIZATION

This chapter is dedicated to the characterization of the sample after synthesis (Co-GR(Cl) phases) and after an exchange with sulphate anions (Co-GR(SO_4 phases). For the samples obtained after an exchange with carbonate species, the results are presented in the next chapter (Chapter V).

IV.1 Chemical composition

IV.1.1 Layer Structural Formula & Interlayer Anion Content - EPMA

According to EPMA (Table IV.1), the structural formulas for the two synthesized samples were :

— Micro-Co-GR(Cl) - $[Fe^{2+}_{0.42(8)}Fe^{3+}_{0.25(4)}Co^{2+}_{0.33(4)}(OH)_2]\cdot[Cl^{-}_{0.25(4)}\cdot mH_2O]$

— Nano-Co-GR(Cl) - $[Fe^{2+}_{0.29(6)}Fe^{3+}_{0.20(3)}Co^{2+}_{0.51(5)}(OH)_2]\cdot[Cl^{-}_{0.20(3)}\cdot mH_2O]$

After exchange with ${SO_4}^{2-}$, structural formulas became:

— Micro-Co-GR(SO_4) - $[Fe^{2+}_{0.44(4)}Fe^{3+}_{0.22(2)}{Co^{2+}}_{0.34(2)}(OH)_2]\cdot[(SO_4)^{2-}_{0.11(1)}\cdot mH_2O]$

— Nano-Co-GR(SO_4) - $[Fe^{2+}_{0.37(5)}Fe^{3+}_{0.16(2)}Co^{2+}_{0.48(3)}(OH)_2]\cdot[(SO_4)^{2-}_{0.08(1)}\cdot mH_2O]$

The transformation of nano-Co-GR(Cl) and micro-Co-GR(Cl) samples into their sulphate forms, nano-Co-GR(SO_4) and micro-Co-GR(SO_4), respectively, did not change significantly their layer composition. Two Cl^- ions were replaced by one ${SO_4}^{2-}$ ion.

IV.1.2 Iron content - 1,10-phenanthroline method

The amounts of Fe deduced from the 1,10-phenanthroline method were 7.386 $\pm$ 0.001 $mmol\cdot g^{-1}$ for micro-Co-GR(Cl) and 4.686 $\pm$ 0.001 $mmol\cdot g^{-1}$ for nano-Co-GR(Cl) (Table IV.2). Those numbers

Table IV.1 – Stoichiometries of Fe, Co, Cl and S contents in nano-Co-GR and micro-Co-GR determined by EPMA (on the basis of Fe + Co = 1). Each number is an average on the number of independent measurements (n; ± standard deviation). Fe^{3+} stoichiometry is inferred from Cl stoichiometry or S stoichiometry times 2 and $Fe^{2+} = Fe - Fe^{3+}$.

Sample	n	Fe	Co	Fe^{3+}	Fe^{2+}	Cl	S
Micro-Co-GR(Cl)	61	0.67 ± 0.04	0.33 ± 0.04	0.25 ± 0.04	0.42 ± 0.08	0.25 ± 0.04	0 ± 0
Micro-Co-GR(SO_4)	49	0.66 ± 0.02	0.34 ± 0.02	0.22 ± 0.02	0.44 ± 0.04	0 ± 0	0.11 ± 0.01
Nano-Co-GR(Cl)	35	0.49 ± 0.05	0.51 ± 0.05	0.2 ± 0.03	0.29 ± 0.06	0.2 ± 0.03	0 ± 0
Nano-Co-GR(SO_4)	53	0.52 ±0.03	0.48± 0.03	0.16 ± 0.02	0.37 ± 0.05	0 ± 0	0.08 ± 0.01

compared well with those obtained with EPMA results (7.97 and 4.63 $mmol \cdot g^{-1}$, for micro-Co-GR(Cl) and nano-Co-GR(Cl) respectively).

Table IV.2 – Iron content for nano-Co-GR(Cl) and micro-Co-GR(Cl) deduced from results of 1,10-phenanthroline method (Nb - measurement number; [Fe] - total Fe concentration; Std Dev - standard deviation).

				Total Fe quantity ($mmol \cdot g^{-1}$)		
Sample Name	Nb	Absorbance	[Fe] ($mmol \cdot L^{-1}$)	Calculated	Mean	Std Dev
Micro-Co-GR(Cl)	1	1.41	2.22	7.39		
	2	1.41	2.22	7.39		
	3	1.41	2.22	7.39	7.39	0.001
Nano-Co-GR(Cl)	1	0.89	1.40	4.69		
	2	0.89	1.40	4.69		
	3	0.89	1.40	4.69	4.69	0.001

IV.1.3 Water content - TGA

TGA measurements gave similar results for the nano-Co-GR(Cl) and the micro-Co-GR(Cl) samples (Figure IV.1). From room temperature to 140 – 150 °C, a mass loss of approximately 15 % was attributed to interparticle (capillary) pore water (Yun and Pinnavaia, 1995). The additional mass loss (5 %) from 150 to 250 °C was attributed to interlayer water loss (Miyata and Okada, 1977; Yun and Pinnavaia, 1995; Bearcock et al., 2006; Palmer et al., 2008). Mass losses were endothermic, thus supporting a water vaporization mechanism. The stoichiometry of water m was calculated at 0.43 for micro-Co-GR(Cl) and 0.40 for nano-Co-GR(Cl) with equation III.2 (Table IV.3). In regard to EPMA results (Table IV.1), each chloride anion in the interlayer was surrounded by approximately two water molecules for both samples.

The TGA results for nano-Co-GR(SO_4) were similar to those of nano-Co-GR(Cl) (Figure IV.2A). Interparticle water evaporated between 20 and 180 °C with a mass loss of approximately 15 %, and interlayer water evaporated from 180 to 230 °C with a mass loss of 5 %. The stoichiometry of water m was calculated at 0.23 for nano-Co-GR(SO_4) with equation III.2 (Table IV.3). For micro-Co-GR(SO_4),

the first mass loss was around 10 % from 20 to 140 °C (Figure IV.2B). The second mass loss was also 10 % from 140 to 310 °C. The latter temperature was much higher than the upper temperature obtained for the second mass loss of micro-Co-GR(Cl) (240 °C). In addition, the process began to be exothermic at 140 °C, which questioned the interpretation of vaporization of the interlayer water. In the following, the mass loss was attributed entirely to interlayer water which gave a water stoichiometry m of 0.6 for micro-Co-GR(SO_4) (Table IV.3).

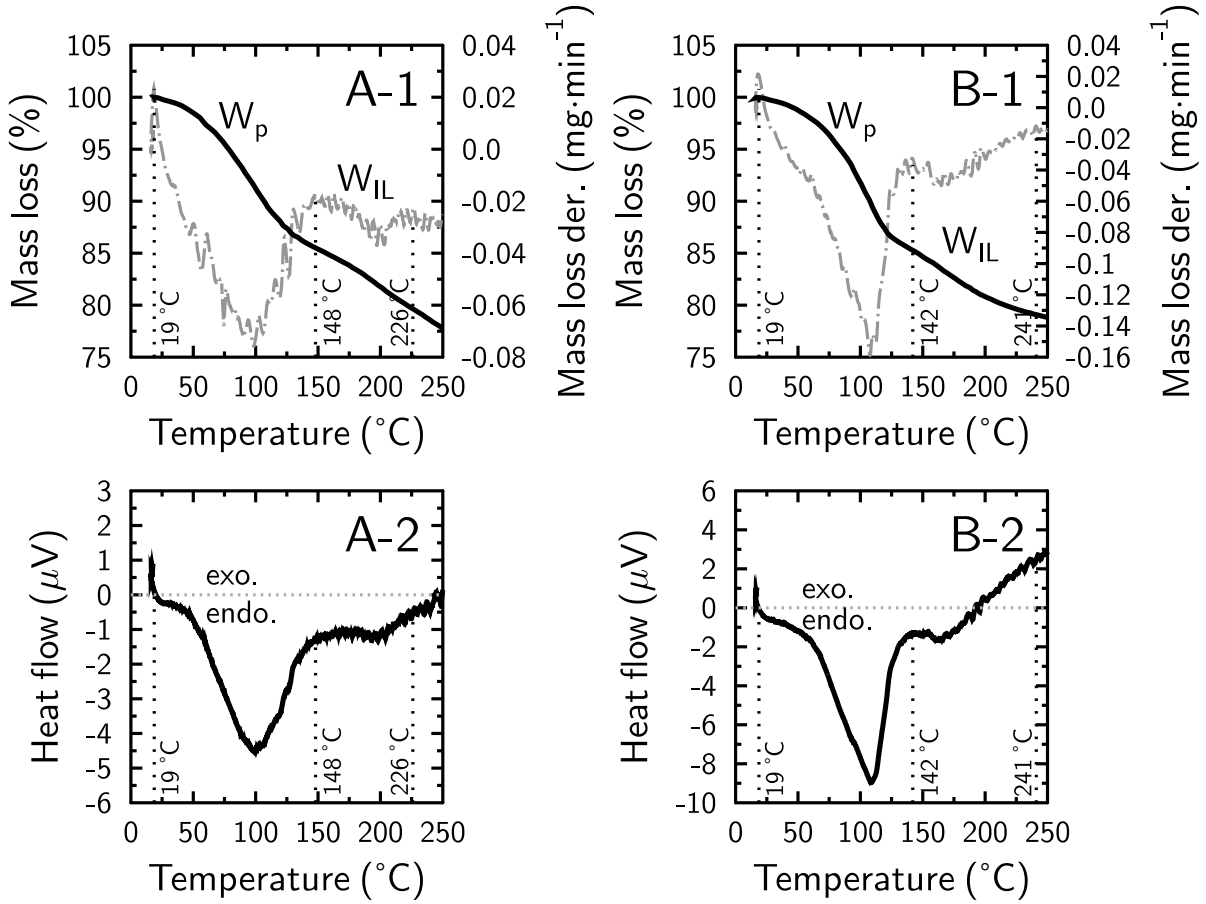

Figure IV.1 – TGA results for nano-Co-GR(Cl) (A-1) and micro-Co-GR(Cl) (B-1; full black line - mass loss; dashed grey line - mass loss derivative; W_p - interparticle (capillary) pore water; W_{IL} - interlayer water) with DSC results for nano-Co-GR(Cl) (A-2) and micro-Co-GR(Cl) (B-2; endo. - endothermic and exo. - exothermic).

IV.1.4 Summary of results

According to EPMA (Table IV.1) and TGA (Table IV.3), the structural formulas for the two synthetized samples were :

— Micro-Co-GR(Cl) - $[Fe^{2+}_{0.42(8)}Fe^{3+}_{0.25(4)}Co^{2+}_{0.33(4)}(OH)_2]\cdot[Cl^-_{0.25(4)}\cdot 0.43H_2O]$

— Nano-Co-GR(Cl) - $[Fe^{2+}_{0.29(6)}Fe^{3+}_{0.20(3)}Co^{2+}_{0.51(5)}(OH)_2]\cdot[Cl^-_{0.20(3)}\cdot 0.40H_2O]$

After exchange with $SO_4{}^{2-}$, structural formulas became:

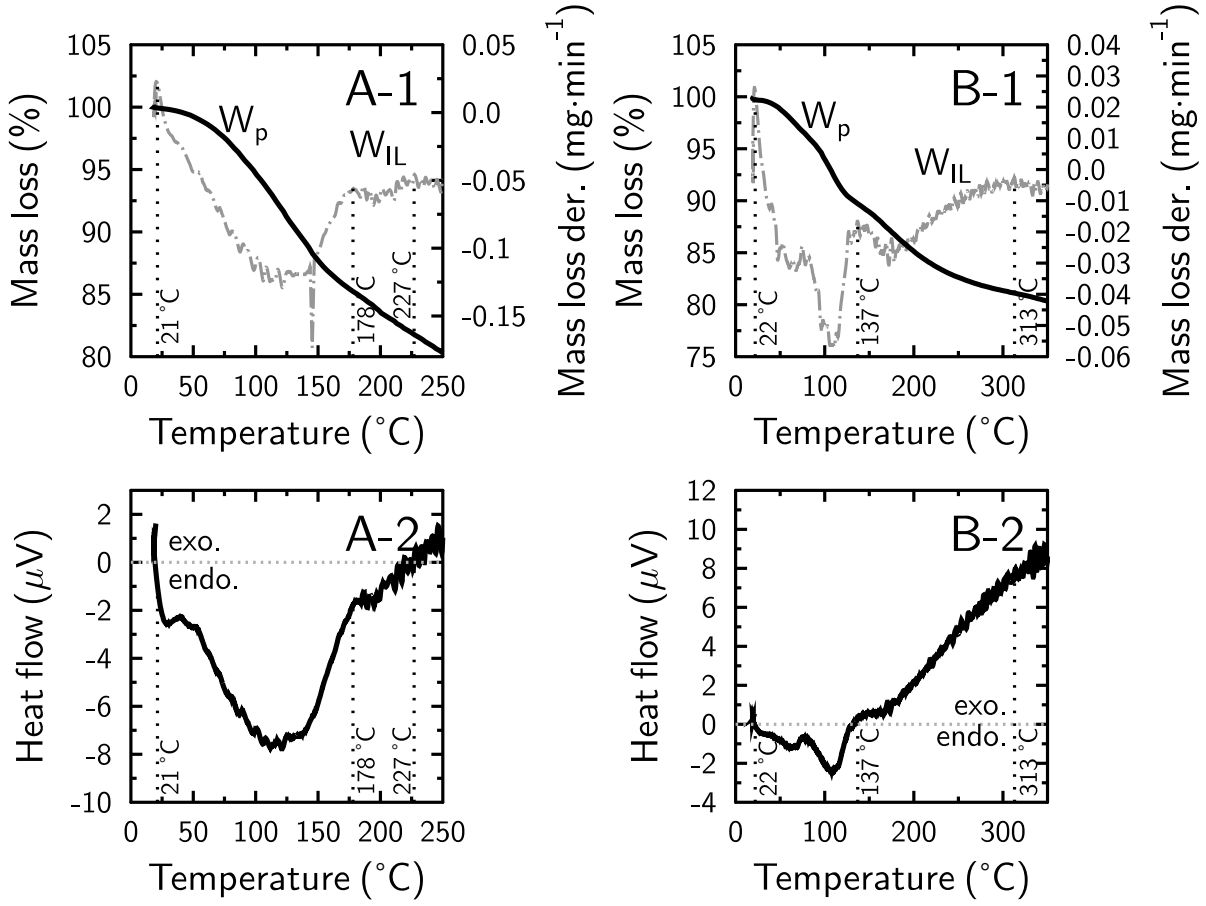

Figure IV.2 – TGA results for nano-Co-GR(SO_4) (A-1) and micro-Co-GR(SO_4) (B-1; full black line - mass loss; dashed grey line - mass loss derivative; W_p - interparticle (capillary) pore water; W_{IL} - interlayer water) with DSC results for nano-Co-GR(SO_4) (A-2) and micro-Co-GR(SO_4) (B-2; endo. - endothermic and exo. - exothermic).

Table IV.3 – TGA results for nano-Co-GR and micro-Co-GR (mass loss nb - mass loss number; MM - molar mass; GR_{anh} - anhydrous green rust; ΔTG - mass loss attributed to water vaporization during the TGA measurement; m - water stoichiometry calculated with equation III.2).

Sample	Mass loss nb	MM of GR_{anh} ($g \cdot mol^{-1}$)	ΔTG (mg)	Mass of GR_{anh} (mg)	m
Micro-Co-GR(Cl)	1	99.74	8.22	44.23	1.03
	2	99.74	3.47	44.23	0.43
Micro-Co-GR(SO_4)	1	101.48	3.60	29.13	0.70
	2	101.48	3.09	29.13	0.60
Nano-Co-GR(Cl)	1	98.53	5.48	30.14	0.99
	2	98.53	2.23	30.14	0.40
Nano-Co-GR(SO_4)	1	99.59	12.35	68.58	1.00
	2	99.59	2.90	68.58	0.23

— Micro-Co-GR(SO_4) - $[Fe^{2+}_{0.44(4)}Fe^{3+}_{0.22(2)}Co^{2+}_{0.34(2)}(OH)_2]\cdot[(SO_4)^{2-}_{0.11(1)}\cdot 0.60H_2O]$

— Nano-Co-GR(SO_4) - $[Fe^{2+}_{0.37(5)}Fe^{3+}_{0.16(2)}Co^{2+}_{0.48(3)}(OH)_2]\cdot[(SO_4)^{2-}_{0.08(1)}\cdot 0.23H_2O]$

IV.2 Structure - XRD

IV.2.1 Examination of XRD patterns

The qualitative examination of XRD patterns from micro-Co-GR(Cl) compared to XRD pattern of fougerite demonstrates that micro-Co-GR(Cl) may be considered as a synthetic analog of fougerite (Figure IV.3; Trolard et al. (2007)). Micro-Co-GR(Cl) peak indexing ((*hkl*) reflections) followed the model presented by Trolard et al. (2007) except for several unassigned peaks which were associated to magnetite impurity (Wechsler et al., 1984).

Micro-Co-GR(Cl) XRD pattern was modelled with the fougerite structure and a minor amount of magnetite using a Rietveld refinement (14 % of magnetite; R_{wp} = 33 %, R_{exp} = 8 %, GoF = 17; Figure IV.5). The only significant difference with the fougerite model of Trolard et al. (2007) was a 4-fold increase in the quantity of interlayer water, which was explained by the difference in the hydration state of the studied samples during measurements. Layer symmetry was hexagonal and could be described with a system where $a = b = 3.1640$ Å, $c = 23.8515$ Å and $\gamma = 120$ °. a and b were slightly lower than a and b of fougerite (3.190 Å) probably due to the high proportion of Co^{2+} into the layer of micro-Co-GR and the fact that the ionic radius of Co^{2+} is ≈ 5% smaller than that of Fe^{2+} in octahedral coordination (Shannon, 1976).

The sole symmetrical reflections found in the nano-Co-GR(Cl) XRD pattern were at q = 0.80 and 1.59 Å and match fougerite *00l* reflections (Figure IV.3). All other reflections were broad, most of them were asymmetrical, and their intensity was low compared to peaks observed in micro-Co-GR(Cl). A simulated XRD patterns of fougerite shows that *00l* is broader for a nano-sized fougerite than for a micro-sized fougerite (Figure IV.4A). Broadening of *00l* reflections in XRD pattern of nano-Co-GR(Cl) was attributed to nanocrystallinity. However, the XRD pattern of nano-Co-GR(Cl) was incompatible with a nanometric and 3D-ordered fougerite, for which Bragg peaks would be extremely broad, yet still present (Figure IV.4B and C). The asymmetrical peaks of low intensity were diagnostic for turbostratic disorder (Warren, 1941; Drits and Tchoubar, 1990). Turbostratism is defined by the systematic occurrence of random translations parallel to the layers and/or rotations about the normal direction to the layers between successive layers. Indeed, the XRD pattern of the turbostratic structure only contains *00l* reflections and unsolved *hk* bands (Warren, 1941). In turbostratic layered Mn oxides,

which have a layer structure very close to GR and an XRD pattern that is very similar to that observed here for nano-Co-GR(Cl), two layer symmetries have been described (Drits et al., 2007). The first one is the hexagonal symmetry that can be described equally with $a = b$ and $\gamma = 120°$ or with the equivalent $a = \sqrt{3} \times b$, $\gamma = 90°$ system (Figure IV.6), and the second one is the orthogonal layer symmetry ($a > \sqrt{3} \times b$ and $\gamma = 90°$). Hexagonal and orthogonal layer symmetries can be distinguished from the ratio of the d-spacing of the 11,20 and 31,02 bands (using an indexing with $\gamma = 90°$) and the shape of the 31,02 band: in the hexagonal layer symmetry, it is equal to $\sqrt{3}$, and the 31,02 band is almost symmetrical. In this study, the ratio of the d-spacing of the two bands at $q = 2.34$ and ≈ 4.03 Å^{-1}, assigned to be the 11,20 and 31,02 bands, respectively, was 1.72, close to $\sqrt{3}$. Consequently, nano-Co-GR had, like micro-Co-GR, hexagonal layer symmetry (Drits et al., 2007; Grangeon et al., 2010, 2017b). This observation reinforced the hypothesis of nano-Co-GR(Cl) being a nanometric and turbostratic variation of micro-Co-GR(Cl).

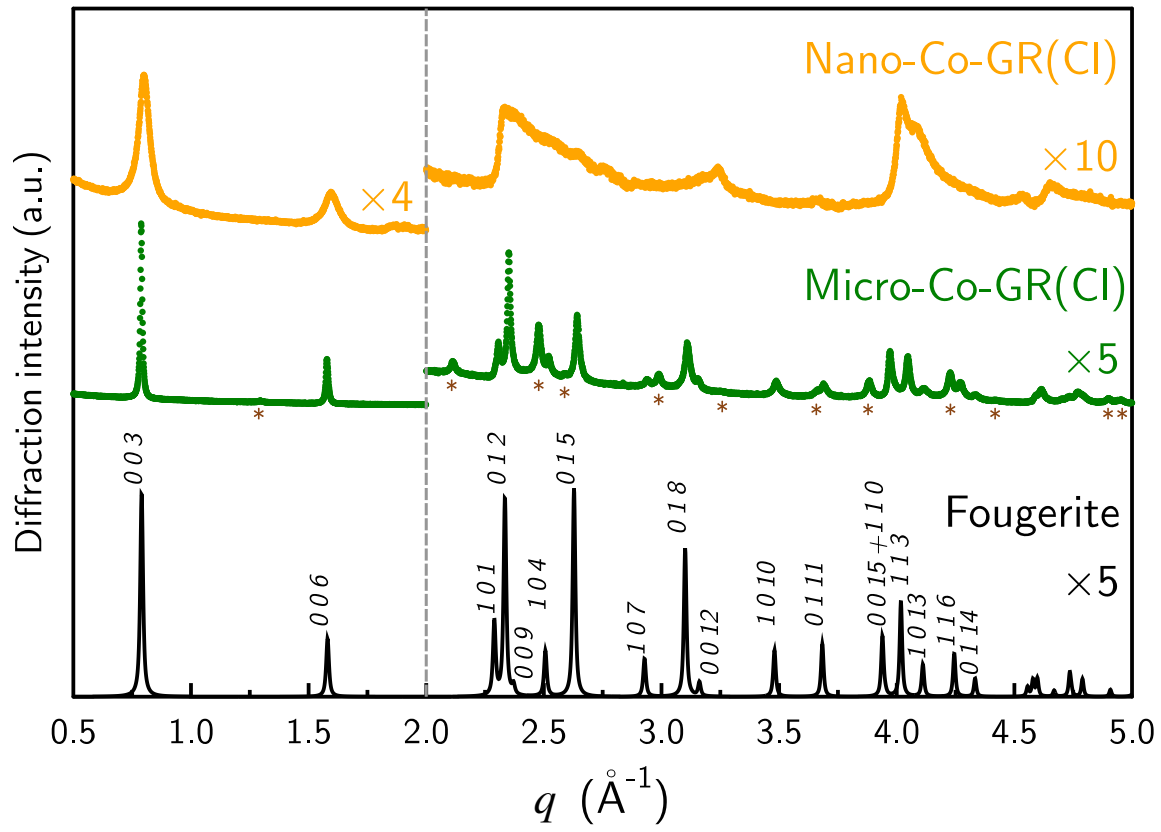

Figure IV.3 – XRD pattern of nano-Co-GR(Cl) (orange) and micro-Co-GR(Cl) (green) compared to the published XRD pattern of fougerite from Trolard et al. (2007) (black). Intensities have been multiplied by 4 between 0.5 and 2 Å^{-1} and by 10 for q higher than 2 Å^{-1} for nano-Co-GR. Intensities have been multiplied by 5 for q higher than 2 Å^{-1} for micro-Co-GR and fougerite. $*$ denotes reflections attributable to magnetite. Nano-Co-GR(Cl) and micro-Co-GR(Cl) XRD patterns were measured at Alba synchrotron with $\lambda = 0.82575$ Å.

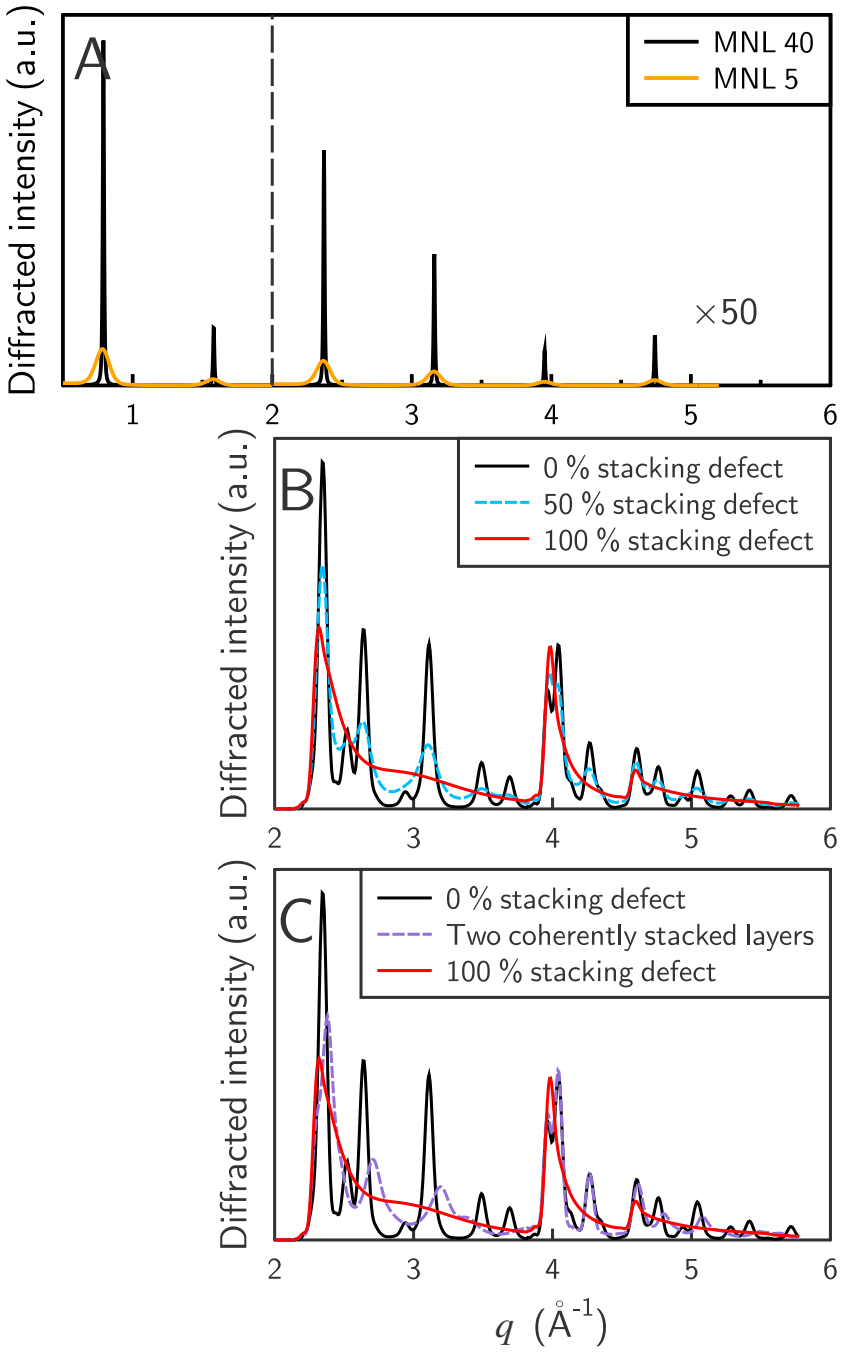

Figure IV.4 – Influence of various structural parameters on modelled XRD patterns of fougerite. (A) Influence of mean number of layer (MNL) on 00*l* reflections (black line - 40 MNL, orange line - 5 MNL, intensities have been multiplied by 50 for $q > 2$ Å). (B) and (C) Influence of the quantity of random stacking faults on the *hkl* reflections (black line - 0 % of random stacking faults, red line - 100 % of random stacking defects = turbostratism, light blue dashed line - 50 % of random stacking faults, purple dashed line - two coherently stacked green rust sheets on average, assuming a lognormal distribution).

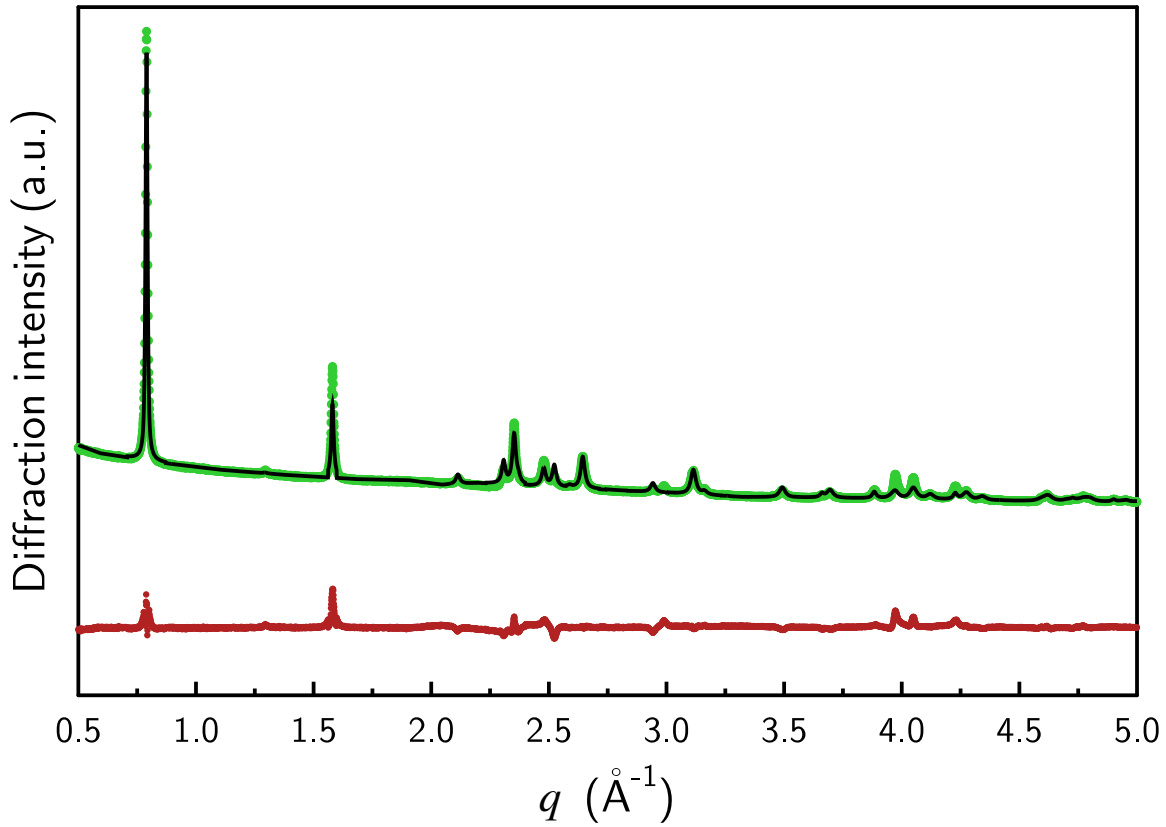

Figure IV.5 – Rietveld refinement results (black line) on micro-Co-GR(Cl) XRD pattern (green marker). Red markers are the residue between the data and the refinement results.

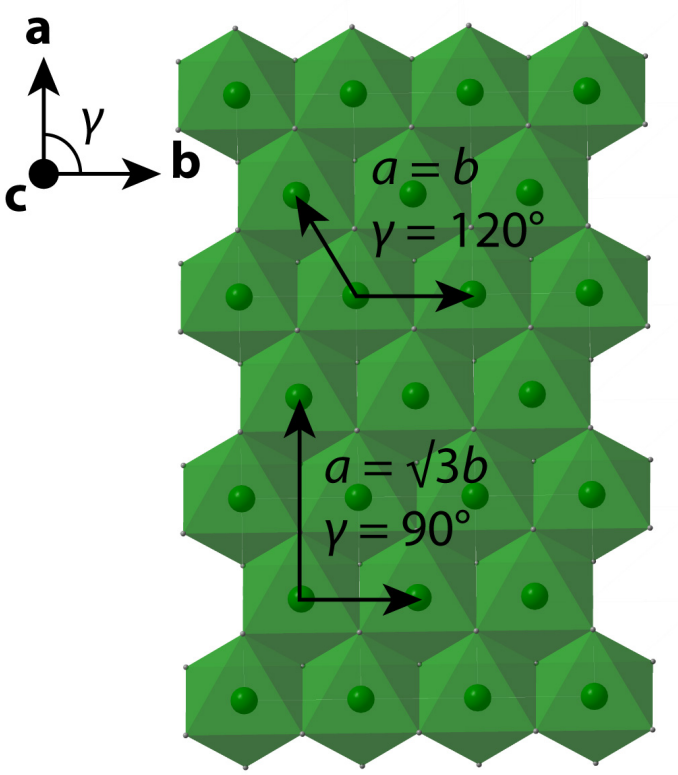

Figure IV.6 – Two equivalent hexagonal layer symmetries. If the layer symmetry is lowered, a becomes different from $\sqrt{3} \times b$ and the layer would not be hexagonal anymore.

IV.2.2 Pair Distribution Function

Despite the distinctive shapes of micro-Co-GR(Cl) and nano-Co-GR(Cl) XRD patterns, the PDF of both samples were overlaid for r values lower than 5.95 Å, which correspond to the layer-to-layer distance of a green rust containing interlayered Cl^- (7.95 Å) minus the layer thickness (2 Å, Figures IV.7A and IV.8). Because the area of a PDF correlation is directly proportional to the number of atoms involved in the correlation, and to their nature (Egami and Billinge, 2012b), this overlay at low r values indicated that nano- and micro-Co-GR(Cl) had the same layer structure and further supported the hypothesis of nano-Co-GR(Cl) being a disordered (turbostratic) variation of micro-Co-GR(Cl). In the layer of micro-Co-GR(Cl),the shortest Me-O distances was 2.07 Å and the shortest Me-Me distance was 3.15 Å (Me = $Fe^{2+,3+}$, Co^{2+}). This Me-Me value was not far from a or b lattice parameters obtained by Rietveld refinement (3.1640 Å) which correspond also to Me-Me distances inside the layer. For the layer of nano-CO-GR(Cl), it was 2.05 Å and 3.12 Å for the shortest Me-O and Me-Me distances respectively.

At r values higher than 5.95 Å, several correlations that were present in the PDF of the micro-Co-GR(Cl) sample were absent in the PDF of the nano-Co-GR(Cl) sample. The same correlations were present in the calculated fougerite PDF, whereas they were absent in the calculated PDF of a single

fougerite sheet (Figure IV.7B). Calculation of a partial PDF showed that these missing correlations were attributable to Me-Me atomic pairs with the two atoms being located in distinct layers because they were absent in the calculated PDF of a single fougerite layer (Figure IV.7C). In contrast, the Me-Me pairs that were observed in the two calculated PDF (e.g., at 8.02, 12.25, 12.1 – 12.3, and 15 Å, Figure IV.7C), and that could thus be attributed to Me-Me atomic pairs within a given layer, were also observed in the experimental PDF of both nano-Co-GR(Cl) and micro-Co-GR(Cl) (Figures IV.7A and IV.8).

Finally, the Me-Me correlations gradually shifted toward low r values with increasing r in the PDF of nano-Co-GR(Cl) relative to those of micro-Co-GR(Cl). This data confirmed the difference noted earlier between shortest Me-Me distances of nano-Co-GR(Cl) and micro-Co-GR(Cl) (3.12 and 3.15 Å respectively. Consequently, the in-plane lattice parameters of nano-Co-GR(Cl) were slightly smaller than those of micro-Co-GR(Cl). Nano-Co-GR(Cl) layers had a higher Co^{2+}/Fe^{2+} ratio than micro-Co-GR(Cl), and the ionic radius of Co^{2+} is ≈ 5% smaller than that of Fe^{2+} in octahedral coordination (Shannon, 1976). Thus, the smaller values of in-plane lattice parameters for nano-Co-GR(Cl) compared to micro-Co-GR(Cl) were consistent with this difference in layer composition.

The PDF of nano-Co-GR(Cl) cancelled at $r \approx 50$ Å, whereas several intense correlations were present at higher r values in the PDF of micro-Co-GR(Cl), consistent with nano-Co-GR(Cl) being nanocrystalline and micro-Co-GR(Cl) being microcrystalline. PDF results were thus in agreement with the interpretation of XRD data.

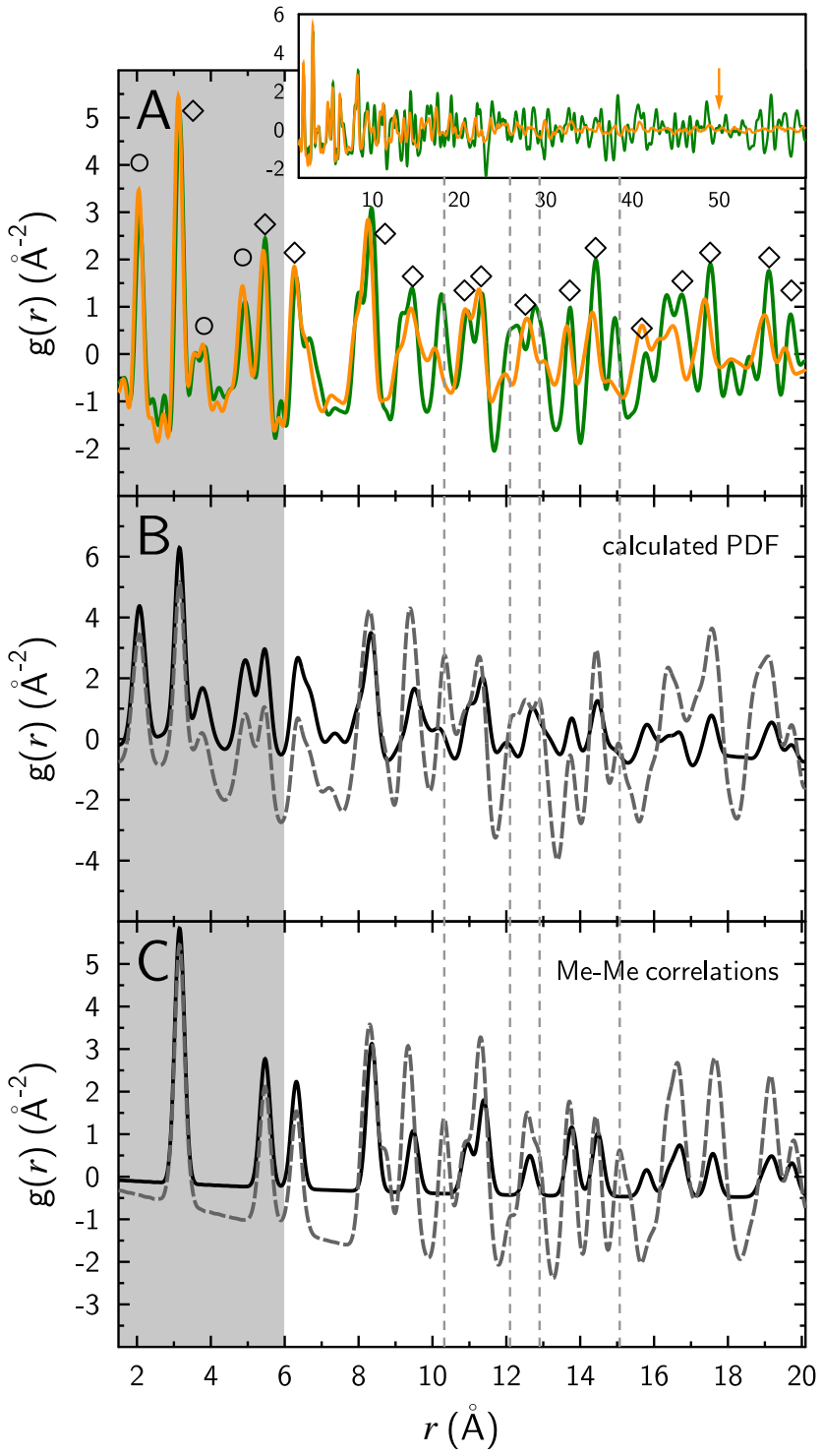

Figure IV.7 – (A) PDF data of nano-Co-GR(Cl) (orange solid line) and micro-Co-GR(Cl) (green solid line). Inset: data up to $r = 60$ Å, with the arrow pointing out to the r value at which the PDF from nano-Co-GR(Cl) is below periodic noise. Main panel: detail of the 1.5 – 20 Å region, with indexation of the main correlations (◇ = Me-Me correlations within a given layer, Me-Me = $Fe^{2+,3+}$-$Fe^{2+,3+}$, $Fe^{2+,3+}$-Co^{2+}, or Co^{2+}-Co^{2+} correlations, Light grey dashed line = Me-Me correlations within two atoms located in distinct layers, ○ - Me-O = $Fe^{2+,3+}$-O or Co^{2+}-O correlations). (B) calculated PDF for a fougerite (black solid line) and for a single fougerite layer (dark grey dashed line) (Trolard et al., 2007). (C) Partial PDF showing only the Me-Me correlations for a fougerite (black solid line) and a single fougerite layer (dark grey dashed line). The greyshaded area corresponds to r values lower than the Me to Me distance in adjacent layers. No data normalization. XRD patterns necessary for the PDF calculations in A were done at SOLEIL synchrotron.

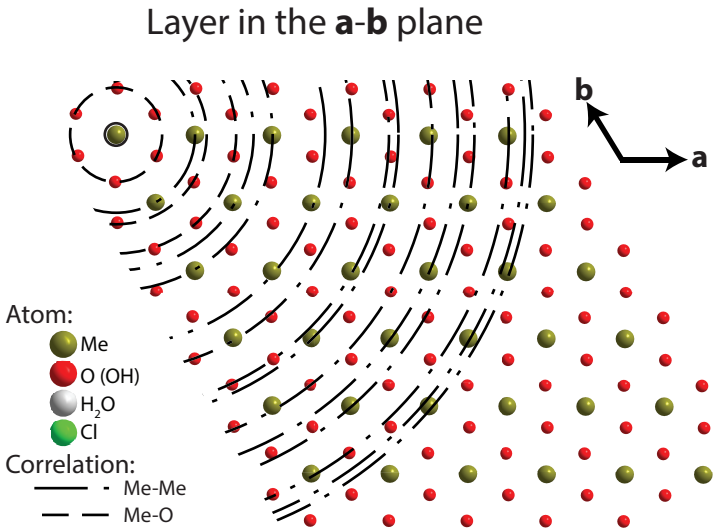

Figure IV.8 – Green rust structure and representation of the different correlations observable with PDF (Figure IV.7).

IV.3 Morphology - TEM

TEM images evidenced two distinct morphologies for nano-Co-GR(Cl) and micro-Co-GR (Figure IV.9). Nano-Co-GR(Cl) crystals were systematically aggregated and xenomorphic. This sample had a high sensitivity to the beam.

No morphological difference appeared between micro-Co-GR(Cl) and micro-Co-GR(SO_4). Their crystals were automorphic and their size in the **a**-**b** plane varied between 0.1 and 1 µm with a maximum thickness along **c*** of 40 nm. Impurities were visible in both micro-Co-GR(Cl) and micro-Co-GR(SO_4) (an example is shown in Figure IV.9 C-1). Thus, only the morphology of micro-Co-GR could be determined with confidence compared to nano-Co-GR.

Layer-to-layer distances, deduced from a fast Fourier transform (FFT) analysis of the images, were 7.1 Å for nano-Co-GR(Cl) and 7.4 Å for micro-Co-GR(Cl) and micro-Co-GR(SO_4). These values were lower than the layer-to-layer distances deduced from XRD analysis due to TEM conditions (vacuum inside the TEM chamber).

Chemical compositions were also verified with the help of EDX spectra (Table IV.4). Fe/Co ratio was higher for micro-Co-GR(Cl) than for nano-Co-GR(Cl) which was coherent with the synthesis method (Table IV.5). Drop-deposited samples were differentiated from epoxy-preserved samples because of the reactivity of green rusts with dioxygen. No significant difference were visible between the two types of micro-Co-GR(Cl) sample for morphology as well as for composition. According EDX results obtained with micro-Co-GR(Cl) and micro-Co-GR(SO_4), anion exchange was complete and

the exchange stoichiometry was 1 Cl replaced by 1 SO_4^{2-} (Table IV.5). The latest result was at variance with the EPMA results (Table IV.1). Drop-deposited samples were dispersed in Milli-Q water, and so, interlayer Cl^- could have been released into the water because of concentration differences, which would decrease the interlayer Cl^- proportion. In this case, the epoxy-preserved samples would have shown a different atomic percentage for Cl which is not the case (Table IV.4). Another explanations include an incorporation of carbonates during the preparation (contamination from atmosphere) and/or volatilization of Cl^- or SO_4^{2-} under the beam. Fe/Co ratios of around 3.8 for micro-Co-GR(Cl) and 1.9 for nano-Co-GR(Cl) were different from those obtained by EPMA (2.03 for micro-Co-GR(Cl) and 1.08 for nano-Co-GR(Cl), Table IV.1 and IV.5). For the chemical composition, EPMA results were used in the following because the number of measurements with EPMA was higher than for EDX, and because EDX results gave inconsistent results for Cl^- and SO_4^{2-} stoichiometries.

Analyzed impurities had similar atomic percentage with nearly no Cl^- and a Fe/Co ratio of about 5.9 (Table IV.5). Coupling this information with XRD results (Figure IV.3), these impurities were considered to be Co-bearing magnetite.

Table IV.4 – Atomic percentage of micro-Co-GR(Cl), micro-Co-GR(SO_4) and nano-Co-GR(Cl) deduced from TEM-EDX characterizations (average values ± standard deviation; *n* - number of independent analyses). Type corresponds to sample preparation: drop - drop deposited and Agar - Agar resin embedded. Impurities values were calculated from measurements made inside micro-Co-GR(SO_4) sample but these impurities can be found in micro-Co-GR(Cl) with the same average values.

			%Atomic			
Sample	Type	*n*	Fe	Co	Cl	S
Micro-Co-GR(Cl)	Drop	3	72 ± 2	18 ± 1	11 ± 1	
	Agar	3	70 ± 2	20 ± 1	10 ± 3	
Micro-Co-GR(SO_4)	Agar	4	69 ± 2	19 ± 1	0.4 ± 0.4	12 ± 2
Nano-Co-GR(Cl)	Drop	4	55 ± 1	29 ± 3	15 ± 2	
Impurities	Agar	4	85 ± 1	15 ± 1	0.8 ± 0.4	

Table IV.5 – Atomic ratios of micro-Co-GR(Cl), micro-Co-GR(SO_4) and nano-Co-GR(Cl) deduced from atomic ratios in Table IV.4 (average values ± standard deviation; *n* - number of independent analyses).

			Ratio		
Sample	Type	*n*	Fe/Co	Cl/(Fe+Co)	S/(Fe+Co)
Micro-Co-GR(Cl)	Drop	3	4.1 ± 0.2	0.1 ± 0.02	
	Agar	3	3.6 ± 0.2	0.1 ± 0.04	
Micro-Co-GR(SO_4)	Agar	4	3.6 ± 0.2	0.0 ± 0.01	0.1 ± 0.03
Nano-Co-GR(Cl)	Drop	4	1.9 ± 0.2	0.2 ± 0.03	
Impurities	Agar	4	5.9 ± 0.2	0.01 ± 0.01	

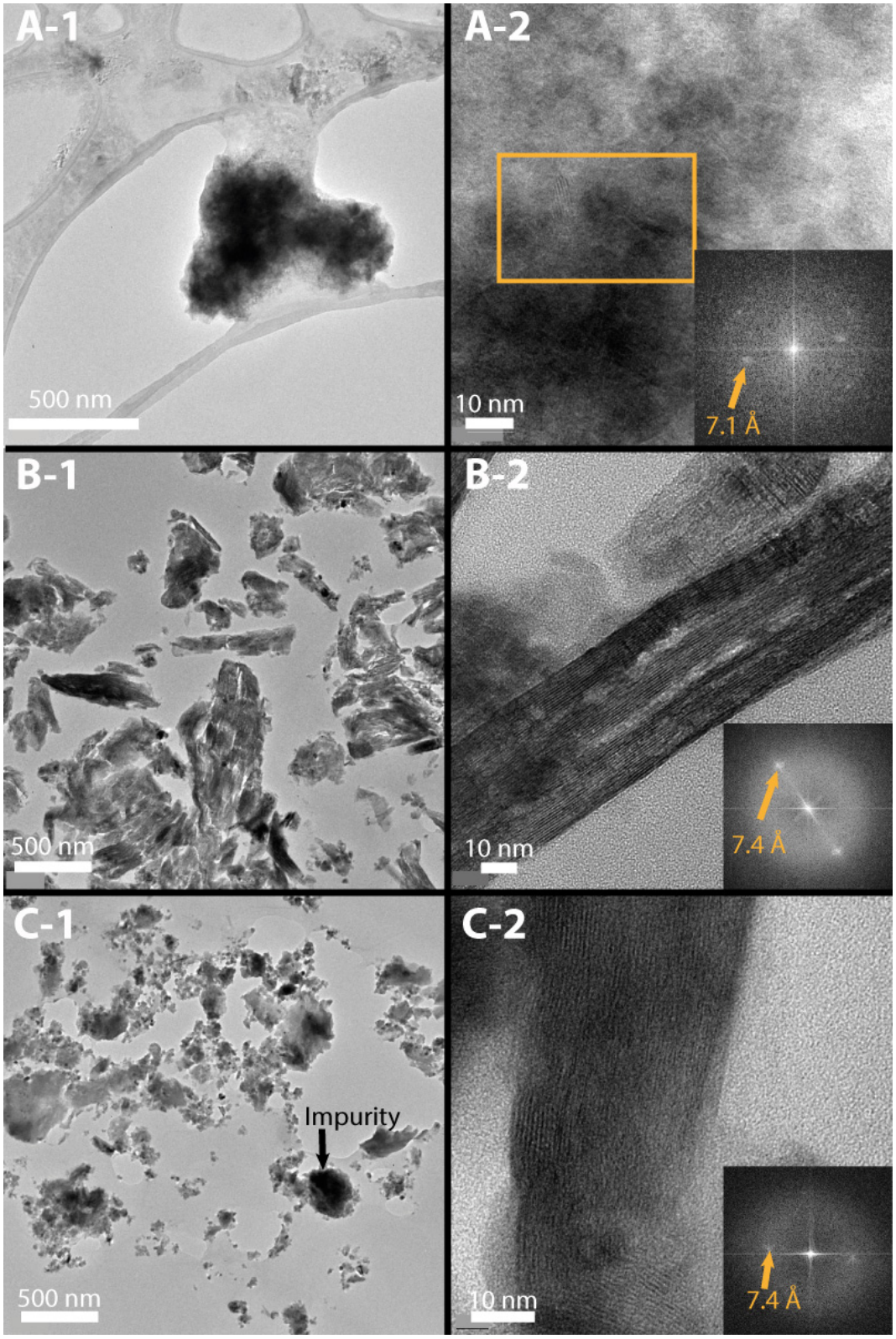

Figure IV.9 – TEM images of nano-Co-GR(Cl) (A), micro-Co-GR(Cl) (B) and micro-Co-GR(SO_4) (C). Inset in A-2 are FFT of the area described by the orange box in A-2. Inset in B-2 and C-2 are FFT analysis of the whole TEM images in B-2 and C-2 respectively. Sample preparation: drop deposited for nano-Co-GR(Cl) (A) and embedded in Agar resin for micro-Co-GR (B and C).

IV.4 Summary - Co-GR characterisation

A summary of determined chemical, structural and morphological characteristics for nano-Co-GR(Cl) and micro-Co-GR(Cl) can be found in Table IV.6.

Table IV.6 – Chemical, structural and morphological characteristics for nano-Co-GR(Cl) and micro-Co-GR(Cl) (MM_{anh} - anhydrous molar mass, L-to-l dist - layer-to-layer distance).

Type	Data	Micro-Co-GR(Cl)	Nano-Co-GR(Cl)
Chemistry	Layer	$[Fe_{0.42(8)}{}^{2+}Fe_{0.25(4)}{}^{3+}Co_{0.33(4)}{}^{2+}(OH)_2]$	$[Fe_{0.29(6)}{}^{2+}Fe_{0.20(3)}{}^{3+}Co_{0.51(5)}{}^{2+}(OH)_2]$
	Interlayer	$[Cl_{0.25(4)}{}^{-}\cdot 0.43H_2O]$	$[Cl_{0.20(3)}{}^{-}\cdot 0.40H_2O]$
	MM_{anh} ($g\cdot mol^{-1}$)	99.74	98.53
Structure	Ordering	3D-ordered	Turbostratic
	a (Å)	3.164	≈ 3.12
	b (Å)	3.164	≈ 3.12
	c (Å)	23.852	23.852
	α (°)	90	90
	β (°)	90	90
	γ (°)	120	120
	L-to-l dist. (Å)	7.95	7.95
Morphology	Crystal size	$0.1-1$ µm	Nanometric

CHAPTER V

ION EXCHANGE MECHANISMS AND PARAMETERS

Motivations

Anion exchange mechanism(s) and associated thermodynamic parameters may be dependent on the type of anion, the structure, or chemical composition of green rust samples. Also, the reversibility of the exchange must be investigated to determine if a thermodynamic equilibrium model can be used to model the reactivity of green rust in natural systems.

In order to start answering these questions, *in situ* XRD measurements were done to assess the mechanism and batch exchange experiments were conducted to quantify and model these exchanges. Exchanges were done for chloride, sulphate and carbonate species on two samples of green rust: a micrometric and 3D-ordered green rust, micro-Co-GR, and a nanometric and turbostratic green rust, nano-Co-GR.

V.1 Mechanism determination

Anion exchange mechanism can be determined by following structure modifications of green rust samples during anion exchange using *in situ* XRD measurements. XRD patterns allowed studying dissolution, precipitation, and structure variations such as changes in lattice parameters or interstratification processes.

Three experiments were carried out on micro-Co-GR samples. The goals of these experiments were, first, to determine the exchange mechanism, second, to determine whether the influence of

parameters such as the types of anion, crystallite size or stacking faults would have had an impact on the mechanism and, and last, to test whether the exchange was reversible. The experiments were carried out with the following reagents addition orders:

— Experiment "Na_2SO_4−XRD" - a solution containing 5 mmol$\cdot L^{-1}$ of Na_2SO_4 and 40 mmol$\cdot L^{-1}$ of NaCl at pH ≈ 9 was flown through a micro-Co-GR sample. After the exchange with sulphate anions was complete, a solution containing only NaCl at 50 mmol$\cdot L^{-1}$ was flown through the reactor.

— Experiment "$NaHCO_3$−XRD" - a solution containing 40 mmol$\cdot L^{-1}$ of $NaHCO_3$ and 10 mmol$\cdot L^{-1}$ of NaCl at pH ≈ 8.5 was flown through a micro-Co-GR sample. After the completion of the exchange with carbonate species, a solution containing only NaCl at 50 mmol$\cdot L^{-1}$ was flown through the reactor.

— Experiment "Na_2CO_3−XRD" - a solution containing 10 mmol$\cdot L^{-1}$ of Na_2CO_3 and 40 mmol$\cdot L^{-1}$ of NaCl at pH ≈ 10.9 was flown through a micro-Co-GR sample.

In addition, experiment "Na_2SO_4−XRD" was also carried out with a nano-Co-GR(Cl) sample, but without the second part with a flow through of NaCl solution.

Several phases have been identified and studied in this section and the following nomenclature is used:

— micro-Co-GR(Cl) phase - a micrometric and 3D-ordered green rust containing Cl^- as interlayer anion,

— micro-Co-GR(SO_4) phase - a micrometric and 3D-ordered green rust containing ${SO_4}^{2-}$ as interlayer anion,

— micro-Co-GR(C(IV)) phase - a micrometric and 3D-ordered green rust containing carbonate species as interlayer anions (${CO_3}^{2-}$, ${HCO_3}^-$, etc.; no attempt was made to discriminate these molecules with XRD measurements on a randomly oriented powder),

— nano-Co-GR(Cl) phase - a nanometric and turbostratic green rust containing Cl^- as interlayer anion,

— nano-Co-GR(SO_4) phase - a nanometric and turbostratic green rust containing ${SO_4}^{2-}$ as interlayer anion,

— magnetite.

Of note, "micro-Co-GR(Cl) phase" (for example) is used as the complete name of the said phase in order to differentiate it from the sample: micro-Co-GR or nano-Co-GR samples contained a mix of various green rust phases previously mentioned and magnetite. The notation d_{003} will be used for the layer-to-layer distance.

V.1.1 Comparison of initial structure of micro-Co-GR(Cl) samples

Several exchange experiments were conducted with various samples of micro-Co-GR(Cl). Their XRD patterns were compared to each other to verify their initial structure. The same synthesized powder was used to prepare the capillaries for experiments "$NaHCO_3$−XRD" and "Na_2CO_3−XRD". XRD patterns of micro-Co-GR(Cl) phases in these two capillaries were similar (Figure V.1). 003 reflection of micro-Co-GR(Cl) phase were at $q = 0.791$ Å^{-1} (equivalent to a d-spacing of 7.94 Å) for both samples. Calculated average crystallite size of micro-Co-GR(Cl) phase was 57 nm along the plane perpendicular to the layers for both samples used in experiments "$NaHCO_3$−XRD" and "Na_2CO_3−XRD" respectively. XRD pattern of micro-Co-GR(Cl) phase used for experiment "Na_2SO_4−XRD" was similar to the two previously mentioned XRD patterns (Figure V.1). Position of 003 reflection was at $q = 0.787$ Å^{-1} ($d = 7.98$ Å), indicating a slightly smaller d_{003} with a difference of 0.04 Å compared to micro-Co-GR(Cl) samples used for experiments "$NaHCO_3$−XRD" and "Na_2CO_3−XRD". Average crystallite size of micro-Co-GR(Cl) phase was 58 nm along the plane perpendicular to the layers for experiment "Na_2SO_4−XRD", which is close to the crystallite size calculated for experiments "$NaHCO_3$−XRD" and "Na_2CO_3−XRD". 110 reflection for experiments "$NaHCO_3$−XRD" and "Na_2CO_3−XRD" was at $q = 3.973$ Å^{-1} and for experiment "Na_2SO_4−XRD" at $q = 3.966$ Å^{-1}. All the samples contained magnetite as impurities. Apart from these small differences, the three samples were considered to have equivalent composition and structure for each of their phases.

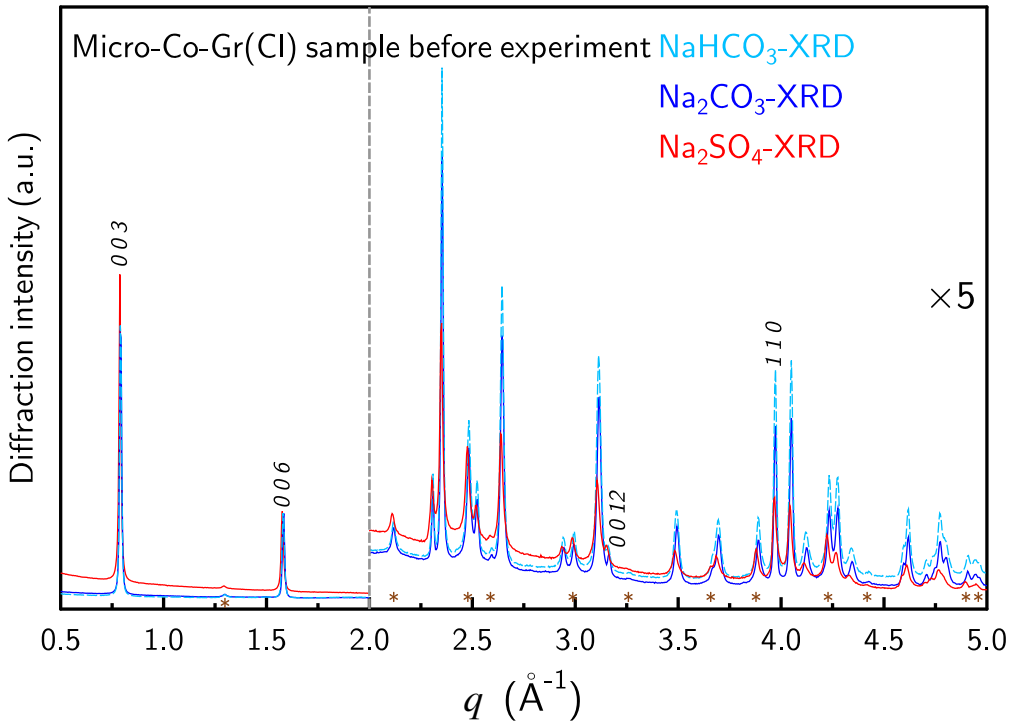

Figure V.1 – XRD patterns recorded *in situ* of micro-Co-GR(Cl) samples before *in situ* XRD exchange experiments "Na_2SO_4-XRD" (red line), "$NaHCO_3$−XRD" (sky blue line), or "Na_2CO_3−XRD" (dark blue line). Intensities were normalized with the intensity of 006 reflections, averaged with a sliding window of 5 points. and multiplied by 5 for $q > 2$ Å^{-1} for all XRD patterns. Brown stars (∗) correspond to magnetite reflections.

V.1.2 Anion influence on the exchange mechanism

Cl - SO_4 exchange

- $Cl \longrightarrow SO_4$

In experiment "Na_2SO_4-XRD", Na_2SO_4 and NaCl solutions flowed through nano- and micro-Co-GR(Cl) samples, thus transforming them to GR(SO_4).

For micro-Co-GR phase, the intensity of the reflection at $q = 0.79$ Å^{-1} (equivalent to a d-spacing of 7.99 Å) steadily decreased with time, while a reflection appeared and increased in intensity at 0.57 Å^{-1} ($d = 11.02$ Å; Figure V.2 A-1 and B-1). Concomitantly, almost all peaks present at higher q values in the XRD pattern of micro-Co-GR phase also shifted, with the noticeable exception of those having *hk0* indices (e.g., the 110 reflection at $q = 3.97$ Å^{-1}). This was most straightforwardly explained by an increase in c during the experiment, while a and b remained unaffected.

Nano-Co-GR phase was a nanosized and turbostratic green rust with the same layer structure as micro-Co-GR phase, as proven by XRD measurements and PDF analysis shown in the precedent chapter (Figure IV.3 and IV.7). For this phase, only the positions of the 00l reflections changed (Figure V.2 A-2 and B-2). 00l reflections related to the presence of Cl^- decreased in intensity and other 00l reflections appeared and increased in intensity at 0.57 and 1.14 Å^{-1}. At higher q values, the position of all hk bands remained unchanged, consistent with c increasing and a and b remaining constant. However, the shape of the high-q side of the 11,20 band at 2.34 Å^{-1} evolved. This was due to a change in the nature, location, and/or density of the atoms in the lattice (Warren, 1941), consistent with an anion exchange.

The increase in c in both samples was consistent with the replacement of Cl^- by SO_4^{2-} in the interlayer. The 00l reflections of nano- and micro-Co-GR(Cl) phases and of nano- and micro-Co-GR(SO_4) phases remained symmetrical and did not exhibit significant width changes during the experiment. The average crystallite size along the plane perpendicular to the layers remained constant throughout the experiments (Figure V.2D). Every reflection of hkl indices with $l \neq 0$ changed from the position corresponding to the Cl^- interlayer presence to the SO_4^{2-} interlayer presence position without a gradual shift and without the appearance of a peak at an intermediate position (Figure V.2C).

Collectively, these observations showed that a simple anion exchange mechanism occurred without dissolution-recrystallization processes, and that an interstratification phenomenon (i.e., ordered or disordered alternations of Cl^- and SO_4^{2-} interlayers within a given crystal) was also unlikely (Drits

and Tchoubar, 1990). A process of physical mixture is more appropriate to describe these exchanges. These experiments evidenced that the same mechanism applied for a nanometric, turbostratic green rust, and a micrometric, 3D-ordered green rust.

• $SO_4 \longrightarrow Cl$

After the previous experiment, and for micro-Co-GR sample only, a solution containing 50 mmol · L^{-1} of NaCl was flown through the sample. The goal of this experiment was to test the reversibility of the ion exchange. The beamline experimental hutch had to be opened to fix a small leak at a pore volume of $V/V_r = 6$. This leak and this manipulation may have affected the sample for a short time: magnetite peak area increased quickly between $V/V_r = 6$ and $V/V_r = 7$ (Figure V.3C).

On micro-Co-GR(SO_4) phase, 00l reflections due to the presence of SO_4^{2-} in the interlayer were still present (Figure V.3A and B). Their intensities slowly decreased during the whole experiment. The area of these 00l reflections also slowly decreased (−11 % for 003 in 27 V/V_r, Figure V.2C). The crystallite size along the plane perpendicular to the layers slowly decreased from 54 nm to 44 nm in 29 V/V_r (−18.5 %, Figure V.3D). These results were consistent with a partial dissolution of micro-Co-GR(SO_4) phase. Some hkl reflections had a sharp decrease, for example at q = 2.33, 2.76, 3.12, and 3.99 $Å^{-1}$ (red arrow on Figure V.3A). They were not 00l reflections. It was not possible to index these disappearing reflections with the R$\bar{3}m$ space group. Thus, the space group could have been modified during the ion exchange between Cl^- and SO_4^{2-}. On micro-Co-GR(Cl) phase, 003 reflections due to the presence of Cl^- ($q = 0.78$ $Å^{-1}$) also decreased in intensity during the whole experiment (Figure V.3A and B). The area of 220 reflection of magnetite at 2.11 $Å^{-1}$ increased quickly between $V/V_r = 6$ and $V/V_r = 7$. Afterwards, it increased very slowly by about 6 % in 22 V/V_r, which meant that magnetite was precipitating. Other reflections of magnetite had the same evolution. All these observations showed a slow dissolution of micro-Co-GR(SO_4) phase and probably also of micro-Co-GR(Cl) phase, with an associated precipitation of magnetite. Magnetite is more stable than green rust, especially since a solution containing only Cl^- was flown through the reactor at pH 9 (Lewis, 1997; Sumoondur et al., 2008; Vodyanitskii and Shoba, 2015).

Two other reflections were observed $q = 0.84$ $Å^{-1}$ ($d = 7.53$ Å, blue arrow near 003 Cl), and q = 1.33 $Å^{-1}$ ($d = 4.72$ Å, orange arrow near the *111* reflection of magnetite). The peak at $q = 1.33$ $Å^{-1}$ had a constant intensity during the experiment. It could be an unidentified impurity. The peak at $q = 0.84$ $Å^{-1}$ slowly increased while the 003 reflections of micro-Co-GR(Cl) and micro-Co-GR(SO_4)

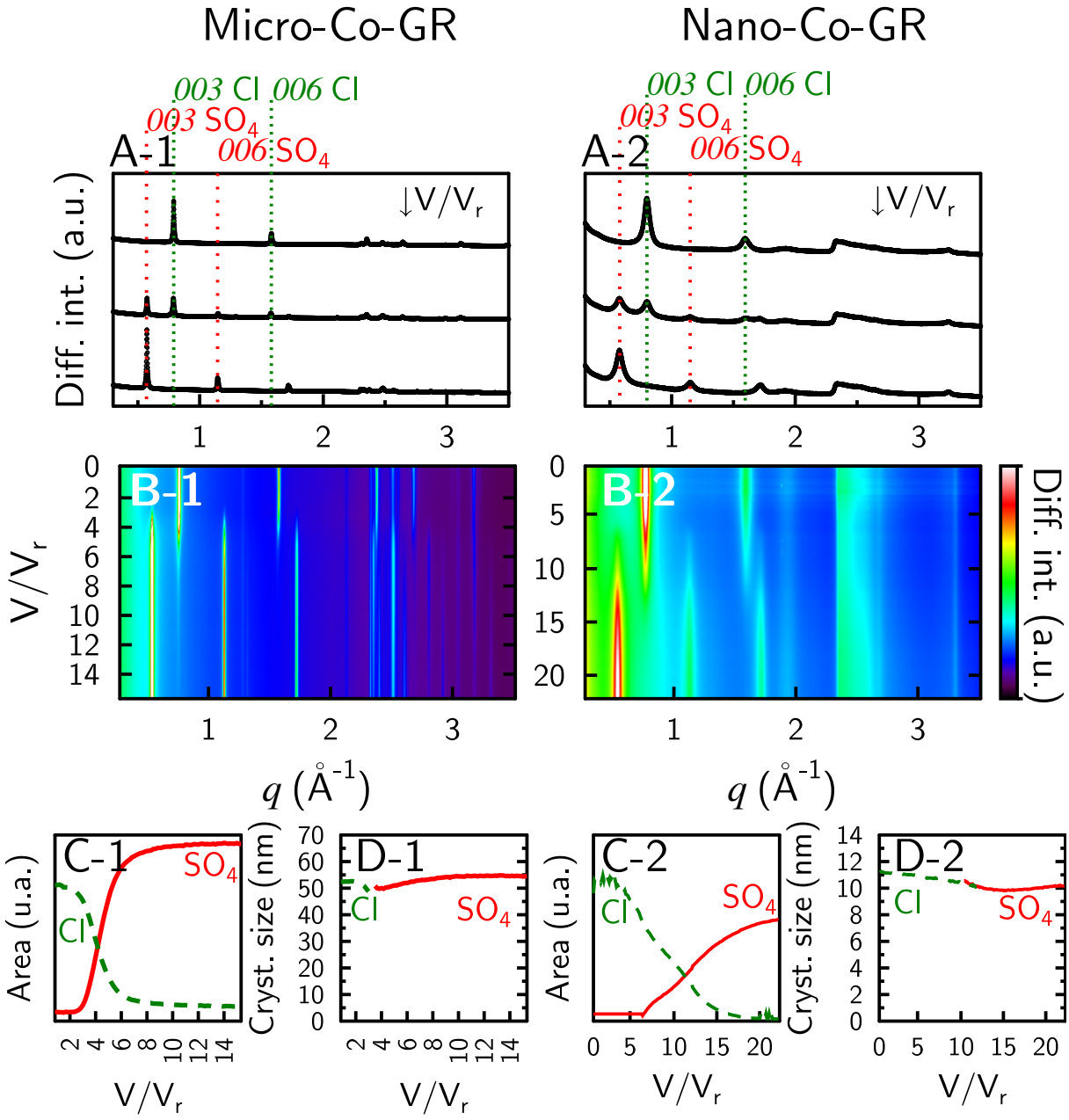

Figure V.2 – XRD patterns recorded *in situ* during experiment "Na_2SO_4-XRD" with micro-Co-GR(Cl) (left-1) and nano-Co-GR(Cl) (right-2). (A-1) Patterns recorded after 2, 4, and 14 pore volumes (V/V_r, Diff. int. - diffracted intensity). (A-2) Patterns recorded after 0, 10, and 20 V/V_r. (B) 2D map of XRD patterns as a function of time expressed in pore volumes. (C) Evolution of the 003 reflection areas at 0.78 $Å^{-1}$ (Cl^- interlayer, green dashed line) and 0.57 $Å^{-1}$ (SO_4^{2-} interlayer, red line) as a function of pore volumes. (D) Estimate of the crystallite size as a function of pore volumes inferred from full width at half maximum of the 003 reflection and Scherrer equation at 0.78 $Å^{-1}$ (Cl^- interlayer, green dashed line) and 0.57 $Å^{-1}$ (SO_4^{2-} interlayer, red line). Note: the same peak indexing formalism was followed for nano-Co-GR phase despite the lack of a 3D-ordered structure.

phase decreased during the whole duration of the experiment. This observation can be interpreted by an anion exchange that induced a decrease in the layer-to-layer distance of green rust, concomitantly with a partial dissolution of the green rust phases. This hypothesis was also reinforced by the fact that no other peak appeared or increased in intensity in the XRD pattern except reflections of magnetite. However, the nature of the anion remained uncertain, it could have been Cl^-, but with a different amount of water or chloride per unit cell than in the initial sample, or it could be a carbonate species because the peak position at $d = 7.53$ Å was also in agreement with the presence of carbonate species in the interlayer.

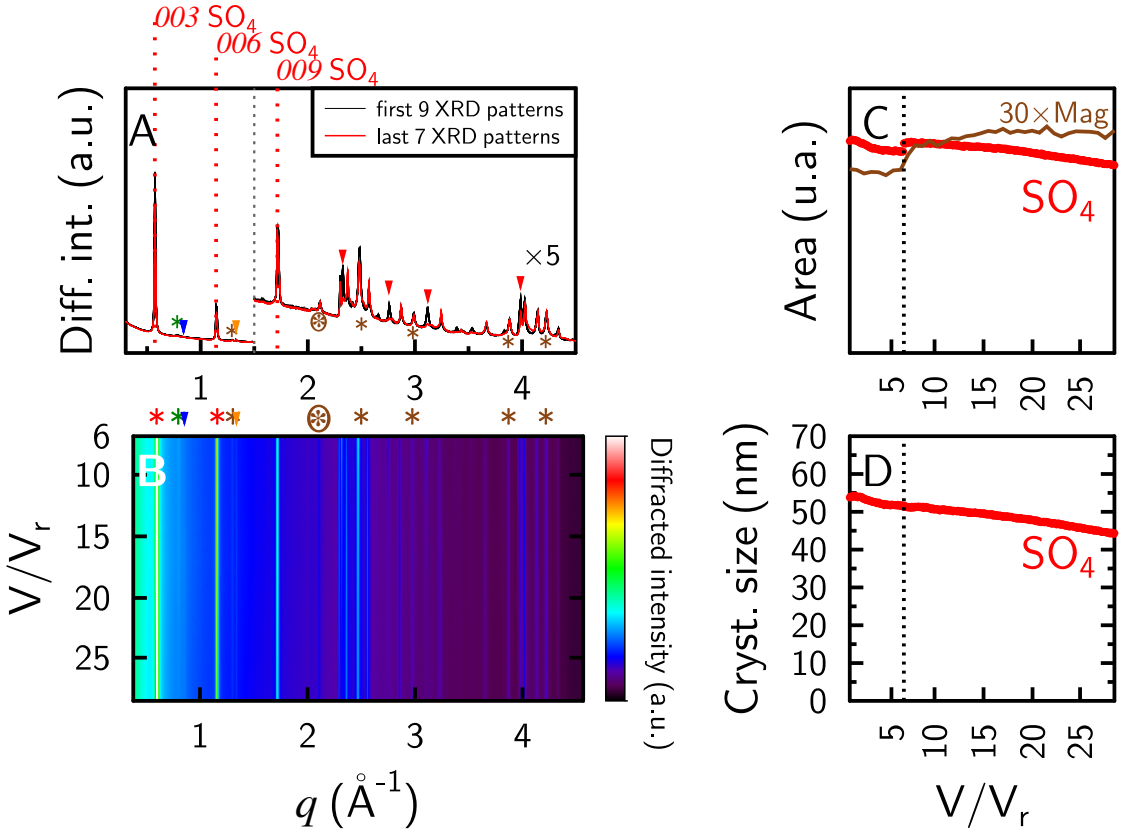

Figure V.3 – XRD patterns recorded *in situ* during a 50 mmol·L^{-1} of NaCl solution flow-through experiment with micro-Co-GR(SO_4) after the experiment shown in Figure V.2 for micro-Co-GR(Cl). The caption is the same as Figure V.2 except for the following details. Red and green stars are reflections of micro-Co-GR(Cl) phase and micro-Co-GR(SO_4) phase respectively. Brown stars are the positions of magnetite reflections (*, rounded * for 220 reflection). (A) First nine (black) and last seven pattern (red) measured during the experiment. (C) Evolution of the 220 reflection area at 2.11 Å^{-1} of magnetite (Mag, multiplied by 30 with a moving average on 10 points, full brown line). Dotted lines on B-C-D graphs displayed the moment where the experiment was shortly stopped to fix a leak.

Cl - Carbonate species exchange

Experiment "$NaHCO_3$–XRD" and "Na_2CO_3–XRD" were carried out on micro-Co-GR samples. The goal of these experiments was, first, to determine the exchange mechanism with carbonate species;

second, to determine whether parameters such as pH or concentrations of each carbonate species would have had an impact on the mechanism and last, to test if the exchange was reversible.

• *Experiment "$NaHCO_3$-XRD" - Cl ⟶ Carbonate species*

For experiment "$NaHCO_3$−XRD", the intensity of the reflection at $q = 0.79$ Å^{-1} (equivalent to a d-spacing of 7.94 Å) steadily decreased from $V/V_r = 3$ to $V/V_r \approx 12$, while a reflection appeared at $V/V_r = 4$ and increased in intensity at 0.83 Å^{-1} ($d = 7.60$ Å; Figure V.4). This reflection at 0.83 Å^{-1} was coherent with a replacement of Cl^- by carbonate species in the interlayer. The difference compared to the exchange between Cl^- and SO_4^{2-} was that $00l$ reflections due to Cl^- in the interlayer shifted gradually from their position and these reflections became asymmetrical (Figure V.4A-2 and V.6A and D). The method used here to quantify asymmetry is shown in figure V.5. In this formalism, if asymmetry is positive, then the maximum of the peak is shifted towards low q values. Reversely, if asymmetry is negative, then the maximum of the peak is shifted towards high q values. $00l$ reflections due to carbonate species in the interlayer shifted but less than $00l$ Cl and their asymmetry was also less visible. Concomitantly, all peaks present at higher q values in the XRD pattern of micro-Co-GR also shifted. The variations of intensity for the reflections of micro-Co-GR(Cl) and micro-Co-GR(C(IV)) phase were smooth (Figure V.6B): fast for V/V_r from 5 to 13 and then slowing down after $V/V_r = 13$ to nearly reach steady state at the end of the experiment ($V/V_r = 24$).

The intensity of reflections for magnetite increased (Figure V.7B). This increase was sharp during the exchange between Cl and carbonate species (+12 % for V/V_r from 5 to 13). Then, after $V/V_r = 13$, the increase in intensity continued but more slowly to reach a 16 % increase or a 19 % increase for 220 and *311* reflections respectively at the end of the experiment ($V/V_r = 24$). The area of magnetite reflections naturally also had the same evolution (Figure V.7C). Thus, a precipitation of magnetite occurred, probably due to the exchange and/or the chemical conditions. Since there was no iron in injected solution, dissolution of green rust probably occurred to induce this precipitation of magnetite.

The decrease in c in micro-Co-GR sample was consistent with the replacement of Cl^- by carbonate species in the interlayer. Due to the small solution volumes used in this experiment, it was not possible to measure the concentrations of each anion, to determine the stoichiometry of the exchange between Cl^- and carbonate species and therefore show which carbonate species were in the interlayer (CO_3^{2-}, HCO_3^-, $NaCO_3^-$, or a mix of them). At the same time, magnetite was also precipitating, so a small amount of green rust probably dissolved. This did not seem to alter the ion exchange. $00l$ reflections of

micro-Co-GR(Cl) and micro-Co-GR(C(IV)) phases were asymmetrical during the exchange, this usually underlines the occurrence of interstratification processes. Further modeling of XRD pattern were necessary in order to define which type of interstratification occurred and to quantify the exchange process.

• *Experiment "$NaHCO_3$-XRD" - models for interstratification processes*

Two layer types were used for the interstratification models: Gr-Cl and Gr-CO_3 (see chapter III and table III.2 for their characteristics). Water stoichiometry for Gr-CO_3 layers was fitted on a file containing 71.5 % of Gr-Cl layers and 28.5 % Gr-CO_3 layers ($V/V_r = 6$, Figure V.8). A stoichiometry of 5 water molecules per CO_3^{2-} gave the best fit. 5 water molecules per CO_3^{2-} was also the stoichiometry found by Génin and Ruby (2008) for a green rust with the same Fe^{3+}/Fe^{2+} as micro-Co-GR phase (1/4), using Mössbauer analysis and ordering of interlayer molecules. For a unit cell with 3 layers of micro-Co-GR phase (6 iron atoms with 1.5 Fe^{3+}, $a = b = 3.164$ Å, $c = 23.85$ Å, layer thickness = 2 Å, volume of the unit cell = 206.8 Å^3), the volume of one layer is 17.3 Å^3 and 52.0 Å^3 for 3 layers so the volume of the interlayer space is 154.8 Å^3. 5 water molecules per CO_3^{2-} gave 3.75 water molecules per unit cell because there was 0.75 CO_3^{2-} per unit cell ($Fe^{3+}/2$). The volume corresponding to this amount of CO_3^{2-} and water are 6.6 and 13.8 Å^3 respectively (assuming a spherical volume with a C-O distance of 1.28 Å and a H-O distance of 0.96 Å in the water molecule) for a total of 20.4 Å^3 which is well below the volume of the interlayer space. 3.75 water molecules per unit cell gave a density of 725 kg/m^3 of interlayer space which was reasonable compared to the density of water. All these results were in agreement to show that 5 water molecules per CO_3^{2-} was a possible stoichiometry, even if TGA measurements would allow to verify this result more accurately.

Various interstratification processes have specific effects on 00l reflections in XRD patterns (Figures V.9 and V.10). Each type of interstratification will impact the intensity ratio of 00l reflections, the position, the symmetry, and the FWHM of these peaks. For every observable 00l reflections, two asymmetrical peaks were visible during the exchange in experiment "$NaHCO_3$-XRD". The position of 00l reflections of Gr-Cl moved slightly along q with a maximum of 0.06 Å displacement for the 003 reflection. After examination of figures V.9 and V.10, it was assumed that the likely interstratification mode here was R = 1 and layer types were highly segregated ($P_{ClCl} > 0.85$). Indeed, the 00l reflections would have shifted from the initial position (003 reflection - $q = 0.79$ Å^{-1}) to final position (003 reflection - $q = 0.83$ Å^{-1}) in R = 0, R = 1 – MPDO and R = 1 with a $P_{ClCl} < 0.85$ cases. In the case of R1

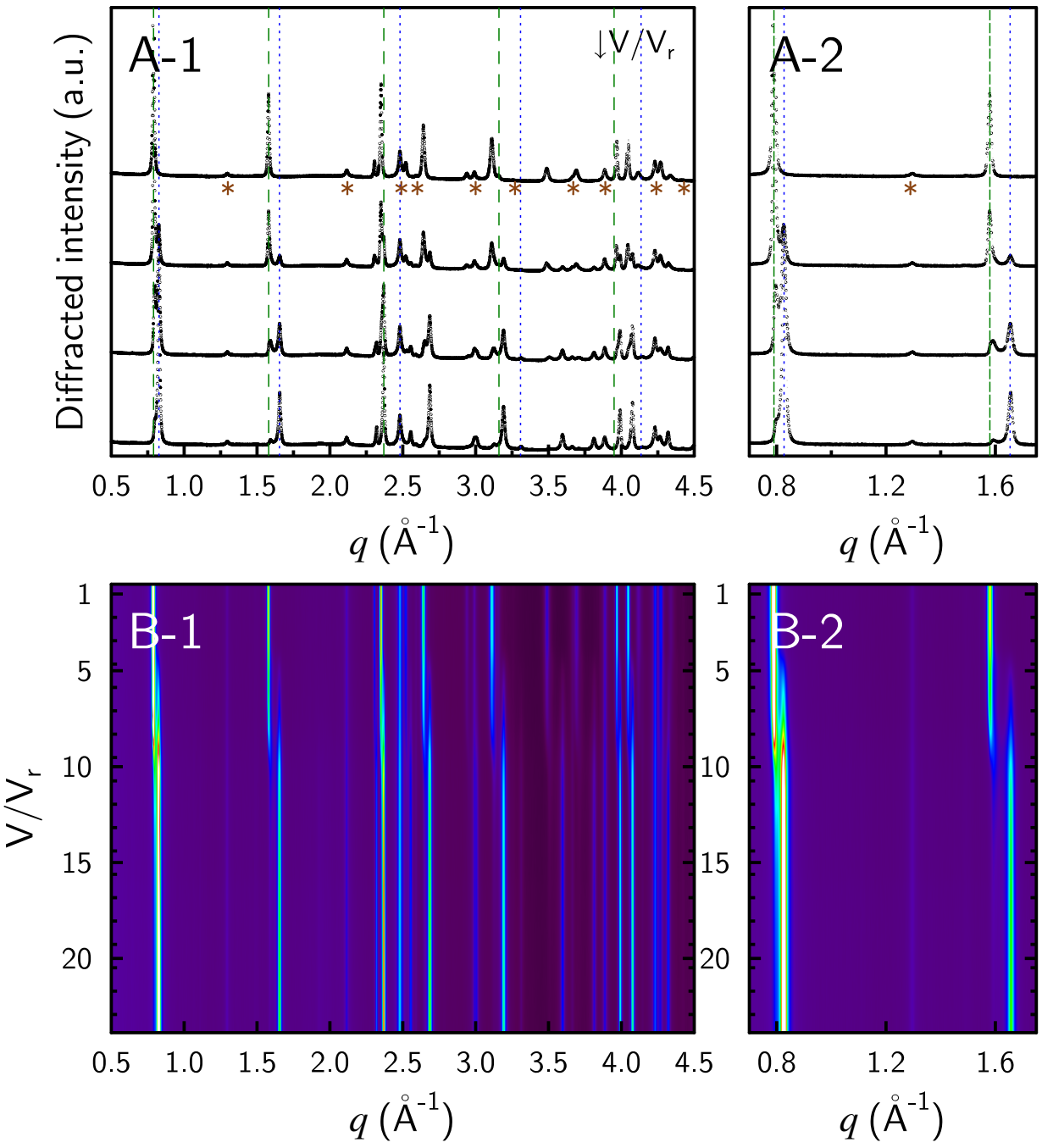

Figure V.4 – XRD patterns recorded *in situ* during experiment "$NaHCO_3$-XRD" (Input solution: 40 mmol·L^{-1}/10 mmol·L^{-1} of $NaHCO_3$/NaCl) with micro-Co-GR(Cl) sample. (A) Patterns recorded after 0.5, 6.8, 9.7 and 14.6 pore volumes (V/V_r). Brown stars display the reflections of magnetite. Dashed green lines are positions of 00l reflections of micro-Co-GR(Cl) and blue dotted lines are positions of 00l reflections of micro-Co-GR(C(IV)). (B) 2D map of XRD patterns as a function of time expressed in pore volumes. (-1) Full recorded pattern. (-2) Zoom on 00l reflections.

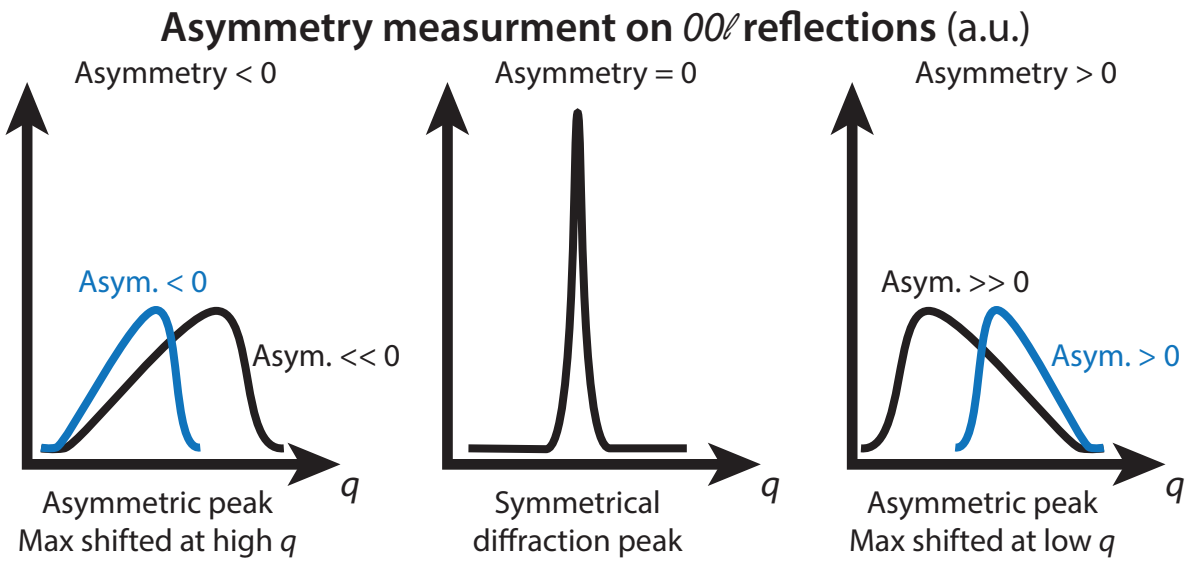

Figure V.5 – Asymmetry measurement of 00l reflections (asym. - assymetry).

interstratification, two parameters must be fitted, namely the abundance of Gr-Cl layers (W_{Cl}) and the probability that a Gr-Cl layer follows another one (P_{ClCl}). Other parameters were deduced from these two (Equation II.1). A good fit was obtained for all patterns (Figure V.11A, all XRD patterns - data & model - are available in appendix). The exchange began after $V/V_r = 2.6$ because of the delay due to the replacement of the solution containing only Cl^- with the solution containing a mix of chloride ions and carbonate species into the capillary. d_{003} for Gr-Cl layers displayed an evolution throughout the exchange from 7.957 to 7.9 Å (Figure V.11C and Table V.1). d_{003} for Gr-CO_3 layers remained at the same position of d_{003} = 7.585 Å. P_{ClCl} and P_{CO_3CO3} were higher than 0.89 and 0.94 respectively, showing that the two layer types were highly segregated. Both P_{ClCl} and P_{CO_3CO3} increased as W_{Cl} and $W_{CO_3CO_3}$ increased respectively, different from the case where P_{ClCl} was calculated from a constant P_{CO_3CO3} (green dotted line on Figure V.11B). This observation means that segregation increased with the progress of the anion exchange reaction. At the end of this experiment, Cl^- was still present in the interlayers with 7 % of Gr-Cl layers and 93 % of Gr-CO_3 layers.

In summary, in "$NaHCO_3$–XRD" exchange experiment, carbonate species replaced Cl^- in the interlayer. Interstratification processes proceeded with two layer types, one layer containing Cl^- and another layer containing carbonate species and R = 1. These two layer types were highly segregated and layer-to-layer distances of Gr-Cl layers decrease of 0.057 Å throughout the experiment. The water stoichiometry was different in the two layer types: Gr-Cl layers contained two water molecules per

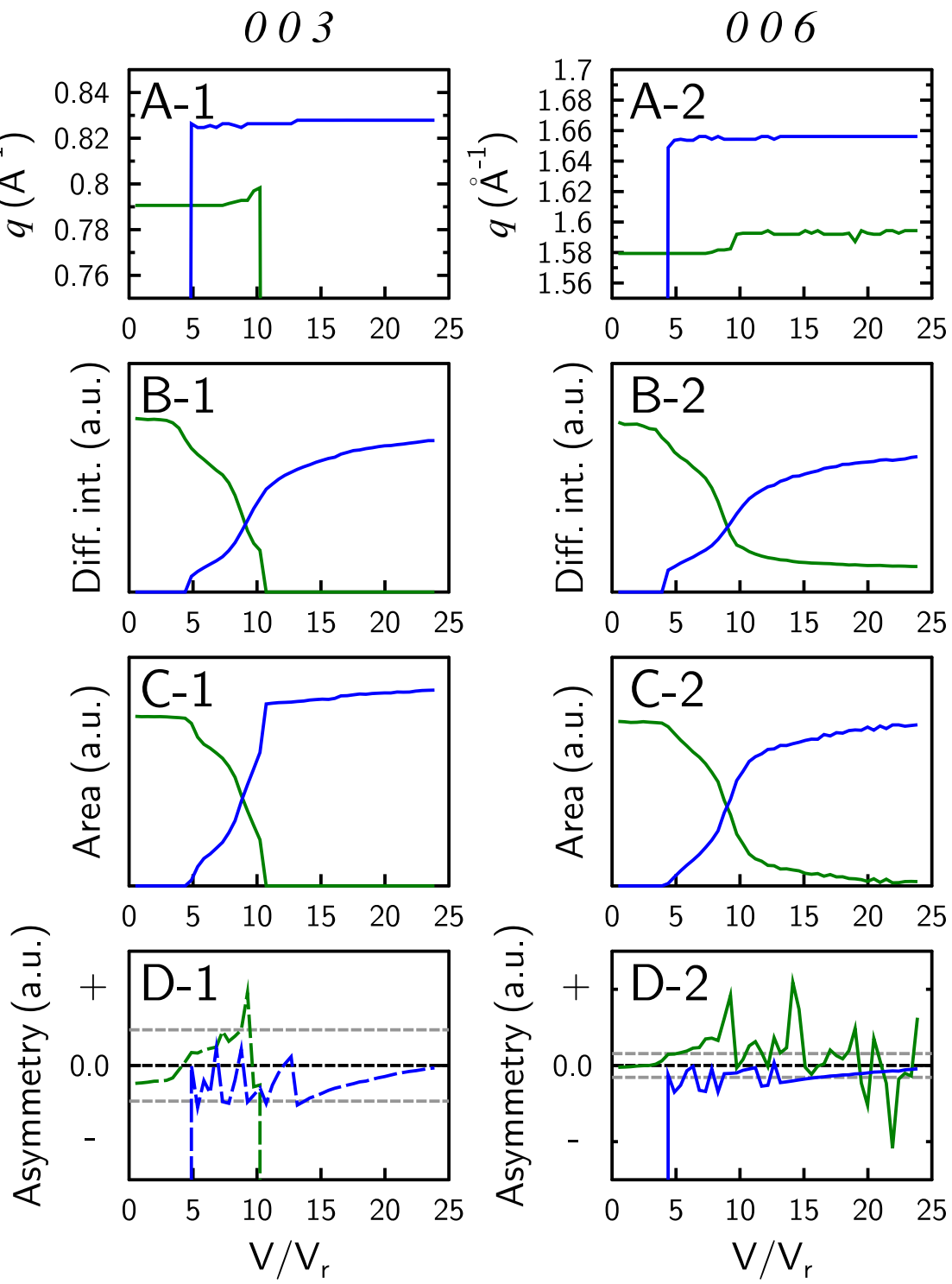

Figure V.6 – Analysis of 003 (left -1) and 006 reflections (right -2) of micro-Co-GR phase on XRD patterns measured during experiment "$NaHCO_3$-XRD" (XRD patterns on Figure V.4). Green lines refer to 003 reflections attributed to interlayer distances with Cl^- in the interlayer and, in the same way, blue lines are for CO_3^{2-} as the interlayer anion. (A-B-C) Evolution of the position (A), diffracted intensity (B) and area (C) of each peak. (D) Measurements of the asymmetry of each peak. A value of 0 means that the peak was perfectly symmetrical, positive or negative values mean an asymmetrical peak, see Figure V.5 for more details. The grey dashed lines represent the interval between the position of two measured points. Asymmetry measurements were significant if they were not in the interval between those two grey lines.

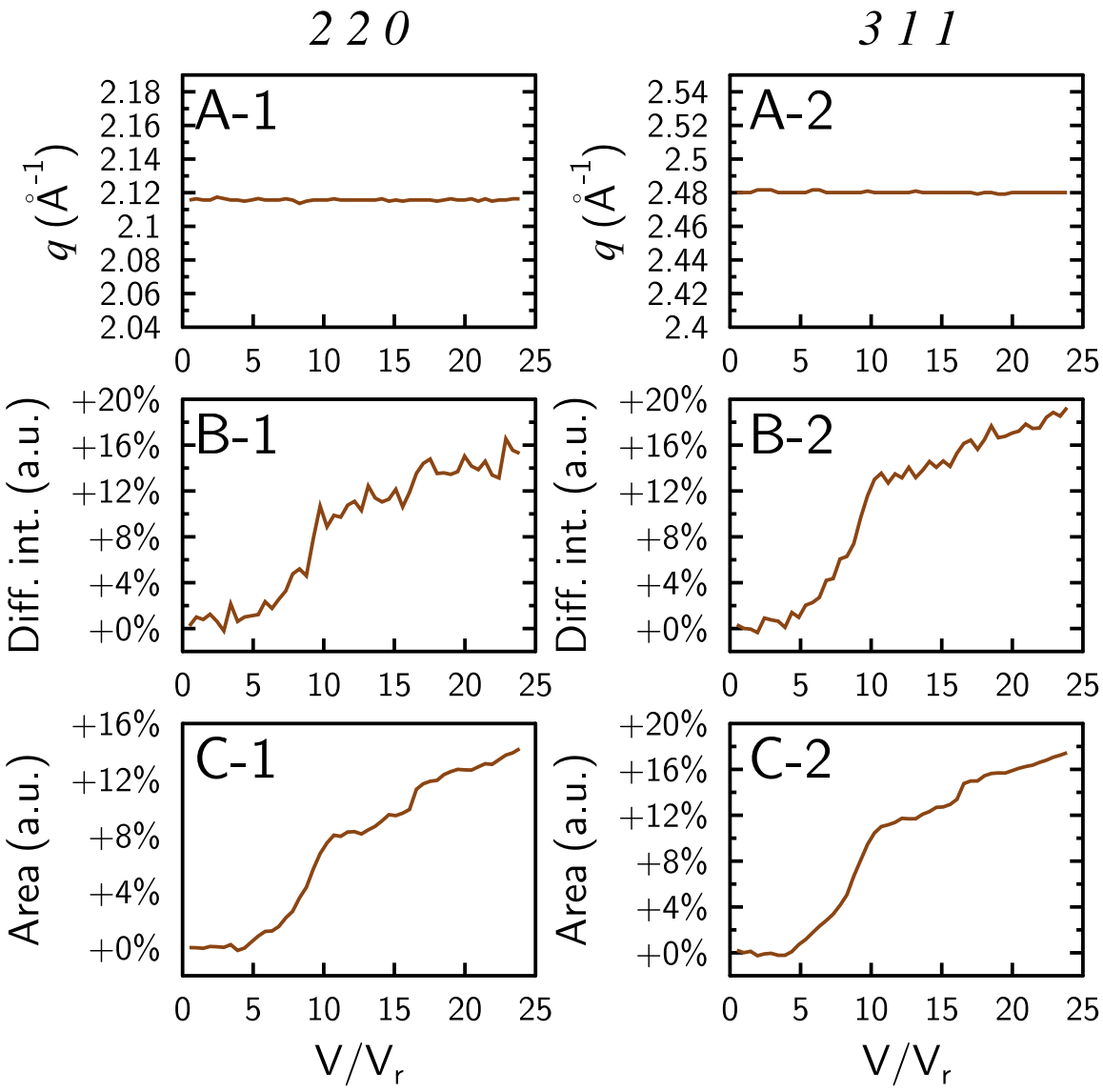

Figure V.7 – Analysis of 220 and 331 reflections of magnetite on XRD patterns measured during experiment "$NaHCO_3$-XRD"(XRD patterns on Figure V.4). Caption is the same as Figure V.6 except for the following details. (B-C) Intensity and area given in percentage increase compared to the initial value.

Table V.1 – List of parameters to model XRD patterns of interstratified micro-Co-GR phase during "$NaHCO_3$-XRD" experiment.

V/V_r	R	W_{Cl}	W_{CO_3}	P_{ClCl}	$P_{CO_3CO_3}$	d_{003} Gr-Cl (Å)	d_{003} Gr-CO_3 (Å)
0.0	1	1	0	1	-	7.957	-
2.6	1	1	0	1	-	7.957	-
3.8	1	0.890	0.110	0.993	0.943	7.957	7.585
6.0	1	0.715	0.285	0.985	0.962	7.952	7.585
7.2	1	0.520	0.480	0.963	0.960	7.945	7.585
8.1	1	0.340	0.660	0.945	0.972	7.910	7.585
8.9	1	0.260	0.740	0.940	0.979	7.900	7.585
12.3	1	0.140	0.860	0.910	0.985	7.900	7.585
18.7	1	0.080	0.920	0.890	0.990	7.900	7.585
20.4	1	0.070	0.930	0.890	0.992	7.900	7.585

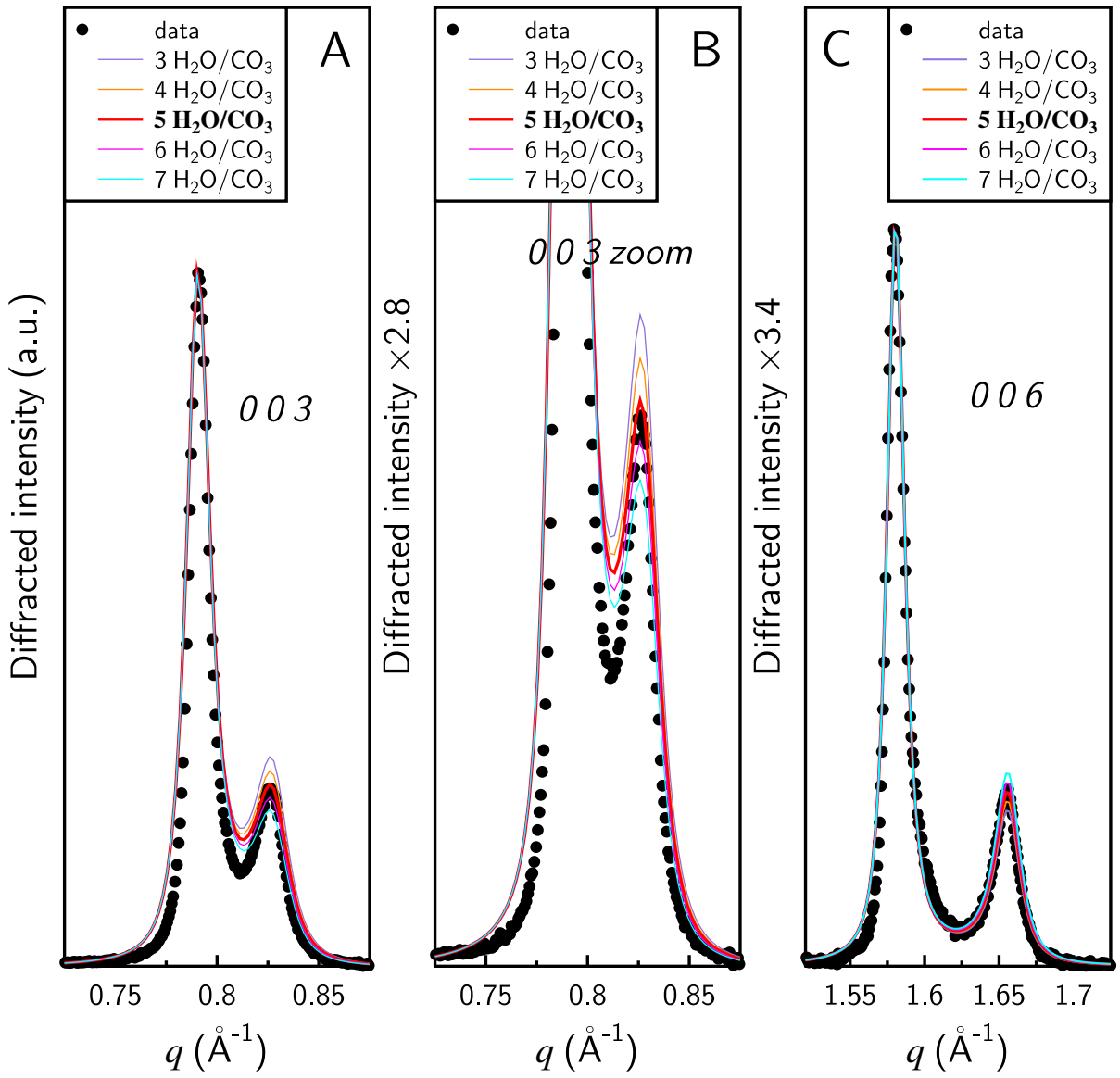

Figure V.8 – Fit of water proportion in Gr-CO_3 layers to model XRD patterns of 00l reflections of interstratified micro-Co-GR phase (A - 003 reflections, B - zoom on 003 reflections and C - 006 reflections). XRD data were taken at $V/V_r = 6$. Set of parameters for the model: R = 1, $W_{Cl} = 0.715$, $W_{CO_3} = 0.285$, $P_{ClCl} = 0.985$, $P_{ClCl} = 0.962$, d_{003} of Gr-Cl layer = 7.952 and d_{003} of Gr-CO_3 layer = 7.585.

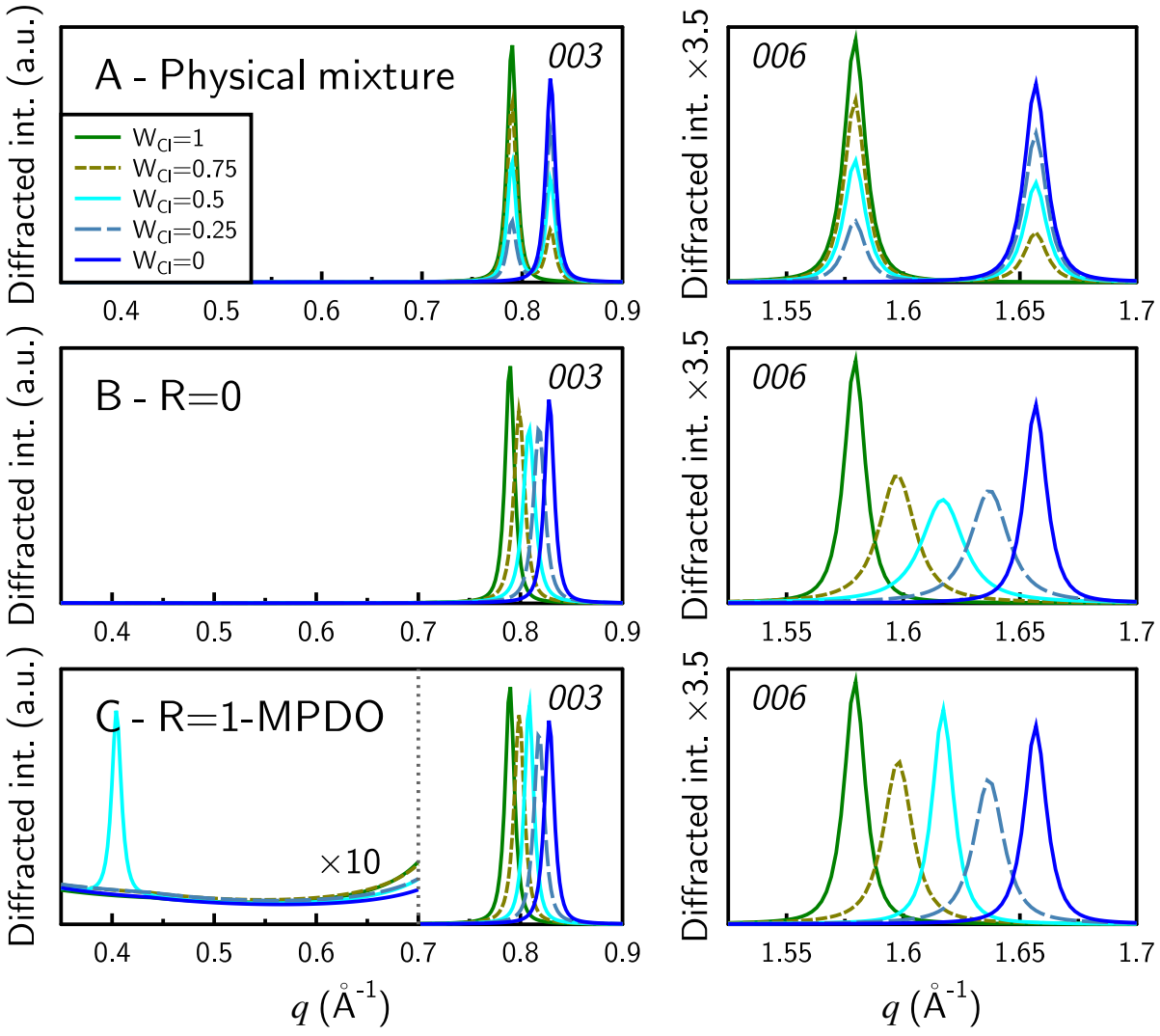

Figure V.9 – Influence of various types of interstratification on 00l reflections of micro-Co-GR phase XRD patterns. Two layer types were interstratified: Gr-Cl layers with d_{003} = 7.957 Å, an abundance W_{Cl} (same color scale for every graph) and a probability that this type of layer follows itself P_{ClCl}; and Gr-CO_3 layers with d_{003} = 7.585 Å (Table III.1 and III.2 for other instrumental, sample and structural parameters). Cases of interstratification processes are physical mixture (A) or described by the Reichweite parameter (R) with R = 0 (B), or R = 1 – MPDO (C).

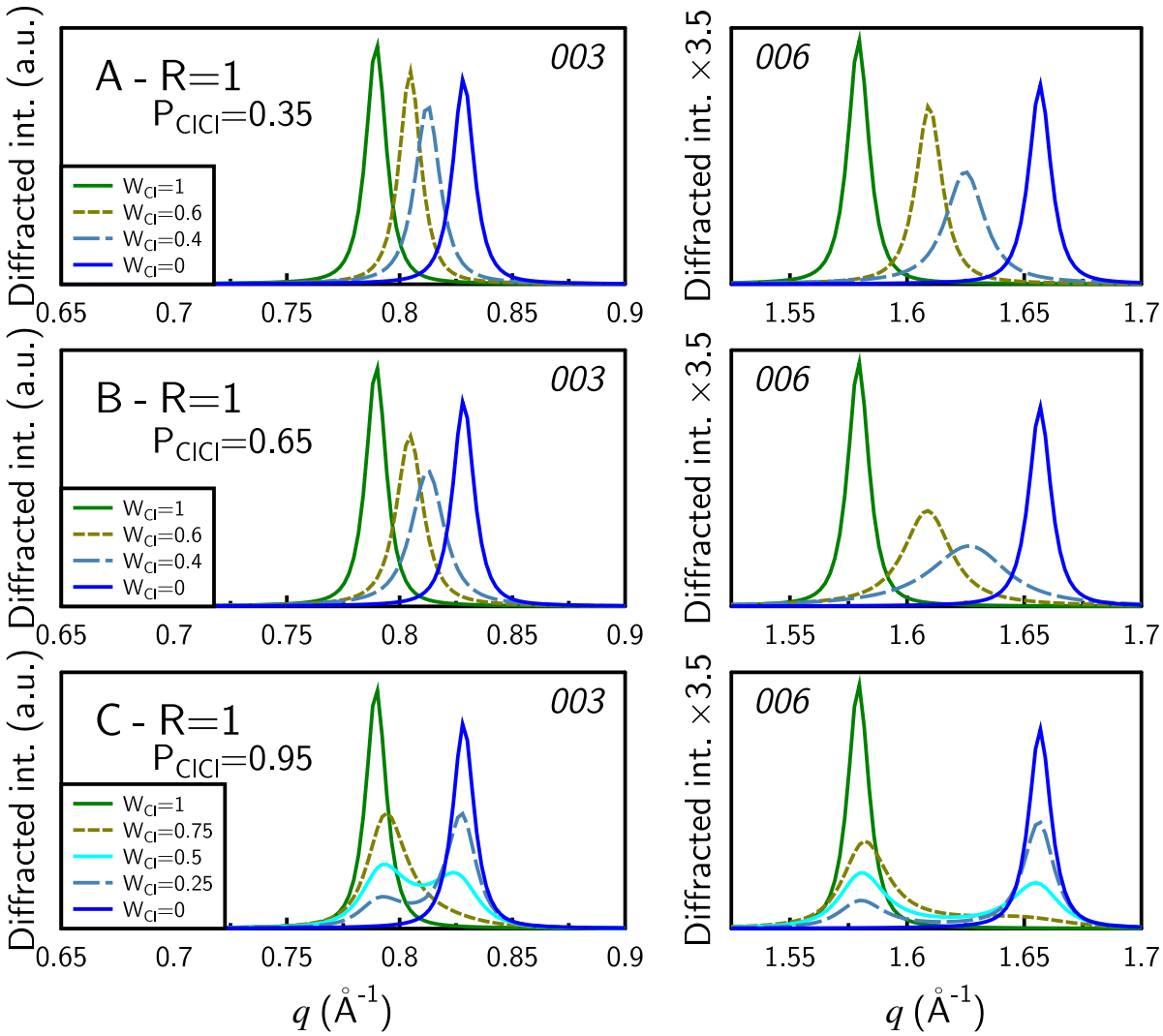

Figure V.10 – Influence of various types of interstratification on 00*l* reflections of micro-Co-GR phase XRD patterns for R = 1. The caption is the same as Figure V.9. Probabilities are P_{ClCl} = 0.35 (A),P_{ClCl} = 0.65 (B) and P_{ClCl} = 0.95 (C).

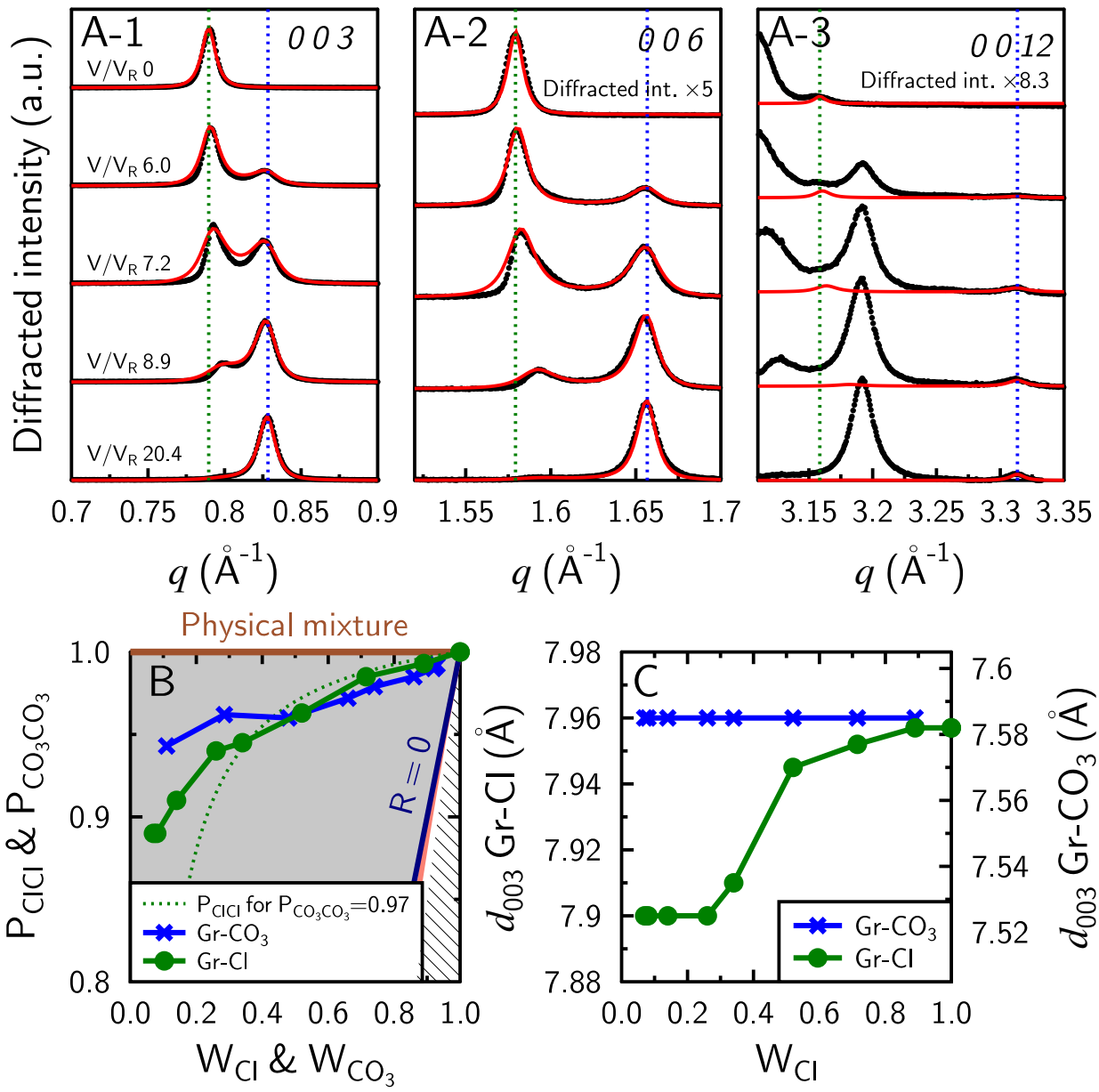

Figure V.11 – Interstratification processes on micro-Co-GR(Cl) during "$NaHCO_3$-XRD" experiment (input solution concentration: 40 mmol·L^{-1} of $NaHCO_3$ and 10 mmol·L^{-1} of NaCl). Measured XRD patterns are available in Figure V.4. (A) XRD patterns at various V/V_r (Red line - model, black points - data, V/V_R - pore volumes, A_1-zoom on 003 reflection, A_2 - zoom on 006 reflection and A_3 - zoom on the 0012 reflection). (B) Evolution of the probabilities according to the abundance of an anion in the interlayer (W_{Cl}-Abundance of Gr-Cl layer, W_{CO_3}-Abundance of Gr-CO_3 layer, P_{ClCl} - Probability of a Gr-Cl layer to follow itself, $P_{CO_3CO_3}$ - Probability of Gr-CO_3 layer to follow itself, brown line - result for samples with a physical mixture process, blue line - results for samples with R = 0 type of interstratification and salmon line - results for samples with R = 1 – MPDO type of interstratification, dotted green line - P_{ClCl} as a function of W_{Cl} if $P_{CO_3CO_3}$ is constant and equal to 0.97). (C) Evolution of the interlayer distances for Gr-Cl and Gr-CO_3 layer. For B and C graphs, green color refers to Gr-Cl and blue color refers Gr-CO_3 layers. Five XRD patterns are shown in A but ten were modelled (results in B and C graphs). All XRD patterns (data & model) are available in appendix and all parameters are listed in table V.1.

chloride ion and Gr-CO_3 layers contained five water molecules per carbonate species.

• *Experiment "$NaHCO_3$-XRD" - Carbonate species ⟶ Cl*

After the exchange of Cl^- by carbonates species, a solution containing 50 mmol $\cdot L^{-1}$ of NaCl was flown through the micro-Co-GR sample in order to test the reversibility of the exchange. $00l$ reflections linked to the presence of Cl^- in the interlayer decreased in intensity (Figure V.12). Once carbonate species were in the interlayer, the structure did not came back to that of the initial micro-Co-GR(Cl) phase. However, all the peak of micro-Co-GR phase, especially the $00l$ reflections, evolved by decreasing in intensity. Other peaks increased in intensity next each of these $00l$ reflections at higher q. For example with the 006 reflection, the peak at $q = 1.66$ Å^{-1} decreased and a first peak increased at $q = 1.68$ Å^{-1} and a second one increased after at $q = 1.70$ Å^{-1}. Consequently, layer-to-layer distance decreased from $d = 7.585$ Å to $d = 7.45$ Å and $d = 7.41$ Å. The reason for this behavior could not be elucidated. Yet, it could be concluded that the exchange was not reversible in these experimental conditions.

Magnetite peaks increased by 40 % in intensity (Figure V.13B). Areas of magnetite reflections also increased by 40 % in 300 V/V_r (Figure V.13C). Cumulated with the first step of experiment "$NaHCO_3$-XRD" where Cl^- was exchanged by carbonate species, the total increase in intensity and areas of magnetite peak was 60 %. This experiment was very long with $V/V_r = 298$ at the end, and these observations are compatible with a slow dissolution of micro-Co-GR(C(IV)) phase and precipitation of magnetite during the experiment.

In summary, once carbonate species were in the interlayer of micro-Co-GR phase, an exchange process occurred but the structure did not come back to the initial structure of micro-Co-GR(Cl) phase. The exchange was not reversible in the present experimental conditions. Over a long period of time ($V/V_r = 298$), magnetite continued to precipitate slowly while micro-Co-GR(C(IV)) phase was dissolving.

• *Experiment "Na_2CO_3-XRD" - Cl ⟶ carbonate species*

Experiments "$NaHCO_3$-XRD" and "Na_2CO_3-XRD" were similar (Figure V.14), but with differences on the following points. 003 reflection of micro-Co-GR(C(IV)) phase shifted from $q = 0.83$ Å^{-1} to their final positions at $q = 0.82$ Å^{-1} and they were also more asymmetrical, peak maximum shifted at high q, than $00l$ peaks of micro-Co-GR(Cl) phase (Figure V.15A and D). Changes in peak position

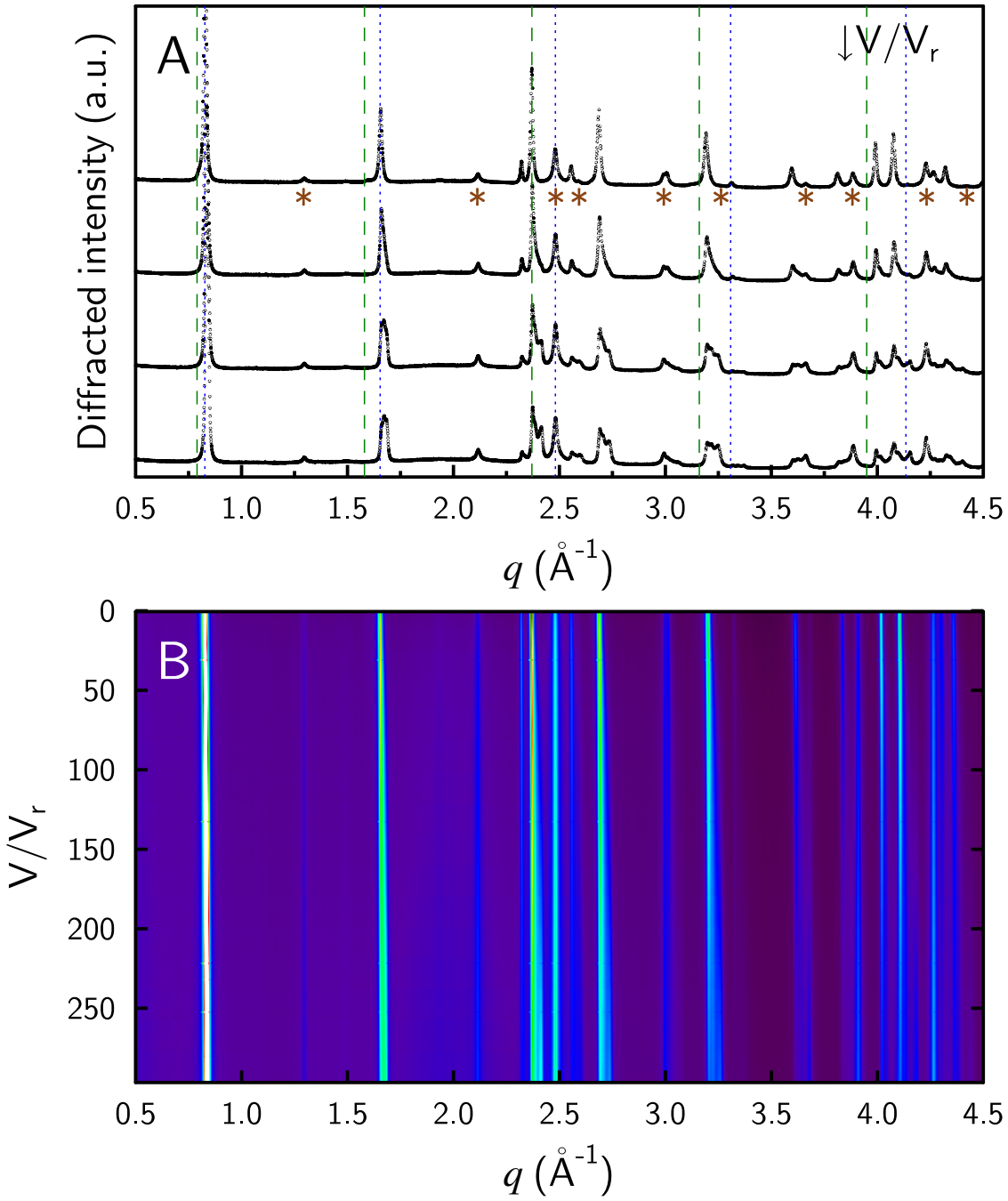

Figure V.12 – XRD patterns recorded *in situ* during a 50 mmol·L^{-1} of NaCl solution flow-through with micro-Co-GR(C(IV)) sample after experiment shown in Figure V.4. Caption is the same as Figure V.4 except for the following details.
(A) Patterns recorded after 0.5, 121.8, 243.6 and 292.3 pore volumes (V/V_r).

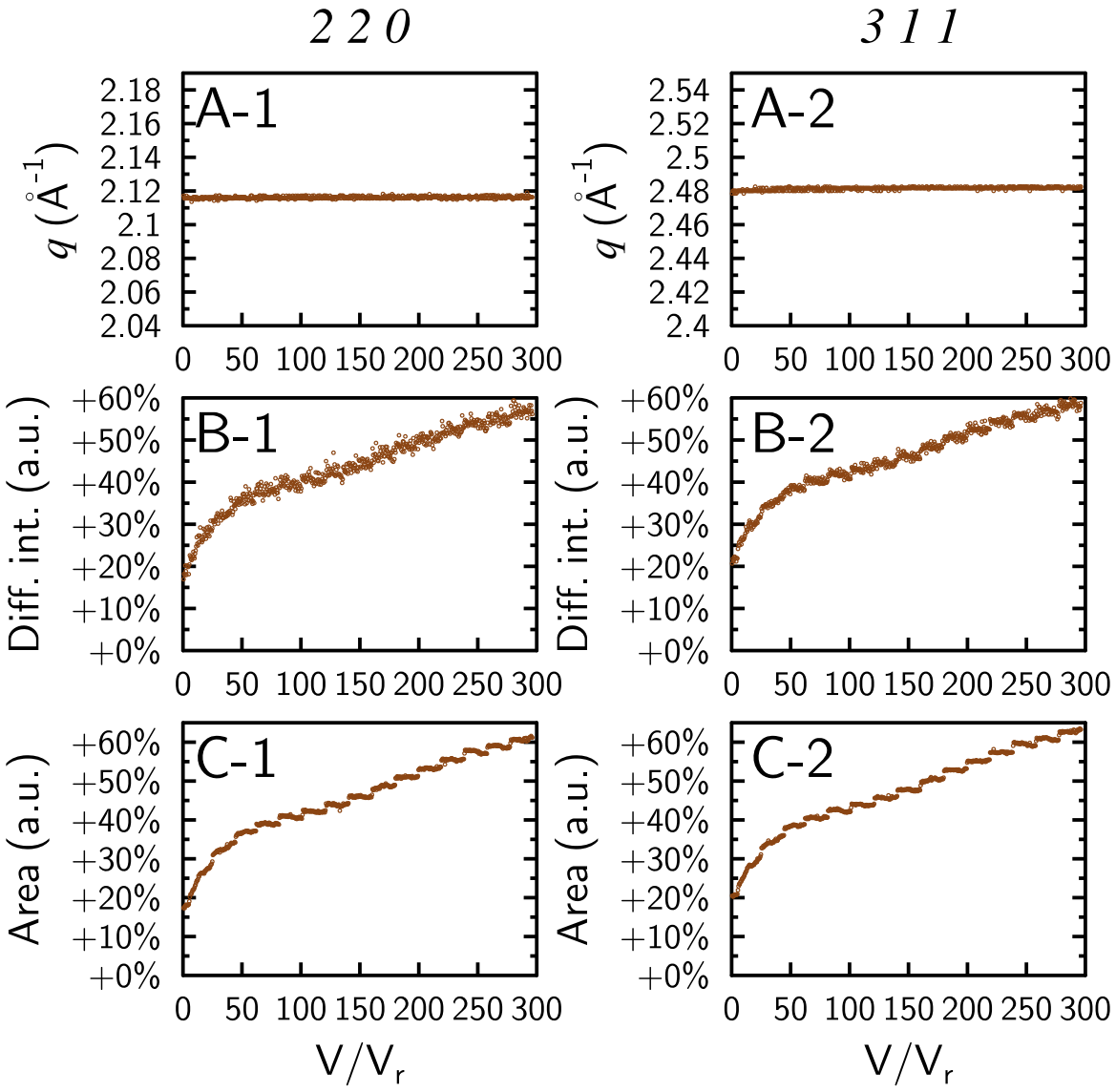

Figure V.13 – Analysis of 220 and 331 reflections of magnetite on XRD patterns recorded *in situ* during a 50 mmol $\cdot$ L^{-1} of NaCl solution flow-through with micro-Co-GR(C(IV)) sample after experiment shown in Figure V.4. Caption is the same as Figure V.6 except for the following details.
(B-C) Intensities and areas given in percentage increases compared to the initial values. They did not start at 0 % because the choice was made to keep the value from Figure V.7 since this experiment was realized just after the previous experiment on the same micro-Co-GR sample.

and asymmetry suggested interstratification. The 003 reflection of micro-Co-GR(Cl) phase remained at a constant position of $q = 0.79$ Å^{-1} (Figure V.15A). The second main difference was the evolution of magnetite reflections. Their intensities also increased but only by a maximum of 7.5 % in 16 V/V$_r$ compared to ≈ 18 % in 24 V/V$_r$ for experiment "NaHCO$_3$-XRD" (Figure V.16B). The area increase depended on the reflection with a 3 % increase for the 220 reflection and 7.5 % increase for the *311* reflection in 16 V/V$_r$ (Figure V.16C). These increases in intensities and areas were at least twice less important than during experiment "NaHCO$_3$-XRD" (20 % increase for the *311* reflection).

The last difference was absence of micro-Co-GR(Cl) phase reflections at the end of the experiment, suggesting that the exchange reached completion.

For experiment "Na$_2$CO$_3$-XRD", interstratification processes occurred during anion exchange. It was accompanied by a slight dissolution of micro-Co-GR and precipitation of magnetite.

• *Experiment "Na$_2$CO$_3$-XRD" - Cl ⟶ carbonate species - Interstratification model with two layers*

For models with MLM2C, sample and instrumental parameters were the same as experiment "NaHCO$_3$-XRD" (see chapter III and table III.1). At start, two layer types were implemented in the model: Gr-Cl and Gr-CO$_3$ layers, with the same characteristics as experiment "NaHCO$_3$-XRD" (Table III.2). The difference was that only 2 water molecules per CO_3^{2-} were needed for Gr-CO$_3$ layers. Eight XRD patterns were modelled.

Starting at V/V$_r$ = 6.8, the agreement between model and data was not good if only two layer types were considered (Figure V.17 and Table V.2). At the end of the exchange (V/V$_r$ = 13.2 and 16.6), data display another reflection near $q = 0.845$ Å^{-1}. To improve the quality of the data modeling, it was assumed that another layer type took also part in this exchange (Figure V.18). This third layer type could improve the model for all the patterns after V/V$_r$ = 6.8.

Table V.2 – List of parameters to model XRD patterns of interstratified micro-Co-GR phase with 2 layer types, Gr-Cl and GR-CO$_3$, during "Na$_2$CO$_3$-XRD" experiment with MLM2C code.

V/V$_r$	R	W$_{Cl}$	W$_{CO_3}$	P$_{ClCl}$	P$_{CO_3CO_3}$	d_{003} Gr-Cl (Å)	d_{003} Gr-CO$_3$ (Å)	σ*
0.0	1	1	0	1	-	7.95	-	0.65
1.3	1	0.94	0.06	0.997	0.953	7.965	7.52	0.80
3.8	1	0.86	0.14	0.992	0.951	7.965	7.58	0.80
6.8	1	0.57	0.43	0.965	0.954	7.975	7.61	0.80
7.7	1	0.455	0.545	0.964	0.970	7.98	7.62	1
8.9	1	0.26	0.74	0.95	0.982	7.97	7.63	0.75
13.2	1	0	1	-	1.000	-	7.62	0.70
16.6	1	0	1	-	1.000	-	7.61	0.7

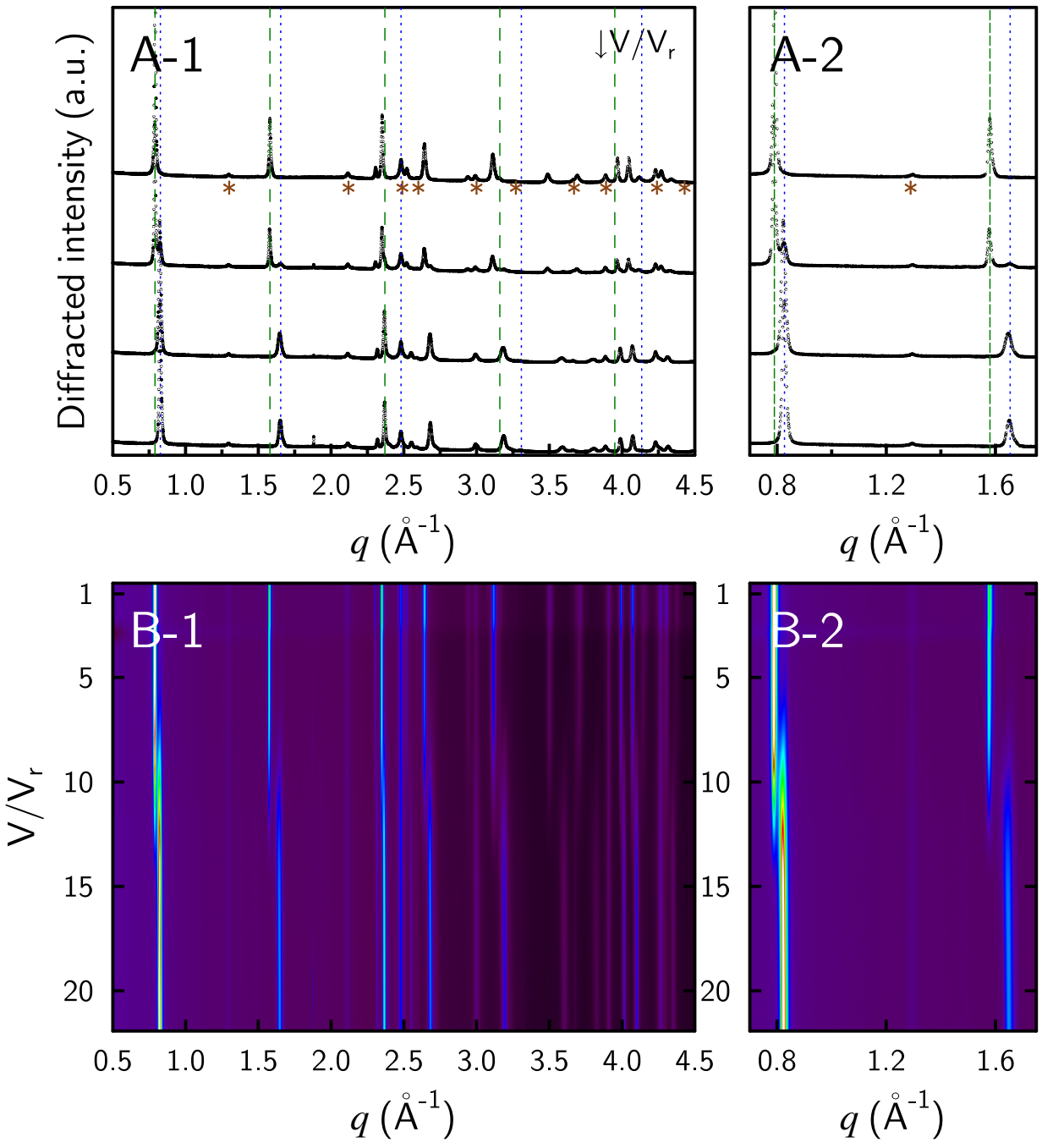

Figure V.14 – XRD patterns recorded *in situ* during experiment "Na_2CO_3-XRD" with micro-Co-GR(Cl) sample (Input solution concentration: 40 mmol·L^{-1} NaCl and 10 mmol·L^{-1} Na_2CO_3, pH = 10.9). Caption is the same as Figure V.4, except for the following details. (A) Patterns recorded after 0.5, 7.3, 14.6 and 21.4 pore volumes (V/V_r).

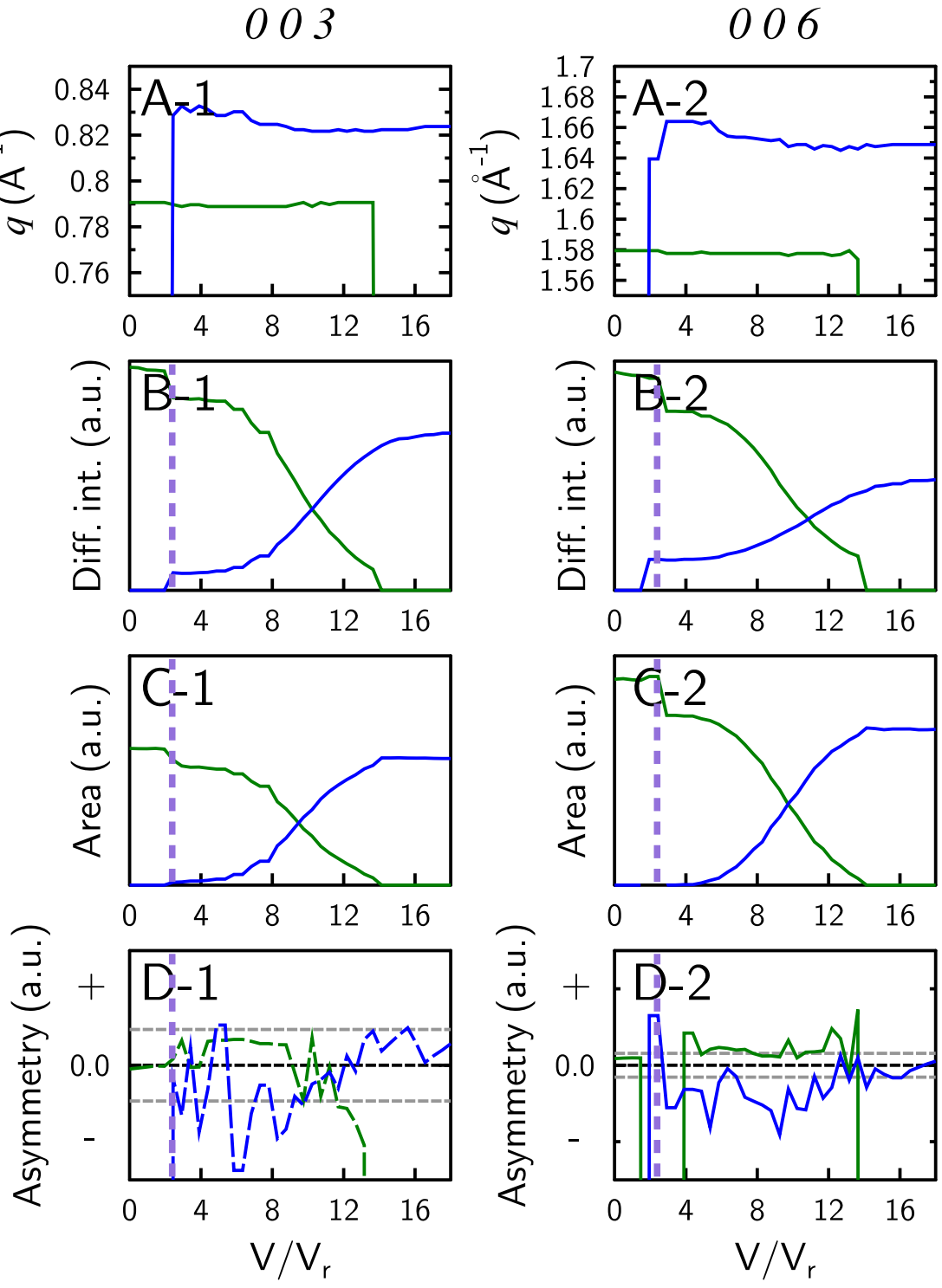

Figure V.15 – Analysis of 003 (left -1) and 006 reflections (right -2) on XRD patterns measured during exepriment "Na_2CO_3-XRD" with micro-Co-GR(Cl) sample (Input solution concentration: 40 mmol·L^{-1} NaCl and 10 mmol·L^{-1} Na_2CO_3, pH = 10.9, XRD patterns on Figure V.14). Caption is the same as Figure V.6 except for the following details. Purple lines show the moment were the hutch was opened to check the setup, change the solution from a solution containing 50 mmol·L^{-1} of NaCl to the solution with a mix of NaCl and Na_2CO_3. The capillary was probably moved in the process.

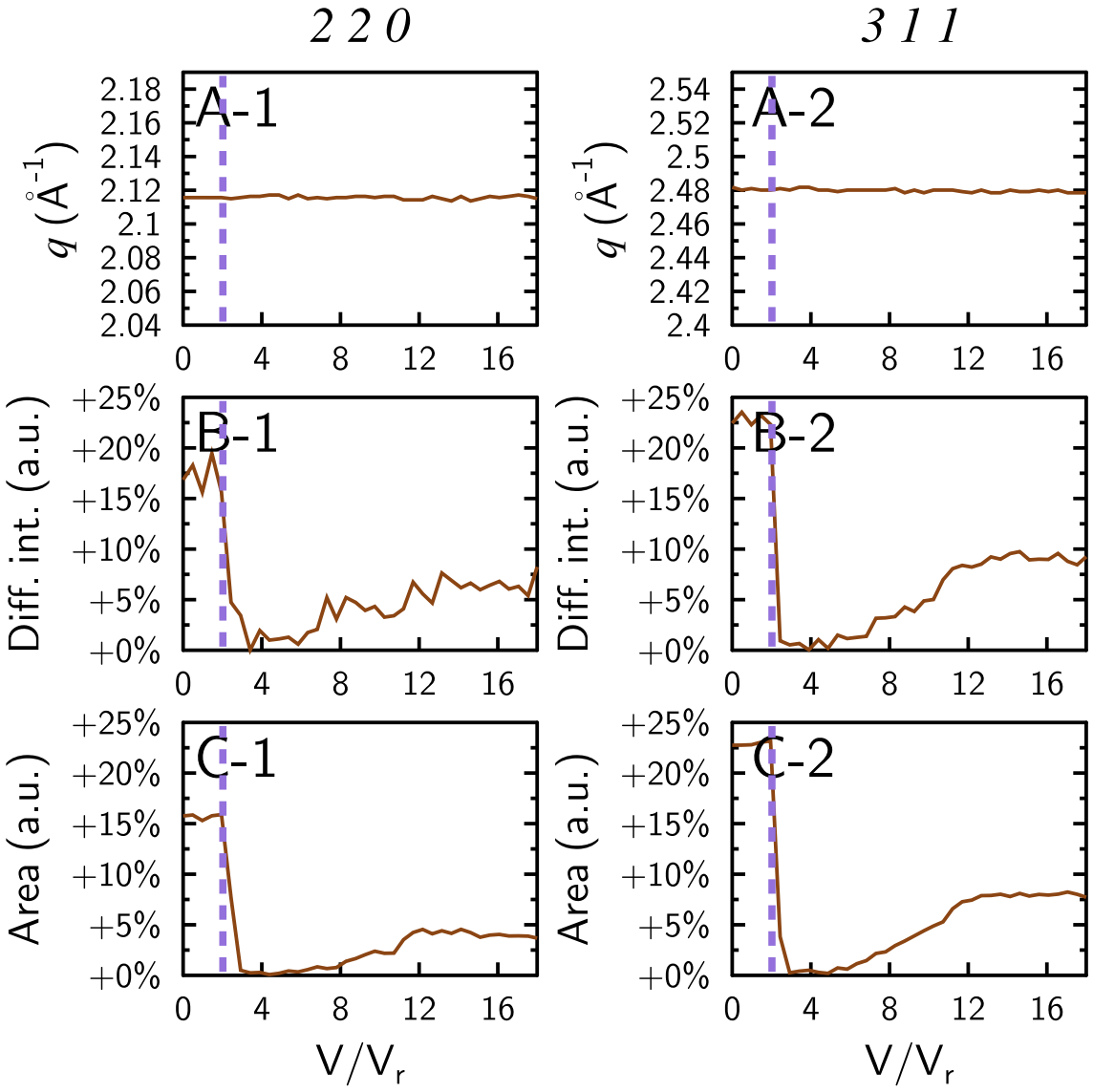

Figure V.16 – Analysis of 220 and 331 reflections of magnetite on XRD patterns measured during an exchange with carbonate species at pH = 10.9 (Input solution concentration: 40 mmol·L^{-1} NaCl and 10 mmol·L^{-1} Na_2CO_3, XRD patterns on Figure V.14). Caption is the same as Figure V.6 except for the following details. Purple lines displayed the moment were the hutch was opened to check the setup, change the solution from a solution containing 50 mmol·L^{-1} of NaCl to the solution with a mix of NaCl and Na_2CO_3. The capillary was probably moved in the process. (B-C) Intensity and area given in percentage increase compared to the initial value. Values before the purple line should not be considered because of the capillary move.

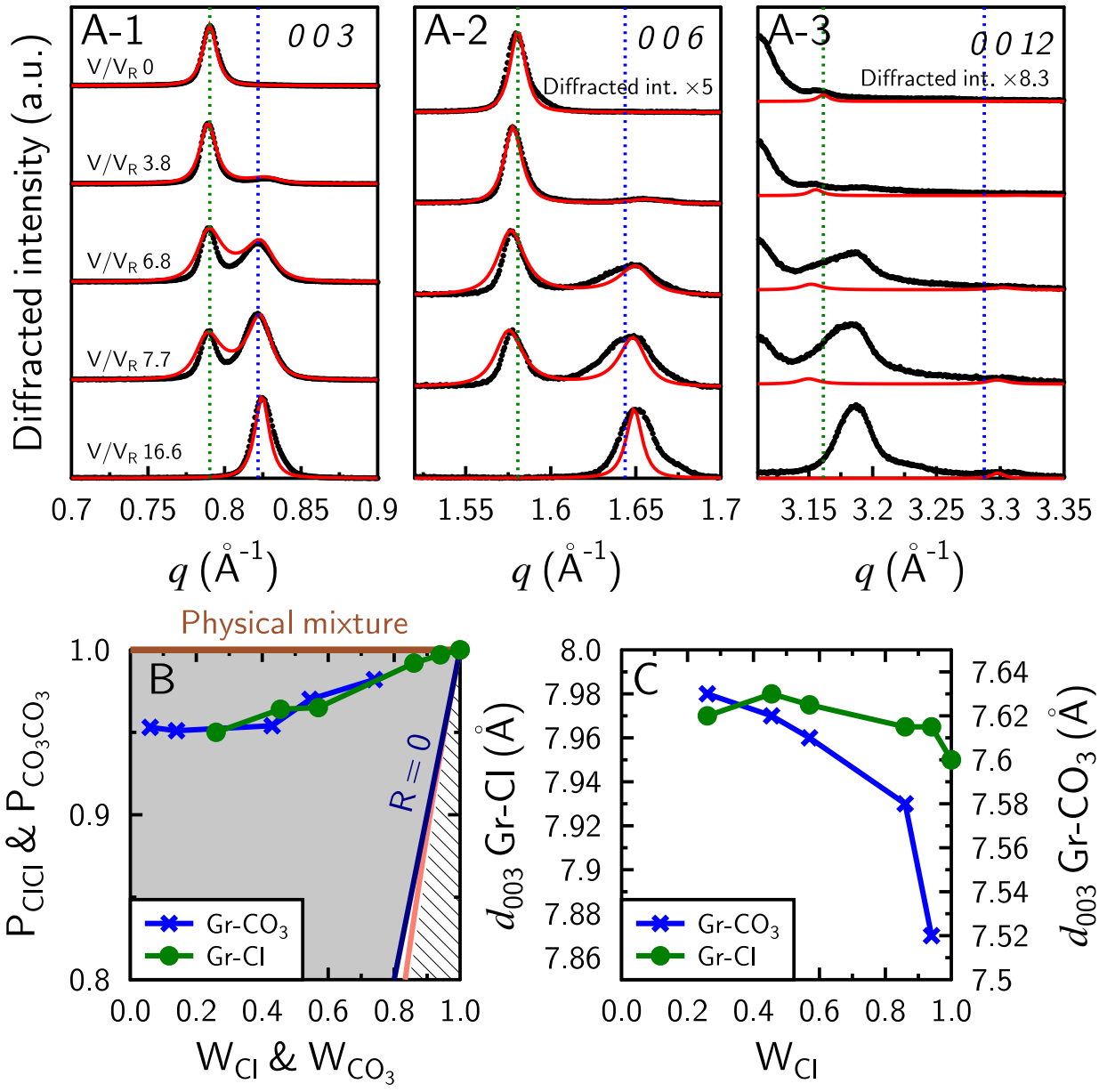

Figure V.17 – Interstratification processes on micro-Co-GR(Cl) during experiment "Na_2CO_3-XRD" (Input solution concentration: 10 mmol·L^{-1} of Na_2CO_3 and 40 mmol·L^{-1} of NaCl). Measured XRD pattern are available in Figure V.14. Caption is the same as Figure V.11. Five XRD patterns are shown in A but 8 were modelled (results in B and C graphs). All XRD patterns (data & model) are available in appendix and all parameters are listed in table V.2.

• *Experiment "Na_2CO_3-XRD" - Cl ⟶ carbonate species - Interstratification model with three layers*

A third layer type was added to the model. It was hypothesized that it contained carbonate species because of its position at $q = 0.845$ Å^{-1}. Thus, the structural model of the previous Gr-CO_3 layers was duplicated into Gr-CO_3-1, the same as Gr-CO_3, and Gr-CO_3-2, with the same chemical composition as Gr-CO_3 but d_{003} was around 7.5 Å. No attempt was made to refine the interlayer occupancy of these two models due to the lack of constraints in the XRD patterns (for example presence of a well-defined series of 00l reflections). In order to limit the number of refined parameters, it was arbitrary chosen to model the XRD patterns assuming that only these two "carbonate" phases could be interstratified, and that the Cl was only present in a pure phase. Otherwise stated, it was assumed that the sample was built of two types of crystallites: one containing only Cl and one with two different interstratified "carbonate" phases. Such modeling hypothesis was justified by the high segregation (> 0.95) of Cl in the previous modeling exercise.

A better fit of 006 reflection was achieved with this model for all the experimental XRD patterns at $V/V_r > 3.8$ (Figure V.19A-2). The fit was not perfect in-between 00l reflections of Gr-Cl on one side and Gr-CO_3-1 and Gr-CO_3-2 on the other side ($q \approx 0.8$ and 1.6 Å^{-1}): the modelled intensities were below the measured intensities. In the model with two layer types for experiment "$NaHCO_3$-XRD", in which interstratification processes increased, the intensity between the two types of 00l reflections as the P_{ClCl} decreased (Figures V.11). Thus, interstratification processes between the three layer types could have resolved this misfit for experiment "Na_2CO_3-XRD", but modeling with a three-components interstratified phase was not attempted, due to a lack of constraints.

To summerize, before $V/V_r \approx 4$, only 2 layer types were necessary to model the system: Gr-Cl and Gr-CO_3 (with d_{003} varying from 7.51 to 7.58 Å). This system was highly segregated with probabilities higher than 0.99 for P_{ClCl} or 0.95 for $P_{CO_3CO_3}$. After $V/V_r \approx 4$, three layer types were probably interstratified. Probabilities of Gr-CO_3-1 and Gr-CO_3-2 layer types point towards a mostly segregated system (Table V.3). P_{ClCl} was close to 1. Layer-to-layer distance of Gr-Cl layers remained fairly constant during the whole experiment but d_{003} of Gr-CO_3-1 varied from 7.51 to 7.7 Å (Figure V.19C).

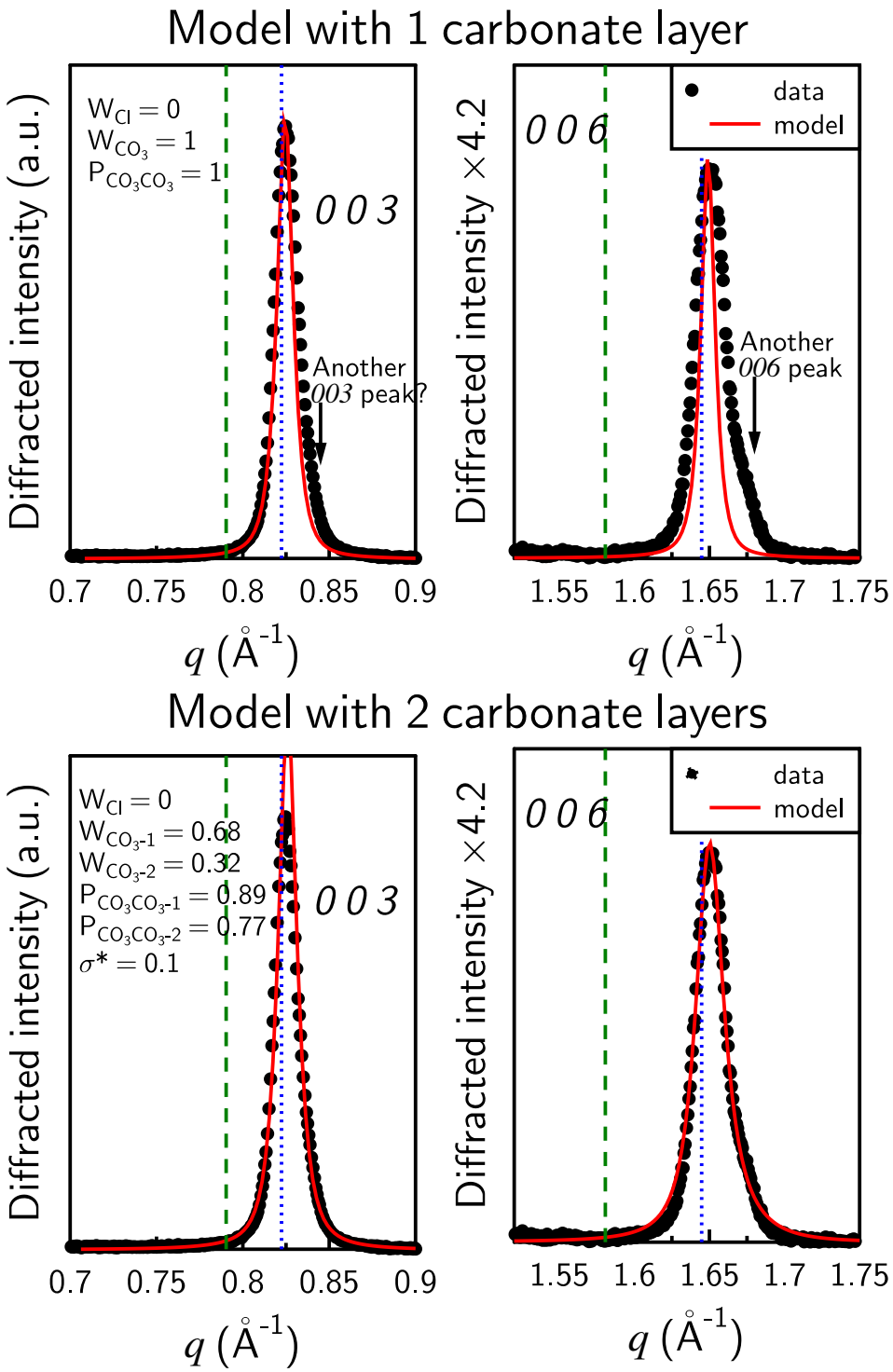

Figure V.18 – Comparison between a model with two layer types (Gr-Cl and Gr-CO_3) and a model with three layer types (Gr-Cl, Gr-CO_3-1 Gr-CO_3-2) at V/V_r = 19.5.

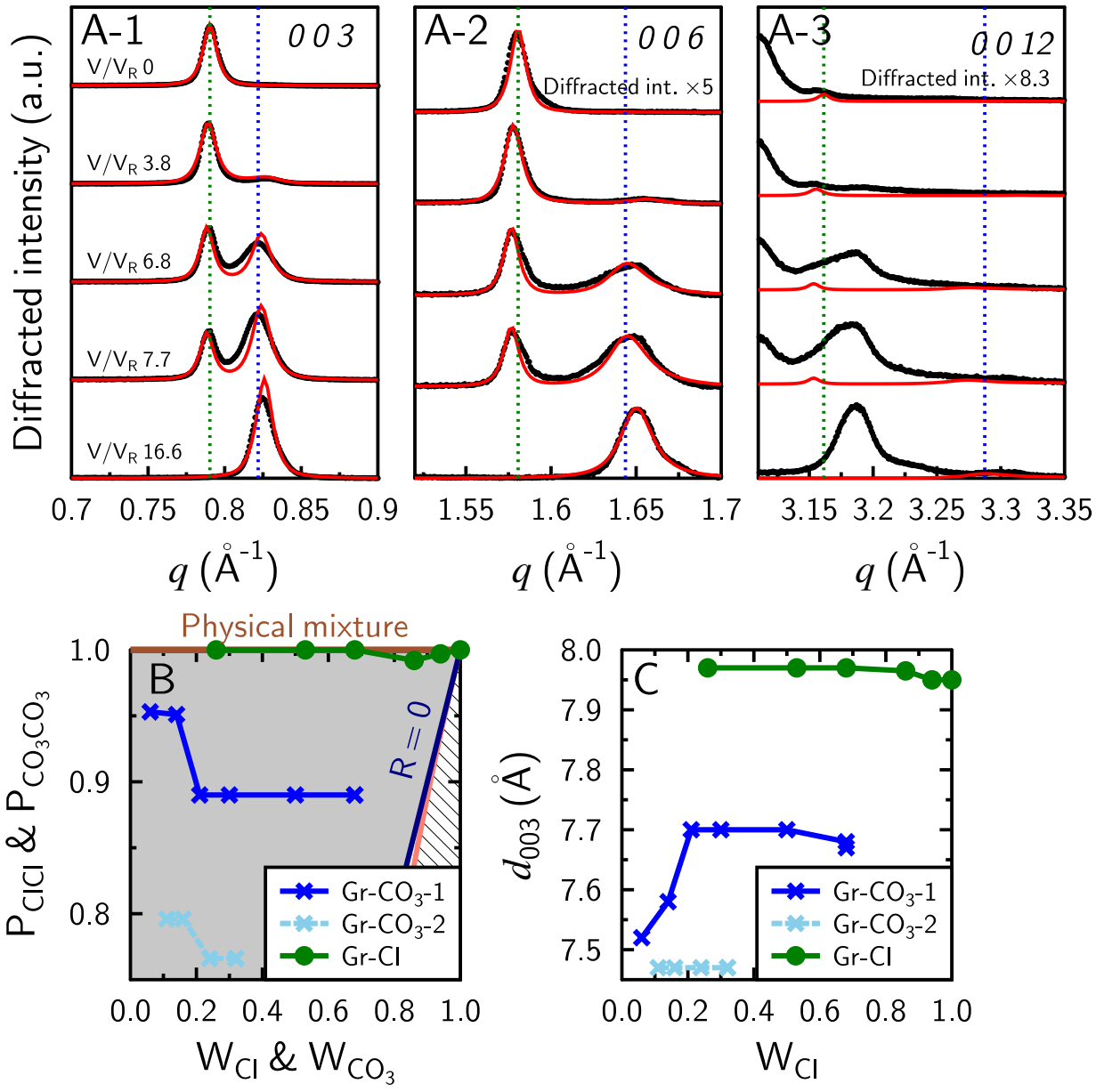

Figure V.19 – Interstratification processes on micro-Co-GR(Cl) during "Na_2CO_3-XRD" experiment with a 3 layer types model (Input solution concentration: 10 mmol·L^{-1} of Na_2CO_3 and 40 mmol·L^{-1} of NaCl). Measured XRD patterns are available in Figure V.14. Caption is the same as Figure V.11. Five XRD patterns are shown in A but 8 were modelled (results in B and C graphs). All XRD patterns (data & model) are available in appendix and all parameters are listed in table V.3.

Table V.3 – List of parameters to model XRD patterns of interstratified micro-Co-GR phase with 3 layer types, Gr-Cl, GR-CO_3−1 and Gr-CO_3−2, during "Na_2CO_3-XRD" experiment with MLM2C code.

		Abundance			Gr-Cl			Gr-CO_3-1 & Gr-CO_3-2 interstratified				
Model	V/V_r	W_{Cl}	W_{CO_3-1}	W_{CO_3-2}	P_{ClCl}	d_{003} Gr-Cl	σ*	$P_{CO_3CO_3-1}$	$P_{CO_3CO_3-2}$	d_{003} Gr-CO_3−1	d_{003} Gr-CO_3−2	σ*
2 layer types	0.0	1	0	0	1	7.950	0.55	-	-	-	-	0.55
	1.3	0.94	0.06	0	0.997	7.950	0.65	0.953	-	7.520	-	0.65
	3.8	0.86	0.14	0	0.992	7.965	0.80	0.951	-	7.580	-	0.80
3 layer types	6.8	0.68	0.21	0.11	1	7.970	1.20	0.890	0.796	7.700	7.470	0.1
	7.7	0.53	0.30	0.16	1	7.970	1.20	0.890	0.796	7.700	7.470	0.1
	8.9	0.26	0.50	0.24	1	7.970	1.20	0.890	0.766	7.700	7.470	0.1
	13.2	0.00	0.68	0.32	-	-	-	0.890	0.766	7.680	7.470	0.1
	16.6	0.00	0.68	0.32	-	-	-	0.890	0.766	7.670	7.470	0.1

As a summary on the interstratification models on experiment "Na_2CO_3-XRD", the presence of a three-components interstratified phase was likely, even if it could not be quantified. The three layer types building up this phase are: one layer type with interlayer Cl^- and two layers with interlayer carbonate species. These layer types were highly segregated, especially the layers containing Cl^- compared to the two layer types with carbonate species. Due to the close proximity of $00l$ reflections of the two layer types containing carbonate species, it was difficult to obtain a good precision on their structure, compositions and interstratification parameters (abundances and probabilities).

• *Summary on exchange experiments with carbonate species*

There were similarities between experiments "$NaHCO_3$-XRD" and "Na_2CO_3-XRD" (Figure V.20). The initial parameters to model the structure of each micro-Co-GR(Cl) sample were the same, showing that these experiments started on the same base. Interstratification processes happened during the exchange between Cl^- and carbonate species. The interstratification type was R = 1. The various layer types were highly segregated. Finally, magnetite proportions were increasing in both experiments but it was more important in "$NaHCO_3$-XRD" experiment.

The differences between experiments "$NaHCO_3$-XRD" and "Na_2CO_3-XRD" were also numerous (Figure V.20). First, for the interstratification models, two layer types were used to model the result of experiment "$NaHCO_3$-XRD", one layer type with Cl as interlayer anion and one layer type with carbonate species. An additional layer type was necessary to model the result of experiment "Na_2CO_3-XRD". This third layer type probably contained carbonate species, but it had a slightly smaller d_{003} than the other layer type with carbonate species (7.5 Åcompared to 7.7 Å). This could be explained by small differences in chemical composition, such as water content for example. Second, the carbonated layer type in experiment "$NaHCO_3$-XRD" contained five water molecules per carbonate species but the most abundant carbonated layer type of experiment "Na_2CO_3-XRD" contained only two water molecules per carbonate species (water content could not be determined for the second carbonated layer type). Finally, at the end of the experiments, Cl^- were completely exchanged by carbonate species for experiment "Na_2CO_3-XRD" (duration of this experiment: 18 V/V_r) but Cl^- was still present (around 7 %) at the end of experiment "$NaHCO_3$-XRD" (duration: 24 V/V_r). The affinity of micro-Co-GR phase for carbonate species may have been different due to differences in chemical conditions between the two experiments (experiment "$NaHCO_3$-XRD": pH≈ 8.5, input solution concentration of 40 $mmol \cdot L^{-1}$ of $NaHCO_3$ and 10 $mmol \cdot L^{-1}$ of NaCl; and experiment "Na_2CO_3-XRD": pH≈ 11, input solution concentration of 10 $mmol \cdot L^{-1}$ of Na_2CO_3 and 40 $mmol \cdot L^{-1}$ of NaCl). These variations in

chemical conditions probably explained the other differences exhibited by the two experiments such as different magnetite proportions. Further chemical experiment and chemical data are necessary to further determine the origin of these differences.

In experiment "$NaHCO_3$-XRD", the system did not reverse back to the initial structure of micro-Co-GR(Cl) phase following an input of 50 mmol$\cdot$L^{-1} of NaCl solution (duration 300 V/V$_r$). Magnetite did also precipitate, probably due to the dissolution of micro-Co-GR phase. The 00l reflections corresponding to d_{003} = 7.59 Å decreased in intensity during the whole experiment but two other reflections increased nearby with d_{003} = 7.45 Å and d_{003} = 7.41 Å. These distances were close to the d_{003} value of the third layer type displayed in experiment "Na_2CO_3-XRD". An hypothesis is there were variations in the interlayer content due to modifications of the layer following heterogeneous dissolution processes (variations in Fe(III) content implies variations in the layer charge and so, variations in the interlayer content).

Carbonate species - SO_4 exchange

After an exchange between Cl^- and carbonated species on micro-Co-GR sample similar to experiment "$NaHCO_3$-XRD", a solution containing 50 mmol$\cdot$L^{-1} of Na_2SO_4 was flown through the sample.

00l reflections of micro-Co-GR(C(IV)) phase decreased in intensity and a shift in position towards higher q during the whole duration of the experiment (duration: 82 V/V$_r$, Figure V.21A and B) This shift of 00l reflections was from q = 0.83 Å^{-1} (d = 7.57 Å) to q = 0.84 Å^{-1} (d = 7.50 Å). This was previously observed for the exchange between carbonate species and Cl^- in the second part of "$NaHCO_3$-XRD". A large diffraction maximum, centered at $\tilde{q}$ = 1.9 Å^{-1} (d = 3.30 Å) was observed in this experiment, and its intensity increased with V/V$_r$. This suggests that an amorphous or cryptocrystalline phase was present at the beginning of the experiment, and that its content increased with time. This phase was not ferrihydrite, the most common poorly crystalline Fe oxide, because its main peaks are centered at q = 2.43 Å^{-1} (d = 2.59 Å) and q = 4.22 Å^{-1} (d = 1.49Å). No other reflection appeared or increased. No magnetite precipitation was observed during the experiment.

Because no reflections of micro-Co-GR(SO_4) phase or any other lamellar phase but micro-Co-GR(C(IV)) was detected, it was concluded that no exchange occurred between carbonate species and SO_4^{2-}. This could be due to, either a higher affinity for carbonate species compared to sulphate anions

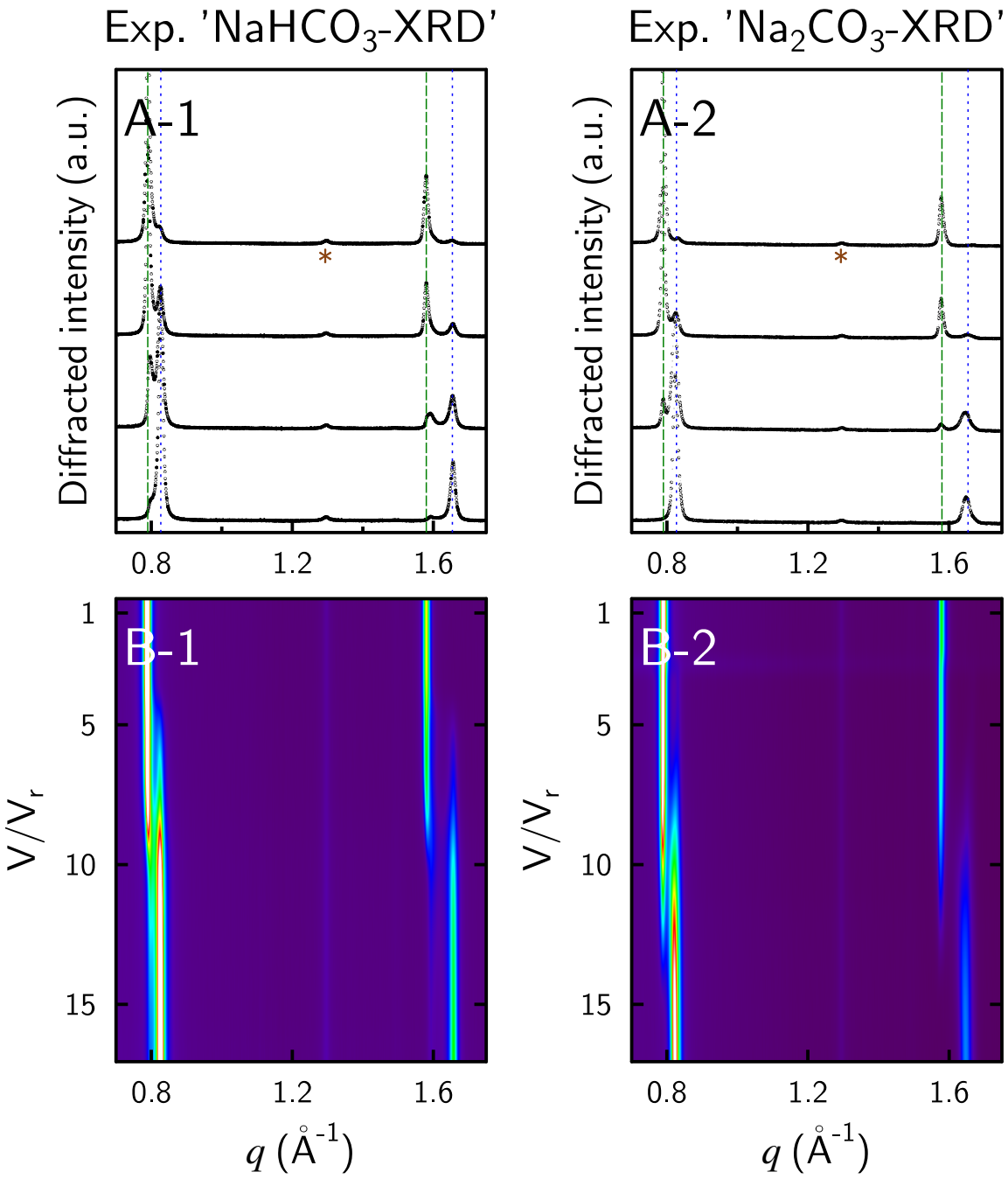

Figure V.20 – Comparison between XRD patterns recorded *in situ* during experiment "$NaHCO_3$-XRD" (-1) and experiment "Na_2CO_3-XRD" (-2). (A-1) Patterns recorded after 4.9, 7.3, 9.7 and 17 pore volumes (V/V_r) for experiment "$NaHCO_3$-XRD". (A-2) Patterns recorded after 0.5, 4.9, 9.7 and 14.6 pore volumes (V/V_r) for experiment "Na_2CO_3-XRD". (B) 2D map of XRD patterns as a function of time expressed in pore volumes. Brown stars display magnetite reflections.

for micro-Co-GR phases, or the non-reversibility of the exchange between carbonate species and SO_4^{2-} with the chemical conditions and time scales explored in this study.

V.1.3 Comparison of structure of micro-Co-GR(Cl) samples after anion exchange experiments

XRD patterns of each micro-Co-GR sample were compared after the exchange experiments with sulphate or carbonate species (not taking into account the experiments on the reversibility of those exchanges). The 006 reflection of micro-Co-GR(C(IV)) phase after experiment "$NaHCO_3$-XRD" was at $q = 1.66$ Å^{-1}, in between the two 006 reflections at $q = 1.65$ Å^{-1} and $q = 1.68$ Å^{-1} of micro-Co-GR(C(IV)) phases after experiment "Na_2CO_3" (Figure V.22). The two 006 reflections after experiment "Na_2CO_3" were assumed to be due to two different micro-Co-GR(C(IV)) phases, modelled by two layer types containing CO_3^{2-} in interstratification models. This result showed that all layer types contained carbonate species. They probably had differences in their composition inducing various layer-to-layer distance and so, different positions for 00l reflections. This difference in composition could be the type of carbonate species, solvatation degree, or carbonate occupancy within the interlayer due to a modification of the layer charge. An hypothesis would be that this difference in layer charge was induced by differences in dissolution processes between the two experiments. The other hkl reflections with $h \neq 0$ and $k \neq 0$ for micro-Co-GR(C(IV)) phase in both experiments were at similar positions showing that the exchange modified the structure similarly in both experiments. An attempt was made to index the reflections of micro-Co-GR(C(IV)) phase by using a modified structural model from micro-Co-GR(Cl) phase with a different c lattice parameter ($c = 22.8$ Å). Cl was replaced by C and the occupancy was divided by 2 (from 0.083 to 0.042, position (0;0;0.167). Oxygen from CO_3^{2-} were at position (0.09;-0.09;0.5) and occupancy at 0.042. All hkl reflections from this modelled structure can be found on the XRD pattern of micro-Co-GR(C(IV)) phase for both experiments (Figure V.22). For the most intense reflections after $q = 2$ Å (position at $q = 2.3, 2.6, 3.2, 3.9$ and 4.1 Å), the modeled relative intensities did not correspond to the measured relative intensities. It could be due to position of interlayer anion which was not known. It was assumed that C were at the same position as Cl. However, if the carbonate specie is CO_3^{2-}, its position should be different from Cl^- because CO_3^{2-} are twice less abundant as Cl^-, so as Fe^{3+}. The space group remained the same after an exchange between Cl^- and carbonate species. Micro-CO-GR(SO_4) sample had a totally different XRD pattern. It was induced by a sharp increase in layer-to-layer distances due to the presence of SO_4^{2-} in the interlayers and a probable modification of the space group during the exchange (Figure V.22).

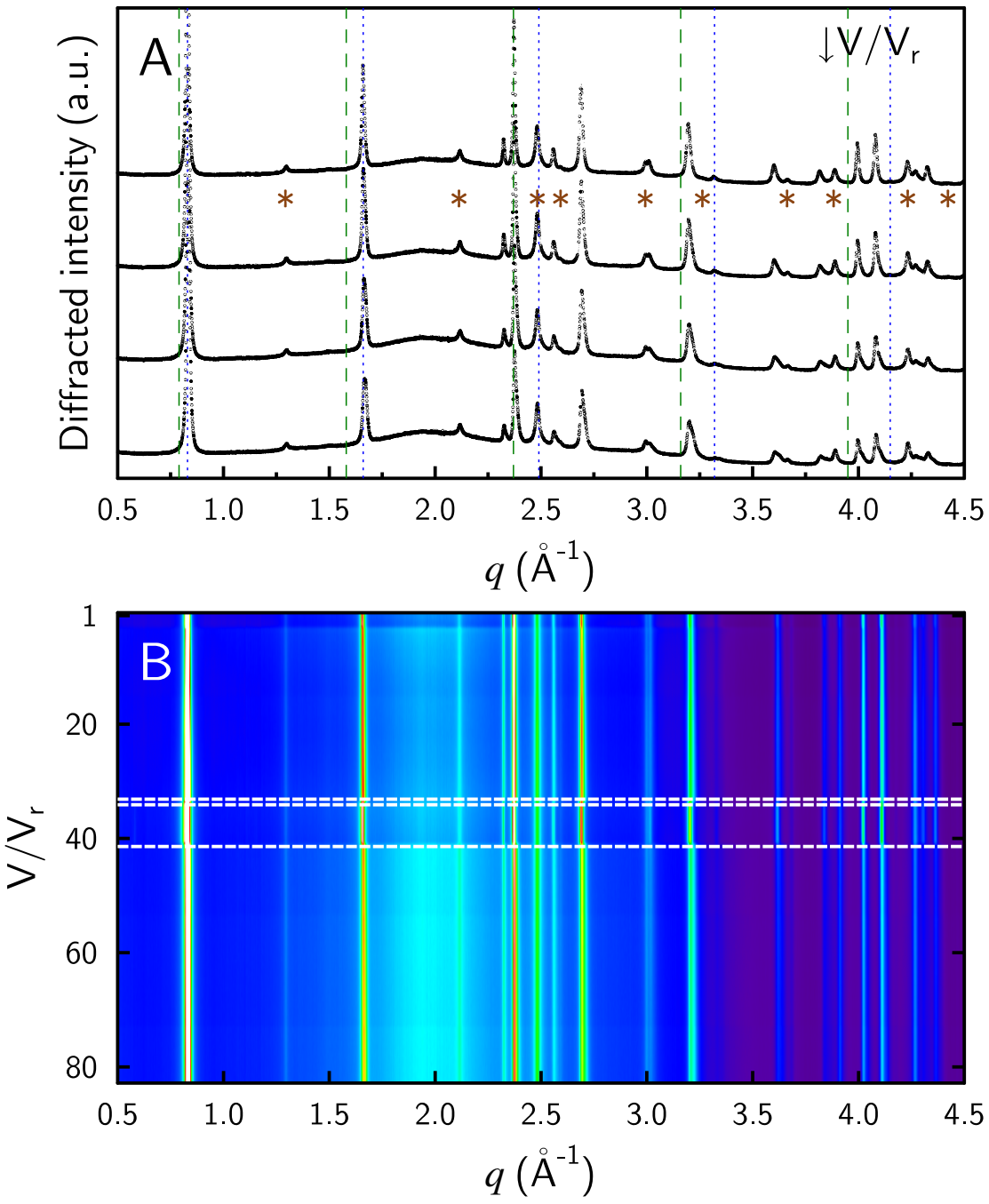

Figure V.21 – XRD patterns recorded *in situ* during a 25 mmol·L^{-1} of Na_2SO_4 solution flow-through experiment with micro-Co-GR(C(IV)) phase after an experiment similar to the one shown in Figure V.4. Caption is the same as in Figure V.4, except for the following details. (A) Patterns recorded after 0.5, 26.8, 53.6 and 82.8 pore volumes (V/V_r). (B) White dashed lines display moments where a short translation of the capillary position was done to check that XRD patterns were otherwise similar elsewhere in the capillary. The capillary was put back at its initial position after $V/V_r = 40$.

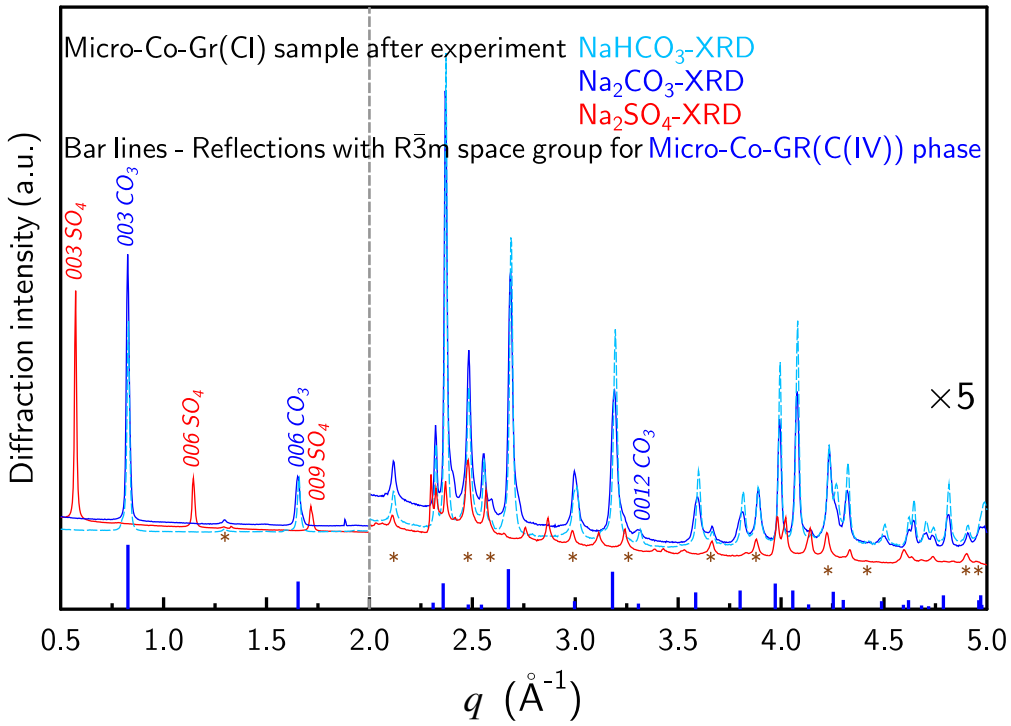

Figure V.22 – XRD patterns recorded *in situ* of micro-Co-GR(Cl) samples after *in situ* XRD exchange experiments "Na_2SO_4-*XRD" (red line), "$NaHCO_3$-XRD" (sky blue line) and "Na_2CO_3-XRD" (dark blue line). Intensities were normalized with the intensity of 006 reflection. Intensities were averaged with a sliding window of 5 points. Intensities were multiplied by 5 for $q > 2$ Å^{-1} for all XRD patterns. $00l$ SO_4 are the reflections attributable to micro-Co-GR(SO_4) phase. $00l$ CO_3 are the reflections attributable to micro-Co-GR(C(IV)) phase. Brown $*$ correspond to magnetite reflections.

V.1.4 Summary on mechanism of ion exchange in green rusts

For the $Cl^- \longrightarrow {SO_4}^{2-}$ and $Cl^- \longrightarrow {CO_3}^{2-}$, *In situ* XRD experiments showed that the exchange structural modifications occurred without dissolution and recrystallization for the exchange between chloride, sulphate and carbonate on green rusts. Interlayer species exchanged readily with solution species without layer modifications. For the exchange of chloride with sulphate anions, the exchange can be described as a physical mixture of two phases, micro-Co-GR(SO_4) and micro-Co-GR(Cl). No dissolution or precipitation of any phase occurred during this exchange (pH ≈ 9). This mechanism was not dependant on the crystallite size nor stacking defects. For the exchange of chloride with carbonate species, interstratification processes occurred between layers containing chloride and layers containing carbonate species. The interstratification type was R = 1 and layer types were highly segregated. The abundance and probability parameters varied depending on the chemical conditions such as pH, and composition of the solution or of the interlayers. Micro-Co-GR phases slightly dissolved, inducing magnetite precipitation. This was explained by the instability of this green rust phase compared to magnetite at the tested chemical conditions. The ion exchange mechanism was dependant on the anion and the chemical conditions but not on the structure variations such as stacking defects or changes in crystal size.

Once micro-Co-GR phases contained carbonate species, it was not possible to reverse it to a micro-Co-GR(Cl) phase with the same structure as the initial samples or to a micro-Co-GR(SO_4) phase. Similarly, once micro-Co-GR phases contained sulphate anions, a exchange occurred upon Cl^- addition, but the newly formed phase did not have the same structure as the initial micro-Co-GR(Cl) phase. During the reversibility tests, green rust dissolution occurred, and magnetite or amorphous phases precipitated.

Study of ion exchange by *in situ* XRD had the advantage to constrain the mechanism of the exchange. The main limitation of this approach was the lack of quantified chemical information such as the interlayer anionic composition, the quantity of anion that was adsorbed or desorbed during the exchange, or the affinity of each anion for green rust interlayers . Batch exchange experiments were conducted to provide the missing information (Tournassat et al., 2011; Ma et al., 2018).

V.2 Quantitative analysis anion exchange in green rusts

V.2.1 Anion Exchange Capacity (AEC)

One of the key parameters for the quantitative understanding of LDH reactivity is the determination of the AEC that is representative of the quantity of anion that can be adsorbed by a given mass of LDH. AEC was first calculated from the structural formula of nano-Co-GR(Cl) and micro-Co-GR(Cl) samples obtained from EPMA results, assuming that all Cl^- was exchangeable. The calculated AEC was 2 ± 0.2 and 2.5 ± 0.2 moles of electric charge per kilogram of anhydrous green rust ($mol_c \cdot kg^{-1}_{\text{anhydrous GR}}$; Table V.5) for nano-Co-GR and micro-Co-GR samples respectively. The AEC was also calculated for the reacted samples, assuming that all SO_4^{2-} was exchangeable, with 1.8 ± 0.2 and 2 ± 0.3 $mol_c \cdot kg^{-1}_{\text{anhydrous GR}}$ for nano-Co-GR and micro-Co-GR samples respectively (Table V.5). Additionally, batch exchange experiments were also conducted on micro-Co-GR(Cl) and nano-Co-GR(Cl) samples, and the AEC was inferred from the quantity of anions desorbed or adsorbed by a weighted amount of green rust during various exchange experiments at different chemistry conditions (Table V.4 for micro-Co-GR phase, "AEC exchange"). For micro-Co-GR sample, two mass corrections were made: first the percentage of humidity was removed (20 % of the dry mass according to TGA results - Table IV.3) and then, the percentage of magnetite in the synthetic samples (14 % of the dry mass according to Rietveld refinements results - Figure IV.5). In Agnel et al. (2020), only the correction of humidity was made, so the AEC values were different from the values given in this manuscript. AEC inferred from adsorbed sulphate or carbonate species gave variable results for two main reasons. First, SO_4^{2-} or CO_3^{2-} amounts adsorbed by green rust samples were half of the desorbed amounts of Cl^- (Table V.4). Second, the difference between initial and equilibrium concentrations of these anions (between 5 to 7.5 %) was small compared to concentration measurement uncertainties. Consequently, AEC values calculated from the leached Cl^- concentrations (2.5 ± 0.2 $mol_c \cdot kg^{-1}_{\text{anhydrous GR}}$) were considered to be the most reliable . For nano-Co-GR sample, one batch exchange experiment was carried out with an exchange solution containing 25 $mmol \cdot L^{-1}$ of Na_2SO_4. Magnetite was absent in this sample, the mass of which was corrected from the humidity only (20 % of the wet sample mass). The amount of desorbed Cl^- was 0.29 ± 0.05 mmol. The SO_4^{2-} concentrations measured after equilibrium were close to the concentrations of the stock solutions. Thus, the amount of adsorbed SO_4^{2-} could not be determined with a good accuracy, and the AEC for nano-Co-GR phase was only calculated from

desorbed Cl^-, *i.e.* 1.6 ± 0.2 $mol_c \cdot kg^{-1}_{anhydrous\ GR}$ (Table V.5).

V.2.2 Anion exchange Stoichiometries

Anion exchange stoichiometry was calculated as the ratio of desorbed chloride with adsorbed sulphate or carbonate species on micro-Co-GR phase. This ratio gives evidences about the adsorbed anionic species. For example, a ratio equal to 1 corresponds to an exchange with a monovalent anion (HCO_3^{2-}). A ratio close to 0.5 indicates an exchange with a divalent anion (SO_4^{2-} or CO_3^{2-}). Batch experiments pointed toward a SO_4^{2-}/Cl^- ratio of approximately 0.5 ± 0.1, (Table V.4) and the following reaction was considered for Cl^--SO_4^{2-} exchange on micro-Co-GR phase (represented by Gr exchange site):

$$2\ GrCl + SO_4^{2-} \overset{K_{ex}^{Cl-SO_4}}{=} Gr_2SO_4 + 2\ Cl^- \tag{V.1}$$

For nano-Co-GR samples, only desorbed Cl^- concentration measurements were reliable. SO_4^{2-} measurements were not conclusive, as already explained for the AEC measurement, and stoichiometries could not be calculated for Cl^-:SO_4^{2-} exchange on nano-Co-GR phase. It was considered that the exchange stoichiometry was the same as for micro-Co-GR phase.

For experiments with carbonate species (DIC), various anions were possibly adsorbed: CO_3^{2-}, HCO_3^{2-} or $NaCO_3^-$. According to speciation calculations with PHREEQC, proportions of DIC in a solution of 50 $mmol \cdot L^{-1}$ of $NaHCO_3$ at pH 8.4 were 94.9 % of HCO_3^{2-}, 1.8 % of $NaHCO_3$, 1.7 % of CO_3^{2-}, 0.8 % of $NaCO_3^-$ and 0.8 % of CO_2. HCO_3^- was the major anion in solution but the aqueous speciation is not representative of the surface speciation. A DIC/Cl ratio of 0.5 (Table V.4) was found in experiments with Na_2CO_3 at pH 11, which was consistent with CO_3^{2-} adsorption. Experiments with $NaHCO_3$ at pH 8 resulted in a DIC/Cl ratio of 0.60 ± 0.09, which was also consistent with CO_3^{2-} adsorption. Consequently, it was concluded that, from pH 8 to 11, the dominant exchange reaction with DIC on green rust was:

$$2\ GrCl + CO_3^{2-} \overset{K_{ex}^{Cl-CO_3}}{=} Gr_2CO_3 + 2\ Cl^- \tag{V.2}$$

Table V.4 – Anion exchange and AEC results after total exchange experiments on micro-Co-GR sample (Cor. mass - Corrected mass). Adsorbed anions were SO_4^{2-} (solutions noted S25*) and DIC (solutions noted C25, C50 and HC50*).

Exchange solution*	Cor. mass (g)	Cl desorbed (mmol)	Anion adsorbed (mmol)	Anion/Cl	Corrected AEC from Cl ($mmol_c \cdot kg^{-1}$)	Corrected AEC from anion ($mmol_c \cdot kg^{-1}$)
S25	0.35	0.69 ± 0.05	0.40 ± 0.04	0.58 ± 0.10	2284 ± 719.1	2646 ± 873.8
S25	0.34	0.75 ± 0.06	0.30 ± 0.05	0.40 ± 0.12	2192 ± 546.7	1746 ± 559.1
S25	0.34	0.85 ± 0.05	0.60 ± 0.04	0.70 ± 0.07	2527 ± 640.8	3542 ± 924.9
C25	0.35	0.88 ± 0.08	0.48 ± 0.07	0.55 ± 0.13	2499 ± 622.9	2735 ± 760.6
C50	0.38	0.86 ± 0.04	0.46 ± 0.04	0.53 ± 0.08	2266 ± 467.4	2411 ± 531.3
C50	0.41	1.09 ± 0.04	0.64 ± 0.04	0.58 ± 0.05	2697 ± 477.7	3132 ± 579.4
HC50	0.33	0.94 ± 0.07	0.56 ± 0.04	0.60 ± 0.09	2836.4 ± 772.3	4816.2 ± 1406.8
				Mean	2472	
				Std Dev†	239.1	

* - Initial composition of exchange solutions: S25 - 25 $mmol \cdot L^{-1}$ of Na_2SO_4, C25 - 25 $mmol \cdot L^{-1}$ of Na_2CO_3, C50 - 50 $mmol \cdot L^{-1}$ of Na_2CO_3, HC50 - 50 $mmol \cdot L^{-1}$ of $NaHCO_3$,
† - Standard Deviation,
± - Confidence intervals of 99.7% ($k = 3$, see section III.6.2 Uncertainty calculations).

Table V.5 – Mean AEC ($mol_c \cdot kg^{-1}_{anhydrous\ GR}$) of Nano-Co-GR and micro-Co-GR samples, according to three characterization methods: EPMA measurements of Cl^- or $SO_4 2-$, and batch exchange experiments (AEC exchange details for micro-Co-GR phase are in Table V.4, ± Standard deviation or confidence interval of 99.7 % ($k = 3$) for AEC exchange of nano-Co-GR phase).

Sample	AEC EPMA (Cl^-)	AEC EPMA (SO_4^{2-})	AEC exchange
nano-Co-GR	2 ± 0.2	1.8 ± 0.2	1.6 ± 0.2
micro-GR	2.5 ± 0.2	2 ± 0.3	2.5 ± 0.2

V.2.3 Stepwise anion exchange batch experiments

Cl^- - SO_4^{2-} exchange

Four batch experiments were conducted with micro-Co-GR samples and two batch experiments with nano-Co-GR samples (data on Figure V.26 and V.27). At the first step of each experiment, SO_4^{2-} concentrations were lower than the concentration of the stock solution, while it was the opposite for Cl^-. Green rust adsorbed SO_4^{2-} and desorbed Cl^-. Then, after two to five equilibration steps, depending on the chemical conditions of each of the experiments, SO_4^{2-} and Cl^- concentrations reached the concentration of the stock solution, which is indicative of an equilibrium or steady state condition (Figure V.23). The variations in SO_4^{2-} concentration were measured more accurately than the variations of Cl^- concentration because of the high concentration of Cl^- in the stock solution. For this reason the stoichiometry of the reaction could not been determined accurately at each exchange step.

Cl^- - carbonate species exchange

Three different batch experiments were carried out to study the exchange of Cl^- with carbonate species for micro-Co-GR(Cl) phase:

— Experiment "$NaHCO_3$" - exchange solution with 10 mmol$\cdot L^{-1}$ of $NaHCO_3$ and 40 mmol$\cdot L^{-1}$ of NaCl,

— Experiment "Na_2CO_3 – I" - exchange solution with 10 mmol$\cdot L^{-1}$ of Na_2CO_3 and 30 mmol$\cdot L^{-1}$ of NaCl,

— Experiment "Na_2CO_3 – II" - first exchange solution with 5 mmol$\cdot L^{-1}$ of Na_2CO_3 (4 steps) and 40 mmol$\cdot L^{-1}$ of NaCl and a second exchange solution with 10 mmol$\cdot L^{-1}$ of Na_2CO_3 and 30 mmol$\cdot L^{-1}$ of NaCl (3 steps).

• *Stoichiometries*

In experiment "$NaHCO_3$", from exchange step 1 to 4, the DIC concentrations measured in equilibrium solution were lower than the DIC concentration of the stock solution. Conversely, Cl^- were higher in the equilibrium solution than in the stock solution (Figure V.24A). 0.90 ± 0.02 mmol Cl^- were released and 0.43 ± 0.05 mmol DIC were adsorbed by the sample, which gave a DIC/Cl^- ratio of 0.48 ± 0.06, in agreement with an anion exchange reaction, in which CO_3^{2-} was predominantly

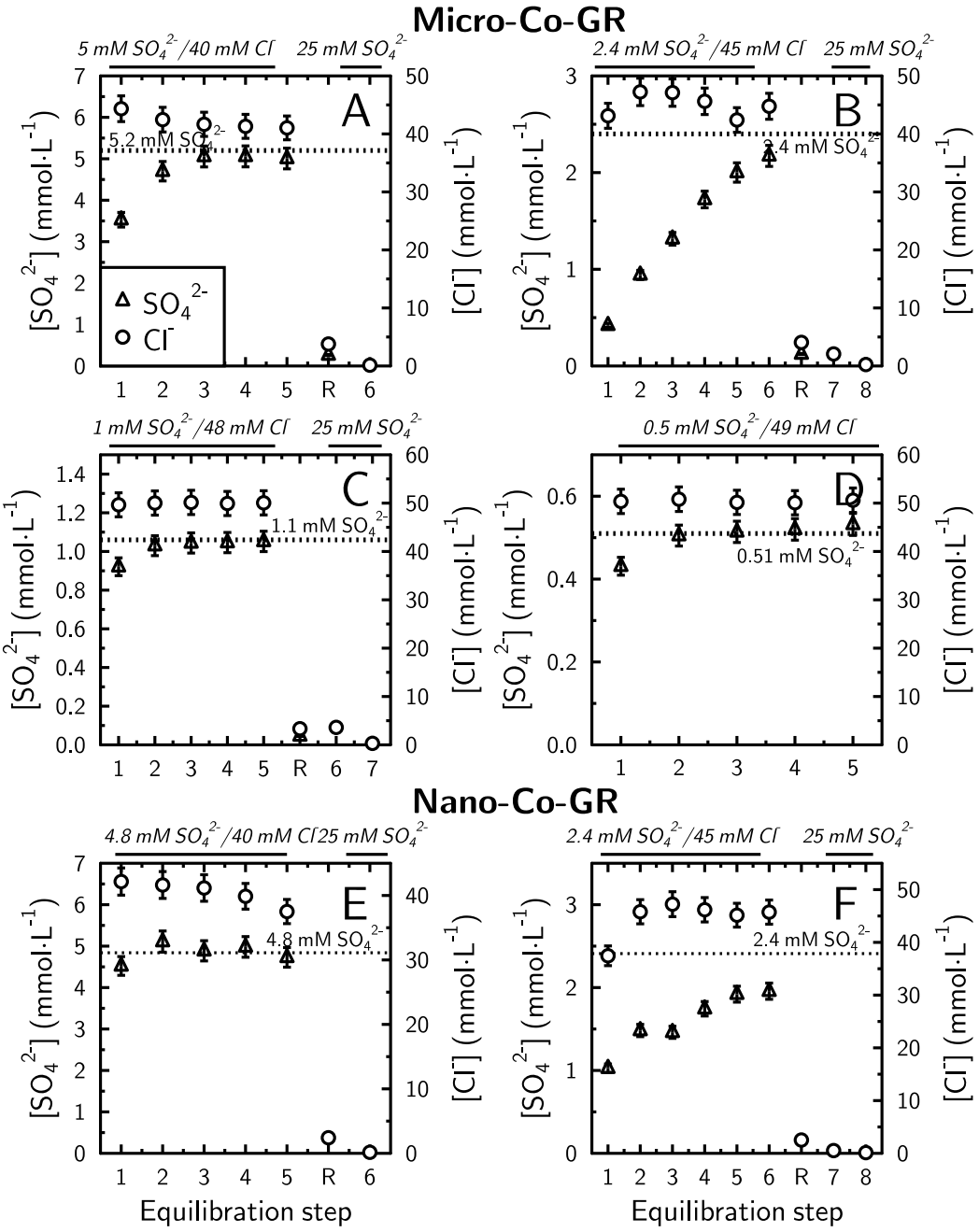

Figure V.23 – SO_4^{2-}-Cl^- exchange data on Co-GR samples (SO_4^{2-} - triangle markers; Cl^- - circles markers). The initial sample was saturated with Cl^-. Steps 1-5 (or 6 on B) corresponded to equilibration with Na_2SO_4-NaCl solutions with total Na concentration of 50 mmol·L^{-1}. The black dashed lines represented the SO_4^{2-} input concentration. Step R corresponded to the rinsing of the sample with ultrapure water. Steps after R corresponded to equilibration steps with 25 mmol·L^{-1} of Na_2SO_4 (or 7 and 8 on B, S25). (A) The exchange solution for steps 1-5 was 5 mmol·L^{-1} of Na_2SO_4 and 40 mmol·L^{-1} of NaCl on micro-Co-GR sample. (B) The exchange solution for steps 1-6 was 2.4 mmol·L^{-1} of Na_2SO_4 and 45 mmol·L^{-1} of NaCl on micro-Co-GR sample. (C) The exchange solution for steps 1-5 was 1 mmol·L^{-1} of Na_2SO_4 and 48 mmol·L^{-1} of NaCl on micro-Co-GR sample. (D) The exchange solution for steps 1-5 was 0.5 mmol·L^{-1} of Na_2SO_4 and 49 mmol·L^{-1} of NaCl on micro-Co-GR sample. (E) The exchange solution for steps 1-5 was 4.8 mmol·L^{-1} of Na_2SO_4 and 40 mmol·L^{-1} of NaCl on nano-Co-GR sample. (F) The exchange solution for steps 1-5 was 2.4 mmol·L^{-1} of Na_2SO_4 and 45 mmol·L^{-1} of NaCl on nano-Co-GR sample.

adsorbed compared to HCO_3^- or any other carbonate species. SO_4^{2-} and Cl^- concentrations reached the concentration of the stock solution at step 5, which is indicative of an equilibrium or steady-state condition. Similar observations were made in experiments "Na_2CO_3-I" and "Na_2CO_3-II" (Figure V.24-B,C).

• *pH variations*

At the start of the experiments, the pH value of the solution in contact with micro-Co-GR sample was always lower than the pH of the stock solution. The pH value increased at each exchange step, and reached a plateau after 2 to 4 steps depending on the experimental conditions (Figure V.24-3). The pH value of the plateau was in agreement with the pH of the stock solution within a margin of ±0.2 pH units. (Figure V.24-1 and -2). Consequently, H^+ was released in solution during Cl^--DIC exchange, a result that was at variance with the results of the Cl^-/SO_4^{2-} exchange experiment.

SO_4^{2-} - carbonate species exchange

The $SO_4^{2-} \longrightarrow$ carbonate species exchange was studied with experiment "$Na_2SO_4/NaHCO_3$". First, micro-Co-GR(Cl) phase was transformed into micro-Co-GR(SO_4) phase through a contact with a solution containing 25 mmol$\cdot$L^{-1} of Na_2SO_4 (Steps 1-3, not shown). Then, the exchange between SO_4^{2-} and carbonate species was studied by adding, several times, a solution containing 10 mmol$\cdot$L^{-1} of $NaHCO_3$ and 20 mmol$\cdot$L^{-1} of Na_2SO_4 (Figure V.46 - Steps 4-10), after insing the sample (R_2).

Data are available in the Thermodynamic models and Discussion section (Figure V.46). During steps 4 to 10, the amount of released SO_4^{2-} was 2.5×10^{-4} mol and the amount of adsorbed carbonate was 2.6×10^{-4} mol. This result confirmed that an exchange reaction took place with the following exchange equation:

$$Gr_2SO_4 + CO_3^{2-} \overset{K_{ex}^{SO_4-CO_3}}{=} Gr_2CO_3 + SO_4^{2-} \quad (V.3)$$

Further modeling were necessary to quantify $K_{ex}^{SO_4-CO_3}$.

The reverse exchange was also studied. The goal of this experiment was to determine if the exchange was reversible or not. First, a solution containing 50 mmol$\cdot$L^{-1} of $NaHCO_3$ was flown through a micro-Co-GR(Cl) sample to make sure that no Cl^- was left in the interlayer (Step 7 and 8). Then, a solution containing 10 mmol$\cdot$L^{-1} of $NaHCO_3$ and 20 mmol$\cdot$L^{-1} of Na_2SO_4) was used (steps

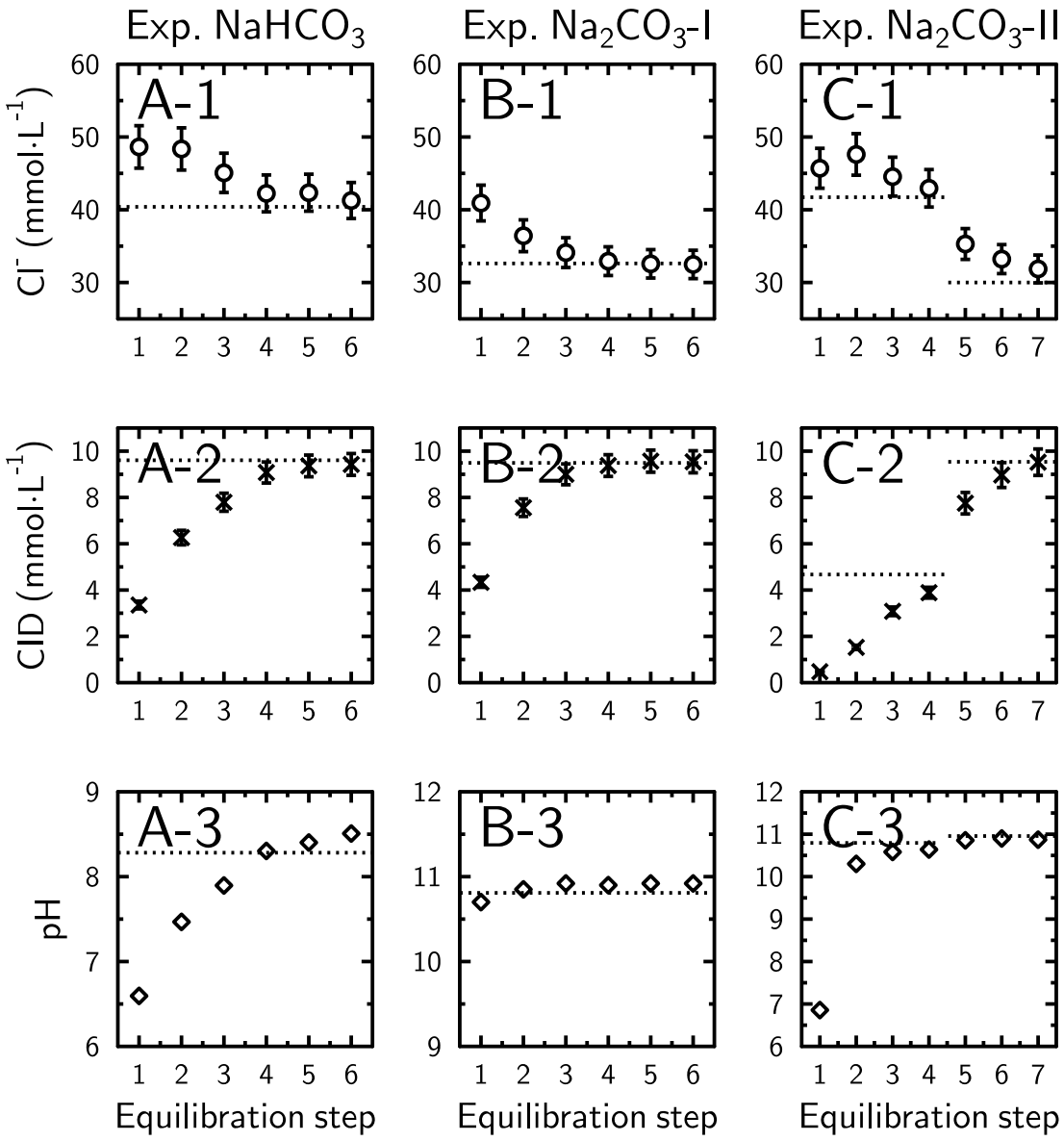

Figure V.24 – DIC-Cl^- exchange data on micro-Co-GR sample for the three exchange experiments (CO_3^{2-} - crosses; Cl^- - circles; pH - diamond, exp. - experiment). pH and concentrations of stock solutions were represented by dotted black lines. (A) Experiment "$NaHCO_3$" - exchange solution with 10 mmol·L^{-1} of $NaHCO_3$ and 40 mmol·L^{-1} of NaCl. (B) Experiment "Na_2CO_3 – I" - exchange solution with 10 mmol·L^{-1} of Na_2CO_3 and 30 mmol·L^{-1} of NaCl. (C) Experiment "Na_2CO_3 – II" - first exchange solution with 5 mmol·L^{-1} of Na_2CO_3 (4 steps) and 40 mmol·L^{-1} of NaCl and a second exchange solution with 10 mmol·L^{-1} of Na_2CO_3 and 30 mmol·L^{-1} of NaCl (3 steps). (-1) Measured Cl^- concentrations (-1), concentration in DIC (-2), and pH values (-3).

9-12). Data are available in the Thermodynamic models and Discussion section (Figure V.48). Models were also necessary to understand the results.

V.3 Thermodynamic models and Discussion

V.3.1 Modeling of stepwise anion exchange experiments and comparison with in situ XRD experiments results

Cl^- - SO_4^{2-} exchange

• *Choice of the model*

According to XRD results, no newly formed phase appeared and peak intensities for magnetite remained the same during an exchange with a solution containing 5 mmol·L^{-1} of Na_2SO_4 40 mmol·L^{-1} of NaCl. Green rust phases crystallite size remained also constant throughout the experiments. These observations were consistent with an anion exchange model with a fast exchange of the species present in the interlayer without change of the layer structure and composition. Consequently, an ion exchange model using the ion exchange theory was used to model the data.

• *Model with Gaines & Thomas convention*

Batch experiment with a solution containing 2.4 mmol $\cdot$ L^{-1} of Na_2SO_4 and 45 mmol $\cdot$ L^{-1} of NaCl was first modelled with the Gaines & Thomas convention (Equation II.5 in section II.2.2, experiment protocol in section III.6.2, Sposito (1981b,a)).

A good fit of Cl^- and SO_4^{2-} concentration data was obtained (Figure V.25A). However,it was not possible to use a constant selectivity coefficient to model this experiment: it was necessary to increase the $log_{10}\, K_{ex,GT}^{Cl-SO_4}$ value at each equilibration step, from −0.3 to 0.5, to obtain a good agreement (Figure V.25B), meaning that the selectivity coefficient increased with the value of SO_4^{2-} occupancy in the exchanger (Figure V.25D).

For all the other batch experiments with micro-Co-GR and nano-Co-GR samples, selectivity coefficient had to be increased to fit the measured data.

• *Model with Rothmund & Kornfeld convention*

Changes of selectivity coefficient value as a function of chemical conditions are usually well captured with a Rothmund & Kornfeld model (Equation II.9, see Section II.2.2 on Anion exchange modeling) (Sposito, 1981b; Bond, 1995). Indeed, an acceptable fit of the data was obtained with a $log_{10}\, K_{ex,RK}^{Cl^- - SO_4^{2-}}$ value of 0.3 and a β value of 2.4 for the micro-Co-GR sample (Figure V.26) and with a $log_{10}\, K_{ex,RK}^{Cl-SO_4}$ value of 0.2 and a β value of 5 for the nano-Co-GR sample (Figure V.27).

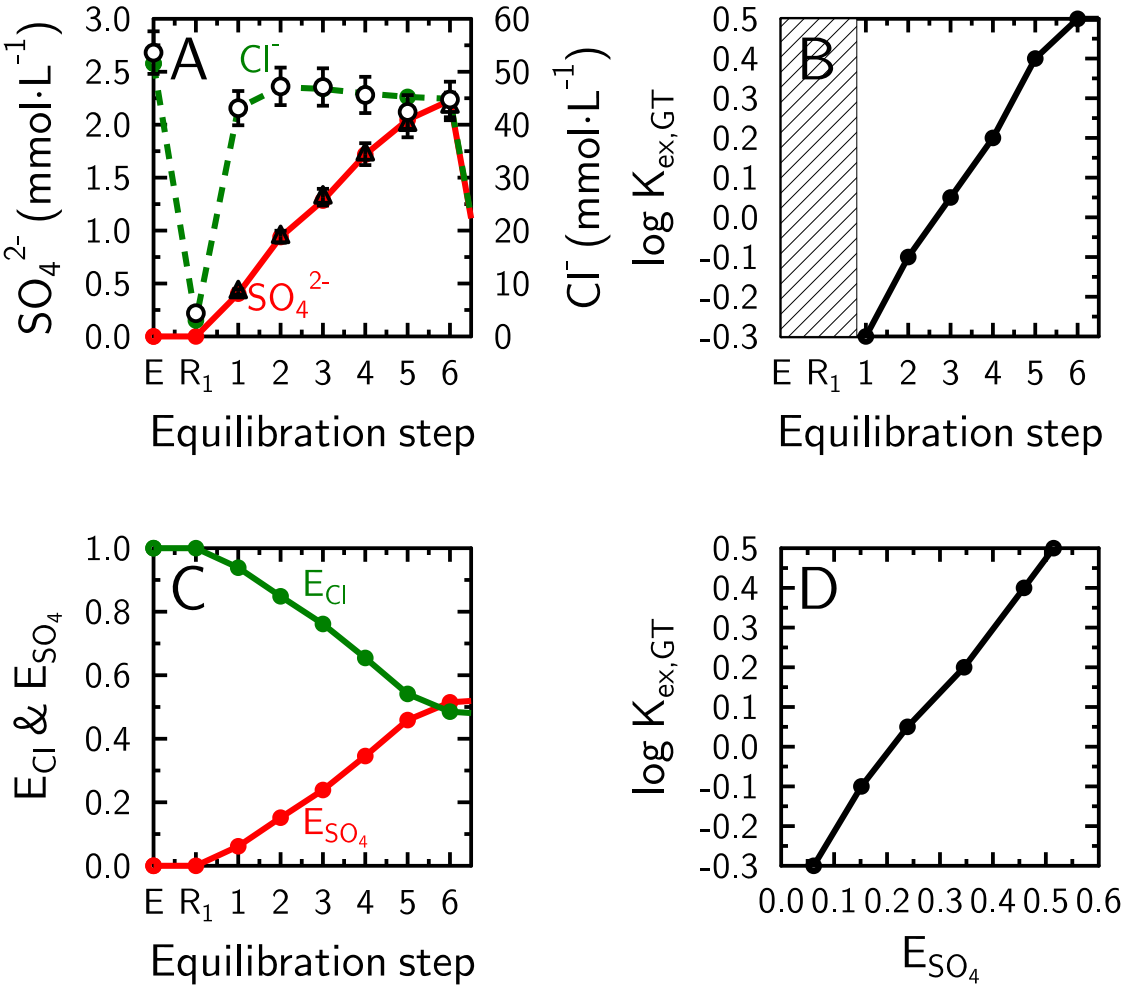

Figure V.25 – SO_4^{2-}-Cl^- exchange data on micro-Co-GR phase with a model using Gaines & Thomas convention. The initial sample was saturated with Cl^- (E). Step R_1 corresponds to the rinsing of the sample with ultrapure water. Steps 1-6 correspond to equilibration with Na_2SO_4-NaCl solution with a concentration of 2.4 mmol·L^{-1} of Na_2SO_4 and 45 mmol·L^{-1} of NaCl. (A) Data and model concentrations of SO_4^{2-} (data - black triangle, model - red line and marker) and Cl^- (data - black circle, model - green dashed line and marker). (B) $log_{10}\, K_{ex,GT}^{Cl-SO_4}$ at each step (No exchange happened in the hatched area). (C) Equivalent fraction (E) of SO_4^{2-} (red line) or Cl^- (green line) on the exchanger. (D) $log_{10}\, K_{ex,GT}^{Cl-SO_4}$ according to the equivalent fraction of SO_4^{2-} on the exchanger.

β values were larger than one, meaning that the Gaines & Thomas selectivity coefficient $K_{ex,GT}$ of the $Cl^- \longrightarrow SO_4^{2-}$ exchange reaction increased with the SO_4^{2-} occupancy on the exchanger, a finding that was consistent with the first direct modeling approach using Gaines & Thomas convention.

The model predicted that 86 % and 95 % of the exchange sites were occupied by SO_4^{2-} in the micro-Co-GR and nano-Co-GR samples, respectively, at equilibrium with an aqueous solution containing 40 $mmol \cdot L^{-1}$ Cl^- and 5 $mmol \cdot L^{-1}$ SO_4^{2-}. These results were in agreement with XRD data that showed that Cl^- interlayers were only a minor component after equilibration of the sample with this aqueous solution composition (Figure V.2).

Cl^- - carbonate species exchange

• *Differences with Cl^--SO_4^{2-} exchange experiments*

Cl^--DIC exchange experiments exhibited marked differences with Cl^--SO_4^{2-} exchange experiments. First, in situ XRD results evidenced a partial transformation of the solid phase with increasing content of magnetite with time in the presence of DIC, but not in the presence of SO_4^{2-}. This result was indicative of a dissolution process taking place at the same time as the exchange process(es). Second, the pH of the equilibrium solution was influenced by the Cl^--DIC exchange, while it was not by the Cl^--SO_4^{2-} exchange. These two observations must be reproduced by the chosen modeling approach.

• *Origin of acidification*

Two possible sources of H^+ release in solution were identified:

— Similarly to clays (Tournassat et al., 2015), green rust phase can buffer the pH of the solution by protonation or deprotonation of its edge surface amphoteric groups (hydroxyl groups).

— The exchange stoichiometry showed that CO_3^{2-} was predominantly adsorbed by micro-Co-GR phase at various pH. For experiment "$NaHCO_3$", the speciation in carbonate species of the stock solution was 93.9 % of HCO_3^-, 2.7 % of CO_3^{2-}, 1.8 % of $NaHCO_3$, 1.2 % of $NaCO_3^-$ and 0.5 % of CO_2. In this case, aqueous HCO_3^- was dissociated into adsorbed CO_3^{2-} and aqueous H^+ during the exchange process:

$$2\,GrCl + HCO^-_{3(s)} = Gr_2CO_3 + H^+_{(s)} + Cl^-_{(s)} \tag{V.4}$$

The first hypothesis can be discarded because it requires a too large amount of surface functional groups to explain the results quantitatively, and also because such acidification was not observed in

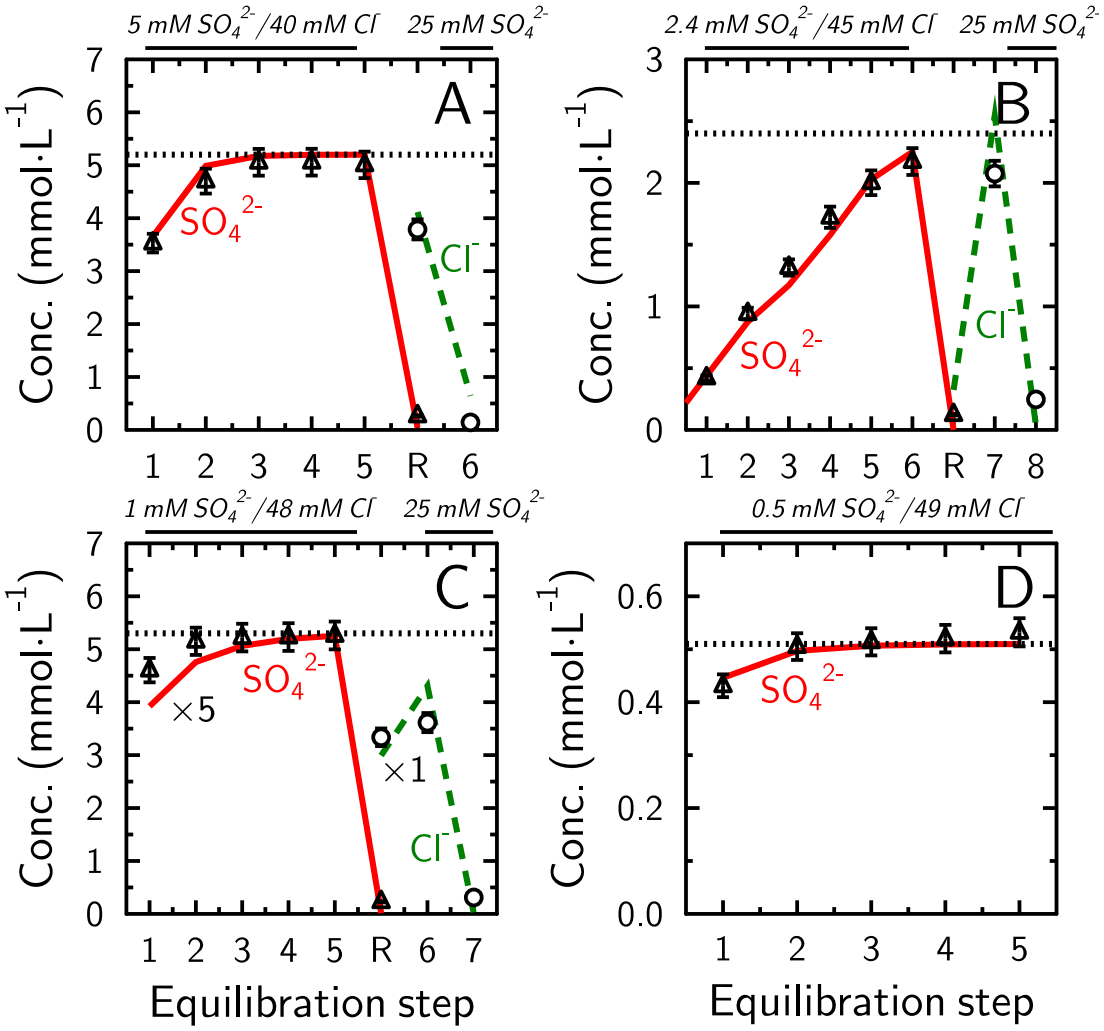

Figure V.26 – SO_4^{2-}-Cl^- exchange data and model on micro-Co-GR sample with Rothmund & Kornfeld convention (Conc: Concentration; SO_4^{2-}: triangle markers for data and red line for model; Cl^-: circles markers for data and green line for model). The initial sample was saturated with Cl^-. Steps 1-5 (or 6 on B) corresponded to equilibration with Na_2SO_4-NaCl solutions with total Na concentration of 50 mmol·L^{-1}. The black dashed lines represented the SO_4^{2-} input concentration (the SO_4^{2-} concentration values are multiplied by 5 on C). Step R corresponded to the rinsing of the sample with ultrapure water. Steps 6 and 8 corresponded to equilibration steps with 25 mmol·L^{-1} of Na_2SO_4 (or 7 and 8 on B, S25). (For every graph) Red and green lines represent the results of the Rothmund & Kornfeld exchange model with $log_{10}\, K_{ex,RK}^{Cl-SO_4} = 0.3$ and $\beta = 2.4$. (A) The exchange solution for steps 1-5 was 5 mmol·L^{-1} of Na_2SO_4 and 40 mmol·L^{-1} of NaCl (S5/Cl40). (B) The exchange solution for steps 1-6 was 2.4 mmol·L^{-1} of Na_2SO_4 and 45 mmol·L^{-1} of NaCl (S2.4/Cl45). (C) The exchange solution for steps 1-5 was 1 mmol·L^{-1} of Na_2SO_4 and 48 mmol·L^{-1} of NaCl (S1/Cl48). (D) The exchange solution for steps 1-5 was 0.5 mmol·L^{-1} of Na_2SO_4 and 49 mmol·L^{-1} of NaCl (S0.5/Cl49).

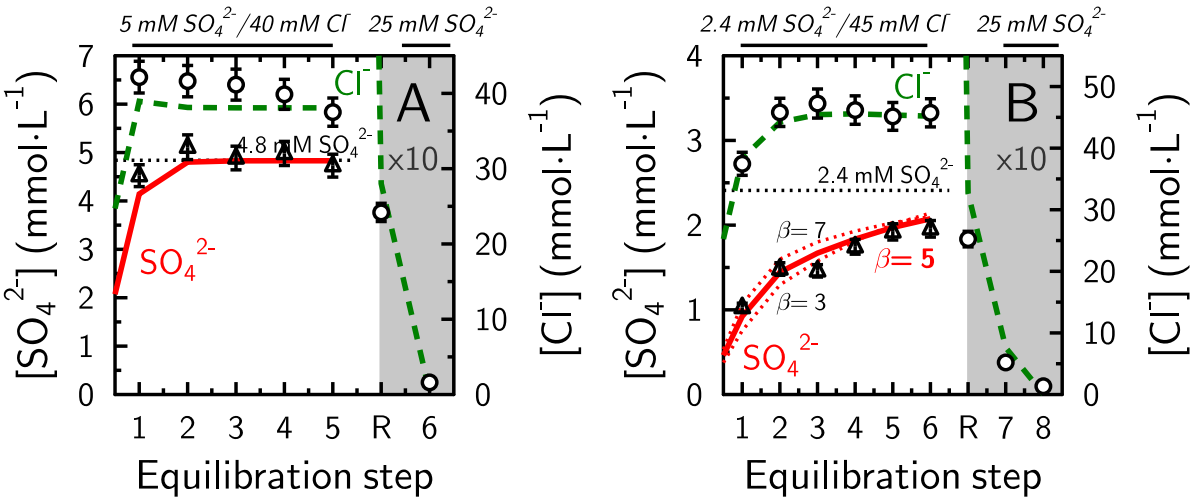

Figure V.27 – SO_4^{2-}-Cl^- exchange data on nano-Co-GR sample with Rothmund & Kornfeld convention (SO_4^{2-}: triangle markers for data and red line for model; Cl^-: circles markers for data and green line for model). The initial sample was saturated with Cl^-. Steps 1-5 (or 6 on B) corresponded to equilibration with Na_2SO_4-NaCl solutions with total Na concentration of 50 mmol·L^{-1} (S5/Cl40 on A and S2.4/Cl45 on B). The black dashed lines represent the SO_4^{2-} input concentration. Step R corresponds to the rinsing of the sample with ultrapure water. Steps 6 and 8 correspond to equilibration steps with 25 mmol·L^{-1} of Na_2SO_4 (or 7 and 8 on B, S25). (For every graph) Colored lines represent the results of the Rothmund & Kornfeld exchange model with $log_{10}\,K_{ex,RK}^{Cl-SO_4} = 0.2$ and β = 5. Concentrations of Cl^- from measurements and model are multiplied by 10 in the grey area. (A) The exchange solution for steps 1-5 was 5 mmol·L^{-1} of Na_2SO_4 and 40 mmol·L^{-1} of NaCl (S5/Cl40). (B) The exchange solution for steps 1-6 was 2.4 mmol·L^{-1} of Na_2SO_4 and 45 mmol·L^{-1} of NaCl (S2.4/Cl45). The red dotted lines were SO_4^{2-} concentrations with β = 3 and β = 7 ($log_{10}\,K_{ex,RK}^{Cl-SO_4} = 0.2$).

SO_4^{2-}-Cl^- exchange experiments, while the initial conditions with regards to the green rust sample surface was identical. The second hypotheses was tested with thermodynamic equilibrium models applied at each step of the exchange experiments. The models were tested with the $NaHCO_3$ experiment first, because it led to large pH differences between equilibrium and stock solution values for more exchange steps than the other experiments.

- *Tested types of anion exchange models*

The macroscopic observation of a 2 : 1 exchange stoichiometry during the Cl^--DIC exchange experiment is not indicative of any exchange mechanism. Contrary to the Cl^--SO_4^{2-} experiments, XRD results indicated that the green rust layers were, at least partially, transformed upon the addition of DIC in the system. The apparent Cl^--DIC exchange may be due to anion exchange mechanisms impacting the interlayer only, which can be modeled using the ion exchange theory as for the Cl^--SO_4^{2-} case, with additional dissolution-precipitation process(es) responsible for the observed changes of magnetite to green rust amount ratio. However, it may also be due to an extensive dissolution-precipitation process which transformed the micro-Co-GR(Cl) phase into a micro-Co-GR(SO4) phase, and for which a phase thermodynamic equilibrium model is suitable, with either pure phases or

solid-solutions. Ion exchange and pure phases equilibrium models were tested against the available data in order to gain insights about the true Cl^--DIC exchange mechanism.

• *Experiment "$NaHCO_3$" - pure phases equilibrium model*

The tested reactions were the dissolution of green rust containing Cl^- and the crystallization of green rust containing CO_3^{2-}. The Thermoddem database (Blanc et al., 2012) was used because it contains the thermodynamic properties of various forms of green rust:

— "greenrust(Cl)" - $Fe_4(OH)_8Cl + 8\ H^+ = 1\ Cl^- + 3\ Fe^{2+} + Fe^{3+} + 8\ H_2O$ and $log_{10}\ K_{sp} = 32.3$ (Refait and Génin, 1993) - same structural formula as micro-Co-GR(Cl) phase if Co^{2+} is considered as Fe^{2+},

— "greenrust(CO_3)" - $Fe_6(OH)_{12}CO_3{\cdot}2\,H_2O + 13\ H^+ = HCO_3^- + 4\ Fe^{2+} + 2\ Fe^{3+} + H_2O$ and $log_{10}\ K_{sp} = 45.3$ (Drissi et al., 1995) - different Fe^{3+}/Fe^{2+} as "greenrust(Cl)",

— "greenrust(OH)" - $Fe_3O_2(OH)_4 + 8\ H^+ = Fe^{2+} + 2\ Fe^{3+} + 6\ H_2O$ and $log_{10}\ K_{sp} = 17.2$. This phase was described as $Fe(OH)_2$,2 FeOOH in the original reference (Chivot, 2004; Olowe, 1988; Olowe and Génin, 1991; Olowe et al., 1994). It was not a green rust but a transition phase for the oxidation of $Fe(OH)_2$ into magnetite (Fe_3O_4). This phase was not considered in the following models.

— "greenrust(OH)-2" - $Fe_3(OH)_7 + e^- + 7\ H^+ = 3\ Fe^{2+} + 7\ H_2O$ and $log_{10}\ K_{sp} = 28.2$ (Bourrié et al., 1999). It was implemented instead of "greenrust(OH)".

Greenrust(Cl) and greenrust(CO_3) were considered in the first modeling attempt. The model did not gave coherent results compared to the measured data (pH, Cl^- or CO_3^{2-} concentrations; Figure V.28). Additionally, the saturation index of greenrust(OH)-2 was always positive (Figure V.28D).

A second model was made in which greenrust(OH)-2 was allowed to react in addition to greenrust(Cl) and greenrust(CO_3). Its initial quantity was set to zero. During the first equilibration step of experiment "$NaHCO_3$", the sample was in contact with a NaCl solution, and according to the model, greenrust(Cl) was completely transformed into greenrust(OH)-2 (Figure V.29C), and then greenrust(OH)-2 remained the only stable green-rust phase for the remaining exchange steps. This result was in contradiction with the stability of the greenrust(Cl) observed during the NaCl equilibration step of in situ XRD experiments. In addition, the modelled pH, Cl^- and DIC concentrations did not fit the experimental data (Figure V.29A and B).

In summary, these tests indicated that a pure phases equilibrium thermodynamic model was not adequate to describe the results. It must also be noted that a solid-solution model that takes into

account the stability of the layer would also fail to reproduce the data because of the too high stability of the greenrust(OH)-2 end-member. These calculations do not disprove a dissolution-precipitation process though: it only disproves local phase thermodynamic equilibrium during the experiment. Models considering reaction kinetics may be more successful to reproduce the data (Marty et al., 2018; Grangeon et al., 2020).

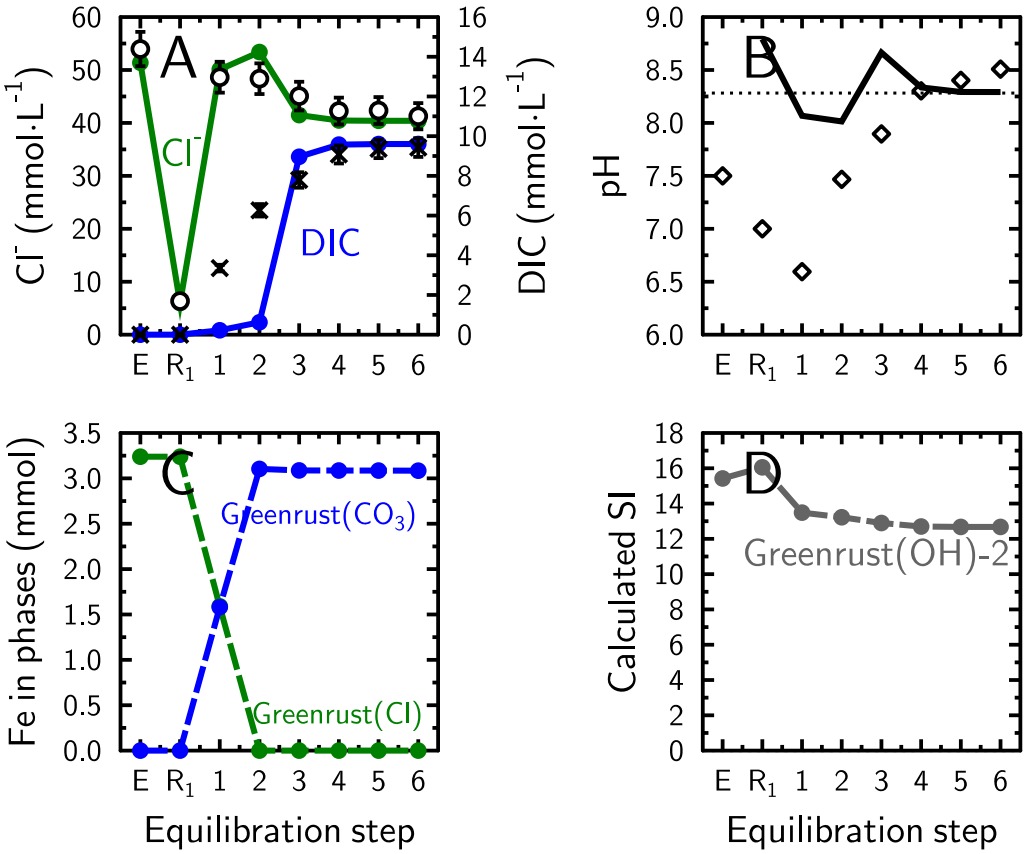

Figure V.28 – modeling results of experiment "$NaHCO_3$" with dissolution/recrystallization of greenrust(Cl) and greenrust(CO_3). The equilibration steps were the same as Figure V.30. (A) Concentrations obtained by the model (Cl^- - green line with green circle; DIC - blue line with blue marker) compared to data (Cl^- - black circles; CO_3^{2-} - black crosses). (B) pH obtained by the model (black line) compared to data (diamond marker). The dotted line represents the pH of the stock solution used for the exchange. (C) Molar quantity of greenrust(Cl) (green line and green circle) and greenrust(CO_3) (blue circle and blue dashed line). (D) Saturation index of greenrust(OH) (light grey dashed line and marker).

- *Experiment "$NaHCO_3$" - simple ion exchange model*

Using the ion exchange theory, a first modeling attempt was set up with a reaction that replaced two Cl^- with one CO_3^{2-} in the interlayer (equation V.2), without any modification of the layer structure. The Gaines & Thomas convention was used, in which the exchange selectivity coefficient was adapted at each exchange step to fit the data. A good fit between measured and modelled concentrations was obtained, and the decrease of pH was also correctly predicted (Figure V.30). However, several inconsistencies appeared. First, the calculated pH was more acidic than the measured pH

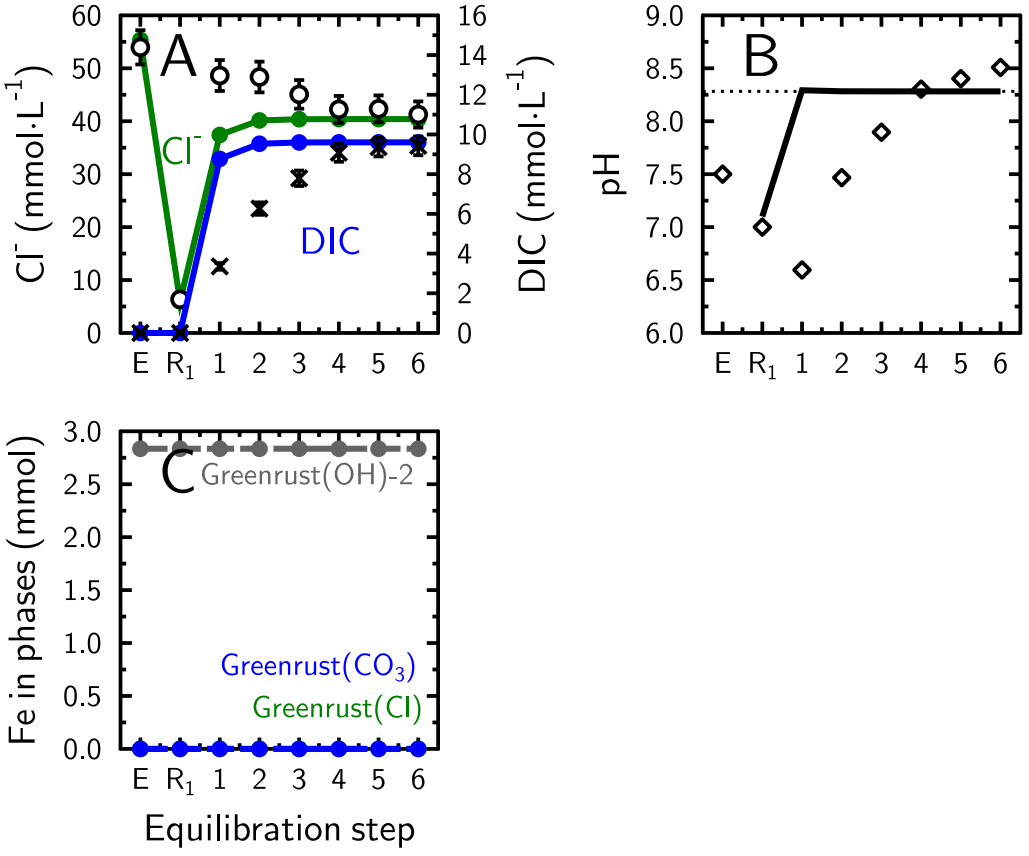

Figure V.29 – modeling results of experiment "$NaHCO_3$" with dissolution/precipitation of greenrust(Cl), greenrust(CO_3) available in Thermoddem database and greenrust(OH)-2 (Bourrié et al., 1999). The caption is the same as Figure V.28

(Figure V.30B). Second, $log_{10}\ K_{ex,GT}^{Cl-CO_3}$ had to be adapted at step 1 to 3 (Figure V.30C). A $log_{10}\ K_{ex,GT}^{Cl-CO_3}$ of 11 was necessary to fit the first step. For step 2 and 3, $log_{10}\ K_{ex,GT}^{Cl-CO_3}$ was set at 5 and 4, respectively. These values are very high compared to selectivity coefficient observed in other layered materials (Miyata, 1983; Tournassat et al., 2009). If true, these values are indicative of a chemisorption process, and not of a physisorption process, the later being usually consistent with ion exchange of hydrated interlayer counter-ions (McBride, 1994). However, the predicted pH were too acidic compared to the measurements, and the fitted values Cl^--CO_3^{2-} selectivity coefficient are highly dependent on the the correctness of the DIC speciation in solution: if the modeled speciation of DIC predicts that H_2CO_3 is the main species in solution instead of CO_3^{2-}, the fitted selectivity coefficient must be increased to compensate the decrease of the predicted CO_3^{2-} activity compared to the measured one. Because Cl^- and CO_3^{2-} concentrations were predicted correctly, a pH buffering reaction must be added to the model.

• *Experiment "$NaHCO_3$" - hypotheses on pH buffering processes*

Several hypotheses were put forward to explain the observed pH buffer:

— protonation of amphoteric edge surface groups,

— anion exchange with OH^- initially present in the interlayer,

— partial oxidation of the green rust sample,

— partial dissolution of the green rust sample.

These hypotheses are explored in the following.

• *Experiment "*$NaHCO_3$*" - simple ion exchange model with protonation of amphoteric edge surface groups*

In this model, the pH was fixed at the measured values and the corresponding release of OH^- in solution was monitored (Figure V.31B). A constant $log_{10}\ K_{ex,GT}^{Cl-CO_3}$ value equal to 3.7 resulted in a good fit at step 1 but did not fit the results at step 2 (full lines compared to dashed lines, Figure V.31A). The selectivity coefficient value had to be set to $log_{10}\ K_{ex,GT}^{Cl-CO_3} = 3$ to fit the data after step 1 (Figure V.31A and C).

During step 1, 1.18×10^{-4} mol of OH^-, corresponding to 0.37 $mol \cdot kg_{GR}^{-1}$ of OH^-, was released in solution to maintain the pH at the measured value, and 0.96 $mol \cdot kg_{GR}^{-1}$ of OH^- was released to fit all experimental data (Figure V.31B). The total amount of released OH^- was calculated to be 38 % of the AEC of micro-Co-GR phase (2.5 $mol_c \cdot kg_{GR}^{-1}$).

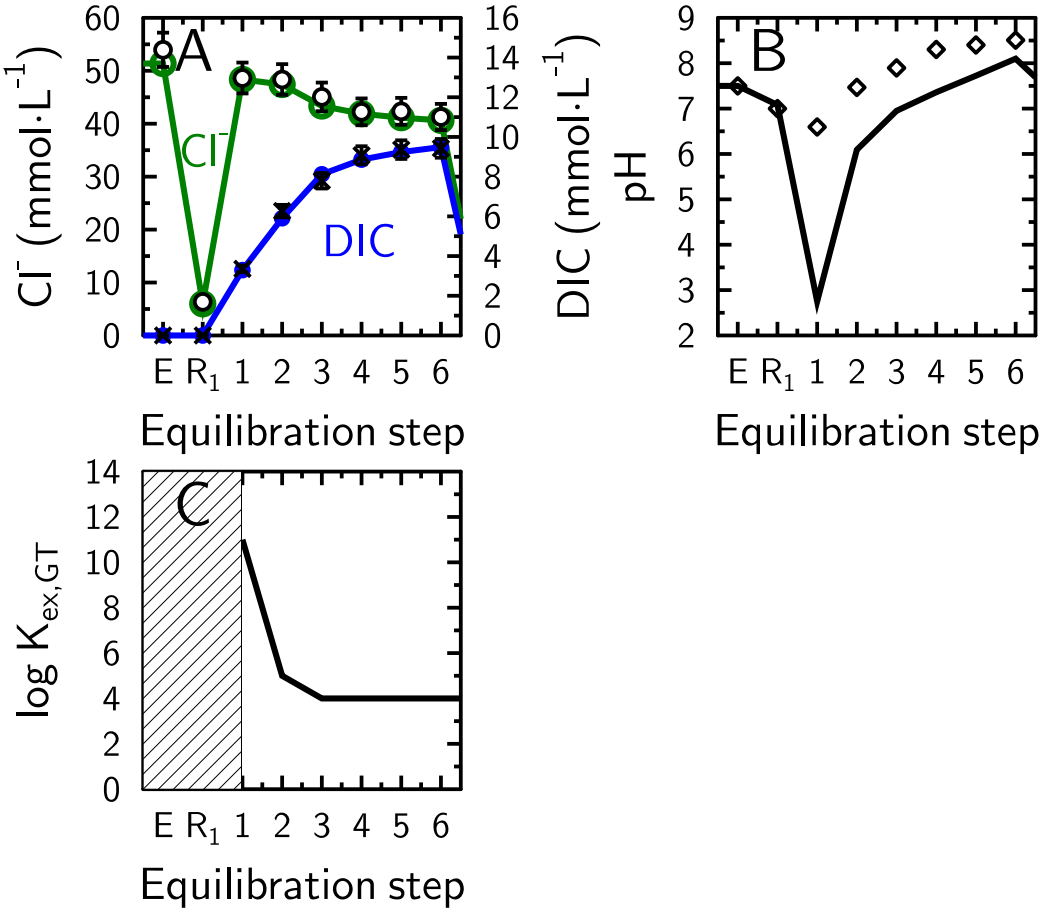

Figure V.30 – modeling results of experiment "$NaHCO_3$" with only equation V.2. The initial sample was saturated with Cl^- (E). Step R_1 corresponds to the rinsing of the sample with ultrapure water. Steps 1-6 correspond to equilibration with $NaHCO_3$-NaCl solution with a concentration of 10 mmol·L^{-1} of $NaHCO_3$ and 40 mmol·L^{-1} of NaCl. (A) Concentrations obtained by the model (Cl^- - green line with green circle; carbonate species - blue line with blue marker) compared to data (Cl^- - black circles; CO_3^{2-} - black crosses). (B) pH obtained by the model (black line) compared to data (diamond). (C) Gaines & Thomas selectivity coefficient for the exchange between Cl^- and CO_3^{2-}. No exchange happened in the hatched area.

The amount of edge surface amphoteric group is proportional to the edge surface area of the particles. The specific edge surface area of layered minerals is proportional to the perimeter to area ratio of the basal surface (Tournassat et al., 2003). For a regular hexagon of diameter D, the perimeter is P = 3D, the area is $\frac{3\sqrt{3}}{8}D^2$, so the perimeter over area ratio is $\frac{P}{A} = \frac{8}{\sqrt{3}D}$, and the specific amount of edge hydroxyl groups available for protonation decreases when particle size increases. It can be calculated that hydroxyl groups on the edges of a micro-Co-GR(Cl) particle with a diameter of 13 nm represent 5.0 % of the total number of hydroxyl groups in the layer. This corresponds to a maximum protonation capacity of 1.0 $mol_{OH\ edge} \cdot kg_{GR}^{-1}$, which is comparable to 40 % of the AEC, and which would thus be sufficient to buffer efficiently the pH in solution. However, the average particle diameter of the micro-Co-GR sample was in the range 0.5 up to 1 mm, which means that amphoteric groups at the edge surface were not present in sufficient amount to account for the observed pH buffer effect.

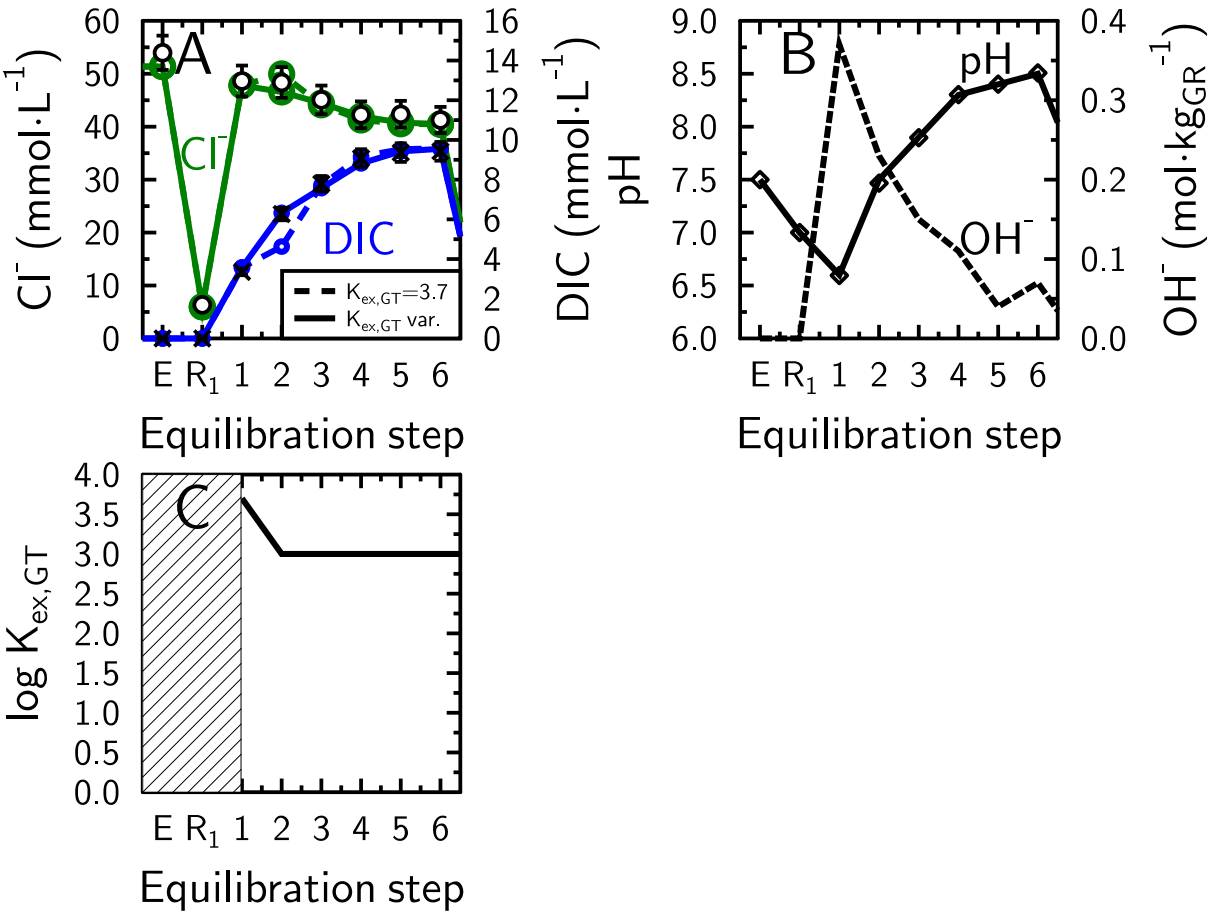

Figure V.31 – modeling results of experiment "$NaHCO_3$" with only equation V.2 and fixing the pH. The caption is the same as Figure V.30 except for the following details. (A) The dashed lines represents the results for the same species (green - Cl^- and blue - carbonate species) but with a constant $log_{10}\ K_{ex,GT}^{Cl-CO_3} = 3.7$ (B) The buffering capacity corresponds to the amount of released OH^- in the model (normalized to the mass of green rust powder) to fix the pH (dashed black line).

• *Experiment "$NaHCO_3$" - simple ion exchange model addition of OH^- exchange reaction*

The hypothesis was that OH^- ions were already in the interlayer and could be exchanged with Cl^- or CO_3^{2-} ions. The following set of equations was used to model this exchange:

$$\begin{cases} GrCl + OH^- \overset{K_{ex}^{Cl-OH}}{=} GrOH + Cl^- \\ 2GrCl + {CO_3}^{-2} \overset{K_{ex}^{Cl-CO_3}}{=} Gr_2CO_3 + 2Cl^- \end{cases} \quad (V.5)$$

The pH values were fixed in the model at the measured values. The value of $log_{10}\, K_{ex,GT}^{Cl-OH}$ was set at 4 because it had an influence on the Cl^- concentrations at the pre-equilibration step E. With a lower $log_{10}\, K_{ex,GT}^{Cl-OH}$ value, the amount of OH^- in the interlayers was not sufficient and the model results were equivalent to the first simple exchange model. With a $log_{10}\, K_{ex,GT}^{Cl-OH} > 5$, Cl^- was predicted to be absent in the interlayers, a prediction that was not coherent with the observed released of Cl^- in solution. A good fit between DIC concentrations of the model and data was obtained with $log_{10}\, K_{ex,GT}^{Cl-CO_3} = 3.7$ at step 1 and 3.1 afterwards (Figure V.32A and C). However, it was still necessary to add an additional pH buffering capacity (Figure V.31-B), which amounted to 0.77 $mol \cdot kg_{GR}^{-1}$. Consequently, the hypothesis that OH^- ions were already present in the interlayer at the beginning of the exchange experiment was not sufficient to explain the observed pH buffering capacity of the sample.

• *Experiment "$NaHCO_3$" - simple exchange model with partial oxidation of micro-Co-GR*

The presence of trace amounts of O_2 can be responsible for an oxidation of green rust during the experiment. Green rust oxidation by O_2 results in a variety of iron oxides or oxy-hydroxides (ferrihydrite, lepidocrocite, goethite, hematite or magnetite) depending on local physical and chemical conditions, and following dissolution and re-precipitation processes (Refait and Génin, 1997; Refait et al., 2003; Rives, 2001). Here, the oxidation is hypothesized to be only partial and to take place within the green rust layer structure, without green rust dissolution, but with oxidation of x layer Fe^{2+} into x layer Fe^{3+} following the reaction:

$$Fe^{III}_{0.25}Fe^{II}_{0.42}Co^{II}_{0.33}(OH)_2Cl_{0.25} + x\ Cl^- = Fe^{III}_{0.25+x}Fe^{II}_{0.42-x}Co^{II}_{0.33}(OH)_2Cl_{0.25+x} + x\ e^- \quad (V.6)$$

The Fe^{3+} content of green rust can not exceed 0.33 (with $Fe^{3+} + Fe^{2+} = 1$) due to charge exclusion. The Fe^{3+} stoichiometry in the micro-Co-GR(Cl) sample was 0.25. Thus, a maximum of 0.08 additional Fe^{3+} can be oxidised into Fe^{2+} with the phase remaining green rust ($0 \leq x \leq 0.08$). Coupling above reaction

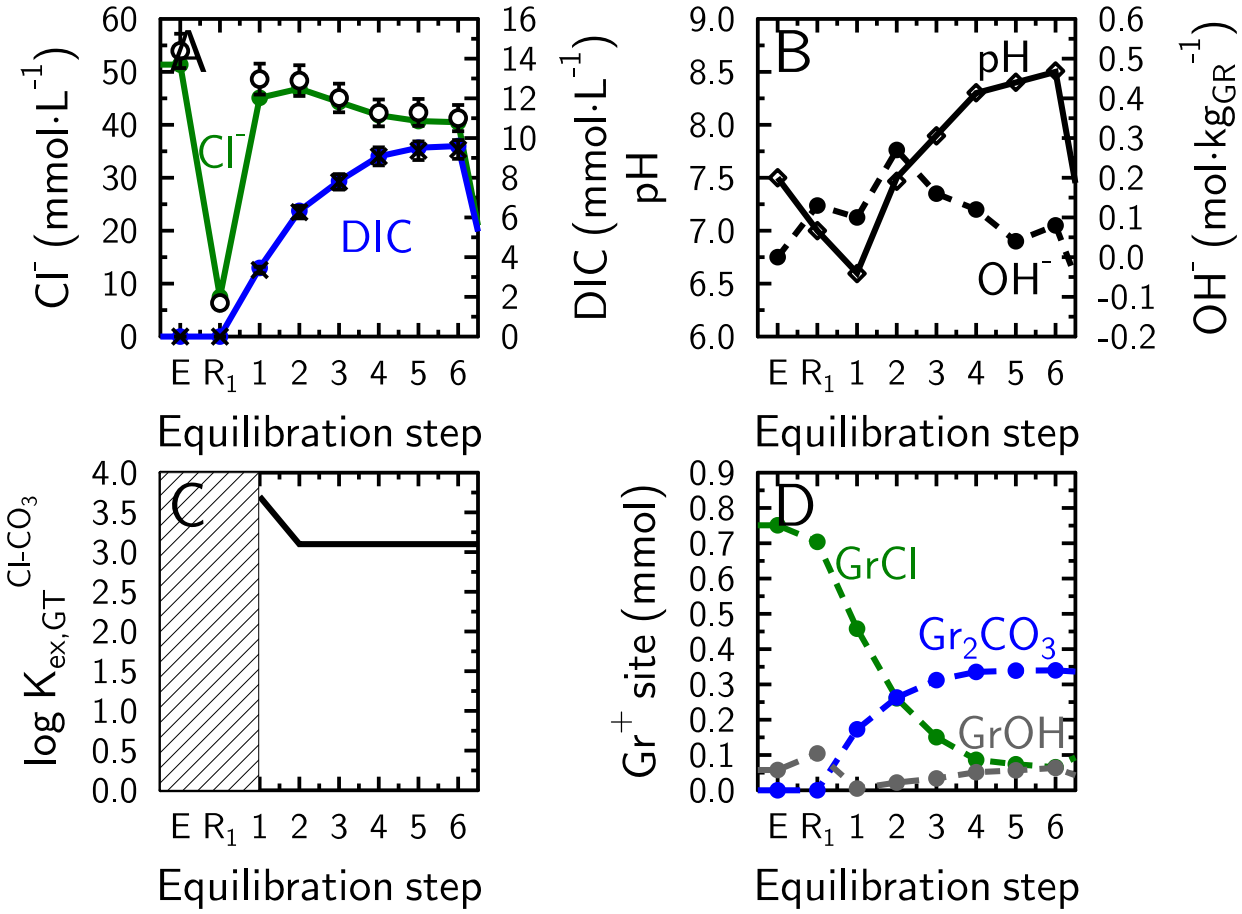

Figure V.32 – modeling results of experiment "$NaHCO_3$" with exchange of Cl^-, CO_3^{2-} and OH^- (Equation V.5). The equilibration steps were the same as Figure V.30. The $log_{10}\ K_{ex,GT}^{Cl-OH}$ was equal to 4 for the whole experiment. (A) Concentrations obtained by the model (Cl^- - green line with green circle; carbonate species - blue line with blue marker) compared to data (Cl^- - black circles; CO_3^{2-} - black crosses). (B) pH obtained by the model (black line) compared to data (diamond). The buffering capacity corresponds to the amount of released OH^- (normalized to the mass of green rust powder) in order to fix the pH (dashed black line). (C) $log_{10}\ K_{ex,GT}^{Cl-CO_3}$ from equation V.5. No exchange happened in the hatched area. The other selectivity coefficient were constant during the whole experiment. (D) Molar quantity of GrOH (grey circles and grey dashed line), GrCl (green circles and green dashed line) and Gr_2CO_3 (blue circles and blue dashed line).

with O_2 reduction yields:

$$Fe^{III}_{0.25}Fe^{II}_{0.42}Co^{II}_{0.33}(OH)_2Cl_{0.25} + \frac{x}{4}O_2 + x\,H^+ + x\,Cl^- = Fe^{III}_{0.25+x}Fe^{II}_{0.42-x}Co^{II}_{0.33}(OH)_2Cl_{0.25-x} + \frac{x}{2}H_2O \quad (V.7)$$

It was mentioned earlier that the release of 1.18×10^{-4} mol of OH^- was necessary to obtain the pH measured at step 1. So $x = 1.18 \times 10^{-4}$, corresponding to the consumption of 2.95×10^{-5} mol of O_2. The partial pressure of O_2 in the glovebox did not exceed 0.1 Pa. Henry's law for O_2 is:

$$p_{O_2} = \frac{c_{O_2}}{H^{cp}_{O_2}} \quad (V.8)$$

where p_{O_2} is the partial pressure of O_2 in the gas phase at equilibrium conditions, c_{O_2} is the concentration of O_2 in the aqueous phase and H^{cp} is the O_2 Henry constant (1.3×10^{-5} mol·m^{-3}Pa^{-1}). Thus, the concentration of O_2 in a solution at equilibrium with the glovebox atmosphere was 1.28×10^{-9} mol·L^{-1}. The volume of solution at step 1 was 29.7 mL, so the molar quantity of $O_{2(aq)}$ in solution was 3.81×10^{-8} mol, which was far below the required amount of O_2 that was necessary to explain the green rust oxidation and the related pH buffering capacity. Aqueous O_2 may be, however, renewed from the dissolution of O_2 present in the glove-box atmosphere. The volume of the glovebox was about 2 m^3, and its gas pressure was nearly identical to the atmospheric pressure. So the glovebox contained 1.97×10^{-3} L of O_2. Considering the molar volume of an ideal gas at standard conditions (22.4 L·mol^{-1}), the molar quantity of O_2 in the glovebox was approximately 9×10^{-5} mol. Thus, at least 33 % of the O_2 present in the glovebox would have been necessary to oxidize the right amount of green rust in order to match the pH value measured at exchange step 1. This seems unlikely, because a maximum of 3.81×10^{-8} mol of $O_{2(aq)}$ was present in solution at a given time at equilibrium with the glovebox atmosphere. In conclusion, the partial oxidation of layer Fe^{2+} alone cannot explain the experimental results.

- *Experiment "*$NaHCO_3$*" - simple ion exchange model with partial dissolution of micro-Co-GR*

The green rust pH buffering capacity could originate from a dissolution process:

$$[Fe_{0.42}{}^{2+}Fe_{0.25}{}^{3+}Co_{0.33}{}^{2+}(OH)_2] + 2\,H^+ = 2\,H_2O + 0.42\,Fe^{2+} + 0.25\,Fe^{3+} + 0.33\,Co^{2+} \quad (V.9)$$

This dissolution was necessarily at thermodynamic disequilibrium (*i.e.* kinetically controlled) because it was shown previously that a dissolution/recrystallization model could not fit the data with tabulated

solubility values. Each mole of dissolved green rust produces 2 moles of OH^- and the dissolution of 4.35 % of green rust was necessary to generate 0.96 $mol \cdot kg_{GR}^{-1}$ of OH^-. For step 1 only, 1.67 % of green rust had to be dissolved to generate 0.37 $mol \cdot kg_{GR}^{-1}$ of OH^-.

The model of experiment "$NaHCO_3$" included an ion exchange between Cl^- and $CO_3{}^{2-}$ and a dissolution of a quantity of micro-Co-GR(Cl) phase that was fitted with the pH variations. These models also gave an information about which phase could precipitate given the experimental conditions. The quantity of exchanger (AEC) was kept constant even if there was a partial dissolution of green rust. Four phases were allowed to precipitate and they were tested independently (a single model per phase): ferrihydrite(2L), magnetite, siderite and greenrust(OH)-2 (same parameters as the model with dissolution/recrystallization). The results of these models gave the amount of phase precipitating, the concentration of Fe^{2+} and Fe^{3+} and the saturation index of two green rusts available in the database, greenrust(Cl) and greenrust(CO_3).

All models gave coherent results with the measured Cl^- and DIC concentrations (Figure V.33, V.34, V.35 and V.36). The fitted $K_{ex,GT}^{Cl-CO_3}$ values were similar for all tested minerals in the list (Table V.6). However, the amount of dissolved green rust changed as a function of the considered mineral, with a maximum amount of green rust dissolution obtained with greenrust(OH)-2 (19 w% at step 1, Table V.6). The percentage of green rust dissolution at step 3 was 13.1 w% with magnetite, 6.9 w% with ferrihydrite(2L) and 5.6 w%, the minimum, with siderite. The percentage of precipitated phase was calculated as the ratio of the mass of this precipitated phase to the total mass of all solid phases present at this step. This percentage of precipitated phase reached a maximum for the greenrust(OH)-2 case with 10.6 w% precipitated, 5.7 w% of magnetite, 2.5 w% of siderite or 1.8 w% of ferrihydrite(2L). Saturation index of greenrust(Cl) and greenrust(CO_3) were always negative for all the models except with the siderite model in which the saturation index of greenrust(CO_3) was positive after step 1.

A problem of the models with siderite or greenrust(OH)-2 was their resulting high aqueous Fe^{3+} concentration, which was higher than Fe^{3+} solubility. Consequently, four new models were run that allowed ferrihydrite or magnetite to precipitate concomitantly with either siderite or greenrust(OH)-2 (Figure V.37, V.38, V.39 and V.40). Those models gave coherent results with the measured concentrations in Cl^- and DIC. For the models with precipitation of greenrust(OH)-2 and another phase, the amount of dissolved micro-Co-GR phase was slightly higher compared to the model with precipitation

of greenrust(OH)-2 only (20.6 *w*%, compared to 19 *w*%, Table V.6). The percentages of precipitated magnetite (1.2 *w*%) and ferrihydrite(2L) (0.9 *w*%) were low compared to the percentage of precipitated greenrust(OH)-2 (20.6 *w*% in both cases). The models with precipitation of siderite and another phase resulted in similar amounts of dissolved green rust as the models with precipitation of one phase only. With these models, saturation index of greenrust(Cl) and greenrust(CO_3) were always negative.

It was not possible to identify the precipitating phase from the chemical information alone because the eight models were in agreement with the available data. If siderite or greenrust(OH) precipitated, another phase had to precipitate to decrease the Fe^{3+} concentration in solution. During the exchange experiment "$NaHCO_3$-XRD" studied with *in situ* XRD, an increase of magnetite quantity was observed (Figure V.7), but no siderite reflections were observed. Therefore, models containing magnetite seem to be the most consistent with the set of available observations in experiment "$NaHCO_3$".

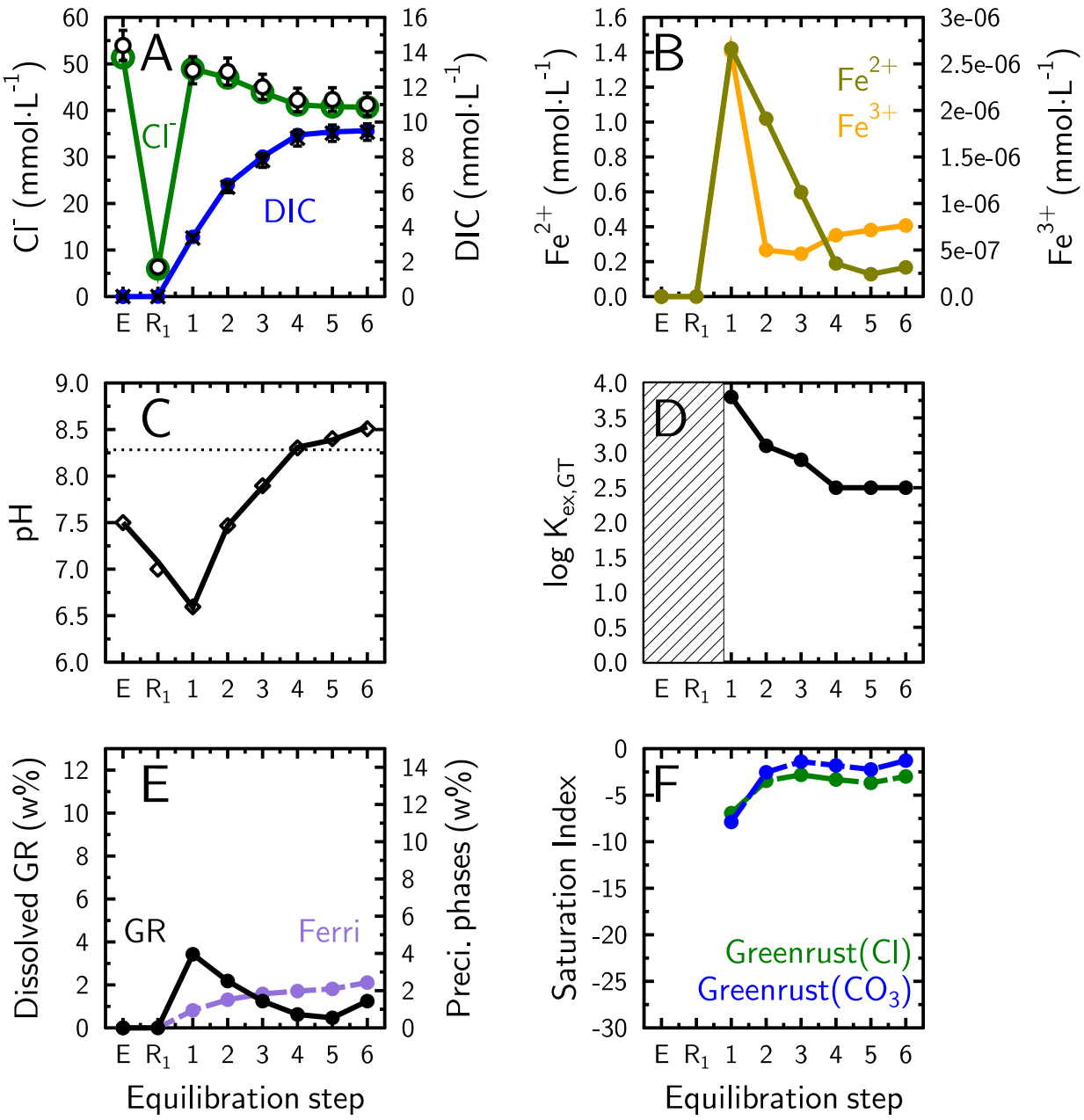

Figure V.33 – modeling results of experiment "$NaHCO_3$" with only equation V.2, dissolution of green rust and precipitation of ferrihydrite(2L). The equilibration steps were the same as Figure V.30. (A) Concentrations obtained by the model (Cl^- - green line with green circle; carbonate species - blue line with blue marker) compared to data (Cl^- - black circles; CO_3^{2-} - black crosses). (B) Fe^{2+} (olive) and Fe^{3+} (orange) concentrations in solution from the model. (C) pH obtained by the model (black line) compared to data (diamond marker). The dotted line represents the pH of the stock solution used for the exchange. (D) Gaines & Thomas selectivity coefficient for the exchange between Cl^- and CO_3^{2-}. No exchange happened in the hatched area. (E) Weight percentage of green rust dissolved to fit the model (black line and black circle) and weight percentage of precipitated ferrihydrite(2L) (purple circle and purple dashed line). Percentage calculated on the total mass of various phases. (F) Saturation index of greenrust(Cl) (green) and greenrust(CO_3) (blue).

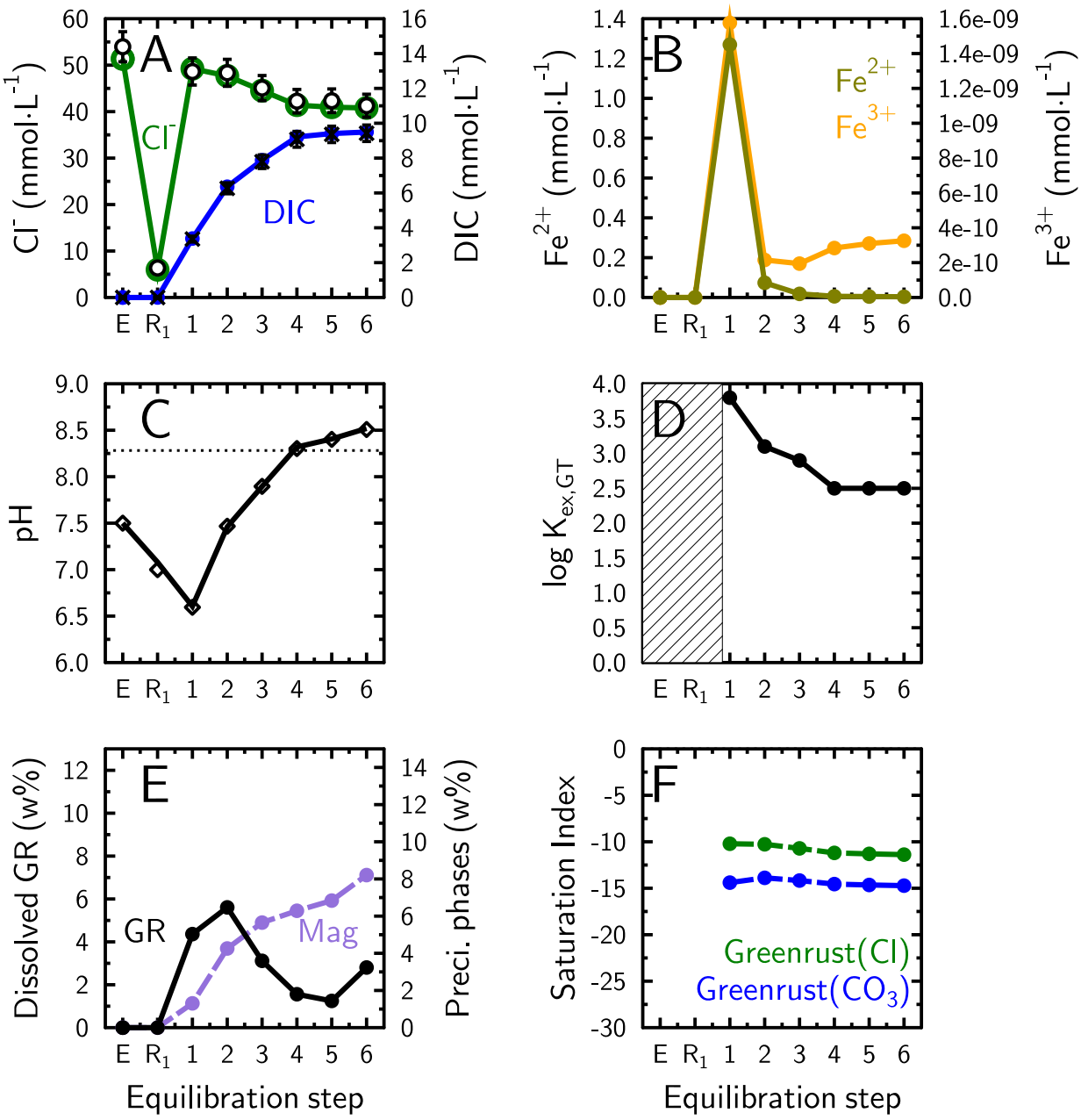

Figure V.34 – modeling results of experiment "$NaHCO_3$" with only equation V.2, dissolution of green rust and precipitation of magnetite. The caption is the same as Figure V.33.

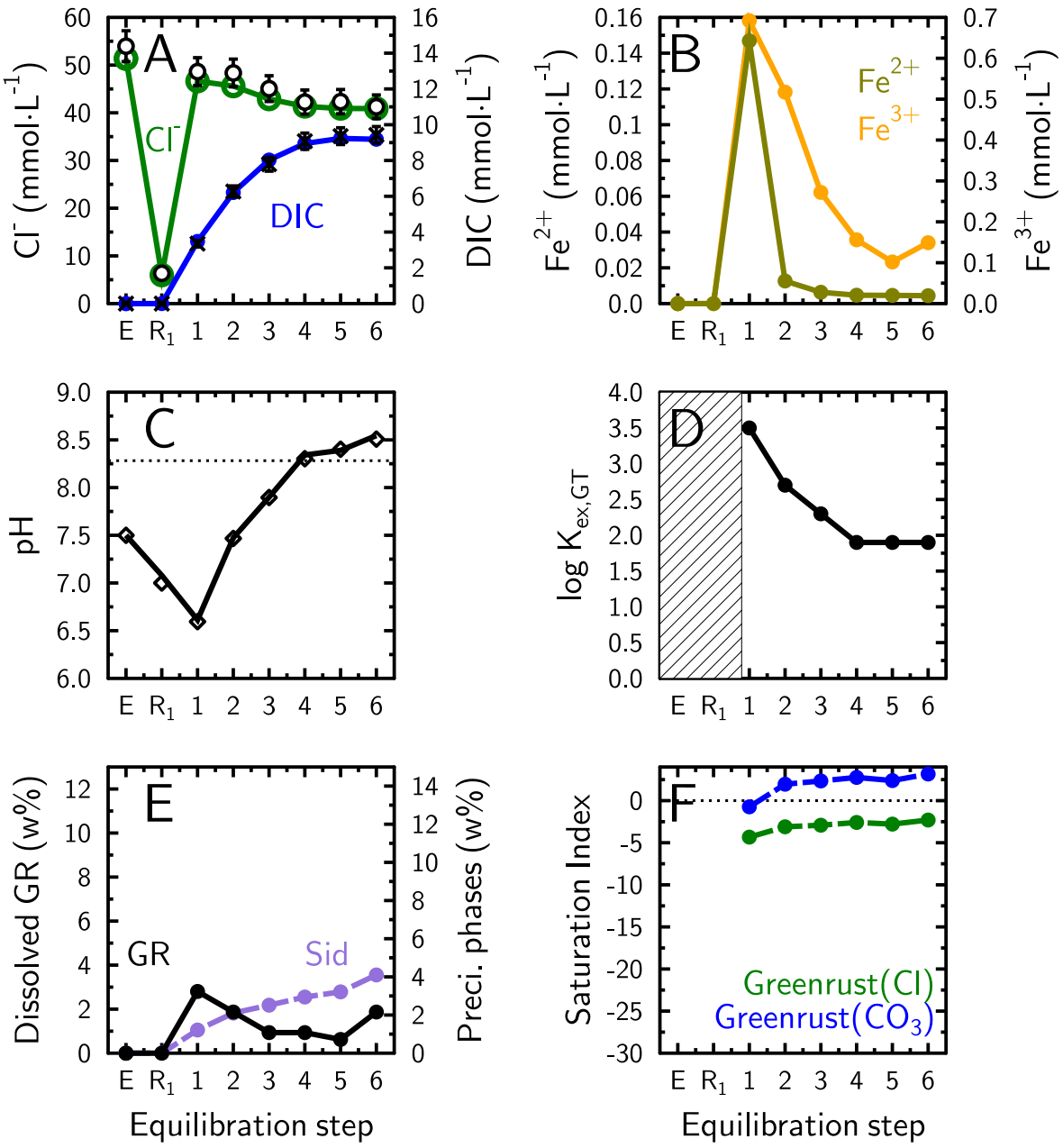

Figure V.35 – modeling results of experiment "$NaHCO_3$" with only equation V.2, dissolution of green rust and precipitation of siderite. The caption is the same as Figure V.33.

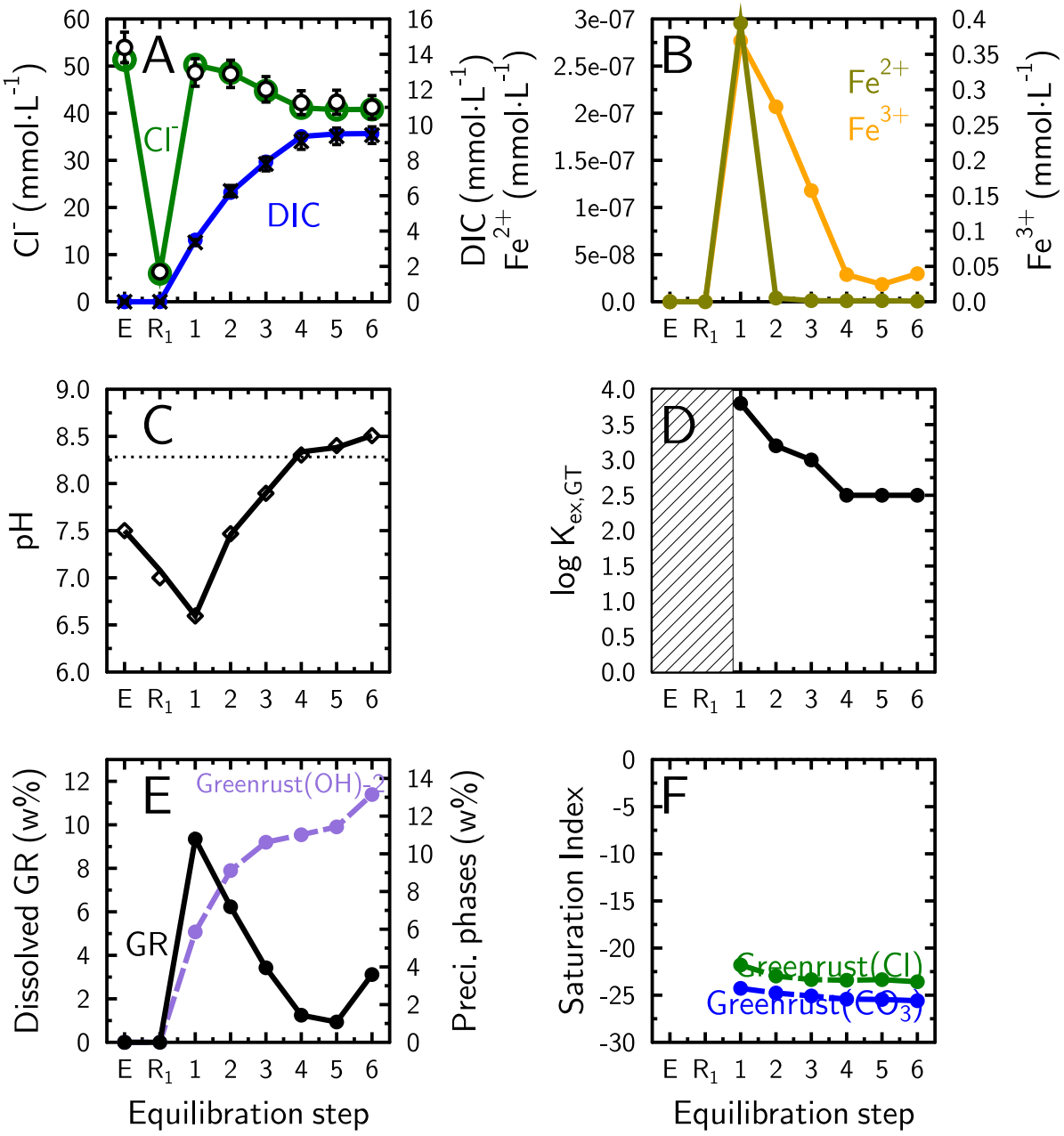

Figure V.36 – modeling results of experiment "$NaHCO_3$" with only equation V.2, dissolution of green rust and precipitation of greenrust(OH)-2. The caption is the same as Figure V.33.

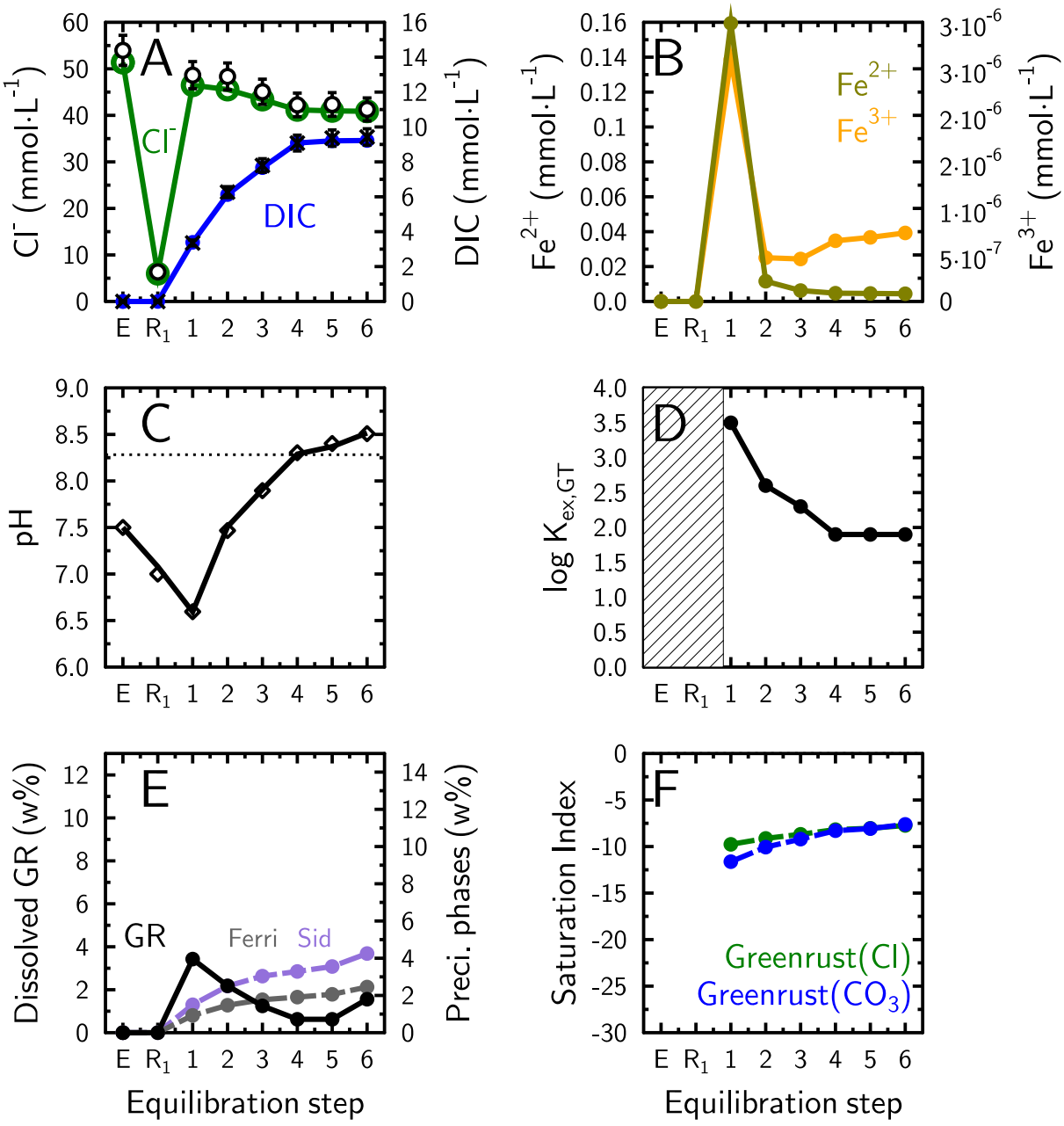

Figure V.37 – modeling results of experiment "$NaHCO_3$" with only equation V.2, dissolution of green rust and precipitation of two phases: siderite (purple in E) and ferrihydrite(2L) (grey in E). The caption is the same as Figure V.33.

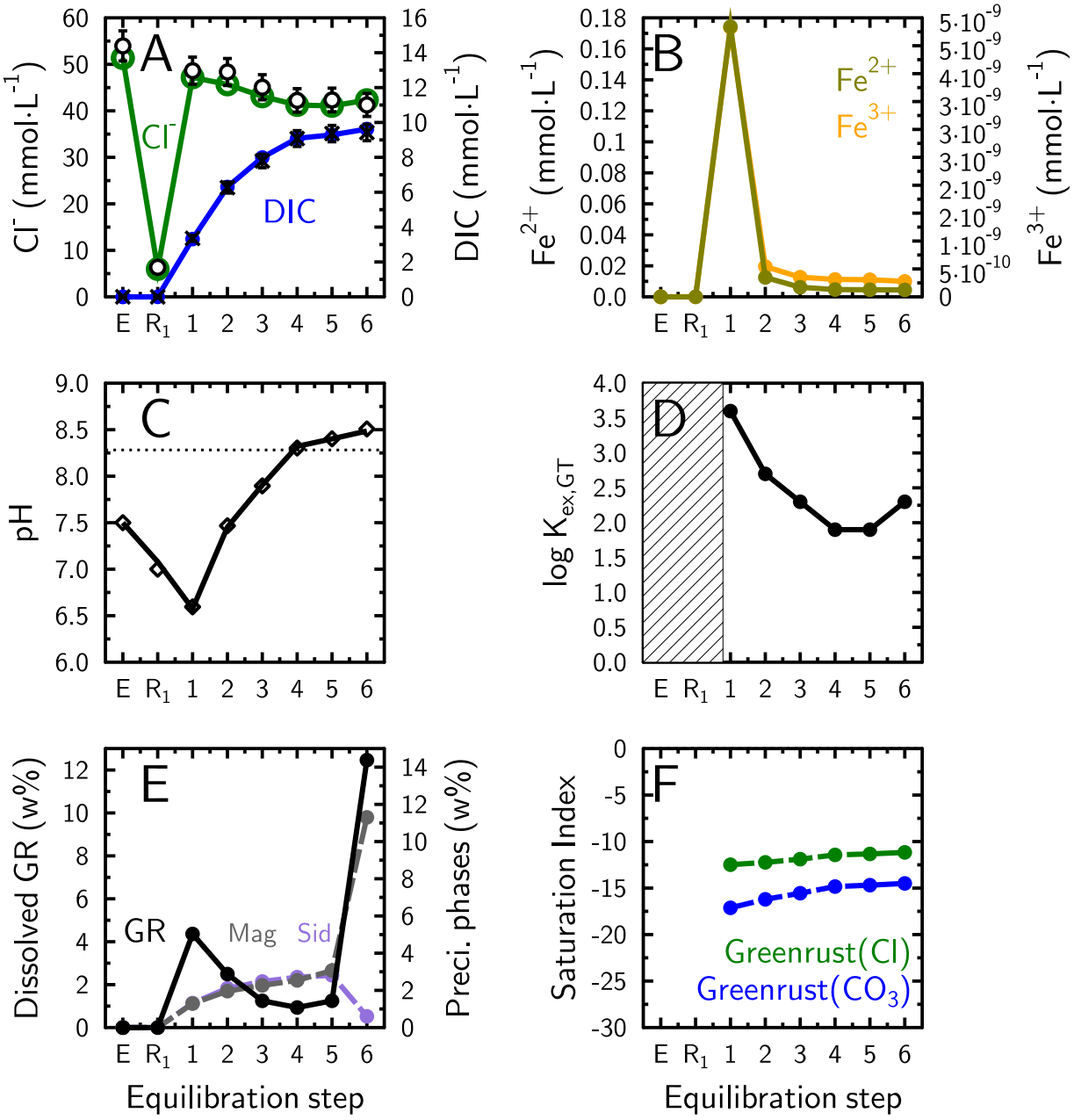

Figure V.38 – modeling results of experiment "$NaHCO_3$" with only equation V.2, dissolution of green rust and precipitation of two phases: siderite (purple in E) and magnetite (grey in E). The caption is the same as Figure V.33.

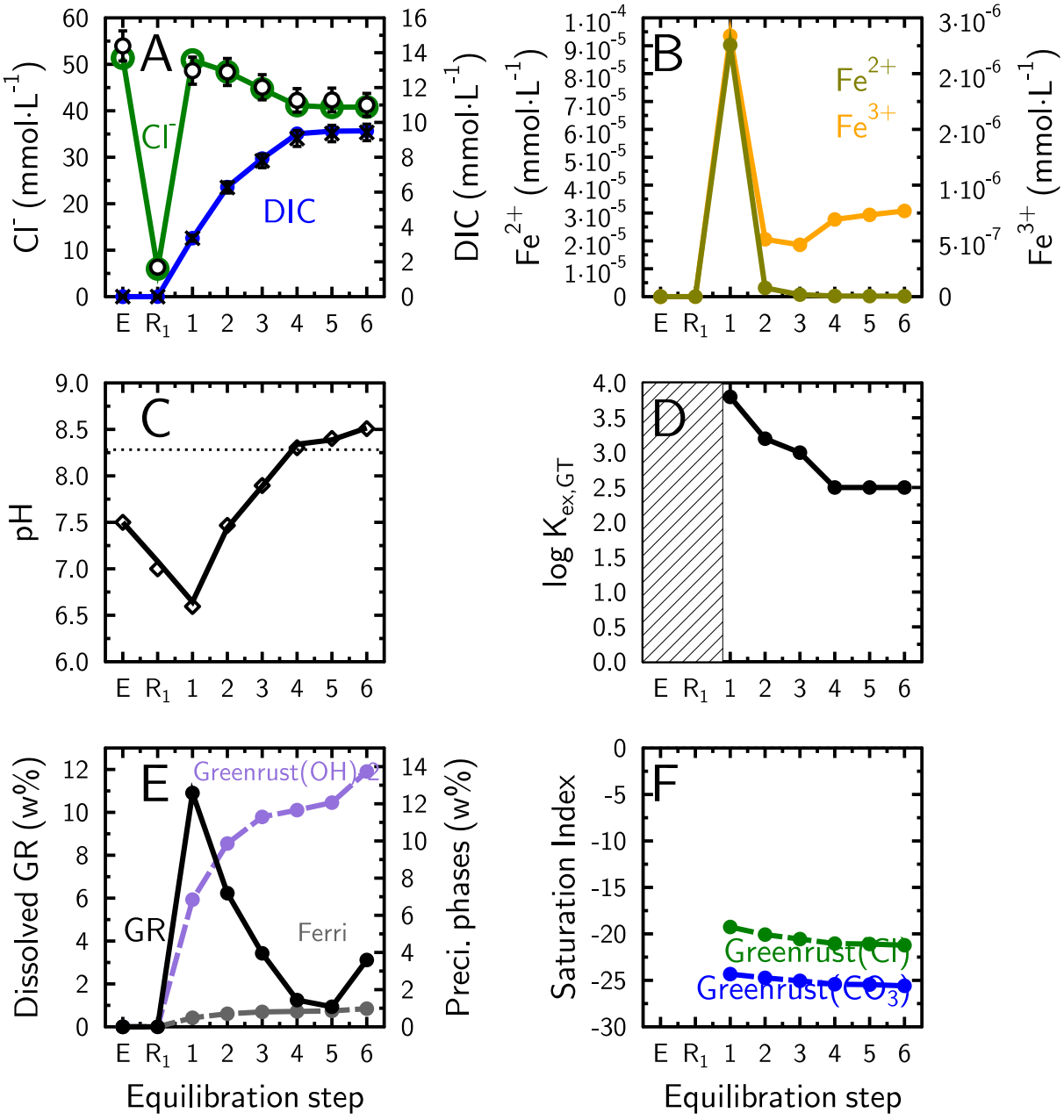

Figure V.39 – modeling results of experiment "$NaHCO_3$" with only equation V.2, dissolution of green rust and precipitation of two phases: greenrust(OH)-2 (purple in E) and ferrihydrite(2L) (grey in E). The caption is the same as Figure V.33.

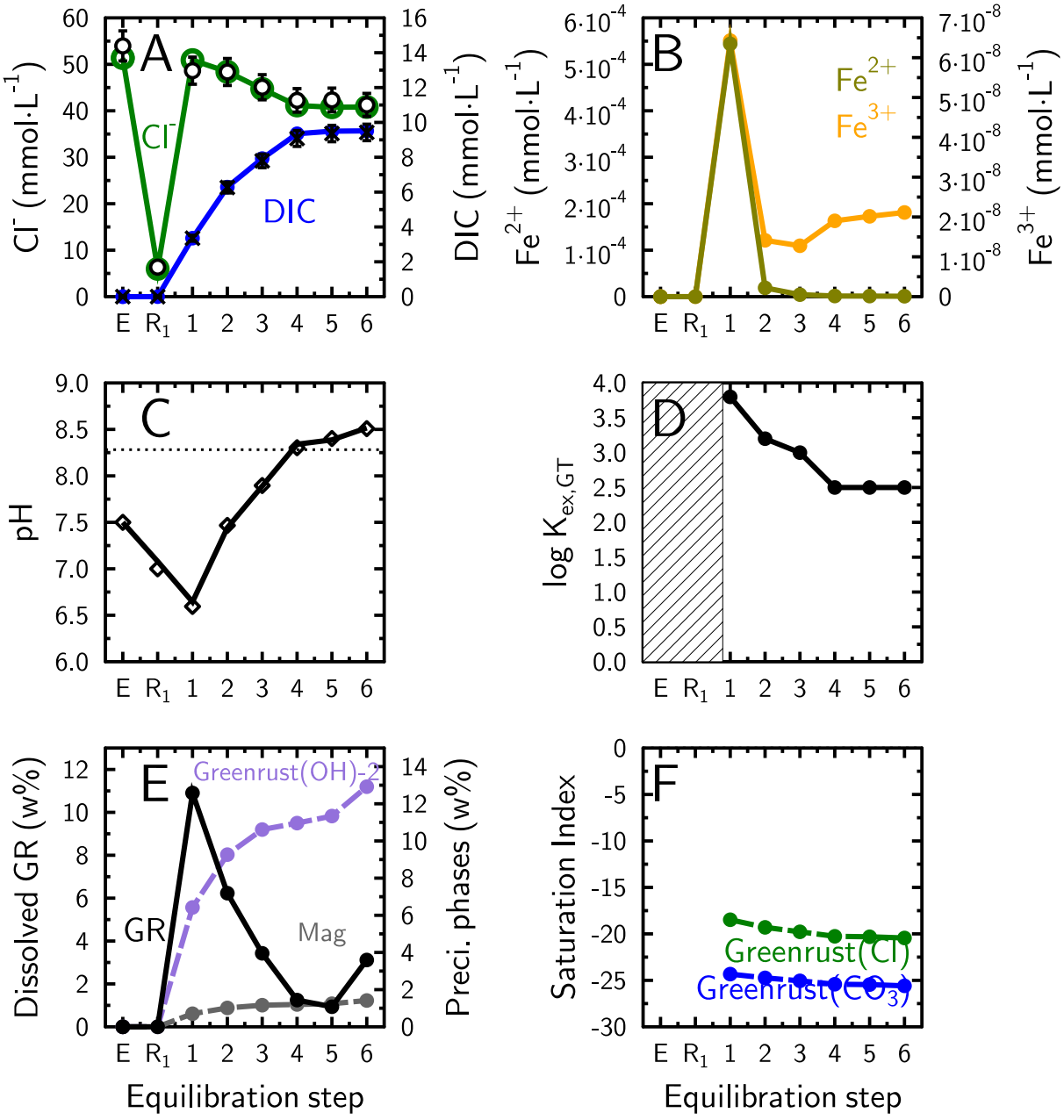

Figure V.40 – modeling results of experiment "$NaHCO_3$" with only equation V.2, dissolution of green rust and precipitation of two phases: greenrust(OH)-2 (purple in E) and magnetite (grey in E). The caption is the same as Figure V.33.

Table V.6 – Table to summarize and compare the results from the models of partial dissolution of green rust during experiment "$NaHCO_3$" shown in figure V.33 (ferryhydrite(2L) - ferri), figure V.34 (magnetite - magn), figure V.35 (siderite - sid), figure V.36 (greenrust(OH)-2 - GR(OH)), figure V.37 (siderite and ferrihydrite(2L)), figure V.38 (siderite and magnetite), figure V.39 (greenrust(OH)-2 and ferrihydrite(2L)) and figure V.40 (greenrust(OH)-2 and magnetite). If needed, the equilibration step was written, "1-2-3" meant that this parameter was summed during step 1, 2 and 3 and "1 (Max)" meant that this parameter was at its maximum during step 1 and the value is given for this step. The percentage of precipitated phase was calculated by the ratio between the mass of this phase at step 6 and the sum of the mass of all phases. Saturation index were for greenrust(Cl) (GR(Cl)) and greenrust(CO_3) (GR(CO_3). (Abbreviations: Diss. - Dissolved, mM - mmol·L^{-1})

	Step	Ferrihydrite	Magnetite	Siderite	Greenrust(OH)-2
$log_{10}\ K_{ex,GT}^{Cl-CO_3}$	1	3.8	3.8	3.5	3.8
	2	3.1	3.1	2.7	3.2
	3	2.9	2.9	2.3	3
Diss. GR (w%)	1-2-3	6.9	13.1	5.6	19.0
Phase 1 (w%)	3	1.8	5.7	2.5	10.6
Fe^{2+} (mM)	1 (max)	1.42	1.27	0.15	2.95×10^{-7}
Fe^{3+} (mM)	1 (max)	2.63×10^{-6}	1.58×10^{-9}	0.69	0.37
SI GR(Cl)	min ; max	-6.9 ; -2.8	-11,4 ; -10.2	-4.3 ; -2.3	-23.6 ; -21.8
SI GR(CO_3)	min ; max	-7.9 ; -1.3	-14.7 ; -13.9	-0.7 ; 3.2	-25.6 ; -24.3

	Step	Sid (1) + Ferri (2)	Sid (1) + Mag (2)	GR(OH) (1) + Ferri (2)	GR(OH) (1) + Mag (2)
$log_{10}\ K_{ex,GT}^{Cl-CO_3}$	1	3.5	3.6	3.8	3.8
	2	2.6	2.7	3.2	3.2
	3	2.3	2.3	3	3
Diss. GR (w%)	1-2-3	6.9	8.1	20.6	20.6
Phase 1 (w%)	3	3.0	2.5	11.4	10.6
Phase 2 (w%)	3	1.8	2.3	0.9	1.2
Fe^{2+} (mM)	1 (max)	0.16	0.04	9.03×10^{-5}	5.44×10^{-4}
Fe^{3+} (mM)	1 (max)	2.60×10^{-6}	4.83×10^{-9}	2.34×10^{-6}	6.43×10^{-8}
SI GR(Cl)	min ; max	-9.8 ; -7.7	-12.5 ; -11.2	-21.2 ; -19.3	-20.4 ; -18.53
SI GR(CO_3)	min ; max	-11.6 ; -7.6	-17.1 ; -14.5	-25.6 ; -24.3	-25.6 ; -24.3

• *Experiment "Na_2CO_3-I" - simple exchange model*

For experiment "Na_2CO_3-I", a simple model with only an ion exchange between Cl^- and CO_3^{2-} was used (Equation V.2). The modeled pH was close to the measured value at each step of the experiment, so there was no need to buffer the pH (Figure V.41B). A good fit between the model and the experimental data for Cl^- and DIC concentrations was obtained, with a constant $log_{10}\, K_{ex,GT}^{Cl-CO_3} = 0$ for all exchange steps (Figure V.41A). The sensitivity of the results to $log_{10}\, K_{ex,GT}^{Cl-CO_3}$ modifications was tested by varying $log_{10}\, K_{ex,GT}^{Cl-CO_3}$ from -0.4 to 0.4 (Figure V.41A).

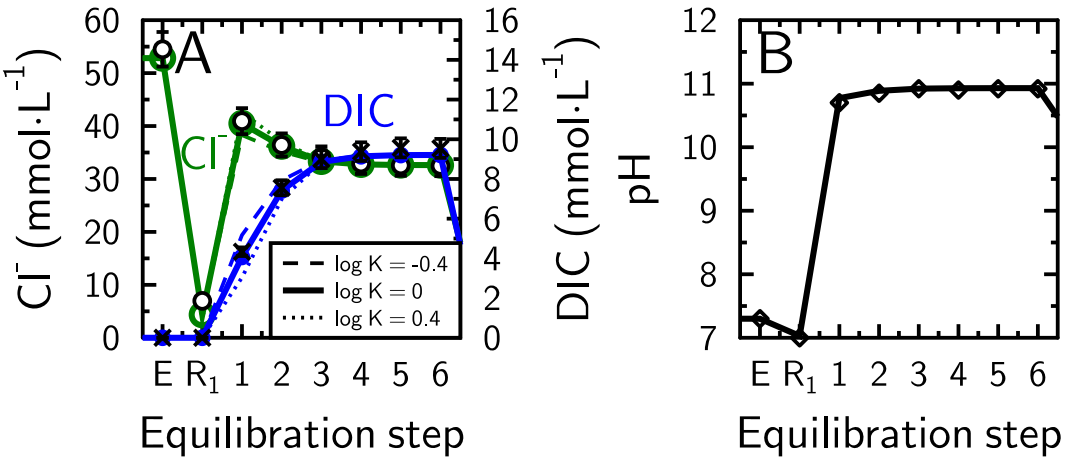

Figure V.41 – modeling results of experiment "Na_2CO_3–I" with a constant selectivity coefficient $log_{10}\, K_{ex,GT}^{Cl-CO_3} = 0$. The initial sample was saturated with Cl^- (E). Step R_1 corresponds to the rinsing of the sample with ultrapure water. Steps 1-6 correspond to equilibration with Na_2CO_3-NaCl solution with a concentration of 10 mmol·L^{-1} of Na_2CO_3 and 30 mmol·L^{-1} of NaCl. (A) Concentrations obtained by the model (Cl^- - green line with green circle; carbonate species - blue line with blue marker) compared to data (Cl^- - black circles; DIC - black crosses). $log_{10}\, K_{ex,GT}^{Cl-CO_3}$ were equal to 0 (full lines), −0.4 (dashed line) and 0.4 (dotted line). (B) pH obtained by the model (black line) compared to data (diamond).

• *Experiment "Na_2CO_3-II" - simple model with buffering capacity of micro-Co-GR*

For experiment "Na_2CO_3-II", a model was done with only the exchange between Cl^- and CO_3^{2-} (data not shown). The modeled pH values were too high compared to the measured pH values. Contrary to experiment "$NaHCO_3$", H^+ were released during experiment "Na_2CO_3-II". A first hypothesis to explain the release of H^+ is that micro-Co-GR phase was buffering the pH by releasing H^+ (deprotonoation of edge amphoteric groups). A model was developed with a fixed pH (in order to find the amount of H^+ released by micro-Co-GR phase, Figure V.42B) and an exchange equation between Cl^- and CO_3^{2-} was used (Equation V.2). The Gaines & Thomas selectivity coefficient had to be adjusted in order to obtain a good fit between the measured and modelled concentrations (Figure V.42A and C). During steps 1-4, corresponding to the equilibration with Na_2CO_3-NaCl solution with a concentration

of 5 mmol·L^{-1} of Na_2CO_3 and 40 mmol·L^{-1} of NaCl, a total of 0.17 mol·kg^{-1} of H^+ were released by micro-Co-GR phase (6.8 % of the AEC value). During steps 5-7, corresponding to the equilibration with Na_2CO_3-NaCl solution with a concentration of 10 mmol·L^{-1} of Na_2CO_3 and 30 mmol·L^{-1} of NaCl, a total of 0.33 mol·kg^{-1} of H^+ were released by micro-Co-GR phase (13.2 % of the AEC value). Over the whole experiment, a total of 0.20 mol·kg^{-1} of H^+ were released (20 % of the AEC value). Similarly to experiment "$NaHCO_3$", this quantity of released H^+ was too high to be explained only by the deprotonation of edge surface amphoteric groups. There could be another process buffering the pH. Dissolution/precipitation or oxidation processes can not explain the results of "$Na_2CO_3 - II$" because H^+, instead of OH^-, were released in solution. However, the pH was high for experiment "Na_2CO_3-II" ($pH \approx 11$), thus the exchange of OH^- with Cl^- or CO_3^{2-} could have been in this case be a possible explanation for this pH discrepancy.

• *Experiment "Na_2CO_3-II" - simple model exchange with addition of OH^- exchange*

Exchange with OH^- on green rust exchange sites was written similarly as for the tests for experiment "$NaHCO_3$":

$$\begin{cases} GrCl + OH^- \overset{K_{ex}^{Cl-OH}}{=} GrOH + Cl^- \\ 2\,GrCl + CO_3^{-2} \overset{K_{ex}^{Cl-CO_3}}{=} Gr_2CO_3 + 2\,Cl^- \end{cases} \tag{V.10}$$

A first attempt was made by modeling the whole experiment with exchange of Cl^-, CO_3^{2-}, and OH^-, and with one selectivity coefficient for each exchange reaction in equation V.10. Those selectivity coefficients were adjusted on step 1 with $log_{10}\,K_{ex,GT}^{Cl-CO_3} = 3.5$ and $log_{10}\,K_{ex,GT}^{Cl-OH} = 4.2$ (Figure V.43). With these constraints, modelled concentrations and pH did not match the experimental data after step 1 (Figure V.43A and B).

The second attempt was to model the whole experiment with exchange of Cl^-, CO_3^{2-}, and OH^-, with one selectivity coefficient for each exchange reaction in equation V.10, while fixing the pH at the measured values. The selectivity coefficients were also adjusted at step 1 with $log_{10}\,K_{ex,GT}^{Cl-CO_3} = 3.5$ and $log_{10}\,K_{ex,GT}^{Cl-OH} = 4.2$ (Figure V.44). With this model, all Cl^- initially present in micro-Co-GR phase were desorbed at step 2 and replaced by OH^-. CO_3^{2-} ions adsorbed during step 1 were also desorbed at step 2 and after. Once again, this model could not correctly reproduce the data.

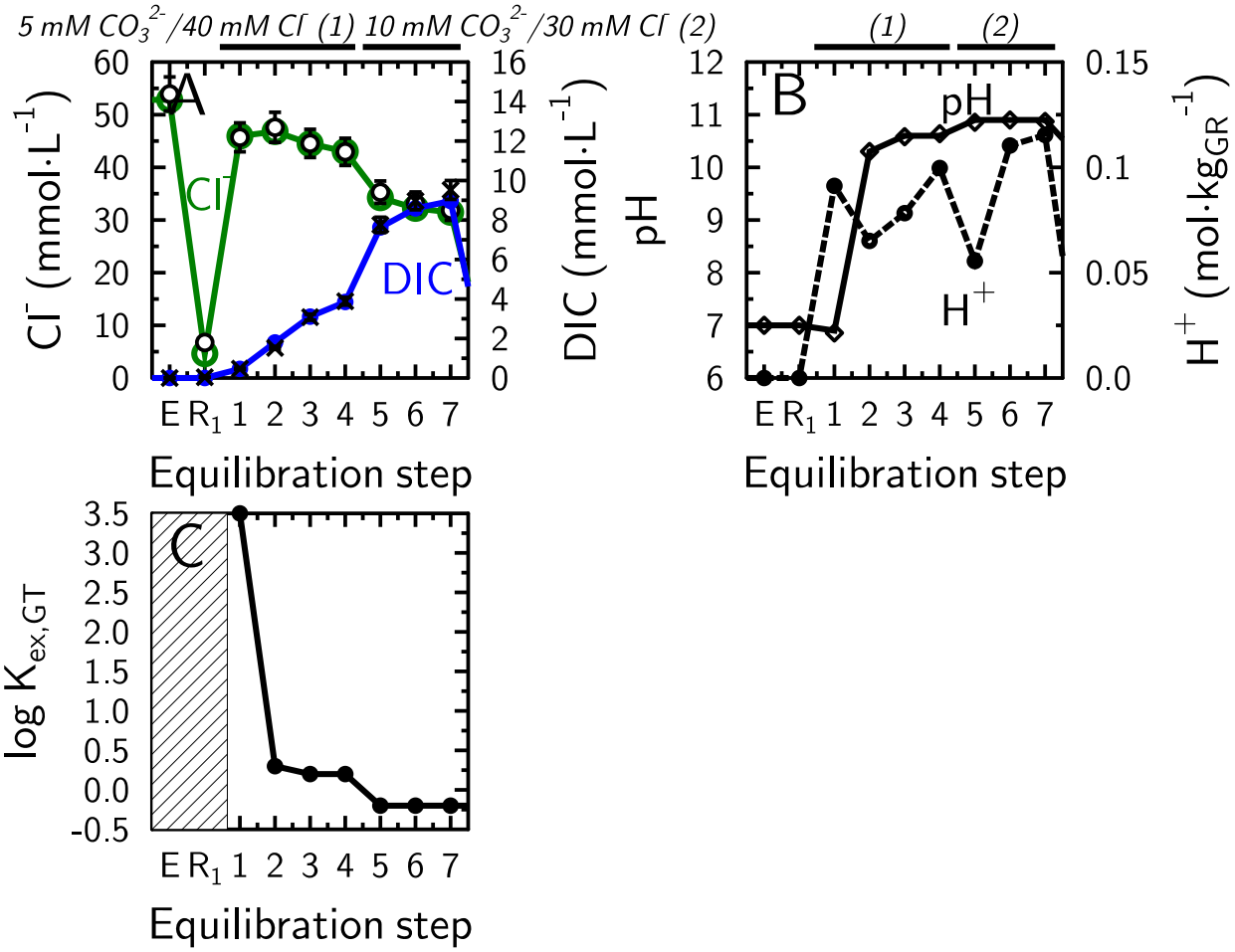

Figure V.42 – modeling results of experiment "Na_2CO_3 – II" with only equation V.2 and fixing the pH. The initial sample was saturated with Cl^- (E). Step R_1 corresponds to the rinsing of the sample with ultrapure water. Steps 1-4 correspond to equilibration with Na_2CO_3-NaCl solution with a concentration of 5 mmol·L^{-1} of Na_2CO_3 and 40 mmol·L^{-1} of NaCl (C5/Cl40). Steps 5-7 correspond to equilibration with Na_2CO_3-NaCl solution with a concentration of 10 mmol·L^{-1} of Na_2CO_3 and 30 mmol·L^{-1} of NaCl (C10/Cl30). (A) Concentrations obtained by the model (Cl^- - green line with green circle; carbonate species - blue line with blue marker) compared to data (Cl^- - black circles; DIC - black crosses). (B) pH obtained by the model (black line) compared to data (diamond). The buffering capacity corresponds to the amount of released H^+ (normalized to the mass of green rust powder) in order to fix the pH (dashed black line). (C) Gaines & Thomas selectivity coefficient for the exchange between Cl^- and CO_3^{2-}. No exchange happened in the hatched area.

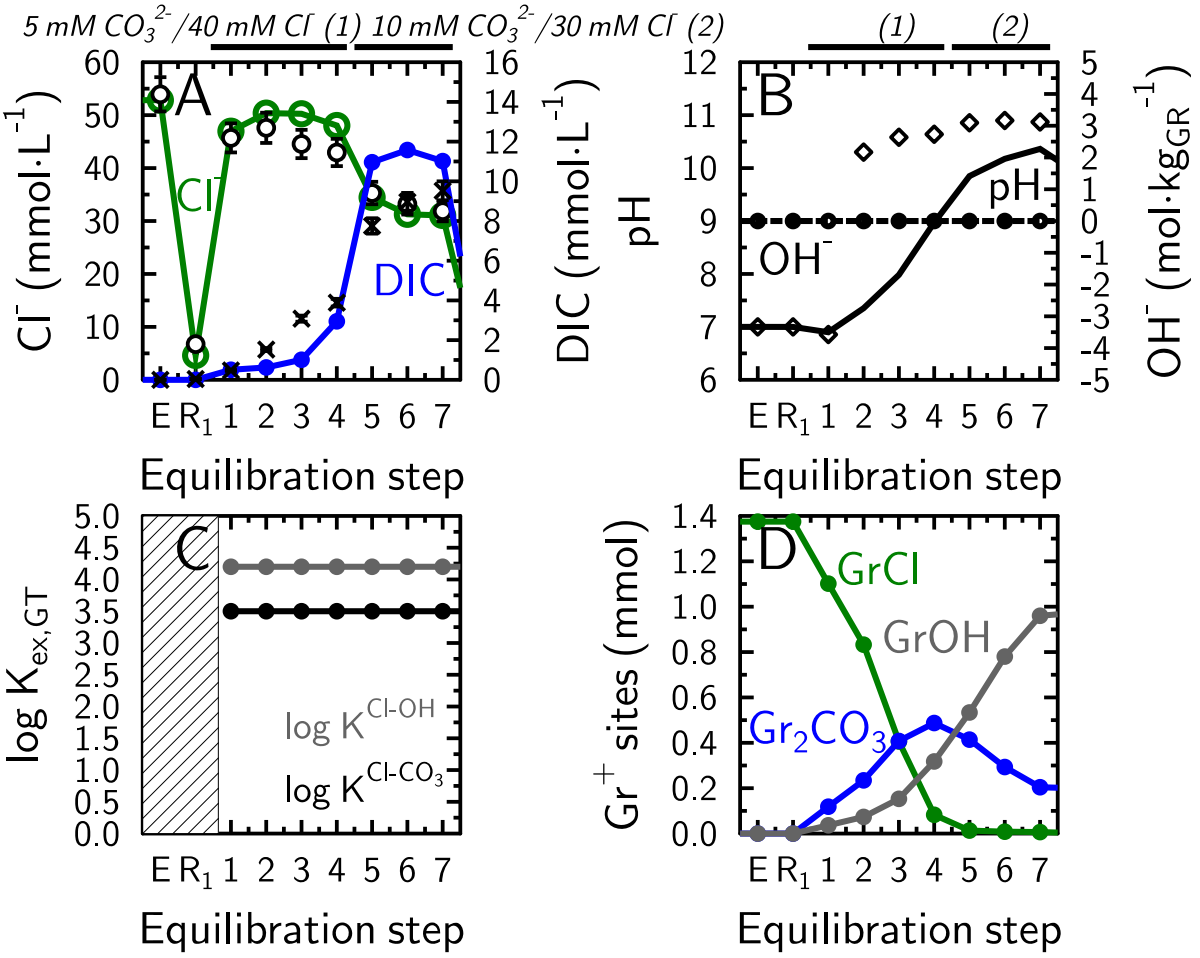

Figure V.43 – modeling results of experiment "Na_2CO_3 – II" with the exchange of Cl^-, CO_3^{2-} and OH^- and equation V.10. The caption is the same as Figure V.42 except for the following details. (B) The buffering capacity corresponds to the amount of released OH^- (normalized to the mass of green rust powder) in order to fix the pH (dashed black line). (C) Gaines & Thomas selectivity coefficient for the exchange between Cl^- and CO_3^{2-} (black line) and for the exchange between Cl^- and OH^- (grey line). No exchange happened in the hatched area. (D) Molar quantity of each exchange sites and their adsorbed anion (GrOH - grey line, GrCl - green line and Gr_2CO_3 - blue line).

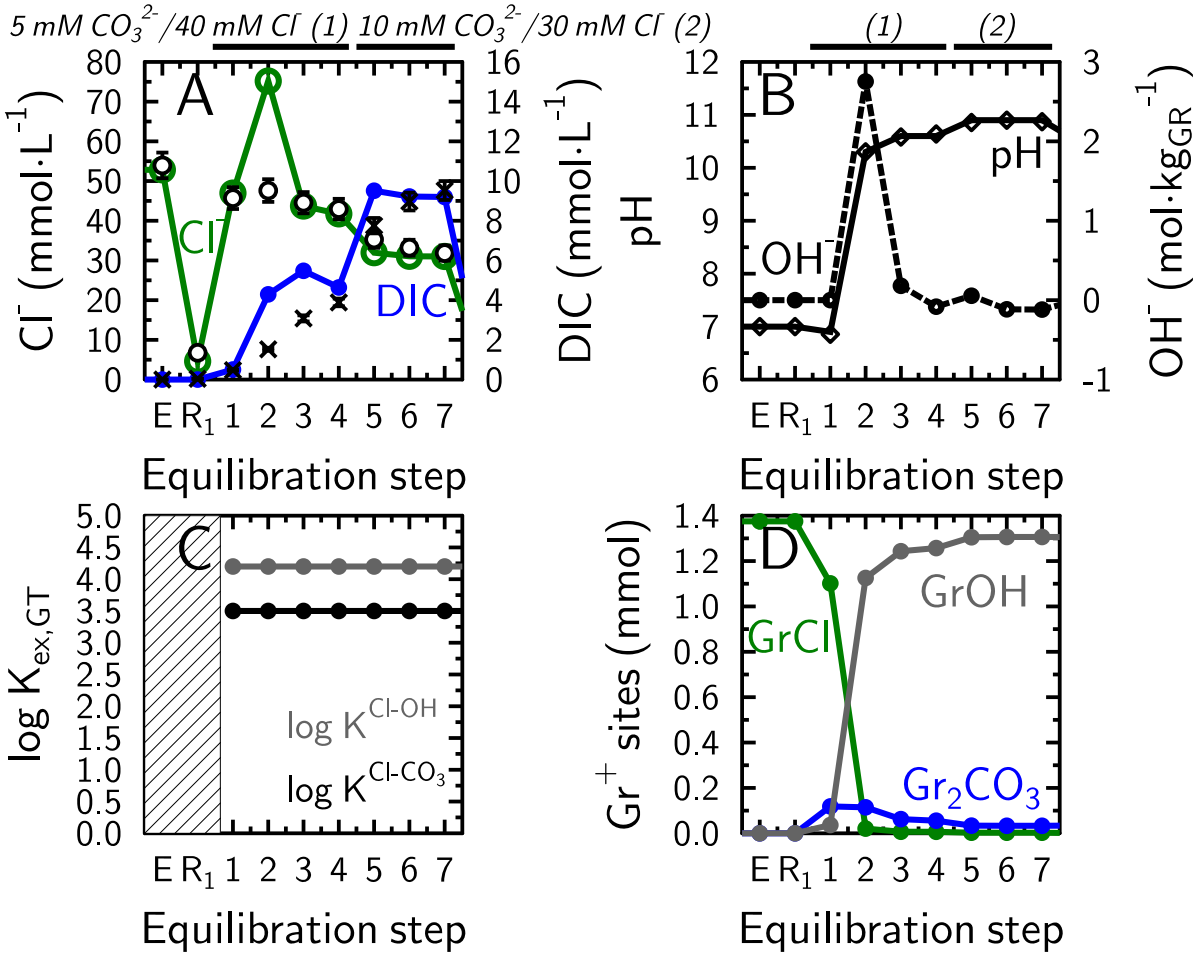

Figure V.44 – modeling results of experiment "Na_2CO_3 – II" with the exchange of Cl^-, CO_3^{2-} and OH^- (equation V.10) and fixing the pH. The caption is the same as Figure V.43.

The third and last attempt was to model the experiment with an exchange of Cl^-, CO_3^{2-} and OH^-, at fixed pH values, with an adjustment of the Cl^--CO_3^{2-} selectivity coefficient at each step, while the $log_{10}\ K_{ex,GT}^{Cl-OH}$ value remained constant at a value of 1 (Figure V.45C). At neutral pH for step 1, $log_{10}\ K_{ex,GT}^{Cl-CO_3}$ was equal to 3.5, i.e. a value similar to that obtained in experiment "$NaHCO_3$" within the same pH range (step 1 of experiment "$NaHCO_3$", Table V.6). From step 2 to 4, $log_{10}\ K_{ex,GT}^{Cl-CO_3}$ was equal to 0.3. From step 5 to 7, in which a solution containing 10 mmol·L^{-1} of Na_2CO_3 and 30 mmol·L^{-1} of NaCl was used, $log_{10}\ K_{ex,GT}^{Cl-CO_3}$ was equal to 0, i.e. a value that was the same as in experiment Na_2CO_3 – I in similar pH value condition. The amount of OH^- released in solution was oscillating from −0.12 mol·kg^{-1} to 0.15 mol·kg^{-1}. Over the whole experiment, total OH^- uptake compared to 8.5 % of the AEC of the micro-Co-GR sample. Finally, at the end of the experiment 11.3 % of the exchange capacity were occupied by OH^-, 36 % to Cl^- and 53 % to CO_3^{2-} (2 sites per CO_3^{2-}, Figure V.45D).

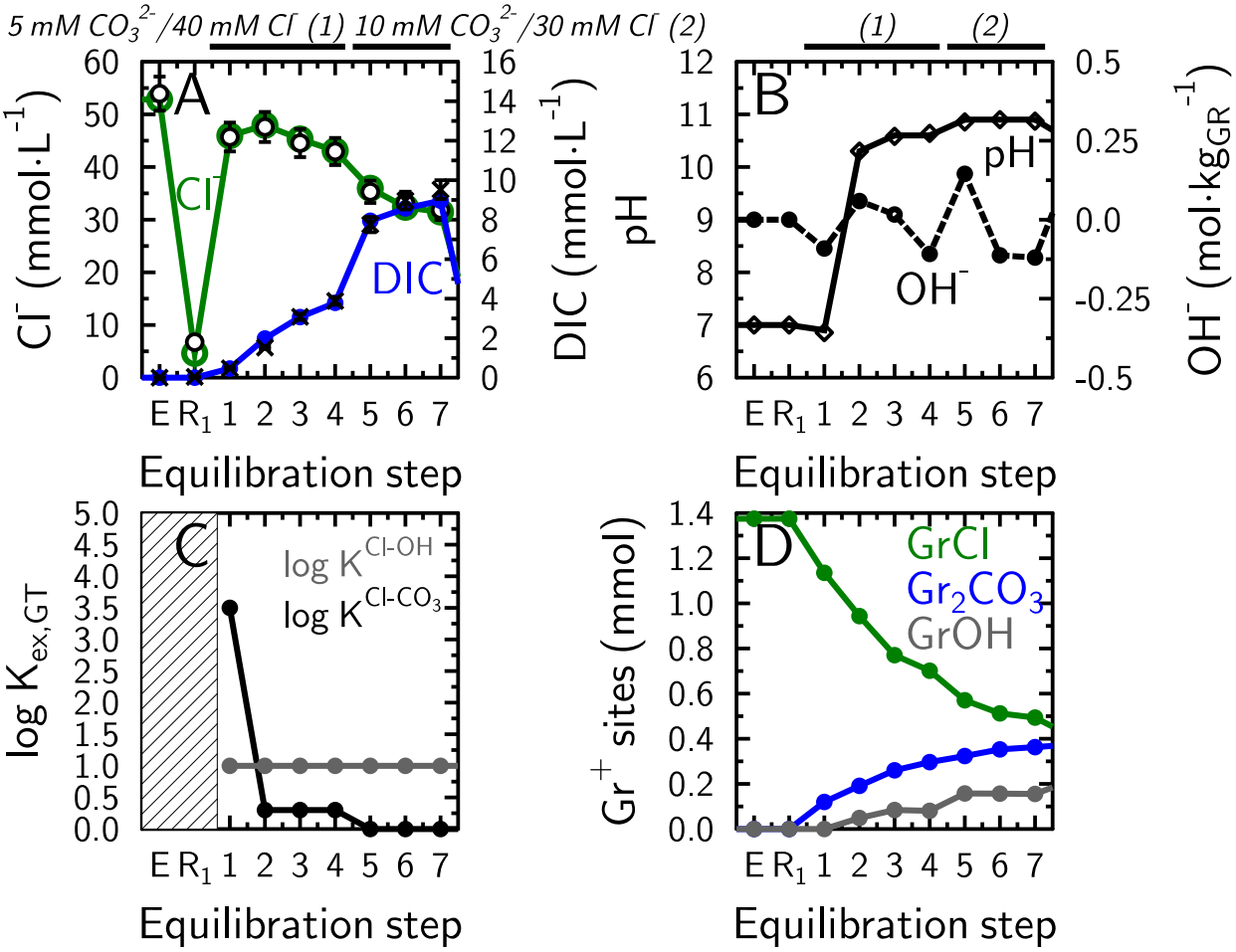

Figure V.45 – modeling results of experiment "Na_2CO_3 – II" with the exchange of OH^- and equation V.10 by fixing the pH and fitting $log_{10}\ K_{ex,GT}^{Cl-CO_3}$. The caption is the same as Figure V.43.

$SO_4^{2-} \longrightarrow CO_3^{2-}$ exchange

The exchange between SO_4^{2-} and carbonate species was studied with experiment "$Na_2SO_4/NaHCO_3$".

The model was done in two consecutive steps in order to avoid incompatibilities between Rothmund & Kornfeld and Gaines & Thomas conventions modeling with PHREEQC (Figure V.46):

— Steps E to R_2 - equation V.1 with a Rothmund & Kornfeld conventions and the parameters determined for Cl^--SO_4^{2-} exchange ($\beta = 2.4$ and $log_{10}\, K_{ex,\mathrm{RK}}^{Cl-SO_4} = 0.3$),

— Steps R_2 to 10 - equation V.3 with either a Gaines & Thomas convention or a fitted $log_{10}\, K_{ex,\mathrm{RK}}^{SO_4-CO_3}$.

In the first modeling attempt, pH was fixed at the measured values. The model results clearly showed that a SO_4^{2-}-CO_3^{2-} exchange was necessary to fit the data at exchange step 4 (Figure V.46A and B). However, the fit was not good for DIC and SO_4^{2-} concentrations at step 5 and 6. A second problem is that this model gave a total OH^- released by micro-Co-GR phase of 1.04 $mol \cdot kg^{-1}$, which corresponded to 42 % of the AEC. As for experiment "$NaHCO_3$", the quantity of OH^- was too high to be explained simply by the protonation/deprotonation of edge amphoteric groups. Because the chemical conditions for step 4 to 10 were similar to experiment "$NaHCO_3$", the partial dissolution of the micro-Co-GR sample and the precipitation of magnetite were considered.

In this following model, the $log_{10}\, K_{ex,\mathrm{GT}}^{SO_4-CO_3}$ value and the dissolved quantity of micro-Co-GR(SO_4) sample ($Fe_{0.67}Co_{0.33}(OH)_2(SO_4)_{0.125}$) were adjusted to fit the measured pH values as well as DIC and SO_4^{2-} concentrations (Figure V.47A, C and D). $log_{10}\, K_{ex,\mathrm{RK}}^{SO_4-CO_3}$ varied from 2.5 to 1.8 (Figure V.47D). The modelled concentrations were in good agreement with the measured data except for the SO_4^{2-} concentration at step 4. From steps 4 to 7, the amount of dissolved micro-Co-GR phase was 23.5 w% (Figure V.47E). At step 7, 6.2 w% of magnetite precipitated (Figure V.47E).

$CO_3^{2-} \longrightarrow SO_4^{2-}$ exchange

In situ XRD data did not evidence any exchange between carbonate species and SO_4^{2-} in micro-Co-GR phase (Figure V.21). It was interpreted either that the $SO_4^{2-} \longrightarrow CO_3^{2-}$ exchange was not reversible, or that the affinity for carbonate species was very high compared to the affinity for sulphate. The second part of experiment "$NaHCO_3$" shown in Figure V.24 was carried out to understand the origin of this apparent irreversibility.

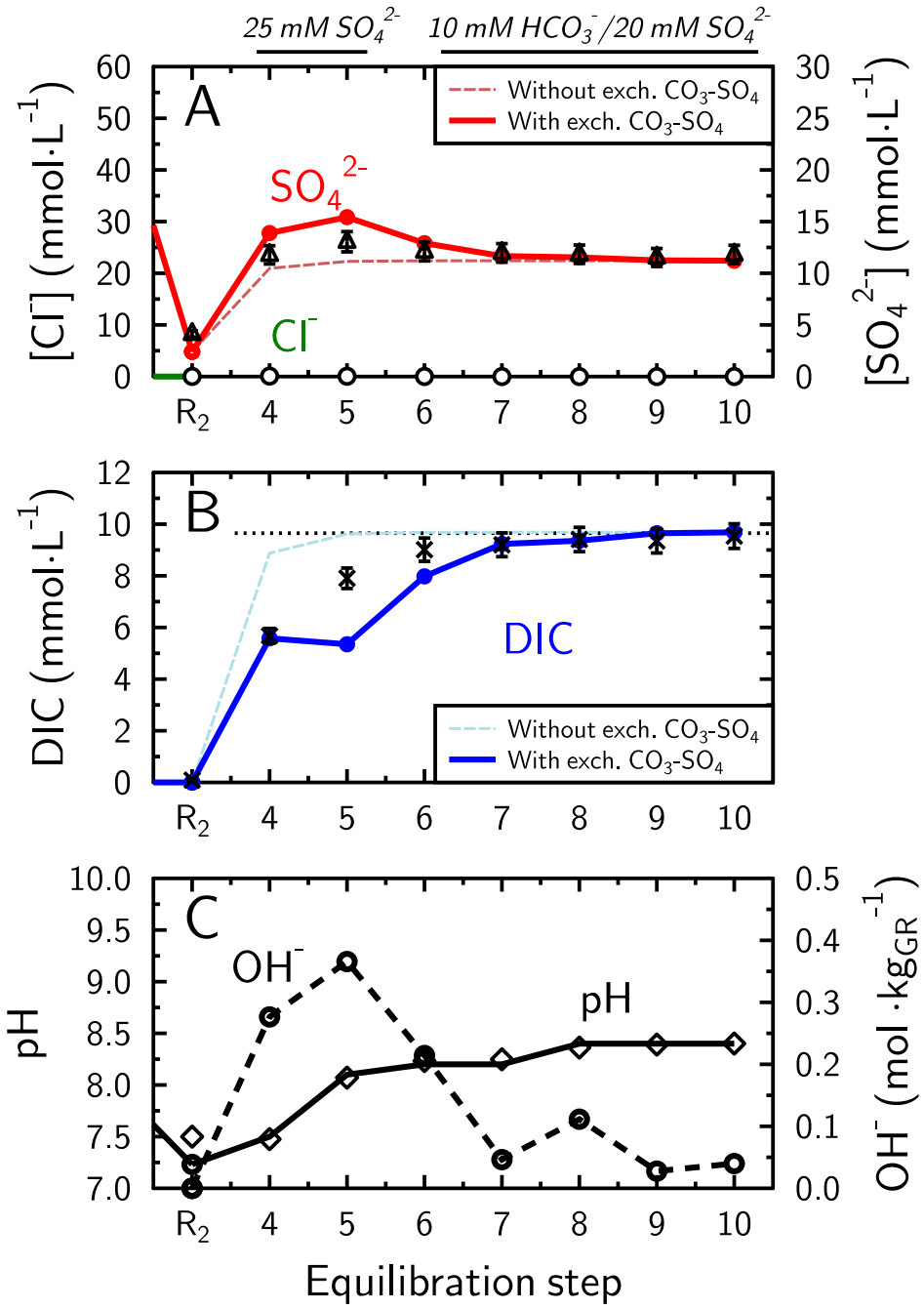

Figure V.46 – CO_3^{2-}, SO_4^{2-} & Cl^- exchange data and model on micro-Co-GR sample with one selectivity coefficient and fixing the pH. Steps R_2 corresponds to the rinsing of the sample with ultrapure water. Steps 4-10 correspond to equilibration with $NaHCO_3$-Na_2SO_4 solutions with a concentration of 10 mmol$\cdot$ L^{-1} of $NaHCO_3$ and 20 mmol$\cdot$ L^{-1} of Na_2SO_4 (HC10/S20). (A) Cl^- and SO_4^{2-} concentrations obtained by the model compared to data (Cl^- - black circles; SO_4^{2-} - black triangles). Colored lines are the results of the model if equation V.3 was added to the model with a Gaines & Thomas exchange model and a $log_{10}\, K_{ex,GT}^{SO_4-CO_3} = 2.5$ (full red lines). The colored dashed line is the modelled results without equation V.3. (B) Concentrations of carbonate species obtained by the model compared to data (CO_3^{2-} - black crosses). Colored lines are the results of the model with the same cases as figure A ($log_{10}\, K_{ex,GT}^{SO_4-CO_3} = 2.5$ full blue lines). The colored dashed line is the modelled results without equation V.3. The black dashed lines represent the total DIC input concentration. (C)pH (diamond - data ; full line - model) and quantity of OH^- released by micro-Co-GR phase to buffer the pH (dashed black line). pH was partially fixed in the model from step 4 to step 10.

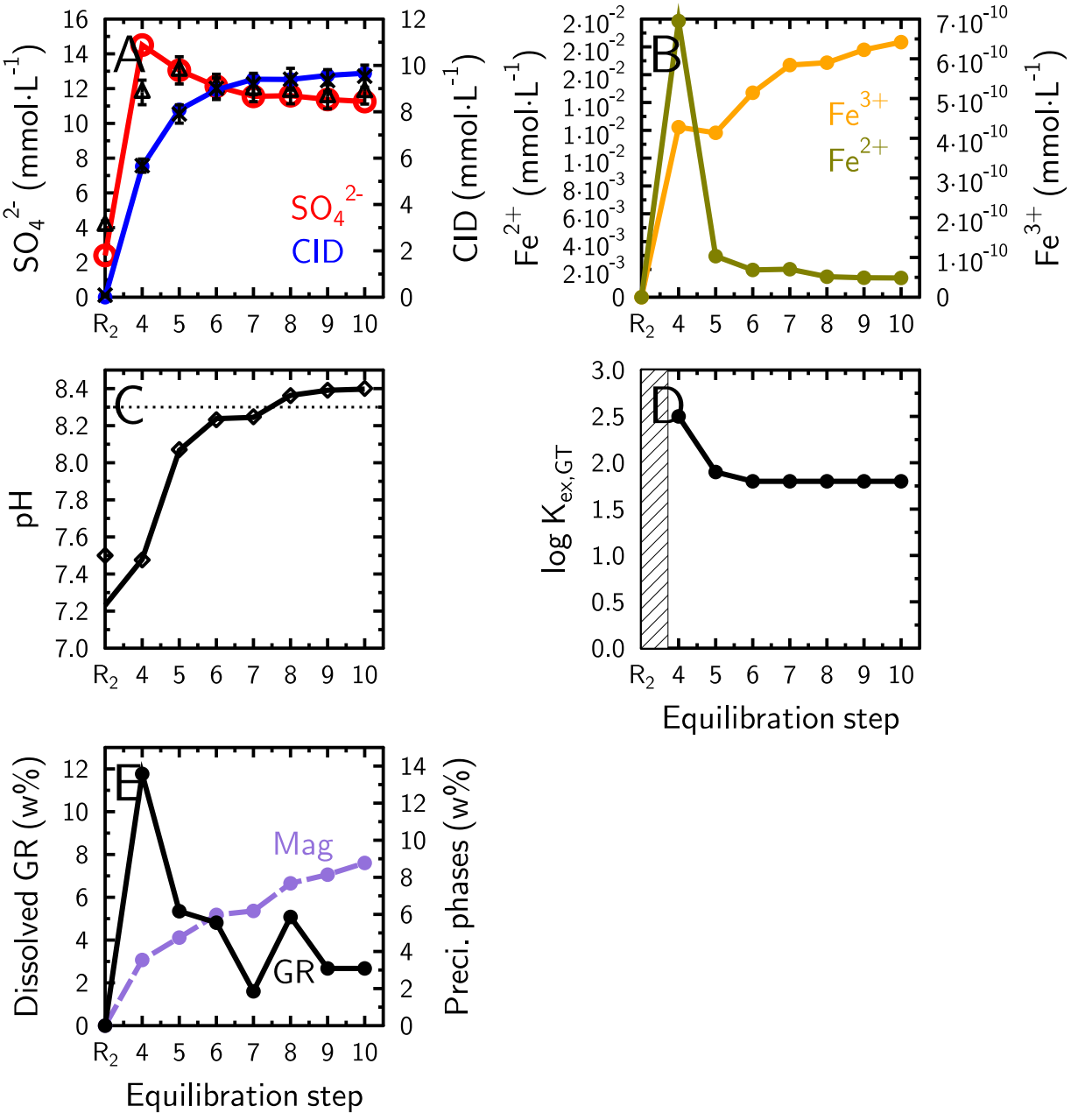

Figure V.47 – Modelled results of experiment with an exchange between CO_3^{2-} and SO_4^{2-} with equation V.3, dissolution of green rust and precipitation of magnetite. The equilibration steps were the same as Figure V.46. (A) Concentrations obtained by the model (SO_4^{2-} - red line with red circle; carbonate species - blue line with blue marker) compared to data (SO_4^{2-} - black triangles; CO_3^{2-} - black crosses). (B) Fe^{2+} (olive) and Fe^{3+} (orange) concentrations in solution from the model. (C) pH obtained by the model (black line) compared to data (diamond marker). The dotted line represents the pH of the stock solution used for the exchange. (D) Gaines & Thomas selectivity coefficient for the exchange between SO_4^{2-} and CO_3^{2-}. No exchange happened in the hatched area. (E) Weight percentage of green rust dissolved to fit the model (black line and black circle) and weight percentage of precipitated magnetite (purple circle and purple dashed line). Percentage calculated on the total mass of solid at the end of each step. (F) Gaines & Thomas selectivity coefficient according to the pH (black circle) with a linear regression (black dashed line).

Models with partial dissolution of micro-Co-GR phase and precipitation of magnetite (from step 1 to 6) were used to initiate the conditions for the modeling of experiment "$NaHCO_3$" after step 6. However, after step 6, the model did not include any dissolution of micro-Co-GR phase because it was not necessary to adjust the pH from step R_2 to R_3 (Figure V.48). The pH measured at step R_2 was 6.4 and the pH given by the model was 7.6 for a rinsing with pure milliQ water at pH 7 (Figure V.48C). This pH was not taken into account because 30 mL of milliQ water was quickly added on micro-Co-GR sample and directly filtrated (1-2 min compared to other steps that lasted 30 min). In absence of additional data, it was not possible to constrain a model for the processes occuring with micro-Co-GR phase within this short period of time. The pH values given by the model at step 7, 8 and R_3 were close to the measured values (Figure V.48C).

SO_4^{2-} and DIC concentrations were in good agreement with the measured data when equation V.3 was not added to the model (dashed lines in Figure V.48), while the modelled results were not in good agreement with the measured data (SO_4^{2-} and DIC concentrations, and pH) when equation V.3 was added to the model with $log_{10}\, K_{ex,\mathrm{RK}}^{SO_4-CO_3} = 1.7$ (full lines in Figure V.48). Consequently, at these chemical conditions and in the timeframe of the experiment, no exchange occurred with SO_4^{2-} once CO_3^{2-} was present in the interlayer (Figure V.49), in agreement with *in situ* XRD results.

Conclusion on models of anion exchange on green rust and parameters summary

Thermodynamic parameters for Cl^-, SO_4^{2-} and CO_3^{2-} exchanges were determined for a 3D-ordered green rust (micro-Co-GR phase, Figure V.52). For the reaction of a chlorinated green rust with SO_4^{2-} in solution, an ion exchange model using the Rothmund & Kornfeld convention was a good method to simulate the chemical experimental results. Stacking defects did not change the convention needed to model this system (comparison between nano-Co-GR and micro-Co-GR phases on a Cl^--SO_4^{2-} exchange). However the thermodynamic parameters had to be adapted to match the modelled results with the experimental results for both phases.

In the reaction of a chlorinated green rust with carbonate species in solution, CO_3^{2-} replaced Cl^- in the interlayer by an ion exchange process and Gaines & Thomas convention was used. The associated thermodynamic parameters were dependant on the pH. For pH between 6 and 8.5, a partial dissolution of micro-Co-GR phase was necessary to model this system, with the precipitation of another iron phase, most probably magnetite. XRD data showed an increase of the magnetite proportion in the

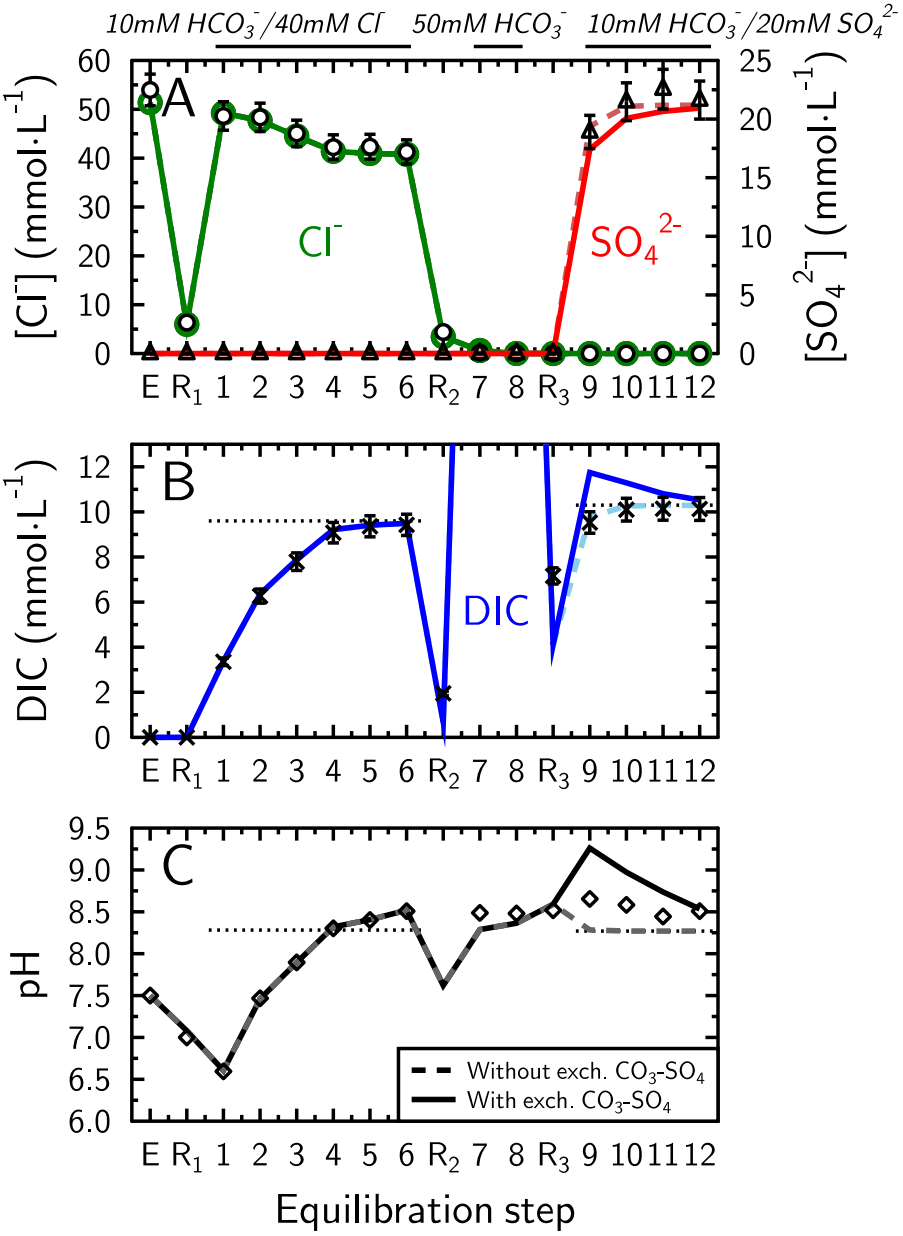

Figure V.48 – CO_3^{2-}, SO_4^{2-} & Cl^- exchange data and model on micro-Co-GR sample for experiment "$NaHCO_3$". The initial sample was saturated with Cl^- (E). Steps R correspond to the rinsing of the sample with ultrapure water. Steps 1-6 correspond to equilibration with a solution with a concentration of 10 mmol·L^{-1} of $NaHCO_3$ and 40 mmol·L^{-1} of NaCl. Steps 7-8 correspond to equilibration with Na_HCO_3 solution with a concentration of 50 mmol·L^{-1}. Steps 9-12 correspond to equilibration with a $NaHCO_3$-Na_2SO_4 solution with a concentration of 10 mmol· L^{-1} of $NaHCO_3$ and 20 mmol· L^{-1} of Na_2SO_4. Steps E to 6 were modelled with the partial dissolution of micro-Co-GR phase and precipitation of magnetite (see Figure V.34 for details). (A) Cl^- and SO_4^{2-} concentrations obtained by the model compared to data (Cl^- - black circles; SO_4^{2-} - black triangles). Full lines are the results of the model if equation V.3 were added to the model after stepR_3 with a Gaines & Thomas exchange model, and a $log_{10}\ K_{ex,GT}^{SO_4-CO_3} = 1.7$ (full red lines). The light red dashed line are the modelled results without equation V.3. (B) Concentrations of carbonate species obtained by the model compared to measured data (CO_3^{2-} - black crosses). Colored lines are the results of the model with the same cases as figure A ($log_{10}\ K_{ex,GT}^{SO_4-CO_3} = 1.7$ after step R_3 - full blue lines). The light blue dashed line is the model result without equation V.3. The black dashed lines represent the total DIC input concentration. (C) pH during the experiment (diamond - data; full line - model with equation V.3 and grey dashed line - model without equation V.3).

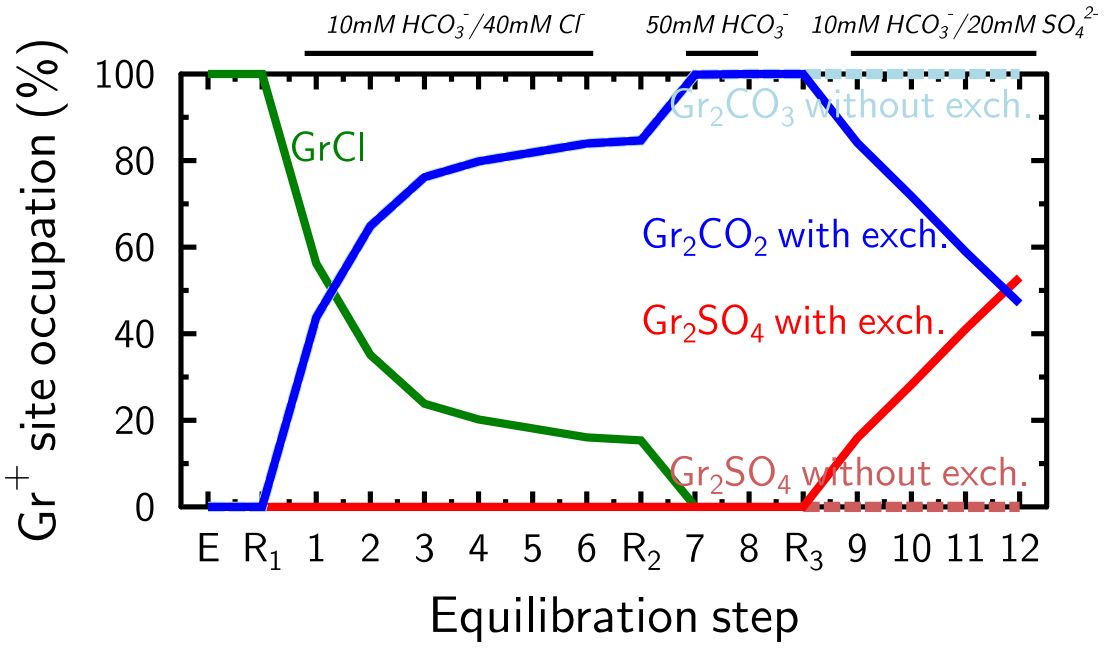

Figure V.49 – Site occupation during experiment "$NaHCO_3$" shown in Figure V.48 (Full lines - exchange between Cl^- and CO_3^{2-} with equation V.2, and exchange between CO_3^{2-} and SO_4^{2-} with equation V.3 were added to the model, Dashed lines - only exchange between Cl^- and CO_3^{2-} with equation V.2 was added to the model, Green line - GrCl, blue lines - Gr_2CO_3 and red lines - Gr_2SO_4; Gr_2CO_3 and Gr_2SO_4, exch. - exchange CO_3–SO_4). Occupations were multiplied by two because two sites Gr^+ were bonded to divalent anions.

solid phase as the exchange reactions proceeded, in agreement with this hypothesis. For pH values higher than 10, $log_{10}\,K_{ex,GT}^{Cl-CO_3}$ were lower (between 0.3 and 0) than $log_{10}\,K_{ex,GT}^{Cl-CO_3}$ for pH between 6 and 8.5. The best model for experiment "Na_2CO_3-II" included an exchange between Cl^-, CO_3^{2-} and also OH^-, associated with protonation/deprotonation of edge amphoteric groups of micro-Co-GR(Cl) phase. Experiment "Na_2CO_3-I", in which the pH was always higher than 10 was modelled with an exchange between Cl^- and CO_3^{2-} only (equation V.2), and it was not necessary to buffer the pH with a specific mechanism. The $log_{10}\,K_{ex,GT}^{Cl-CO_3}$ values obtained with experiment "Na_2CO_3-I" were equal to those obtained in experiment "Na_2CO_3-II" for the same pH conditions (steps 5 to 7 of experiment "Na_2CO_3-II"). A summary of the different experiments is available in Figure V.50 and displays the different hypotheses and models implemented to explain the result for each of these experiments. In order to find a connection between all those experiments, the link between $log_{10}\,K_{ex,GT}^{Cl-CO_3}$ and pH or equivalent fraction of CO_3^{2-} on the exchanger (E_{CO_3}) was evaluated (Figure V.51). No relationship was found between $log_{10}\,K_{ex,GT}^{Cl-CO_3}$ and E_{CO_3}, but a linear relationship was found between $log_{10}\,K_{ex,GT}^{Cl-CO_3}$ and pH, with $log_{10}\,K_{ex,GT}^{Cl-CO_3} = -0.90\,pH + 9.79$ and $r^2 = 0.996$ (Figure V.51A).

The reaction of a sulphate green rust with carbonate species in solution was only studied at pH of 7.4 to 8.4. SO_4^{2-} were exchanged by CO_3^{2-}. Gaines & Thomas convention was used with

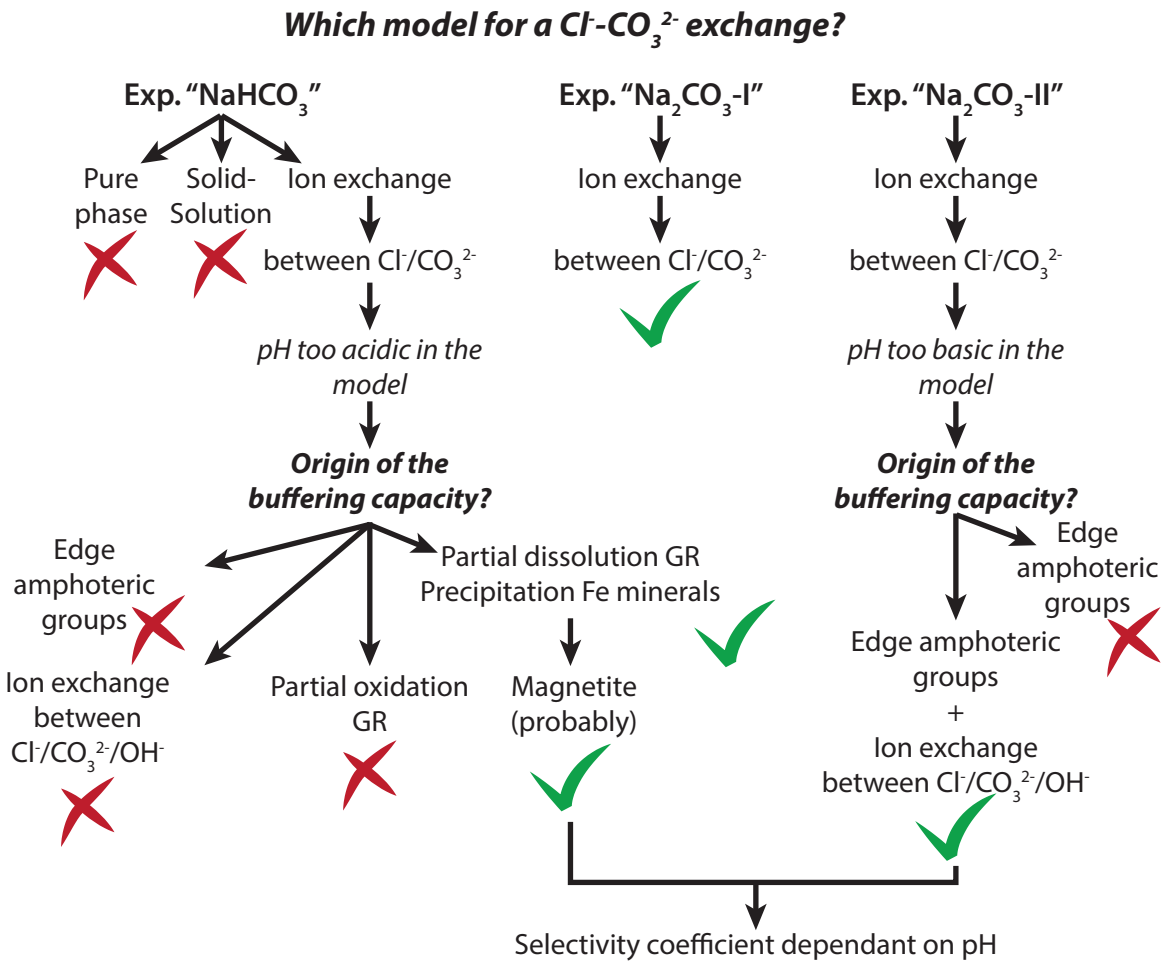

Figure V.50 – Summary of the results and models for Cl^- ⟶ Carbonate species exchange for all the experiments (Exp. - Experiment, GR - micro-Co-GR phase, red x mark - the model results were not in agreement with the measured data, green check mark - the model results were in agreement with the measured data).

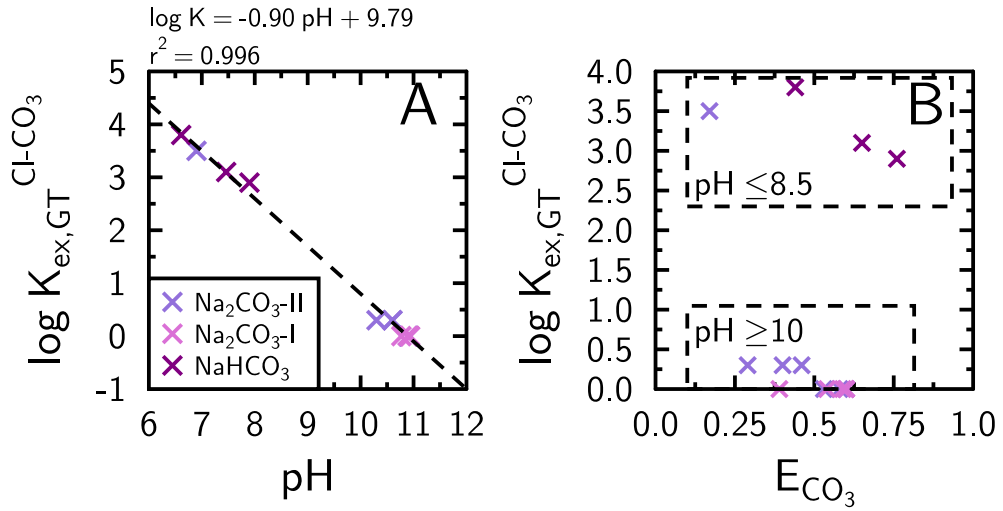

Figure V.51 – Summary of the selectivity coefficients for Cl^- ⟶ Carbonate species exchange with all the experiments: "$NaHCO_3$" (model with dissolution of micro-Co-GR phase and precipitation of magnetite, only step 1 to 3, pink crosses), "Na_2CO_3-I" (violet crosses) and "Na_2CO_3-II" (model with OH^- exchange, fixed pH and $K_{ex,GT}^{Cl-CO_3}$ fitted; purple crosses). (A) $log_{10}\ K_{ex,GT}^{Cl-CO_3}$ according to pH with a linear regression on all the points (black dashed line). (B) $log_{10}\ K_{ex,GT}^{Cl-CO_3}$ according to equivalent fraction (E_{CO_3}) of CO_3^{2-} on the exchanger.

varying $log_{10}\ K_{ex,GT}^{SO_4-CO_3}$ from 2.5 to 1.8. Micro-Co-GR phase partially dissolved into another iron phase, probably magnetite. However, once green rusts was carbonated, carbonate ions in the interlayer could not be exchanged with sulphate ions.

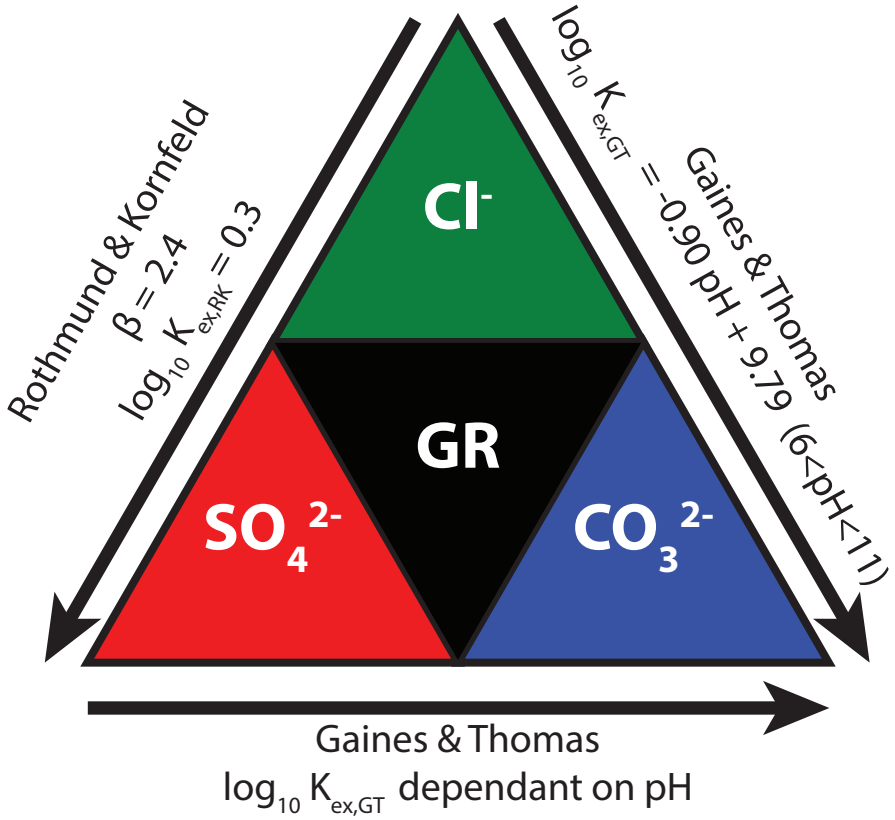

Figure V.52 – Summary of thermodynamic parameters to model an anion exchange between Cl^-, SO_4^{2-} and CO_3^{2-} on a 3D-ordered green rust (micro-Co-GR phase).

V.3.2 Ion exchange mechanism in green rust compared to other LDH

For the exchange between Cl^- and SO_4^{2-} on green rust, the mechanism was an ion exchange without dissolution/recrystallization or interstratification processes. The exchange could be described as a physical mixture of two green rust phases, *i.e.* layer containing Cl^- were not in the same crystal as layer containing SO_4^{2-}. The presence of each layer type is governed by their abundance. The mechanism was the same for a nanometric and turbostratic green rust and a micrometric and 3D-ordered green rust. Exchange processes were also observed was also observed for various LDH in Ay et al. (2007); Goh et al. (2009); Dessalegne et al. (2016); Ma et al. (2017, 2018); Marty et al. (2018); Grangeon et al. (2020).

For the exchange between Cl^- and CO_3^{2-} on green rust, interstratification processes happened during the exchange and a precipitation of magnetite. Interstratification processes were also observed in LDH during exchange experiments wih R = 0 and R = 1 (Taviot-Guého et al., 2010; Marty et al., 2018; Grangeon et al., 2020).

V.3.3 Ion exchange models in green rust compared to other LDH

The AEC of a micrometric and 3D ordered green rust was 2.5 $mol_c \cdot kg^{-1}$ which is in agreement with AEC observed in LDH with a range of $2-4$ $mol_c \cdot kg^{-1}$ (Taviot-Guého et al., 2018).

The order of affinity shown by Miyata (1983) for hydrotalcite was verified for green rust for three anions: $CO_3^{2-} > SO_4^{2-} > Cl^-$. However, different convention, parameters or processes were witnessed in this work as a function of the exchanged anions.

For a $Cl^- \longrightarrow SO_4^{2-}$ exchange and both green rust (nano-Co-GR and micro-Co-GR), experiments could be modelled with ion exchange models following Rothmund & Kornfled convention. β values were larger than one, meaning that the Gaines & Thomas selectivity coefficient $K_{ex,\mathrm{GT}}$ of the $Cl^- \longrightarrow SO_4^{2-}$ exchange reaction increased with the SO_4^{2-} occupancy on the exchanger. A large increase of the $A \longrightarrow B$ selectivity coefficient with an increase of the exchanger occupancy by species B is at variance with observations made on cationic clays for which the reverse tendency has been observed frequently. The decrease of the selectivity in clays is usually linked to the presence of several types of adsorption sites with decreasing affinities for species B compared to species A (Poinssot et al., 1999; Staunton and Roubaud, 1997; Steefel et al., 2003; Tournassat et al., 2009; Tremosa et al., 2012). Consequently, the mechanism of anion exchange in GR interlayers may be different from ion exchange in cationic clay mineral interlayers. Miyata (1983) observed various trends between the selectivity coefficient and the exchanger occupancy on Mg-Al hydrotalcite-like compounds. The only case of a monotonous increase between the selectivity coefficient with the exchanger occupancy was for a $NO_3^- \longrightarrow Br^-$ exchange. Because of the similarities of the structure between Mg-Al LDH and GR, it was speculated that the peculiar anion exchange properties of GR could be related to the structuration of anions in the interlayer, which is influenced by the geometry of the anion (spherical and point charge for Cl^-, tetrahedral oxyanion for SO_4^{2-}), the high charge density (0.18 $C.m^{-2}$ for micro-GR compared to -0.11 $C.m^{-2}$ for Wyoming montmorillonite), and the high surface occupation (Génin et al., 2006; Tournassat et al., 2015).

For the Cl^- ⟶ DIC exchange on micro-Co-GR, this work confirmed the validity of the common assumption that CO_3^{2-} is the carbonate species adsorbed in the interlayer. HCO_3^- has been observed into the interlayer of different LDH (Mg-Al, Mg-Ga and Mg-Fe LDH) by Di Bitetto et al. (2017), however it was after a contact with air and $CO_{2(g)}$. The authors confirmed the presence of CO_3^{2-} in the initial phase (before contact with air) with infrared and Raman spectra. For the modeling, Cl^- ⟶ DIC exchange experiments could be modelled with simple ion exchange following Gaines & Thomas conventionFor LDH, Gaines & Thomas convention is more commonly used to model the ion exchange (Table V.7). A link between pH and the amount of anion uptake was found in several studies on LDH (Ookubo et al., 1993; Hayashi et al., 2009). However, to our knowledge, this study presents for the first time a quantification of the link between pH and selectivity coefficient for LDH. Complementary experiments would be needed to first, verify the linear relationship between pH and selectivity coefficient at more diverse pH for a Cl^- ⟶ CO_3^{2-} exchange, and secondly, to show if similar relationship exists for other ions. At high pH, a competition between three anions (OH^-, Cl^- and CO_3^{2-}) has been witnessed in this work for the experiment "Na_2CO_3−II" at pH between 10 and 11. This competition has also been observed between three anions including OH^- and Cl^- ion and a divalent anion (pH higher than 11, Table V.7, Marty et al. (2018); Grangeon et al. (2020)). Consequently, at high pH, a competition with OH^- might be at play on the exchanger on green rust. Green rust seemed to be also affected by these high pH with deprotonation of edge amphoteric groups. If more analyses are conducted, special attention has to be made to decipher the action of each process on the exchange and the reactivity of green rust. In Cl^- ⟶ CO_3^{2-} exchange experiments during *in situ* XRD, a precipitation of magnetite has been witnessed. This precipitation was more important for pH around 8.5 than for pH above 10. Models on batch exchange experiments confirmed that magnetite precipitation could occur in order to buffer the pH and obtain a good fit with measured pH value. This magnetite precipitation was only necessary in the models of experiments with pH around 8.5, and not for experiment at pH above 10, which seemed in agreement with the results of *in situ* XRD experiments. In the literature, several studies have witnessed the transformation of green rust in magnetite. Sumoondur et al. (2008) showed with *in situ* XRD that sulphate green rust can form rapidly from ferrihydrite and $Fe^{2+}_{(aq)}$ (under 6 minutes), and then transform into magnetite by dissolution-reprecipitation. The time needed for this transformation into magnetite depended on Fe(II)/Fe(III) ratio of the ferrihydrite and $Fe^{2+}_{(aq)}$ (420 min at Fe(II)/Fe(III) = 1 and 100 min at Fe(II)/Fe(III) = 0.5). At pH 7 and Fe(II)/Fe(III) = 0.5, sulphate green rust was stable and did not transform into magnetite. A slow transformation from sulphate green rust, to carbonated green rust (80 % of the solid phase after 15 days) and then, magnetite was observed

also by Perez et al. (2021) during an ageing experiment of green rust in deep aquifer groundwater (pH = 7.5 ± 0.3). A partial dissolution of sulphate green rust was shown with the increase of Fe^{2+} in solution during the transformation to carbonate green rust. Trace amount of magnetite were visible after 15 days. The transformations of green rust into magnetite seemed to be inevitable but the rate of transformation varies depending on the chemical conditions. The *in situ* XRD experiment of this study lasted a few hours and the chemical composition of micro-Co-GR was different from the green rust studied by Sumoondur et al. (2008) and Perez et al. (2021). These differences could have influenced the rate of transformation into magnetite.

The high affinity for carbonate on LDH and more especially green rust is well-known (Miyata, 1983; Rives, 2001). In this work with the help of *in situ* XRD and batch experiment, it was shown that once green rust contained CO_3^{2-}, it could not be reversed to its initial structure *i.e.* a green rust containing Cl^- or SO_4^{2-} at the time scale investigated in this work. A first possible explanation would be an hysteresis effect for these exchanges *i.e.* the affinity of the interlayer for the species is not the same depending on reagent addition order. This type of hysteresis has been shown with clays (Benson, 1982; Verburg and Baveye, 1994) and LDH (Rives, 2001; Halajnia et al., 2013). However, *in situ* XRD showed that it was not possible to come back to micro-Co-GR(Cl) phase once it was change to micro-Co-GR(SO_4) or micro-Co-GR(C(IV)) phases, even if the exchange solution contained only Cl^- (Concentration of NaCl at 50 mmol$\cdot$L^{-1}). The same result was shown for micro-Co-GR(SO_4) phase once it was changed to micro-Co-GR(C(IV)) phase (Concentration of Na_2SO_4 at 25 mmol$\cdot$L^{-1}) which was confirmed by batch exchange experiments. The second explanation would be the irreversible nature of the exchange, once green rust contains CO_3^{2-}, this anion can not be exchanged by another anion. In the LDH literature, reverse exchange of carbonate was shown to be possible using acid such as HCl (Costantino et al., 1998; Okamoto et al., 2006; Iyi and Sasaki, 2008) or calcination of LDH (Wang, 2018). A nonequilibrium kinetic model was developed by Ebner et al. (2007) with three reversible reactions at various kinetics. They verified their model with experiments at high temperature (400 °C) ans sorption-desorption cycles by flushing $CO_{2(g)}$ (sorption) or $He_{(g)}$ (desorption). They concluded that the reactions were a combination of completely reversible adsorption, diffusion, and reaction phenomena. Their experimental conditions were very different from the experimental conditions and may not be applicable in this work and (experiments with solutions and around 25 °C). Further study should be done to validate the irreversible nature of the exchange with carbonate species or

to determine the conditions, selectivity coefficients and kinetics of an exchange between carbonate species and other anions.

Table V.7 – Comparative study on ion exchange models and parameters for LDH (Ini. ion - initial ion, Exch. ion - exchanged ion, Afm - Ca–Al LDH, HT - hydrotalcite a Mg-Al LDH, ZnAl - a Zn-Al LDH, GR - green rust, Vans. - Vanselow, G&T - Gaines & Thomas, R&K - Rothmund & Kornfeld, SSM - solid-solution modeling, Var. - variable, Dep. - dependant)

Citation	Phase	Ini. Ion	Exch. Ion	Convention	$log\ K_{ex}$	Note
Aimoz et al. (2012)	Afm	SO_4^{2-}	I^-	Vans.	-4	Better result with SSM
Marty et al. (2018)	Afm	Cl^-	MoO_4^{2-}	G&T	1.3	Competition Cl/OH/MoO_4
Marty et al. (2018)	Afm	OH^-	MoO_4^{2-}	G&T	-0.8	
Grangeon et al. (2020)	Afm	Cl^-	SeO_4^{2-}	G&T	2.5	Competition Cl/OH/SeO_4
Grangeon et al. (2020)	Afm	OH^-	SeO_4^{2-}	G&T	-0.5	Better result with SSM
Miyata (1983)	HT	NO_3^-	OH^-	G&T	1.42	
Miyata (1983)	HT	NO_3^-	F^-	G&T	1.19	
Miyata (1983)	HT	NO_3^-	Cl^-	G&T	0.26	
Miyata (1983)	HT	NO_3^-	Br^-	G&T	0.08	
Miyata (1983)	HT	NO_3^-	I^-	G&T	-0.6	
Miyata (1983)	HT	NO_3^-	CO_3^{2-}	G&T	1.84	
Miyata (1983)	HT	NO_3^-	NYS^{2-}	G&T	1.46	
Miyata (1983)	HT	NO_3^-	SO_4^{2-}	G&T	1.39	
Goh et al. (2009)	HT	NO_3^-	As(V)	G&T	1.49	
Dessalegne et al. (2016)	HT	CO_3^{2-}	F^-	G&T	0.3	
Israëli et al. (2000)	ZnAl	Cl^-	OH^-	G&T	1.8	
Israëli et al. (2000)	ZnAl	Cl^-	NO_3^-	G&T	-0.63	
This work	GR	Cl^-	SO_4^{2-}	R&K	0.3	$\beta = 2.4$; micro-Co-GR
This work	GR	Cl^-	SO_4^{2-}	R&K	0.2	$\beta = 5$; nano-Co-GR
This work	GR	Cl^-	CO_3^{2-}	G&T	Var.	$K_{ex,GT} = -0.9\ pH + 9.8$
This work	GR	SO_4^{2-}	CO_3^{2-}	G&T	Var.	$K_{ex,GT}$ dep. on pH

CHAPTER VI

CONCLUSION & PERSPECTIVES

VI.1 Summary

The objective of this work was to develop a thermodynamic model for anion uptake in green rust that is grounded on molecular-scale foundations.

Two green rust samples were studied: nano-Co-GR and micro-Co-GR. Micro-Co-GR was a micrometric and 3D-ordered green rust with the following structural formula:

$[Fe^{2+}_{0.42(8)}Fe^{3+}_{0.25(4)}Co^{2+}_{0.33(4)}(OH)_2][Cl^{-}_{0.25(4)} \cdot 0.43\ H_2O]$

Nano-Co-GR was a nanometric and turbostratic green rust with the following structural formula:

$[Fe^{2+}_{0.29(6)}Fe^{3+}_{0.20(3)}Co^{2+}_{0.51(5)}(OH)_2][Cl^{-}_{0.20(3)} \cdot 0.40\ H_2O]$

The layer structure of nano-Co-GR was similar to micro-Co-GR as shown with PDF analysis.

The exchange mechanism between chloride and sulphate ion was a simple anion exchange mechanism without dissolution-recrystallization or interstratification processes. However, the exchange between chloride and carbonate species was also an ion exchange but interstratification processes occurred during the exchange (interstratification type R = 1) and the different layer types were highly segregated.

The anion exchange capacity was 2.5 $mol_c \cdot kg^{-1}_{anhydrous\ GR}$ for micro-Co-GR and 1.6 $mol_c \cdot kg^{-1}_{anhydrous\ GR}$ for nano-Co-GR. Ion exchange models were able to model the experimental results, on the contrary to

pure phase assemblage models. The exchange equations were:

$$\begin{cases} 2\,\mathrm{G}r\mathrm{C}l + \mathrm{SO}_4^{2-} \overset{\mathrm{K}_{ex}^{\mathrm{Cl}^- - \mathrm{SO}_4^{2-}}}{=} \mathrm{G}r_2\mathrm{SO}_4 + 2\,\mathrm{C}l^- \\ 2\,\mathrm{G}r\mathrm{C}l + \mathrm{CO}_3^{2-} \overset{\mathrm{K}_{ex}^{\mathrm{Cl}^- - \mathrm{CO}_3^{2-}}}{=} \mathrm{G}r_2\mathrm{CO}_3 + 2\,\mathrm{C}l^- \\ \mathrm{G}r_2\mathrm{SO}_4 + \mathrm{CO}_3^{2-} \overset{\mathrm{K}_{ex}^{\mathrm{SO}_4^{2-} - \mathrm{CO}_3^{2-}}}{=} \mathrm{G}r_2\mathrm{CO}_3 + \mathrm{SO}_4^{2-} \end{cases} \quad \text{(VI.1)}$$

with Gr is the cationic exchange site. The thermodynamic convention that could describe the Cl^--SO_4^{2-} exchange was the Rothmund & Kornfeld convention. The parameters of these models depended on the crystal size or the stacking defects. Micro-Co-GR had a selectivity coefficient $log_{10}\,\mathrm{K}_{ex,\mathrm{RK}}^{\mathrm{Cl}^- - \mathrm{SO}_4^{2-}}$ value of 0.3 and a β value of 2.4. For nano-Co-GR, $log_{10}\,\mathrm{K}_{ex,\mathrm{RK}}^{\mathrm{Cl}^- - \mathrm{SO}_4^{2-}} = 0.2$ and $\beta = 5$. For the Cl^--CO_3^{2-} exchange, the Gaines & Thomas convention was followed however the selectivity coefficient were dependant on the pH: $log_{10}\,\mathrm{K}_{ex,\mathrm{GT}}^{Cl-\mathrm{CO}_3} = -0.90\,\mathrm{pH} + 9.79$ ($6 < p\mathrm{H} < 11$). Additionally, other reactions had to be added to model the experimental results depending on the pH. For a pH value between 6 and 8.5, green rust phases was partially dissolved and an other iron phase had to precipitate, magnetite most probably. At pH higher than 10, green rust phases buffered the pH value, most probably by deprotonation of its edge amphoteric groups and a competition between Cl^-, CO_3^{2-} and OH^- was necessary to model the experimental data. Finally, it was demonstrated that once green rust contained CO_3^{2-} in its interlayer space, neither sulphate nor chloride could be exchanged with it under the chemical conditions tested in this work (solutions with a maximum concentration at 50 $\mathrm{mol}\cdot\mathrm{L}^{-1}$ of monovalent anion, $6 < p\mathrm{H} < 11$).

Even if some discrepancies with clay were observed, ion exchange models developed initially for clay minerals could be applied for green rust and other LDH. This multiscale characterization can serve as a starting point for the building of robust and mechanistic geochemical models that will allow predicting the role of green rust on the geochemical cycle of ions, including nutrients, in gleysols or improve decontamination methods.

VI.2 Perspectives

VI.2.1 Complementary experiments and analyses

Complementary experiments would be necessary for the exchange between Cl^- and CO_3^{2-}. Experiments at a pH value between 6 and 8.5 would be required to determine which phase was precipitating. Magnetite was suspected with the *in situ* XRD experiments but complementary analysis such as the

Fe^{2+} measurement in solution could help to select which phase was precipitating between magnetite, ferrihydrite, siderite or hydroxy-green rust (or a mix of them). Additional experiments at pH higher than 10 would be required to understand better both processes of deprotonation of amphoteric groups and competition between Cl^-, CO_3^{2-} and OH^-. These complementary experiments would also help to verify the relationship demonstrated between $log_{10}\,K_{ex,GT}^{Cl-CO_3}$ and pH. Flow-through experiments would allow also to follow various parameters more precisely during the exchange (pH or ion concentrations) and verify the previous models (Marty et al., 2018).

About the exchange between SO_4^{2-} and CO_3^{2-}, only one batch experiment was performed for each exchange (first,$SO_4^{2-} \longrightarrow CO_3^{2-}$ and second, $CO_3^{2-} \longrightarrow SO_4^{2-}$). The first experiments allowed to calculate a selectivity coefficient. The second experiments, with the *in situ* XRD experiment, proved that CO_3^{2-} could not be exchanged once green rust contained carbonate species, sulphate ions could not take their place under the chemical conditions studied (maximum of 25 $mol \cdot L^{-1}$ of Na_2SO_4). The additional experiments would be an *in situ* XRD experiments and batch experiments. An exchange of micro-Co-GR(SO_4) phase with a solution containing carbonate species could be done followed by *in situ* XRD to determine the mechanism of the exchange. Batch experiments should be carried out with an exchange with a solution containing different concentrations of $NaHCO_3$ and Na_2SO_4 to define which phase was precipitating and increase the accuracy of $log_{10}\,K_{ex,RK}^{SO_4^{2-}-CO_3^{2-}}$ at various chemical conditions. Other experiments with a solution containing different concentrations of Na_2CO_3 and Na_2SO_4 would be to pursue the observation of the behaviour of micro-Co-GR phase at higher pH. A relationship between $log_{10}\,K_{ex,RK}^{SO_4^{2-}-CO_3^{2-}}$ and pH might exist. Finally, with all those points, it would be possible to determine if the Gaines & Thomas was the right convention to describe the SO_4^{2-}-CO_3^{2-} exchange compared to Rothmund & Kornfeld.

The content in Fe^{2+} and Fe^{3+} of solid phases was never measured directly during all the experiments performed in this work. Mössbauer analyses are conventionally used to measure the iron content in solid phases. However, it was proven by Hansen et al. (2001) during a Cl^--SO_4^{2-} exchange that the Fe^{2-}/Fe^{3-} remained constant. It could be interesting to verify this information for the experiments done in this work to confirm that no redox processes occurred.

VI.2.2 Comparison with other iron based LDH

Micro-Co-Gr and nano-Co-GR contained Co^{2+} in the layer chemical composition. It was hypothesized than it was not considered to be a problem because (i) the crystallographic structure of the synthesized solids was almost identical to that of fougerite (see Chapter IV on Material Characteriza-

tion), (ii) the layer charge was not influenced by the Fe^{2+} versus Co^{2+} substitution, and (iii) fougerite has never been observed as a pure Fe^{2+}/Fe^{3+} phase in natural environments because of isomorphic substitutions of Fe by foreign cations such as Mg, Ni, or Zn (Trolard et al., 2007; Zegeye et al., 2012; Johnson et al., 2014). However, this cobalt content was quite high (until 50 % of metal atom in the layer of nano-Co-GR) and could change, for instance, the selectivity coefficient of the exchange (such as crystal size or stacking defect did). Similar exchange experiments could be performed on a "true" green rust containing only Fe^{2-} and Fe^{3-} to compare with the result shown in this work. To continue on the comparison, it would be interesting to compare with an other iron based LDH such as FeMg-LDH for instance because fougerite contained magnesium where it was discovered, or any other close cations.

More generally, it would be interesting to test the methods and models developed in this work on other anions, nutrients or pollutants, which are adsorbed in the interlayer and not on the surface. Nitrogen anions interactions with green rust were already quite well studied and with the objective to understand denitrification processes. It was shown by Hansen and Koch (1998); Hansen et al. (2001) that green rust rapidly oxidised as NO_3^- enters the interlayer space. So precautions would be taken with the choice of the anion to avoid redox processes if the objective is to study the ion exchange property of green rust. Nonetheless, a clear view on the mechanisms of interactions with various anions and their quantification would be necessary to build a complete, robust and geochemical models that will allow predicting the role of green rust on the geochemical cycle of ions. With the models on the redox processes of various iron phases, this work would help to better comprehend the biogeochemical cycles in gleysols.

VI.2.3 Visualisation at the molecular scale

Several questions were raised on the interlayer structuration in green rusts or the interactions of anions with the layer (Rives, 2001; Perez et al., 2018). Preliminary work was performed with molecular dynamic (MD) simulations to answer these questions.

Two cases were studied: a simulation box that represented six layers of green rust (simulation "Layers"), and a simulation box were a particle of green rust was into a solution containing water and 50 $mmol \cdot L^{-1}$ of NaCl (simulation "Particle", Figure VI.1).

MD simulations of green rust layers were stable and gave some interesting results. Simulations "Layers", after equilibration time, gave lattice parameters with $a \approx b = 3.19$ Å, $c = 7.95$ Å, $\alpha \approx \beta = 90°$ and $\gamma = 120°$ (Figure VI.2) coherent with fougerite data (Trolard et al., 2007). Chloride anions remained close to the same position in space (Figure VI.3). In the **a**-**b** plane, they remained close to the same

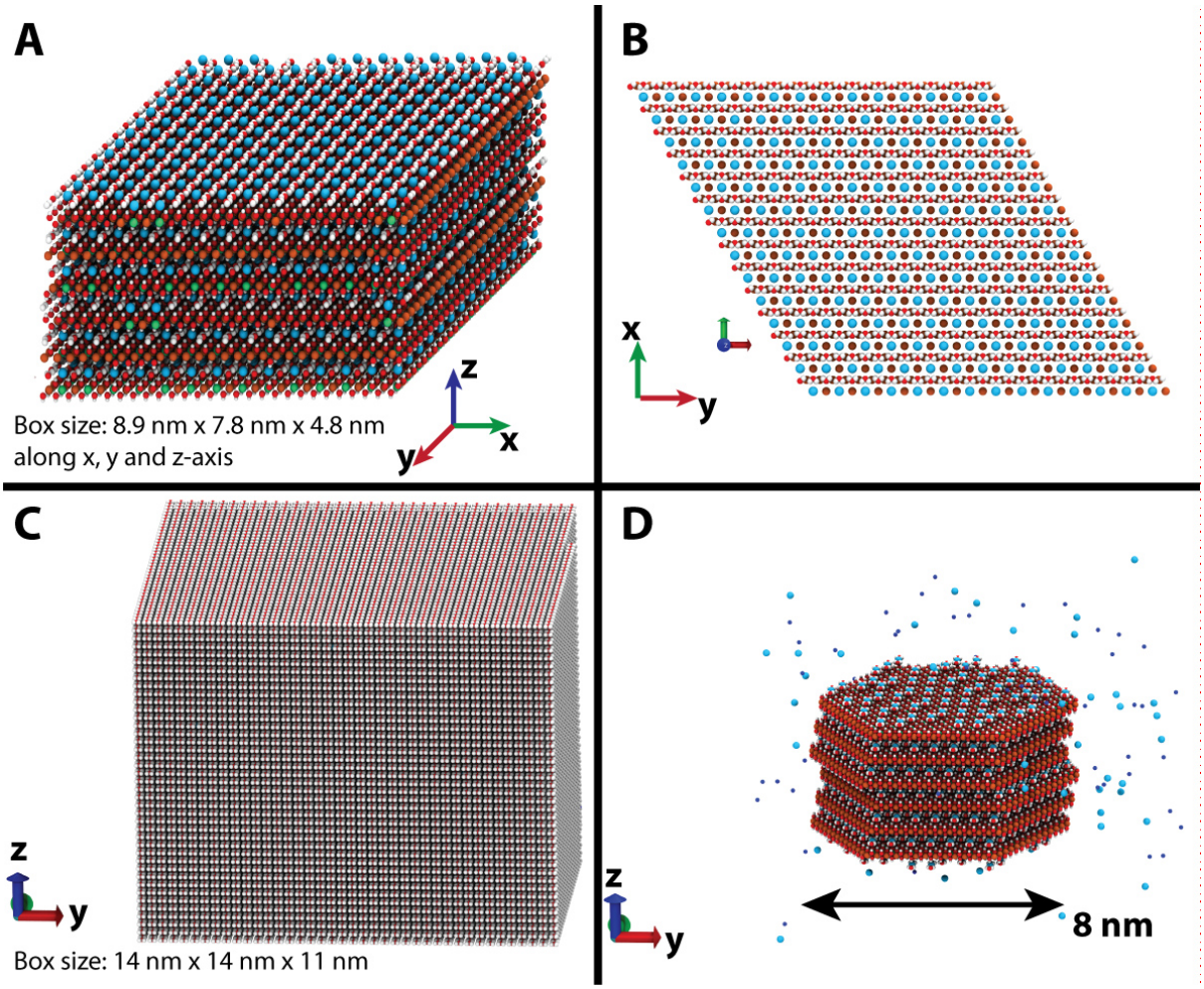

Figure VI.1 – Initial positions of the atoms for MD simulations for a green rust. (A) Simulation box containing 6 layers of green rust. (B) Initial layer structuration for the simulation shown in A. (C) Simulation box containing a green rust particle into a solution containing water and approximately 50 mmol·kg^{-1} of NaCl. (D) Same as C but the water molecules were removed. Color of the atoms: orange - Fe(II), green - Fe(III), red - O, white - H, light blue - Cl, dark blue - Na.

position during 200 *ps* distributed between the Fe^{3+} from the layer above and below (Figure VI.3A). Along **c**, water molecules and Cl^- remained in the same plane in the middle between two layers (Figure VI.3B). Further treatments of this data will allow to calculate the XRD pattern of this structure to compare to the data obtained during this work, and the radial distribution function to observe the hydration of anions for example. Similar simulations with interlayer CO_3^{2-} are also tested.

Simulations "Particle" are also working but the data are currently analyzed. These simulations would help to witness the interactions between water and ions into solution with various part of green rust particle (basal surfaces, edges, or interlayer space).

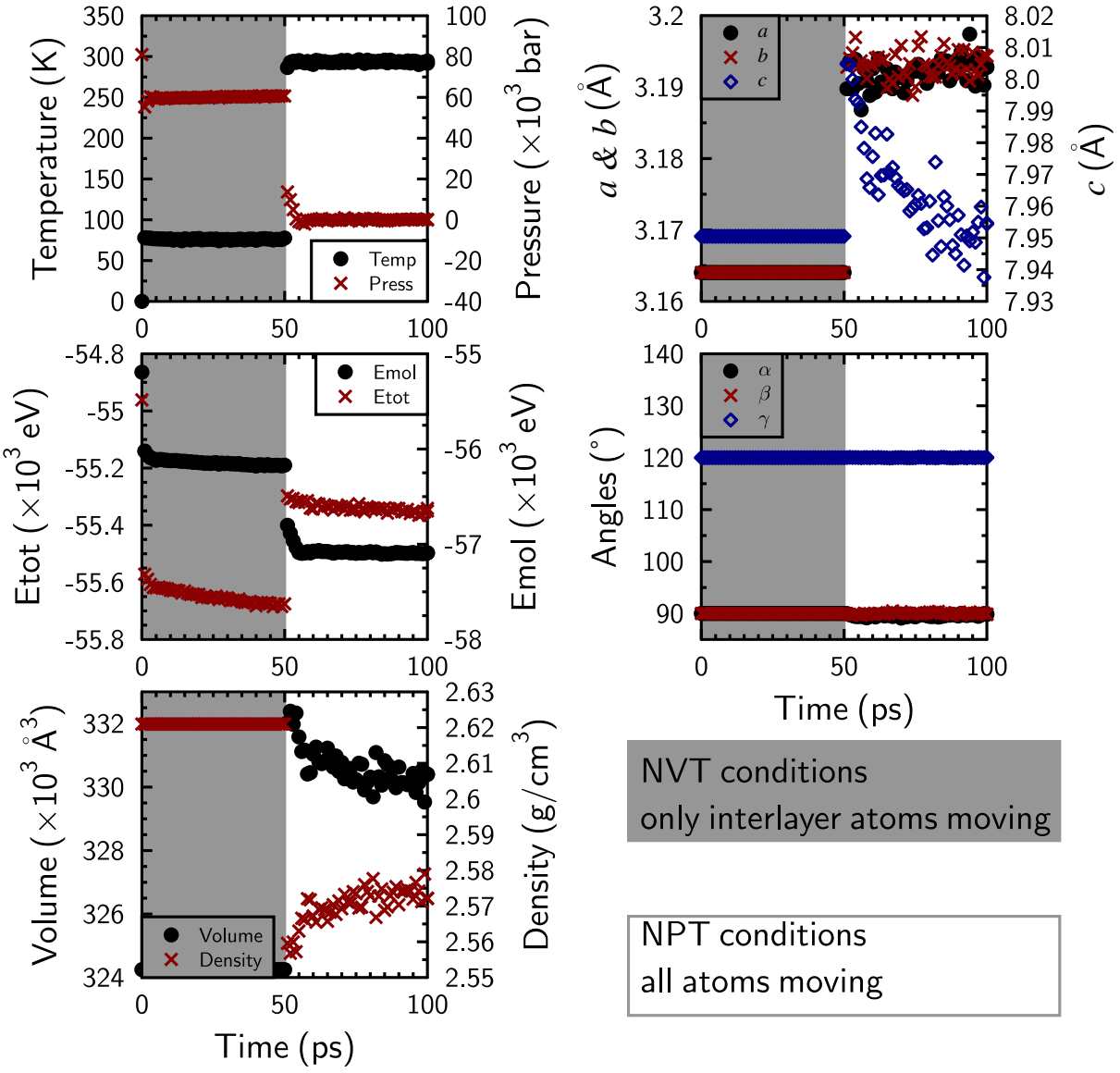

Figure VI.2 – Various parameters measured during a simulation "layers" (Etot - total energy of the system, Emol - molecular energy, NVT conditions - number of atoms, volume and temperature were fixed for equilibration, NPT conditions - number of atoms, pressure and temperature were fixed.

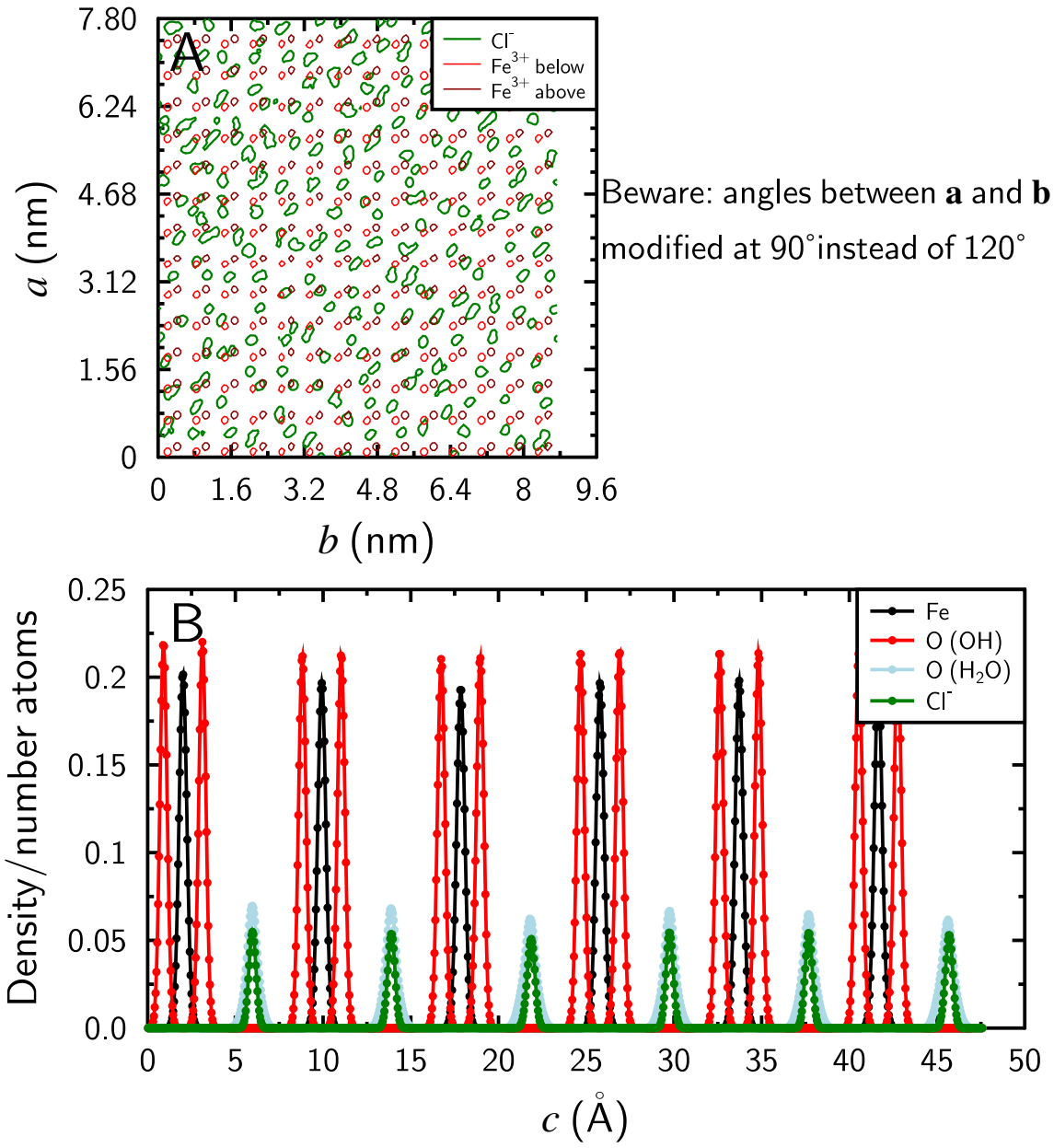

Figure VI.3 – Density profile for simulation "Layers" during 200 ps. (A) Density profile of Cl^- and Fe^{3+} from the layer above and below the Cl^- in the **a**-**b** plane. (B) Density profile of the various atoms along **c**.

CHAPTER VII

RÉSUMÉ ÉTENDU EN FRANÇAIS

VII.1 Introduction

Les rouilles vertes sont des hydroxides double lamellaires (HDL) qui contiennent du Fe^{2+} et Fe^{3+}. Elles ont été identifiées dans des environnements artificiels (corrosion de canalisations métalliques) mais aussi dans des environnements naturels (Stampfl, 1969; Trolard and Bourrié, 2008; Vodyanitskii and Shoba, 2015; Usman et al., 2018; Bhave and Shejwalkar, 2018). La forme naturelle des rouilles vertes a été nommée fougérite (numéro d'identification de l'association internationale de minéralogie : IMA2003-057). Ce minéral est présent dans les sols hydromorphiques tels que les gleysols (Figure VII.1A), ou les sols situés proches des cours d'eau (Trolard et al., 1996; Abdelmoula et al., 1998; Trolard et al., 2007; Trolard and Bourrié, 2008; Christiansen et al., 2009).

La structure des HDL est composée d'empilement de feuillets de type brucitique (Figure VII.1B), c'est-à-dire de feuillets composés d'octaèdres $M_{Oct}O_6$ (M_{Oct} = Al, Mg, Fe, ...) séparés par des espaces interfoliaires. La structure lamellaire des rouilles vertes est responsable d'un rapport surface sur volume élevé (surface spécifique de 492 $m^2 \cdot g^{-1}$). Ces feuillets sont chargés positivement en raison de substitutions isomorphiques de cations divalents par des cations trivalents (par exemple, Fe^{2+} avec Fe^{3+}). Cette charge positive est contre-balancée par des anions hydratés présents dans l'espace interfoliaire. La composition anionique de l'interfoliaire peut changer en fonction des anions disponibles dans la solution environnante. Ces propriétés sont responsables d'une spécificité de réactivité des rouilles vertes : l'échange anionique. Les surfaces de la rouille verte portent une forte capacité d'échange ($2-4$ $mol_c \cdot kg^{-1}$ pour les HDL, Taviot-Guého et al. (2018)). Cette capacité d'échange est étudiée dans le but d'adsorber voire de réduire des polluants organiques ou inorganiques (par example, nitrate -

FIGURE VII.1 – (A) Profil d'un gleysol à Fougères, France. (B) Structure d'une rouille verte ou fougérite (fichier cif de structure d'après Trolard et al. (2007), occupation des atomes interfolaires non représentative).

Grabb et al. (2017) ; selenium - Holmes and Gu (2016) ; chromium - Zhao et al. (2021) ; cuivre, argent, or et mercure - O'Loughlin et al. (2003b) ; uranium - Sihn and In-Ho (2020) ; neptunium - Christiansen et al. (2011b) ; composés organiques - Han et al. (2020)).

L'objectif de ce travail était de développer un modèle thermodynamique pour l'adsorption d'anions dans la rouille verte qui soit compatible avec les informations de mécanismes réactionnels caractérisés jusqu'à l'échelle moléculaire, et ceci afin de mieux comprendre les différents cycles géochimiques dans les environnement de type gleysols (Sparks, 2001). Divers paramètres, tels que le type d'anion, la taille des particule ou les fautes d'empilement qui pourraient en effet influencer les processus d'échanges,ont été testés.

VII.2 Matériels & Méthodes

Les rouilles vertes contiennent du Fe^{2+} ce qui les rend sensibles à l'oxydation. De plus, elles ont une forte affinité pour les espèces carbonatées. La présence de $CO_{2(g)}$ doit donc être éviter pour empêcher sa dissolution en solution et sa transformation en ion carbonate. Par conséquent, toutes les synthèses et expériences en laboratoire ont été faites dans une boîte à gants sous atmosphère de N_2 (MBraun UNIlab Pro). Toutes les autres expériences ou analyses ont été réalisées en minimisant au maximum le contact avec l'oxygène.

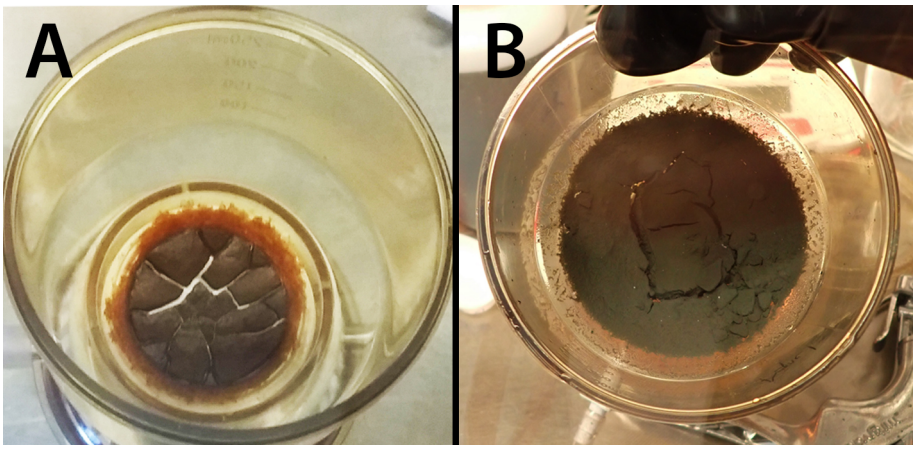

FIGURE VII.2 – Échantillons synthétisés de rouille verte : poudres humides de nano-Co-GR (A) et micro-Co-GR (B).

VII.2.1 Études des échantillons

Synthèse

La méthode de synthèse de Hadi et al. (2014) a été choisie car elle permet de contrôler finement la taille des particules et les fautes d'empilement. L'inconvénient de cette méthode est la substitution partielle du Fe^{2+} par Co^{2+} au sein des feuillets. Cependant, cette propriété n'a pas été considérée comme un problème car (i) la structure cristalline des solides synthétisés est quasi-identique à celle de la fougérite (Figure VII.3), (ii) la charge du feuillet n'est pas influencée par la substitution du Fe^{2+} par Co^{2+}, et (iii) la fougérite n'a jamais été observée comme une phase pure de Fe^{2+}/Fe^{3+} dans des environnements naturels du fait de la substitution isomorphique du fer par d'autres cations comme le magnésium, le nickel ou le zinc (Trolard et al., 2007; Zegeye et al., 2012; Johnson et al., 2014).

Deux solides ont été retenus et étudiés dans ce travail (Figure VII.2) :

— Micro-Co-GR - une rouille verte micrométrique et ordonnée 3D,

— Nano-Co-GR - une rouille verte nanométrique et turbostratique [1].

L'anion interfoliaire est l'ion chlorure dans micro-Co-GR(Cl) et nano-Co-GR(Cl).

Compositions chimiques

La formule structurale des échantillons Co-Gr était $[Fe_{1\text{-}x\text{-}y}{}^{2+}Fe_x{}^{3+}Co_y{}^{2+}(OH)_2]^{+x} \cdot [\frac{x}{n}A^{-n} \cdot mH_2O]^{-x}$, avec A^{-n} un anion de charge n, x et y la stœchiométrie de Fe^{3+} et Co^{2+} respectivement ($\frac{1}{4} \leq x \leq \frac{1}{3}$).

1. Le turbostratisme est défini par l'occurrence systématique entre les couches successives de translations aléatoires parallèles aux couches et/ou de rotations autour de la direction normale aux couches.

Les valeurs de x and y ont été calculées à partir de mesures par microsonde électronique (Cameca SX Five electron). La quantité totale de Fe a été confirmée par la méthode 1,10-phenanthroline modifiée (Amonette and Templeton, 1998; Stucki, 1980; Stucki and Anderson, 1980; Hadi et al., 2013). La teneur en eau (m) a été déterminée par analyses thermogravimétriques et calorimétriques différentielles à balayage (Setaram TGA 92-16.18).

Structures et morphologies

La structure des phases présentes dans le solide a été caractérisée par diffraction des rayons X (DRX) et microscope à transmission (MET).

Les diffractogrammes ont été mesurés soit sur la ligne CRISTAL au synchrotron Soleil ($\lambda = 0.4367$ Å) ou la ligne MSPD au synchrotron Alba ($\lambda = 0.8258$ or 0.8266 Å) dans des capillaires en polyimide. Des affinements de Rietveld ont été réalisé sur certains diffractogrammes avec l'utilisation du logiciel Fullprof (Rodriguez-Carvajal, 1990). Les données de diffusion des rayons X de haute énergie des échantillons séchés collectés au synchrotron Soleil ont permises de calculer la fonction de distribution de paires atomiques. Ces calculs permettent notamment de connaître les distances interatomiques dans une structure cristalline. Ces calculs ont été effectués avec les logiciels FUSION et PDFgetX3 (Ounsy et al., 2013; Juhás et al., 2013). Enfin, des modèles des diffractogrammes ont été obtenus grâce au logiciel MLM2C pour les réflexions $00l$ (Plançon, 1981). Ce logiciel permet notamment d'observer l'influence des phénomènes d'interstratification sur un diffractogramme. [2]

La morphologie des cristaux a été observée grâce à un microscope à transmission (MET) Philips CM20.

VII.2.2 Expériences d'échanges anioniques

Méchanismes des échanges anioniques - DRX in situ

Les évolutions de structure des rouilles vertes ont pu être suivies pendant des réactions d'échange avec des ions chlorures, sulfates ou carbonates au cours de deux sessions synchrotron à Alba, Barcelone ($\lambda = 0.8258$ Å et $\lambda = 0.8266$ Å). Au sein d'un réacteur, une solution passe à travers un capillaire polyimide contenant la poudre de rouille verte grâce à une pompe péristaltique (protocole établi par Grangeon et al. (2017b), flux de la pompe - $1-2$ mL$\cdot$h^{-1}). Les diffractogramme sont mesurés à travers ce capillaire et ils suivent en temps réel l'évolution de la structure. Lesséquences de diffractogrammes obtenus

2. L'interstratification correspond à des cristaux constitués de fragments bidimensionnels ayant des structures et des compositions différentes (Drits and Tchoubar, 1990).

sont pré-traités grâce à des programmes informatiques développés pour cette thèse via Python. Ces programmes détectent les différents pics et mesurent sur des pics spécifiques leurs positions, leurs intensités, leurs aires, leur assymétrie, ainsi que leurs largueurs à mi-hauteur pour pouvoir calculer la taille des cristallites par l'équation de Scherrer (Scherrer, 1918).

Quantification des échanges anioniques - Expériences en batch

Des expériences d'échanges ioniques ont été réalisées pour déterminer tout d'abord la stoichiométrie de l'échange et la capacité d'échange anionique, puis dans une seconde série d'expériences, pour quantifier les échanges à l'aide de paramètres thermodynamiques. Ces expériences ont eu lieu en batch avec ajouts successifs d'une solution contenant uniquement du chlorure, sulfate, cabonate ou bicarbonate de sodium ; ou bien un mélange entre chlorure de sodium et un des autres solutés mentionnés. L'affinité des espèces carbonatées pour les HDL est connue pour être importante (Miyata, 1983). Des expériences en batch ont également été effectuées pour tester la réversibilité d'un échange entre des ions chlorures ou sulfates avec des espèces carbonatées, c'est-à-dire observer s'il était possible de remplacer les espèces carbonatées par un autre anion dans l'espace interfoliaire.

VII.3 Résultats & Discussion

VII.3.1 Caractérisation des échantillons étudiés

L'observation qualitative des diffractogrammes comparés à celui de la fougérite montre que micro-Co-GR(Cl) peut être considéré comme un analogue synthétique de la fougérite (Figure VII.3 ; Trolard et al. (2007)). L'indexation des pics de micro-Co-GR(Cl) (réflexions *hkl*) suivent le modèle présenté par Trolard et al. (2007) à l'exception de plusieurs pics associés à une impureté de magnétite (taux de magnétite 14 % d'après un affinement de Rietveld, Wechsler et al. (1984)).

Les seuls réflexions symétriques observables dans le diffractogramme de nano-Co-GR(Cl) sont à q = 0.80 et 1.59 Å et elles correspondent aux réflexions *00l* de micro-Co-GR(Cl) (Figure VII.3). Toutes les autres réflections sont larges et généralement asymétriques. Leurs intensités étaient faibles comparées aux intensités des pics présents dans micro-Co-GR(Cl). L'élargissement des pics a été attribuée à la taille nanométriques des cristallites, ce qui a été confirmé par les images MET des cristaux. L'asymétrie des pics est diagnostique d'un désordre turbostratique. Le diffractogramme de structures turbostratiques contient uniquement les réflexions 00l et des bandes hk non résolues (Warren, 1941).

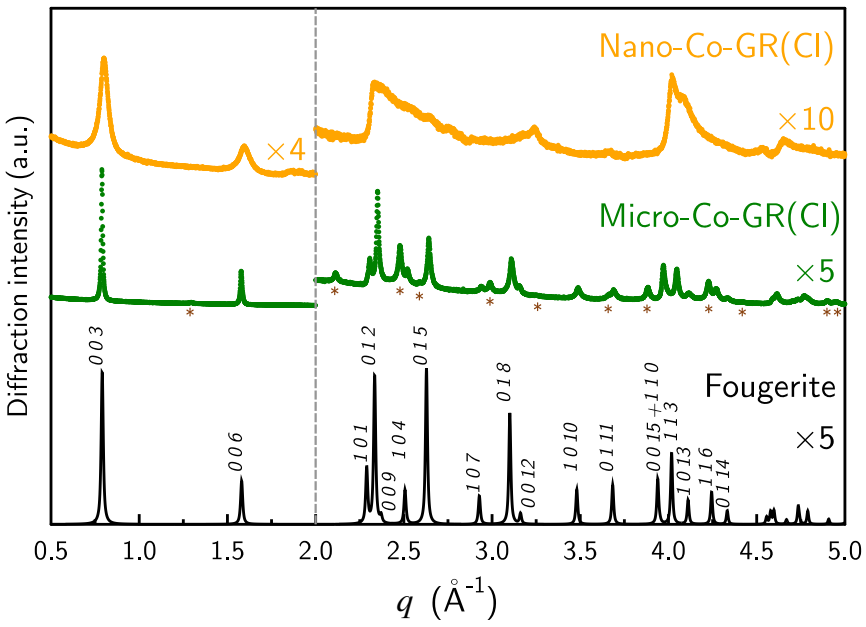

FIGURE VII.3 – Diffractogrammes de nano-Co-GR(Cl) (orange) et micro-Co-GR(Cl) (vert) comparés au diffractogramme publié de la fougérite de Trolard et al. (2007) (noir). Les intensités ont été multipliées par 4 entre 0.5 and 2 $Å^{-1}$ et par 10 pour q plus grand que 2 $Å^{-1}$ pour nano-Co-GR. Les intensités ont été multipliées par 5 pour q plus grand que 2 $Å^{-1}$ pour micro-Co-GR et la fougérite. $*$ montre les réflexions attribuables à la magnétite. Les diffractogrammes de nano-Co-GR(Cl) et micro-Co-GR(Cl) ont été mesurés au synchrotron Alba avec $\lambda = 0.82575$ Å.

L'ensemble des résultats des caractérisations effectuées sur les deux échantillons synthétisés, nano-Co-GR(Cl) et micro-Co-GR(Cl) est résumé dans le tableau VII.1.

VII.3.2 Détermination du mécanisme d'échange

Le mécanisme d'échange peut être :

— un échange anionique simple, c'est-à-dire un remplacement d'un anion par un autre dans l'espace interfoliaire sans altération de la structure du feuillet. Cela peut se passer de manière homogène ou via des processus d'interstratification (cristaux construits par empilement de deux fragments bidimensionnel qui ont des structures et compositions distinctes),

— une dissolution complète d'une première phase lamellaire, et une recristallisation d'une seconde phase lamellaire avec un autre anion interfolaire, cette deuxième phase étant plus stable thermodynamiquement.

Le mécanisme d'échange peut donc être déterminé en suivant les changements structuraux, par exemple par mesures DRX *in situ*.

Trois expériences ont été réalisées sur l'échantillon micro-Co-GR :

TABLE VII.1 – Résumé de toutes les caractéristiques déterminées pour les échantillons nano-Co-GR(Cl) et micro-Co-GR(Cl) (MM_{anh} - masse molaire anhydre, Dist. F-à-F - distance feuillet à feuillet).

Type	Donnée	Micro-Co-GR(Cl)	Nano-Co-GR(Cl)
Chimie	Feuillet	$[Fe_{0.42(8)}^{2+}Fe_{0.25(4)}^{3+}Co_{0.33(4)}^{2+}(OH)_2]$	$[Fe_{0.29(6)}^{2+}Fe_{0.20(3)}^{3+}Co_{0.51(5)}^{2+}(OH)_2]$
	Interfoliaire	$[Cl_{0.25(4)}^{-} \cdot 0.43H_2O]$	$[Cl_{0.20(3)}^{-} \cdot 0.40H_2O]$
	MM_{anh} ($g \cdot mol^{-1}$)	99.74	98.53
Structure	Ordre	Ordoné 3D	Turbostratique
	a (Å)	3.164	≈ 3.12
	b (Å)	3.164	≈ 3.12
	c (Å)	23.852	23.852
	α (°)	90	90
	β (°)	90	90
	γ (°)	120	120
	Dist. F-à-F (Å)	7.95	7.95
Morphologie	Taille des cristaux	0.1 – 1 µm	Nanométrique

— Expérience "Na_2SO_4−XRD" - une solution contenant 5 $mmol \cdot L^{-1}$ de Na_2SO_4 et 40 $mmol \cdot L^{-1}$ de NaCl à pH ≈ 9 a circulé à travers un échantion a micro-Co-GR. Une fois l'échange avec les ions sulfate terminé, une solution contenant seulement du NaCl à 50 $mmol \cdot L^{-1}$ a circulé à travers le réacteur.

— Expérience "$NaHCO_3$−XRD" - une solution contenant 40 $mmol \cdot L^{-1}$ de $NaHCO_3$ et 10 $mmol \cdot L^{-1}$ of NaCl à pH ≈ 8.5 est passée à travers l'échantillon micro-Co-GR. Une fois l'échange terminé, une solution contenant seulement NaCl à 50 $mmol \cdot L^{-1}$ a circulé à travers le réacteur.

— Expérience "Na_2CO_3−XRD" - une solution contenant 10 $mmol \cdot L^{-1}$ de Na_2CO_3 et 40 $mmol \cdot L^{-1}$ de NaCl à pH ≈ 10.9 a circulé à travers l'échantillon micro-Co-GR.

La première étape de l'expérience "Na_2SO_4−XRD" a également été réalisée sur l'échantillon nano-Co-GR(Cl) (circulation d'une solution avec 5 $mmol \cdot L^{-1}$ de Na_2SO_4 et 40 $mmol \cdot L^{-1}$ de NaCl).

Le but de ces expériences était de déterminer le mécanisme d'échange mais aussi de comprendre l'influence de différents paramètres tels que le type d'anion, la taille des cristallites ou des fautes d'empilements sur ces mécanismes d'échanges. Enfin, la réversibilité des échanges a également était testé.

Échange Cl^- - SO_4^{2-} - Expérience "Na_2SO_4−XRD"

Pour la phase micro-Co-GR, l'intensité des réflexions à $q = 0.79$ $Å^{-1}$ ($d = 7.99$ Å) diminuait régulièrement au cours du temps. Une autre réflexion apparassait et augmentait en intensité à 0.57 $Å^{-1}$

(d = 11.02 Å; Figure VII.4 A-1 and B-1). Tous les autres pics à plus haute valeur de q ont également varié en intensité sauf le pic d'indice $hk0$ (par exemple, réflexion 110 à $q = 3.97$ Å^{-1}). Le paramètre c a donc augmenté pendant l'expérience, sans modifier les paramètres a et b.

Pour la phase nano-Co-GR, seulement les réflexions $00l$ ont évolué et de manière similaire aux réflexions $00l$ de micro-Co-GR. Les bandes hk n'ont pas changé de position donc c a augmenté et a et b sont restés constants.

Cette augmentation de c est cohérente avec un replacement de Cl^- par SO_4^{2-} dans l'espace interfoliaire pour les deux échantillons. Les réflexions $00l$ des phases nano- et micro-Co-GR(Cl) et des phases nano- et micro-Co-GR(SO_4) sont restées symétriques et n'ont pas montré de changements de largeur significatifs pendant l'expérience. La taille moyenne des cristallites le long du **c** est restée constante tout au long des expériences (Figure VII.4D). Chaque réflexion des indices hkl avec $l \neq 0$ a changé de la position correspondant à la présence de Cl^- dans l'espace interfoliaire à la position du à la présence de SO_4^{2-} dans l'espace interfolliair,e sans déplacement progressif et sans apparition d'un pic à une position intermédiaire (Figure VII.4C).

Ces observations ont montré qu'un simple mécanisme d'échange d'anions se produisait sans processus de dissolution-recristallisation, et qu'un phénomène d'interstratification était également peu probable (Drits and Tchoubar, 1990). Un processus de mélange physique est plus approprié pour décrire ces échanges. Aussi, ces expériences ont montré que le même mécanisme s'applique pour une rouille verte turbostratique nanométrique, et une rouille verte micrométrique, ordonnée en 3D.

Une expérience d'échange entre SO_4^{2-} et Cl^- a également été menée. Il a été montré que la structure de la rouille verte ne revenait pas à celle de micro-Co-GR(Cl) avant l'échange avec SO^{2-}. Un échange a bien eu lieu, visible par l'apparition d'un pic $00l$ à $q = 0.84$ Å^{-1} , mais la nature de l'anion interfoliaire correspondant à ce pic n'a pas pu être identifié. Une précipitation de magnétite a également été observée lors de cet échange, en lien probable avec une dissolution de la rouille verte.

Échange Cl^- - Espèces carbonatées - Expériences "$NaHCO_3$−XRD" et "Na_2CO_3−XRD"

Des similitudes entre les expériences "$NaHCO_3$-XRD" et "Na_2CO_3-XRD" étaient présentes. Au cours de l'échanges, l'intensité de la réflexion à $q = 0,79$ Å^{-1} (d = 7.94 Å) a diminué régulièrement, tandis qu'une reflexion est apparue et a augmenté en intensité à $q = 0.82 - 0,83$ Å^{-1} ($d \approx 7,60$ Å; Figure VII.5 par example). Les pics $00l$ changeaient légérement de position autour de leur position initiale ou finale après échange (Figure VII.5 par example). Ces réflexions $00l$ étaient asymétriques

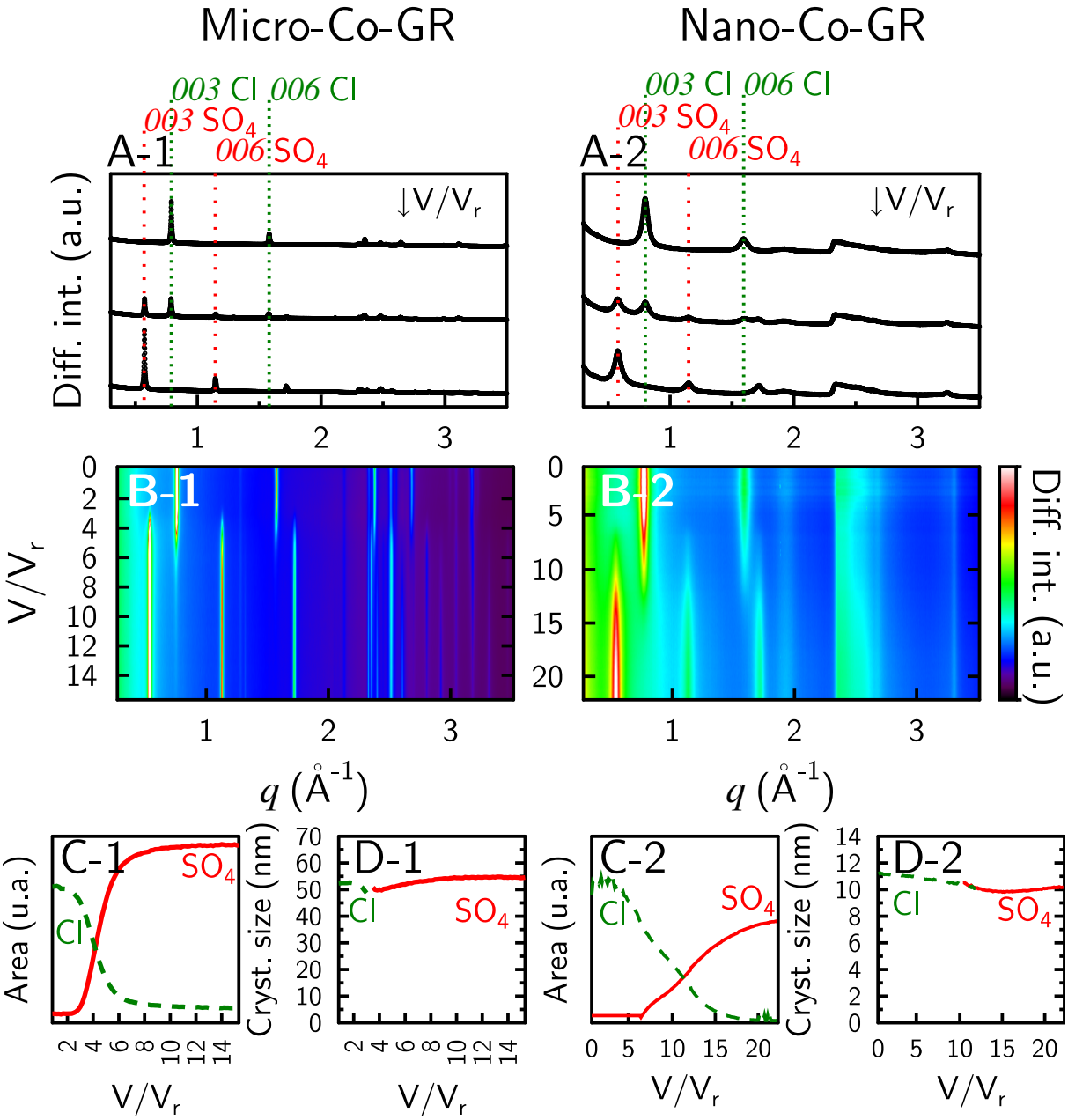

FIGURE VII.4 – Diffractogrammes enregistrés *in situ* pendant l'expérience "Na_2SO_4-XRD" avec l'échantillon micro-Co-GR(Cl) (gauche-1) et nano-Co-GR(Cl) (droite-2). (A-1) Diffractogrammes enregistrés à 2, 4, et 14 volumes poraux (V/V_r, Diff. int. - intensité diffractée). (A-2) Diffractogrammes enregistrés à 0, 10, and 20 V/V_r. (B) Carte 2D des diffractogrammes en fonction du temps exprimé en V/V_r. (C) Évolution des aires des réflexions 003 à 0.78 $Å^{-1}$ (Cl^- interfoliaire, ligne verte pointillée) et 0.57 $Å^{-1}$ (SO_4^{2-} interfoliaire, ligne rouge) en fonction des V/V_r. (D) Estimation des tailles des cristallites en fonction des V/V_r calculée à partir des largeurs à mi-hauteur des réflexions 003 (0.78 $Å^{-1}$ Cl^- interfoliaire, ligne verte pointillée et 0.57 $Å^{-1}$ - SO_4^{2-} interfoliaire, ligne rouge). Note : le même formalisme d'indexation de pic a été utilisé pour la phase nano-Co-GR phase malgré l'absence de structure ordonnée 3D.

(Figure VII.5 par example). La réflexion à $0.82 - 0,83$ Å^{-1} était cohérente avec un remplacement de Cl^- par des espèces carbonatées dans l'espace interfoliaire. Des processus d'interstratification se sont produits pendant l'échange entre les espèces Cl^- et les espèces carbonatées. Le type d'interstratification était R = 1. Les différents types de couches étaient fortement ségrégées (Figure VII.5 par example). Les variations de positions des réflexions de $00l$ pour chaque type de couche ont été montrées tout au long des expériences. Enfin, les proportions de magnétite augmentaient dans les deux expériences mais en particulier dans l'expérience "$NaHCO_3$-XRD".

Les différences entre les expériences "$NaHCO_3$-XRD" et "Na_2CO_3-XRD" étaient également nombreuses. Premièrement, pour les modèles d'interstratification, deux types de couches pouvaient modéliser le résultat de l'expérience "$NaHCO_3$-XRD", un type de couche avec Cl^- comme anion intercouche et un type de couche avec des espèces carbonatées (Figure VII.5). Un type de couche supplémentaire était nécessaire pour modéliser le résultat de l'expérience "Na_2CO_3-XRD". Ce troisième type de couche contenait probablement des espèces carbonatées, mais avec une valeur de d_{003} légèrement plus faible que celle de l'autre type de couche avec des espèces carbonatées (7,5 Å par rapport à 7,7 Å). Cela pourrait s'expliquer par de petites différences dans la composition chimique, comme la teneur en eau par exemple. Deuxièmement, le type de couche carbonatée de l'expérience "$NaHCO_3$-XRD" contenait cinq molécules d'eau par espèce de carbonate mais le type de couche carbonatée le plus abondant de l'expérience "Na_2CO_3-XRD" ne contenait que deux molécules d'eau par espèce de carbonate (la teneur en eau n'a pas pu être déterminée pour le deuxième type de couche carbonatée). Enfin, à la fin de l'expérience "Na_2CO_3-XRD", Cl^- a été complètement échangé par les espèces carbonatées (durée de cette expérience : 18 V/V_r) . Ce n'était pas le cas pour l'expérience "$NaHCO_3$-XRD" pour laquelle Cl^- était toujours présent (environ 7 %) à la fin de l'expérience (durée : 24 V/V_r). L'affinité de la phase micro-Co-GR pour les espèces carbonatées peut donc varier en fonction des conditions chimiques.Ces variations des conditions chimiques expliquent probablement les autres différences observées entre les deux expériences, comme les proportions différentes de magnétite précipitée.

Lors de l'expérience "$NaHCO_3$-XRD", il a été démontré qu'il n'était pas possible de revenir à la structure initiale de la phase micro-Co-GR(Cl) après une expérience d'échange inverse avec une solution d'entrée de 50 mmol$\cdot$L^{-1} de NaCl (durée 300 V/V_r). La magnétite était également précipitée, probablement en raison de la dissolution de la phase micro-Co-GR. Les réflexions $00l$ correspondant à $d_{003} = 7,59$ Å ont diminué d'intensité pendant toute l'expérience mais deux autres réflexions ont augmenté à proximité avec $d_{003} = 7,45$ Å et $d_{003} = 7,41$ Å. Ces distances étaient proches de la valeur d_{003} du troisième type de couche affiché dans l'expérience "Na_2CO_3-XRD". Une hypothèse serait

qu'il y a eu des variations dans le contenu de la couche intermédiaire en raison des modifications de la couche suite aux processus de dissolution (les variations du contenu en Fe(III) impliquent des variations de la charge de la couche et donc, des variations du contenu de la couche intermédiaire).

Échange espèces carbonatées - SO_4^{2-}

Après un échange entre Cl^- et des espèces carbonatées sur un échantillon de micro-Co-GR similaire à l'expérience "$NaHCO_3$-XRD", une solution contenant 50 $mmol \cdot L^{-1}$ de Na_2SO_4 a été passée dans l'échantillon.

Aucune réflexion de la phase micro-Co-GR(SO_4) ou de toute autre phase lamellaire autre que la micro-Co-Gr(C(IV)) n'a été détectée, et donc aucun échange n'a eu lieu entre les espèces carbonatées et SO_4^{2-}. Cela pourrait être dû soit à une affinité des espaces interfoliaires beaucoup plus élevée pour les espèces carbonatées que pour les anions sulfate, soit à une irréversibilité de l'échange entre les espèces carbonatées et SO_4^{2-}, dans les conditions chimiques et les échelles de temps explorées dans cette étude. Une dissolution importante de la rouille verte carbonatée a été observée par la diminution des intensités de ses réflexions, accompagnée par l'augmentation d'un grand maximum de diffraction, centré à $\tilde{q} = 1,9$ Å^{-1} ($d = 3,30$ Å). Ce résultat suggère qu'une phase amorphe ou très peu cristalline était présente au début de l'expérience, et que son contenu augmentait avec le temps.

VII.3.3 Analyse quantitative des échanges anioniques dans les rouilles vertes

Capacité d'échanges anioniques (CEA) & Stœchiométries

Des séries d'expériences ont permis de déterminer la CEA de chaque phase étudiées et la stœchiométrie de chaque échange. La CEA de micro-Co-GR était de 2.5 ± 0.2 $mol_c \cdot kg^{-1}_{\text{anhydrous GR}}$ et de 1.6 ± 0.2 $mol_c \cdot kg^{-1}_{\text{anhydrous GR}}$ pour nano-Co-GR. La stœchiométrie était de 2 :1 pour les échanges entre Cl^- et les espèces sulfatées et carbonatées. Donc Cl a été échangé par SO_4^{2-} et CO_3^{2-}. SO_4^{2-} a été échangé par CO_3^{2-} car la stœchiométrie de la réaction était de 1 :1.

Échange Cl^- - SO_4^{2-}

Diverses expériences d'échanges ont permis de modéliser les résultats grâce à la convention de Rothmund & Kornfeld qui permet de changer la valeur du coefficient de sélectivité en fonction des conditions chimiques (example dans la figure VII.6A, Sposito (1981b); Bond (1995)). En effet, un

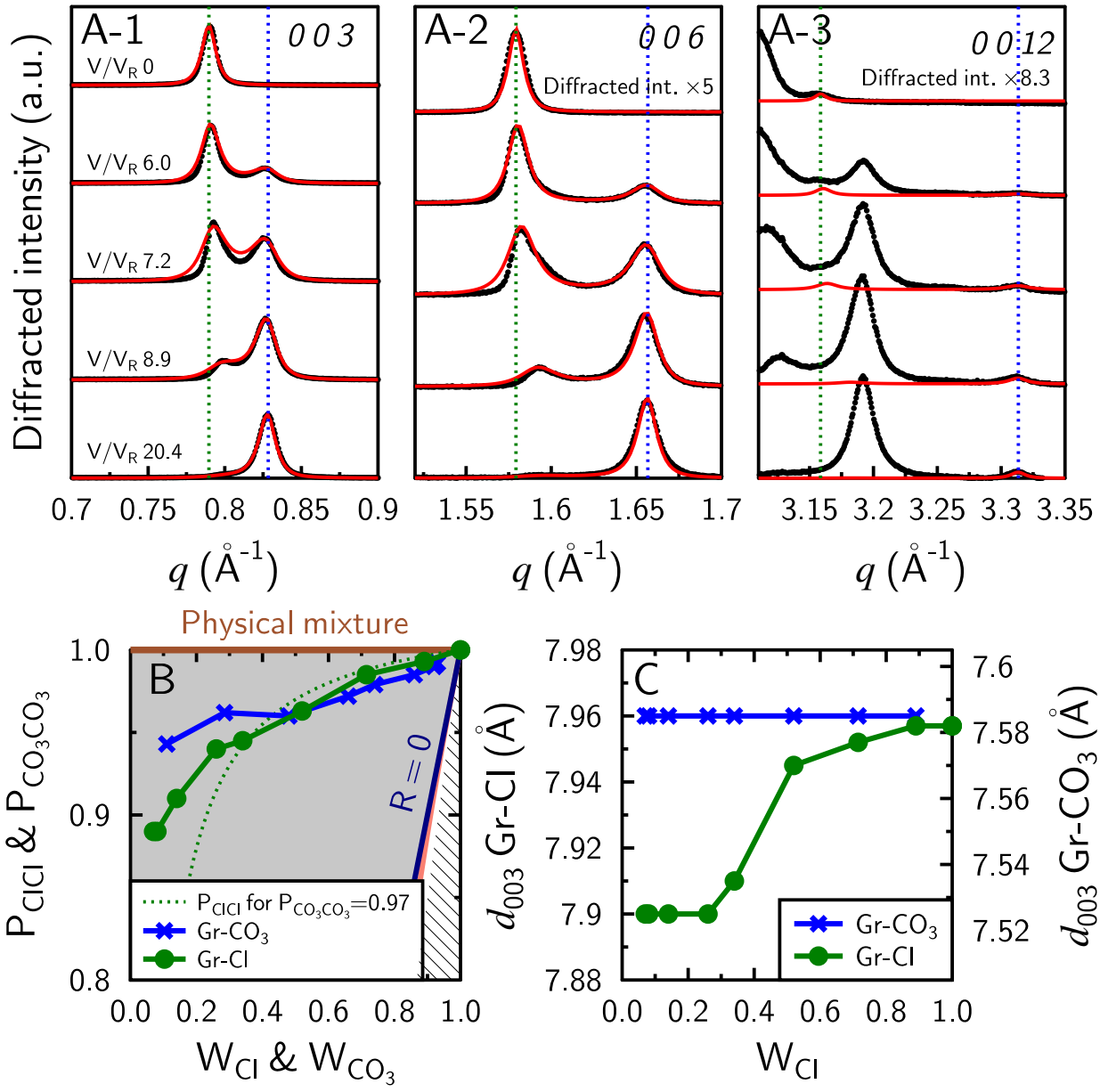

FIGURE VII.5 – Processus d'interstratification sur micro-Co-GR(Cl) pendant l'expérience "$NaHCO_3$-XRD" (concentration de la solution injectée : 40 mmol·L^{-1} de $NaHCO_3$ et 10 mmol·L^{-1} de NaCl). (A) Diffractogrammes à différents V/V_r (Ligne rouge - modèle, points noirs - données, V/V_R - volumes poraux, A_1-zoom sur la réflexion 003 , A_2 - zoom sur la réflexion et A_3 - zoom sur la réflexion 0012). (B) Évolution des probabilités en fonction de l'abondance du type d'anion dans l'interfoliaire (W_{Cl}-Abondance du feuillet Gr-Cl, W_{CO_3}-Abondance du feuillet Gr-CO_3, P_{ClCl} - Probabilité que deux feuillets Gr-Cl se suivent, $P_{CO_3CO_3}$ - Probabilité que deux feuillets Gr-CO_3 se suivent, ligne marron - résultats pour des échantillons suivant un processus de mélange physique, ligne bleu marine - résultats pour des échantillons avec un type d'interstratification R = 0 et ligne saumon - résultats pour des échantillons avec un type d'interstratification R = 1 – MPDO, ligne verte pointillée - P_{ClCl} en fonction de W_{Cl} si $P_{CO_3CO_3}$ était constant et égal à 0.97). (C) Évolution de la distance interfoliaire des types de feuillets Gr-Cl et Gr-CO_3. Pour les graphiques B and C, la couleur verte fait référence au type de feuillet Gr-Cl et la couleur bleue au type de feuillet Gr-CO_3. Cinq diffractogrammes sont représentés en A mais dix ont été modélisés (résultats dans les graphiques B and C). Tous les diffractogrammes (données & modèles) sont disponibles en annexes.

ajustement acceptable des données a été obtenu avec une valeur $log_{10}\,K_{ex,RK}^{Cl^- - SO_4^{2-}}$ de 0,3 et une valeur β de 2.4 pour micro-Co-GR et avec une valeur $log_{10}\,K_{ex,RK}^{Cl-SO_4}$ de 0,2 et une valeur β de 5 pour nano-Co-GR.

Échange Cl^- - CO_3^{2-}

Trois expériences ont été réalisées pour étudier l'échange entre Cl^- et CO_3^{2-} sur les rouilles vertes avec des solutions de composition :

— Expérience "$NaHCO_3$" - 10 mmol·L^{-1} $NaHCO_3$ et 40 mmol·L^{-1} de NaCl,

— Expérience "Na_2CO_3-I" - 10 mmol·L^{-1} Na_2CO_3 et 30 mmol·L^{-1} de NaCl,

— Expérience "Na_2CO_3-II" - 5 mmol·L^{-1} Na_2CO_3 et 40 mmol·L^{-1} de NaCl puis 10 mmol·L^{-1} Na_2CO_3 (4 étapes) et 30 mmol·L^{-1} de NaCl (3 étapes).

Leurs résultat et la modélisation de ces résultats ont permis de montrer l'influence importante du pH sur les paramètres thermodynamiques de l'échange et les processus en jeu (Figure VII.6B et C, et Figure VII.7).

La convention de Thomas de Gaines & a été utilisée dans les différents modèles.Pour un pH entre 6 et 8,5, une dissolution partielle de la phase micro-Co-GR a été nécessaire pour modéliser ce système, avec la précipitation d'une autre phase de fer, très probablement de la magnétite (exemple dans la figure VII.6B). Les données DRX ont montré une augmentation de la proportion de magnétite dans la phase solide au fur et à mesure des réactions d'échange, en accord avec cette hypothèse. Pour des valeurs de pH supérieures à 10, $log_{10}\,K_{ex,GT}^{Cl-CO_3}$ étaient inférieurs (entre 0,3 et 0) à $log_{10}\,K_{ex,GT}^{Cl-CO_3}$ pour un pH entre 6 et 8,5 (Figure VII.6D). Le meilleur modèle pour l'expérience "Na_2CO_3-II" comprenait un échange entre Cl^-, CO_3^{2-} et aussi OH^-, associé à la protonation/déprotonation des groupements amphotères de bordure de la phase micro-Co-GR(Cl). L'expérience "Na_2CO_3-I", dans laquelle le pH était toujours supérieur à 10, a été modélisée avec un échange entre Cl^- et CO_3^{2-} uniquement, et il n'a pas été nécessaire de tamponner le pH avec un mécanisme spécifique. Les valeurs de $log_{10}\,K_{ex,GT}^{Cl-CO_3}$ obtenues avec l'expérience "Na_2CO_3-I" étaient égales à celles obtenues dans l'expérience "Na_2CO_3-II" pour les mêmes conditions de pH (étapes 5 à 7 de l'expérience "Na_2CO_3-II"). Un résumé des différentes expériences est disponible dans la figure VII.7 et présente les différentes hypothèses et modèles mis en œuvre pour expliquer le résultat de chacune de ces expériences. Afin de trouver un lien entre toutes ces expériences, un graphique représentant $log_{10}\,K_{ex,GT}^{Cl-CO_3}$ en fonction du pH a été réalisé (Figure VII.6D). Une relation linéaire empirique a été montrée entre $log_{10}\,K_{ex,GT}^{Cl-CO_3}$ et le pH, avec $log_{10}\,K_{ex,GT}^{Cl-CO_3} = -0.90\,pH + 9,79$ et $r^2 = 0,996$ (Figure VII.6D).

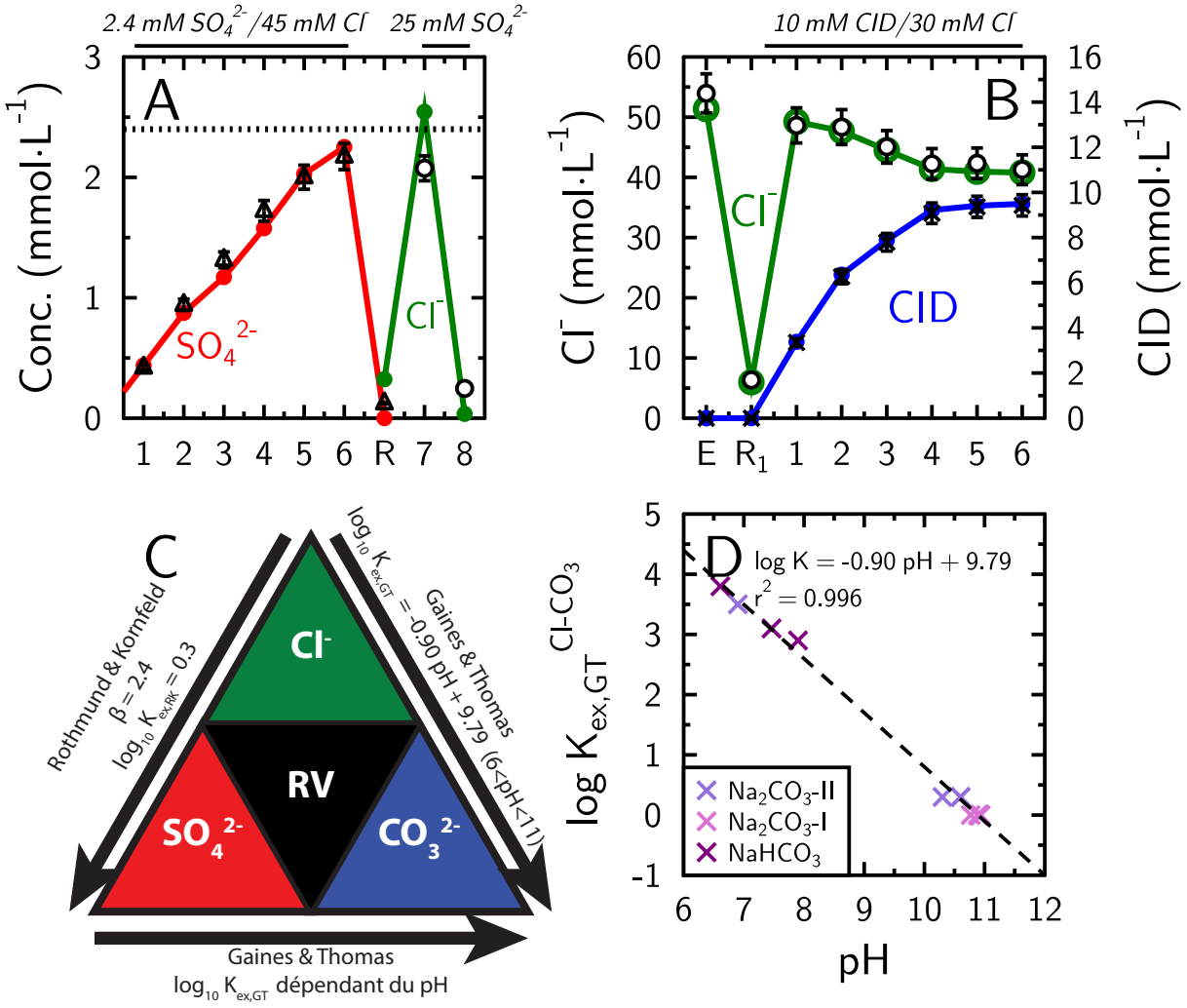

FIGURE VII.6 – Résultats et modèles de diverses expériences d'échanges. (A) Résultats et modèle avec la convention de Rothmund & Kornfeld d'une des expériences d'échange entre Cl^- et SO_4^{2-} (Solution 2.4 mmol·L^{-1} Na_2SO_4 et 45 mmol·L^{-1} de NaCl, marqueur - concentrations mesurées, ligne - résultat du modèle). (B) Résultats et modèle avec la convention de Gaines & Thomas d'une des expériences d'échange entre Cl^- et CO_3^{2-} (Solution 10 mmol·L^{-1} $NaHCO_3$ et 40 mmol·L^{-1} de NaCl, marqueur - concentrations mesurées, ligne - résultat du modèle, CID - carbone inorganique dissous). (C) Résumé des paramètres d'échanges dans le diagramme ternaires $Cl^-/SO_4^{2-}/CO_3^{2-}$ pour les rouilles vertes. (D) Coefficient de sélectivité en fonction du pH pour les expériences d'échanges entre Cl^- et CO_3^{2-} (Solutions d'échange des expériences : $NaHCO_3$ - 10 mmol·L^{-1} $NaHCO_3$ et 40 mmol·L^{-1} de NaCl, Na_2CO_3-I - 10 mmol·L^{-1} Na_2CO_3 et 30 mmol·L^{-1} de NaCl, Na_2CO_3-II - 5 mmol·L^{-1} Na_2CO_3 et 40 mmol·L^{-1} de NaCl puis 10 mmol·L^{-1} Na_2CO_3 et 30 mmol·L^{-1} de NaCl).

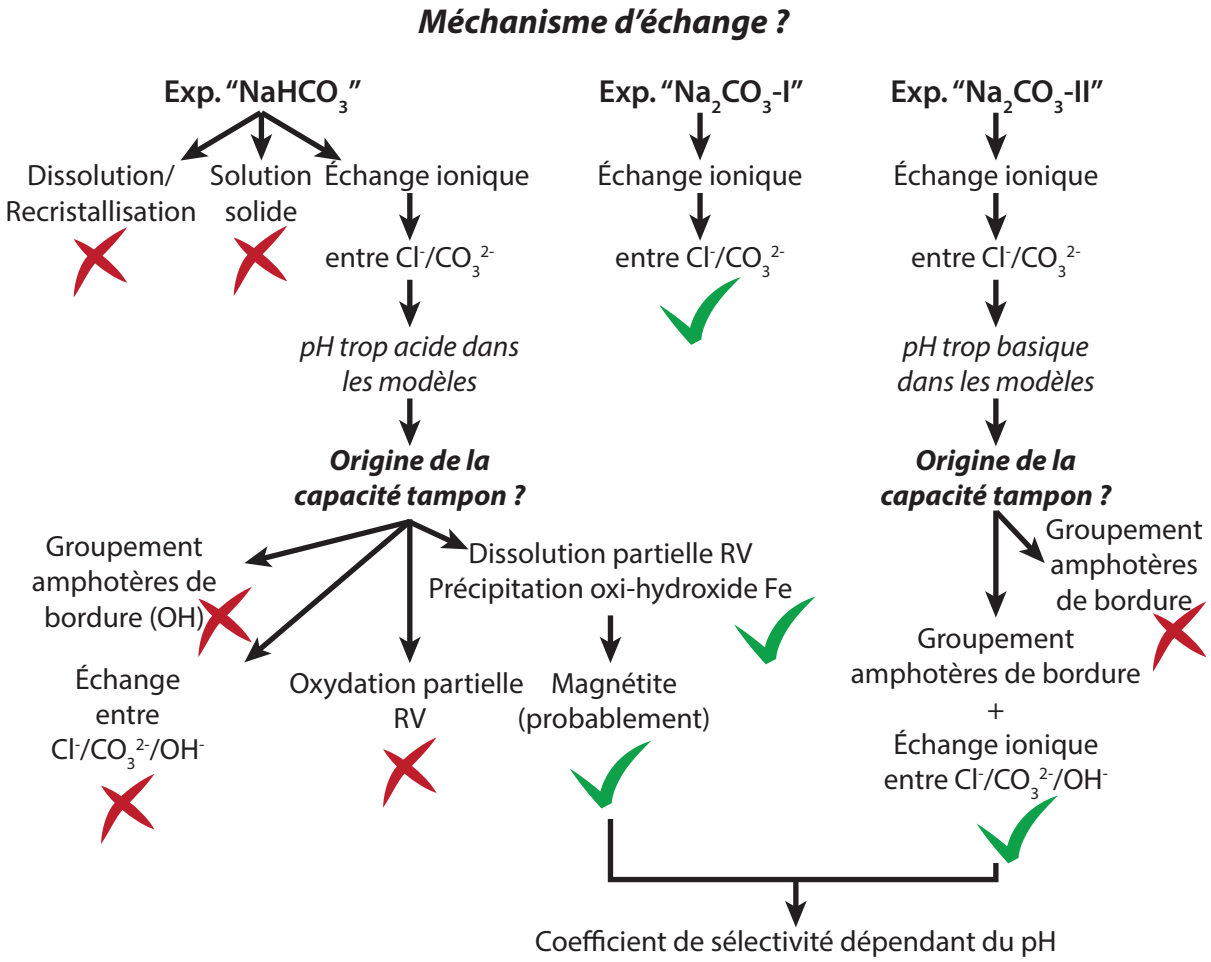

FIGURE VII.7 – Résumé des résultats et des modèles pour l'échange $Cl^- \longrightarrow CO_3^{2-}$ pour toutes les expériences (Exp. - Expérience, RV - phase micro-Co-GR, marque x rouge - les résultats du modèle n'étaient pas en accord avec les données mesurées, coche verte - les résultats du modèle étaient en accord avec les données mesurées).

Échange SO_4^{2-} - CO_3^{2-}

L'échange entre SO_4^{2-} and CO_3^{2-} a été étudié dans les deux sens avec deux expériences.

La première expérience utilisait une solution de 10 mmol $\cdot$ L^{-1} de $NaHCO_3$ et 20 mmol $\cdot$ L^{-1} de Na_2SO_4 sur un échantillon micro-Co-GR contenant des ions sulfates dans l'espace interfoliaire. Tout comme les expériences avec l'échange entre Cl^- et CO_3^{2-}, une dissolution partielle de l'échantillon a été nécessaire pour modéliser les données, accompagné d'une précipitation d'oxy-hydroxyde de fer (probablement de la magnétite d'après les expériences de DRX *in situ*). Le $log_{10}\ K_{ex,\mathrm{GT}}^{SO_4-CO_3}$ varié de 2.5 à 1.8 en fonction du pH.

La seconde expérience utilisait une solution d'échange à 10 mmol$\cdot$ L^{-1} de $NaHCO_3$ et 20 mmol$\cdot$ L^{-1} de Na_2SO_4 et une échantillon micro-Co-GR avec des ions carbonatées dans l'espace interfoliaire. Dans ces conditions chimiques et pendant la durée de l'expérience, aucun échange ne s'est produit avec SO_4^{2-} une fois que CO_3^{2-} était présent dans l'espace interfoliaire, en accord avec les résultats de l'étude DRX *in situ*. Cet échange présente une apparente irréversibilité.

VII.4 Conclusion & Perspectives

Les échanges entre les ions chlorures, sulfates et carbonates ont été étudiés. Le mécanisme d'échange était le remplacement des ions dans l'interfoliaires sans dissolution-reprecipitation. Des structures interstratifiées ont pu être observées pendant l'échange entre les ions chlorures et carbonates. Des tailles de cristallites différent et la présence ou non de fautes d'empilement n'ont pas modifié le mécanisme d'échange. Des modèles thermodynamiques ont pu être développées pour ses échanges grâce à des séries d'expériences d'échange. Les échanges Cl^--CO_3^{2-} et SO_4^{2-}-CO_3^{2-} peuvent être modélisés grâce à la convention de Gaines & Thomas alors que les échanges Cl^--SO_4^{2-} ont été modélisés en suivant la convention de Rothmund & Kornfeld. Les paramètres de ses modèles dépendaient donc du type d'anion échangé, mais aussi du pH, de la taille des cristallites ou bien des fautes d'empillement dans la structure. Une fois que la rouille verte contenait des ions carbonatées dans l'interfoliaire, il n'a pas été possible des les échanger par d'autres anions dû à une apparente irréversibilité des échanges.

Des expériences complémentaires pourraient permettre de préciser les modèles notamment dans le cadre de l'échange Cl^--CO_3^{2-} ou SO_4^{2-}-CO_3^{2-} car certaines résultats doivent être validés (coefficients de selectivité à des pH plus variés, taux de dissolution des rouilles vertes et type de phase

précipités, etc.). Des études avec des échanges avec d'autres anions pourraient permettre d'avoir une meilleure idée globale des processus d'échanges anioniques dans les rouilles vertes. Enfin, des modèles en dynamique moléculaire de la strucutre des rouilles vertes et de ses interactions avec les anions pourraient permettre de mieux comprendre les interactions entre cette phase et les anions en solution.

BIBLIOGRAPHY

Abdelmoula, M., Trolard, F., Bourrié, G., and Génin, J. M. R. (1998). Evidence for the Fe(II)-Fe(III) Green Rust "Fougerite" mineral occurence in hydromorphic soil and its transformation with depth. *Hyperfine Interactions*, 112(1-4):235–238.

Agnel, M. I., Grangeon, S., Fauth, F., Elkaïm, E., Claret, F., Roulet, M., Warmont, F., and Tournassat, C. (2020). Mechanistic and thermodynamic insights into anion exchange by green rust. *Environmental Science and Technology*, 54(2):851–861.

Ahmed, I. A. M., Shaw, S., and Benning, L. G. (2008). Formation of hydroxysulphate and hydroxycarbonate green rusts in the presence of zinc using time-resolved in situ small and wide angle X-ray scattering . *Mineralogical Magazine*, 72(1):159–162.

Ai, J., Ma, H., Tobler, D. J., Mangayayam, M. C., Lu, C., Van Den Berg, F. W. J., Yin, W., and Hansen, H. C. B. (2020). Bone char mediated dechlorination of trichloroethylene by green rust. *Environmental Science and Technology*, 54(6):3643–3652.

Ai, J., Yin, W., and Hansen, H. C. (2019). Fast dechlorination of chlorinated ethylenes by green rust in the presence of bone char. *Environmental Science and Technology Letters*, 6(3):191–196.

Aimoz, L., Kulik, D. A., Wieland, E., Curti, E., Lothenbach, B., and Mäder, U. (2012). Thermodynamics of AFm-(I_2, SO_4) solid solution and of its end-members in aqueous media. *Applied Geochemistry*, 27(10):2117–2129.

Aissa, R., Francois, M., Ruby, C., Fauth, F., Medjahdi, G., Abdelmoula, M., and Génin, J. M. R. (2006). Formation and crystallographical structure of hydroxysulphate and hydroxycarbonate green rusts synthetised by coprecipitation. *Journal of Physics and Chemistry of Solids*, 67(5-6):1016–1019.

Alidokht, L., Oustan, S., Khataee, A., Neyshabouri, M. R., and Reyhanitabar, A. (2016). Enhanced removal of chromate by graphene-based sulfate and chloride green rust nanocomposites. *Journal of the Taiwan Institute of Chemical Engineers*, 68:266–274.

Allmann, R. (1968). The crystal structure of pyroaurite. *Acta Crystallographica Section B*, 24(7):972–977.

Amonette, J. E. and Templeton, J. C. (1998). Improvments to the quantitative assay of nonrefractory minerals for Fe(II) and total Fe using 1,10-phenanthroline. *Clays and Clay Minerals*, 46(1):51–62.

Ay, A. N., Zümreoglu-Karan, B., and Temel, A. (2007). Boron removal by hydrotalcite-like, carbonate-free Mg-Al-NO_3-LDH and a rationale on the mechanism. *Microporous and Mesoporous Materials*, 98(1-3):1–5.

Ayala-Luis, K. B., Koch, C. B., and Hansen, H. C. B. (2010). Intercalation of linear C9-C16 carboxylates in layered FeII-FeIII-hydroxides (green rust) via ion exchange. *Applied Clay Science*, 48(3):334–341.

Barer, R. M. and Brummer, K. (1963). Relations between partial ion exchange and interlamellar sorption in alkylammonium montmorillonites. *Transactions of the Faraday Society*, 59:959–968.

Barthélémy, K., Naille, S., Despas, C., Ruby, C., and Mallet, M. (2012). Carbonated ferric green rust as a new material for efficient phosphate removal. *Journal of Colloid and Interface Science*, 384(1):121–127.

Bearcock, J. M., Perkins, W. T., Dinelli, E., and Wade, S. C. (2006). Fe(II)/Fe(III) 'green rust' developed within ochreous coal mine drainage sediment in South Wales, UK. *Mineralogical Magazine*, 70(6):731–741.

Benson, L. V. (1982). A tabulation and evaluation of ion exchange data on smectites. *Environmental Geology*, 4(1):23–29.

Bernal, J. D., Dasgupta, D. R., and Mackay, A. L. (1959). The oxides and hydroxides of iron and their structural inter-relationships. *Clay Minerals Bulletin*, 4(21):15–30.

Bethke, C. M., Vergo, N., and Altaner, S. P. (1986). Pathways of smectite illitization. *Clays & Clay Minerals*, 34(2):125–135.

Bhave, C. and Shejwalkar, S. (2018). A review on the synthesis and applications of green rust for environmental pollutant remediation. *International Journal of Environmental Science and Technology*, 15(6):1243–1248.

Blanc, P., Lassin, A., Piantone, P., Azaroual, M., Jacquemet, N., Fabbri, A., and Gaucher, E. C. (2012). Thermoddem: A geochemical database focused on low temperature water/rock interactions and waste materials. *Applied Geochemistry*, 27(10):2107–2116.

Blume, H.-P., Brümmer, G. W., Fleige, H., Horn, R., Kandeler, E., Kögel-Knaber, I., Kretzschmar, R., Stahr, K., and Wilke, B.-M. (2010). *Scheffer/Schachtschabel soil science*. Springer, Berlin, Heidelberg.

Bond, W. J. (1995). On the Rothmund-Kornfeld description of cation exchange. *Soil Science Society of America Journal*, 59(2):436–443.

Bourrié, G., Nacib, J. B., Ona-Nguema, G., and Trolard, F. (2019). Absence of solid solution between Fe(II) and Mg(II) hydroxides and consequences on formation of fougerite and smectites. *E3S Web of Conferences*, 98:04003.

Bourrié, G., Trolard, F., Génin, J. M. R., Jaffrezic, A., Maître, V., Abdelmoula, M., Maître, V., and Abdelmoula, M. (1999). Iron control by equilibria between hydroxy-green rusts and solutions in hydromorphic soils. *Geochimica et Cosmochimica Acta*, 63(19-20):3417–3427.

Bourrié, G., Trolard, F., Refait, P., and Feder, F. (2004). A solid-solution model for Fe(II)-Fe(III)-Mg(II) green rusts and fougerite and estimation of their gibbs free energies of formation. *Clays and Clay Minerals*, 52(3):382–394.

Caraballo, M. A., Michel, F. M., and Hochella, M. F. (2015). The rapid expansion of environmental mineralogy in unconventional ways: Beyond the accepted definition of a mineral, the latest technology, and using nature as our guide. *American Mineralogist*, 100(1):14–25.

Chivot, J. (2004). *Thermodynamique des produits de corrosion*. ANDRA.

Christiansen, B. C., Balic-Zunic, T., Dideriksen, K., and Stipp, S. L. S. (2009). Identification of green rust in groundwater. *Environmental Science and Technology*, 43:3436–3441.

Christiansen, B. C., Dideriksen, K., Skovbjerg, L. L., Nedel, S., and Stipp, S. L. S. (2011a). Letter to the editor: On fougerite. *Clays and Clay Minerals*, 59(1):3–9.

Christiansen, B. C., Geckeis, H., Marquardt, C. M., Bauer, A., Römer, J., Wiss, T., Schild, D., and Stipp, S. L. S. (2011b). Neptunyl (NpO_2^+) interaction with green rust, $GR_{Na,SO4}$. *Geochimica et Cosmochimica Acta*, 75(5):1216–1226.

Claret, F. (2001). *Caractérisation structurale des transitions minéralogiques dans les formations argileuses : Contrôles et implications géochimiques des processus d ' illitisation.* PhD thesis, Université Joseph-Fourier - Grenoble I.

Claret, F., Bauer, A., Schäfer, T., Griffault, L., and Lanson, B. (2002). Experimental investigation of the interaction of clays with high-pH solutions: A case study from the Callovo-Oxfordian formation, Meuse-Haute Marne underground laboratory (France). *Clays and Clay Minerals*, 50(5):633–646.

Costantino, U., Marmottini, F., Nocchetti, M., and Vivani, R. (1998). New synthetic routes to hydrotalcite-like compounds - Characterisation and properties of the obtained materials. *European Journal of Inorganic Chemistry*, 1998(10):1439–1446.

Cuttler, A. H., Man, V., Cranshaw, T. E., and Longworth, G. (1990). A Mössbauer study of green rust precipitates: I. Preparations from sulphate solutions. *Clay Minerals*, 25(3):289–301.

Danzer, K. (2007). *Analytical chemistry: Theoretical and metrological fundamentals.* Springer Science & Business Media.

Davesne, E., Dideriksen, K., Christiansen, B. C., Sonne, M., Ayala-Luis, K. B., Koch, C. B., Hansen, H. C. B., and Stipp, S. L. S. (2010). Free energy of formation for green rust sodium sulphate ($NaFe^{II}_6Fe^{III}_3(OH)_{18}(SO_4)_{2(s)}$). *Geochimica et Cosmochimica Acta*, 74(22):6451–6467.

Deiss, E. and Schikorr, G. (1928). Über Das Ferrohydroxyd (Eisen-2-hydroxyd). *Zeitschrift für anorganische und allgemeine Chemie*, 172(1):32–42.

Dessalegne, M., Zewge, F., Pfenninger, N., Johnson, A. C., and Diaz, I. (2016). Layered double hydroxide and its calcined product for fluoride removal from groundwater of Ethiopian Rift Valley. *Water, Air, & Soil Pollution*, 227:381.

Di Bitetto, A., Kervern, G., André, E., Durand, P., and Carteret, C. (2017). Carbonate-hydrogenocarbonate coexistence and dynamics in layered double hydroxides. *The Journal of Physical Chemistry C*.

Drissi, H., Refait, P., and Génin, J. M. R. (1994). The oxidation of $Fe(OH)_2$ in the presence of carbonate ions: Structure of carbonate green rust one. *Hyperfine Interactions*, 90(1):395–400.

Drissi, S. H., Refait, P., Abdelmoula, M., and Génin, J. M. R. (1995). The preparation and thermodynamix properties if Fe(II)-Fe(III) Hydroxyde-carbonate (green rust 1): Pourbaix diagram of iron in carbonate-containing aqueous media. *Pergamon Corrosion Science*, 37(12):2025–2041.

Drits, V. A., Lanson, B., and Gaillot, A.-C. (2007). Birnessite polytype systematics and identification by powder X-ray diffraction. *American Mineralogist*, 92(5-6):771–788.

Drits, V. A., Sokolova, T. N., Sokolova, G. V., and Cherkashin, V. I. (1987). New member of the hydrotalcite-manasseite group. *Clays and Clay Minerals*, 35(6):401–417.

Drits, V. A. and Tchoubar, C. (1990). *X-Ray diffraction by disordered lamellar structures.* Springer-Verlag.

Duval, S., Baymann, F., Schoepp-Cothenet, B., Trolard, F., Bourrié, G., Grauby, O., Branscomb, E., Russell, M. J., and Nitschke, W. (2019). Fougerite: the not so simple progenitor of the first cells. *Interface Focus*, 2019(9).

Ebner, A. D., Reynolds, S. P., and Ritter, J. A. (2007). Nonequilibrium kinetic model that describes the reversible adsorption and desorption behavior of CO_2 in a K-promoted hydrotalcite-like compound. *Industrial & Engineering Chemistry Research*, 46(6):1737–1744.

Egami, T. and Billinge, S. J. L. (2012a). Chapter 3 - The method of total scattering and atomic pair distribution function analysis. In *Underneath the Bragg peaks : structural analysis of complex materials*, volume 16, pages 55–99. Pergamon.

Egami, T. and Billinge, S. J. L. (2012b). *Underneath the Bragg peaks: Structural analysis of complex materials 2nd Edition*, volume 16. Pergamon.

Erbs, M., Hansen, H. C. B., and Olsen, C. E. (1999). Reductive dechlorination of carbon tetrachloride using iron(II) iron(III) hydroxide sulfate (green rust). *Environmental Science and Technology*, 33(2):307–311.

Etique, M. (2014). *Effets de l'activité bactérienne réductrice du fer ferrique et des nitrates sur les transformations des produits de corrosion magnétite et sidérite de l'acier non allié.* PhD thesis, Université de Lorraine.

Etique, M., Jorand, F. P. A., and Ruby, C. (2016). Magnetite as a precursor for green rust through the hydrogenotrophic activity of the iron-reducing bacteria Shewanella putrefaciens. *Geobiology*, 14(3):237–254.

Etique, M., Jorand, F. P. A., Zegeye, A., Grégoire, B., Despas, C., and Ruby, C. (2014a). Abiotic process for Fe(II) oxidation and green rust mineralization driven by a heterotrophic nitrate reducing bacteria (Klebsiella mobilis). *Environmental Science and Technology*, 48:3742–3751.

Etique, M., Zegeye, A., Grégoire, B., Carteret, C., and Ruby, C. (2014b). Nitrate reduction by mixed iron(II-III) hydroxycarbonate green rust in the presence of phosphate anions: The key parameters influencing the ammonium selectivity. *Water Research*, 62:29–39.

Etter, M. and Dinnebier, R. E. (2014). A century of powder diffraction: A brief history. *Zeitschrift fur Anorganische und Allgemeine Chemie*, 640(15):3015–3028.

Everaert, M., Dox, K., Steele, J. A., De Vos, D., and Smolders, E. (2019). Solid-state speciation of interlayer anions in layered double hydroxides. *Journal of Colloid and Interface Science*, 537:151–162.

FAO (1971). FAO-UNESCO soil map of the world. Technical report, Unesco, Paris.

Farrow, C. L., Juhas, P., Liu, J. W., Bryndin, D., Božin, E. S., Bloch, J., Proffen, T., and Billinge, S. J. L. (2007). PDFfit2 and PDFgui: computer programs for studying nanostructure in crystals. *Journal of Physics: Condensed Matter*, 19:335219–335226.

Feder, F., Trolard, F., Klingelhöfer, G., and Bourrié, G. (2005). In situ Mössbauer spectroscopy: Evidence for green rust (fougerite) in a gleysol and its mineralogical transformations with time and depth. *Geochimica et Cosmochimica Acta*, 69(18):4463–4483.

Feitknecht, W. and Keller, G. (1950). Uber die dunkelgrunen Hydroxyverbindungen des Eisens. *Zeitschrift für anorganische und allgemeine Chemie*, 262(1-5):61–68.

Ferrage, E. (2004). *Etude expérimentale de l'hydratation des smectites par simulation des raies 00l de diffraction des rayons X. Implications pour l'étude d'une perturbation thermique sur la minéralogie de l'argilite du site Meuse-Haute Marne.* PhD thesis, Université Joseph Fourier - Grenoble I.

Forano, C., Hibino, T., Leroux, F., and Taviot-Guého, C. (2006). Chapter 13.1 - Layered double hydroxides. In *Developments in Clay Science*, volume 1, pages 1021–1095. Elsevier.

Gaines, G. L. and Thomas, H. C. (1953). Adsorption studies on clay minerals. II. A formulation of the thermodynamics of exchange adsorption. *The Journal of Chemical Physics*, 21(4):714–718.

Géhin, A., Ruby, C., Abdelmoula, M., Benali, O., Ghanbaja, J., Refait, P., and Génin, J. M. R. (2002). Synthesis of Fe(II-III) hydroxysulphate green rust by coprecipitation. *Solid State Sciences*, 4(1):61–66.

Génin, J. M. R., Abdelmoula, M., Ruby, C., and Upadhyay, C. (2006). Speciation of iron, characterisation and structure of green rusts and FeII-III oxyhydroxycarbonate fougerite. *Comptes Rendus Geoscience*, 338(6-7):402–419.

Génin, J. M. R., Aïssa, R., Géhin, A., Abdelmoula, M., Benali, O., Ernstsen, V., Ona-Nguema, G., Upadhyay, C., and Ruby, C. (2005). Fougerite and FeII-III hydroxycarbonate green rust; ordering, deprotonation and/or cation substitution; structure of hydrotalcite-like compounds and mythic ferrosic hydroxide $Fe(OH)_{(2+x)}$. *Solid State Sciences*, 7(5):545–572.

Génin, J. M. R., Bourrié, G., Trolard, F., Abdelmoula, M., Jaffrezic, A., Refait, P., Maitre, V., Humbert, B., and Herbillon, A. (1998). Thermodynamic equilibria in aqueous suspensions of synthetic and natural Fe(II)-Fe(III) green rusts: Occurrences of the mineral in hydromorphic soils. *Environmental Science and Technology*, 32:1058–1068.

Génin, J. M. R., Guérin, O., Herbillon, A. J., Kuzmann, E., Mills, S. J., Morin, G., Ona-Nguema, G., Ruby, C., and Upadhyay, C. (2012). Redox topotactic reactions in Fe II-III (oxy)hydroxycarbonate new minerals related to fougèrite in gleysols: "trébeurdenite and mössbauerite". *Hyperfine Interactions*, 204:71–81.

Génin, J. M. R., Mills, S. J., Christy, A. G., Guérin, O., Herbillon, A. J., Kuzmann, E., Ona-Nguema, G., Ruby, C., and Upadhyay, C. (2014). Mössbauerite, $Fe^{3+}{}_6O_4(OH)_8$ $[CO_3].3H_2O$, the fully oxidized 'green rust' mineral from Mont Saint-Michel Bay, France. *Mineralogical Magazine*, 78(2):447–465.

Génin, J. M. R., Olowe, A. A., Benbouzid-Rollet, N. D., Prieur, D., Confente, M., and Resiak, B. (1992). The simultaneous presence of green rust 2 and sulfate reducing bacteria in the corrosion of steel sheet piles in a harbour area. *Hyperfine Interactions*, 69(1-4):875–878.

Génin, J. M. R., Olowe, A. A., Refait, P., and Simon, L. (1996). On the stoichiometry and Pourbaix diagram of Fe(II)-Fe(III) hydroxy-sulfate or sulphate-containing green rust 2: an electrochemical ans Mössbauer spectroscopy study. *Corrosion Science*, 38(10):1751–1762.

Genin, J. M. R., Olowe, A. A., Resiak, B., Benbouzid, N. D., Confente, M., and Prieur, D. (1993). Marine corrosion of stainless steels: chlorination and microbial effects. In *European Federation Corrosion Series n° 10*, pages 162–166. The Institute of Metals, London.

Génin, J. M. R., Refait, P., Bourrié, G., Abdelmoula, M., and Trolard, F. (2001). Structure and stability of the Fe(II)-Fe(III) green rust "fougerite" mineral and its potential for reducing pollutants in soil solutions. *Applied Geochemistry*, 16(5):559–570.

Génin, J. M. R. and Ruby, C. (2008). Composition and anion ordering in some FeII-III hydroxysalt green rusts (carbonate, oxalate, methanoate): The fougerite mineral. *Solid State Sciences*, 10:244–259.

Girard, A. and Chaudron, G. (1935). Sur la constitution de la rouille. *Comptes rendus hebdomadaires des séances de l ' Académie des sciences, Série B*, 200:127–129.

GIS SOL (2019). Pédologie, les sols dominants en France métropolitaine. Technical report, GIS SOL.

Goh, K.-H., Lim, T.-t., and Dong, Z. (2009). Enhanced arsenic removal by hydrothermally treated nanocrystalline Mg/Al layered double hydroxide with nitrate intercalation. *Environmental Science and Technology*, 43:2537–2543.

Grabb, K. C., Buchwald, C., Hansel, C. M., and Wankel, S. D. (2017). A dual nitrite isotopic investigation of chemodenitrification by mineral-associated Fe(II) and its production of nitrous oxide. *Geochimica et Cosmochimica Acta*, 196:388–402.

Gran, G. (1952). Determination of the equivalence point in potentiometric titrations. Part II. *Analyst*, 77(920):661–671.

Grangeon, S., Fernandez-Martinez, A., Baronnet, A., Marty, N. C. M., Poulain, A., Elkaïm, E., Roosz, C., Gaboreau, S., Henocq, P., and Claret, F. (2017a). Quantitative X-ray pair distribution function analysis of nanocrystalline calcium silicate hydrates: a contribution to the understanding of cement chemistry. *Journal of Applied Crystallography*, 50:14–21.

Grangeon, S., Fernandez-Martinez, A., Claret, F., Marty, N., Tournassat, C., Warmont, F., and Gloter, A. (2017b). In-situ determination of the kinetics and mechanisms of nickel adsorption by nanocrystalline vernadite. *Chemical Geology*, 459:24–31.

Grangeon, S., Lanson, B., Miyata, N., Tani, Y., and Manceau, A. (2010). Structure of nanocrystalline phyllomanganates produced by freshwater fungi. *American Mineralogist*, 95(11-12):1608–1616.

Grangeon, S., Marty, N. C. M., Maubec, N., Warmont, F., and Claret, F. (2020). Selenate sorption by hydrated calcium aluminate (AFm): Evidence for sorption reversibility and implication for the modeling of anion retention. *ACS Earth and Space Chemistry*, 4(2):229–240.

Guerbois, D., Ona-Nguema, G., Morin, G., Abdelmoula, M., Laverman, A. M., Mouchel, J. M., Barthelemy, K., Maillot, F., and Brest, J. (2014). Nitrite reduction by biogenic hydroxycarbonate green rusts: Evidence for hydroxy-nitrite green rust formation as an intermediate reaction product. *Environmental Science and Technology*, 48(8):4505–4514.

Gumsley, A. P., Chamberlain, K. R., Bleeker, W., Söderlund, U., De Kock, M. O., Larsson, E. R., and Bekker, A. (2017). Timing and tempo of the great oxidation event. *Proceedings of the National Academy of Sciences of the United States of America*, 114(8):1811–1816.

Hadi, J., Grangeon, S., Warmont, F., Seron, A., and Greneche, J. M. (2014). A novel and easy chemical-clock synthesis of nanocrystalline iron-cobalt bearing layered double hydroxides. *Journal of Colloid and Interface Science*, 434:130–140.

Hadi, J., Tournassat, C., Ignatiadis, I., Greneche, J. M., and Charlet, L. (2013). Modelling CEC variations versus structural iron reduction levels in dioctahedral smectites. Existing approaches, new data and model refinements. *Journal of Colloid and Interface Science*, 407:397–409.

Halajnia, A., Oustan, S., Najafi, N., Khataee, A. R., and Lakzian, A. (2013). Adsorption-desorption characteristics of nitrate, phosphate and sulfate on Mg-Al layered double hydroxide. *Applied Clay Science*, 80-81:305–312.

Halevy, I., Alesker, M., Schuster, E. M., Popovitz-Biro, R., and Feldman, Y. (2017). A key role for green rust in the Precambrian oceans and the genesis of iron formations. *Nature Geoscience*, 10(2):135–139.

Han, Y., Huang, J., Liu, H., Wu, Y., Wu, Z., Zhang, K., and Lu, Q. (2020). Abiotic reduction of p-chloronitrobenzene by sulfate green rust: influence factors, products and mechanism. *RSC Advances*, 10(33):19247–19253.

Hansen, H. C. B., Borggaard, O. K., and Sørensen, J. (1994). Evaluation of the free energy of formation of Fe(II)-Fe(III) hydroxide-sulphate (green rust) and its reduction of nitrite. *Geochimica et Cosmochimica Acta*, 58(12):2599–2608.

Hansen, H. C. B., Guldberg, S., Erbs, M., and Koch, C. B. (2001). Kinetics of nitrate reduction by green rusts-effects of interlayer anion and Fe(II):Fe(III) ratio. *Applied Clay Science*, 18(1-2):81–91.

Hansen, H. C. B. and Koch, C. B. (1998). Reduction of nitrate to ammonium by sulphate green rust: Activation energy and reaction mechanism. *Clays Minerals*, 33:87–101.

Hansen, H. C. B., Koch, C. B., Nancke-Krogh, H., Borggaard, O. K., and Sorensen, J. (1996). Abiotic nitrate reduction to ammonium: Key role of green rust. *Environmental Science and Technology*, 30(6):20532056.

Hayashi, H., Kanie, K., Shinoda, K., Muramatsu, A., Suzuki, S., and Sasaki, H. (2009). pH-dependence of selenate removal from liquid phase by reductive Fe(II)-Fe(III) hydroxysulfate compound, green rust. *Chemosphere*, 76(5):638–643.

Holmes, A. B. and Gu, F. X. (2016). Emerging nanomaterials for the application of selenium removal for wastewater treatment. *Environmental Science Nano*, 3:982–996.

Hüttig, G. F. and Möldner, H. (1931). Das System Eisen(ll) oxyd/Wasser und seine Übergange zu dem System Eisen(III) oxyd/Wasser. *Zeitschrift für anorganische und allgemeine Chemie*, 196(1):177–187.

Ingram, L. and Taylor, H. F. W. (1967). The crystal structures of sjögrenite and pyroaurite. *Mineralogical Magazine and Journal of the Mineralogical Society*, 36(280):465–479.

Inoue, A. and Minato, H. (1979). Ca-K exchange reaction and interstratification in montmorillonite. *Clays and Clay Minerals*, 27(6):393–401.

Israëli, Y., Taviot-Guého, C., Besse, J.-P., Morel, J.-P., and Morel-Desrosiers, N. (2000). Thermodynamics of anion exchange on a chloride-intercalated zinc-aluminum layered double hydroxide: a microcalorimetric study. *Journal of the Chemical Society, Dalton Transactions*, 0(5):791–796.

Iyi, N. and Sasaki, T. (2008). Deintercalation of carbonate ions and anion exchange of an Al-rich MgAl-LDH (layered double hydroxide). *Applied Clay Science*, 42(1-2):246–251.

Jagodzinski, H. (1949). Eindimensionale Fehlordnung in Kristallen und ihr Einfluss auf die Röntgeninterferenzen. I. Berechnung des Fehlordnungsgrades aus den Röntgenintensitäten. *Acta Crystallographica*, 2(4):201–207.

Johnson, C. A., Freyer, G., Fabisch, M., Caraballo, M. A., Küsel, K., Hochella, M. F., Küsel, K., and Hochella, M. F. (2014). Observations and assessment of iron oxide and green rust nanoparticles in metal-polluted mine drainage within a steep redox gradient. *Environmental Chemistry*, 11(9):377–391.

Johnson, C. A., Murayama, M., Küsel, K., and Hochella, M. F. (2015). Polycrystallinity of green rust minerals and their synthetic analogs: Implications for particle formation and reactivity in complex systems. *American Mineralogist*, 100(10):2091–2105.

Jones, C. J., Chattopadhyay, S., Gonzalez-Pech, N. I., Avendano, C., Hwang, N., Lee, S. S., Cho, M., Ozarowski, A., Prakash, A., Mayo, J. T., Yavuz, C., and Colvin, V. L. (2015). A novel, reactive green iron sulfide (sulfide green rust) formed on iron oxide nanocrystals. *Chemistry of Materials*, 27:700–707.

Juhás, P., Davis, T., Farrow, C. L., and Billinge, S. J. L. (2013). PDFgetX3 : a rapid and highly automatable program for processing powder diffraction data into total scattering pair distribution functions. *Journal of Applied Crystallography*, 46:560–566.

Keller, G. (1948). *Thesis*. PhD thesis, Bern.

Koch, C. B. and Mørup, S. (1991). Identification of green rust in an ochre sludge. *Clay Minerals*, 26:577–582.

Koeksoy, E., Sundman, A., Byrne, J. M., Lohmayer, R., Planer-Friedrich, B., Halevy, I., Konhauser, K. O., and Kappler, A. (2019). Formation of green rust and elemental sulfur in an analogue for oxygenated ferro-euxinic transition zones of Precambrian oceans. *Geology*, 47(3):211–214.

Krause, A. (1928). Über die Oxydation des Ferrohydroxyds an der Luft. *Zeitschrift für anorganische und allgemeine Chemie*, 174(1):145–160.

Kukkadapu, R. K., Zachara, J. M., Fredrickson, J. K., and Kennedy, D. W. (2004). Biotransformation of two-line silica-ferrihydrite by a dissimilatory Fe(III)-reducing bacterium: Formation of carbonate green rust in the presence of phosphate. *Geochimica et Cosmochimica Acta*, 68(13):2799–2814.

Latta, D. E., Boyanov, M. I., Kemner, K. M., O'Loughlin, E. J., and Scherer, M. (2015). Reaction of uranium(VI) with green rusts: Effect of interlayer anion. *Current Inorganic Chemistry*, 5:156–158.

Latta, D. E., Boyanov, M. I., Kemner, K. M., O'Loughlin, E. J., and Scherer, M. M. (2012). Abiotic reduction of uranium by Fe(II) in soil. *Applied Geochemistry*, 27(8):1512–1524.

Legrand, L., Abdelmoula, M., Géhin, A., Chaussé, A., and Génin, J. M. R. (2001). Electrochemical formation of a new Fe(II)-Fe(III) hydroxy-carbonate green rust: characterisation and morphology. *Electrochimica Acta*, 46(12):1815–1822.

Lewis, D. G. (1997). Factors influencing the stability and properties of green rusts. In *Soils and Environment*, pages 345–372. Catena Verlag.

Luo, G., Ono, S., Beukes, N. J., Wang, D. T., Xie, S., and Summons, R. E. (2016). Rapid oxygenation of Earth's atmosphere 2.33 billion years ago. *Science Advances*, 2(5):e1600134.

Ma, B., Fernandez-Martinez, A., Grangeon, S., Tournassat, C., Findling, N., Carrero, S., Tisserand, D., Bureau, S., Elkaïm, E., Marini, C., Aquilanti, G., Koishi, A., Marty, N. C. M., and Charlet, L. (2018). Selenite uptake by Ca-Al LDH: A description of intercalated anion coordination geometries. *Environmental Science and Technology*, 52(3):1624–1632.

Ma, B., Fernandez-Martinez, A., Grangeon, S., Tournassat, C., Findling, N., Claret, F., Koishi, A., Marty, N. C. M., Tisserand, D., Bureau, S., Salas-Colera, E., Elkaïm, E., Marini, C., and Charlet, L. (2017). Evidence of multiple sorption modes in layered double hydroxides using Mo As structural probe. *Environmental Science and Technology*, 51(10):5531–5540.

Mangayayam, M. C., Dideriksen, K., and Tobler, D. J. (2018). Can or cannot green rust reduce chlorinated ethenes? *Energy Procedia*, 146:173–178.

Marty, N. C. M., Grangeon, S., Elkaïm, E., Tournassat, C., Fauchet, C., and Claret, F. (2018). Thermodynamic and crystallographic model for anion uptake by hydrated calcium aluminate (AFm): an example of molybdenum. *Scientific Reports*, 8(1):7943.

McBride, M. B. (1994). *Environmental Chemistry of Soils*. Oxford University Press.

Millero, F. J., Feistel, R., Wright, D. G., and McDougall, T. J. (2008). The composition of standard seawater and the definition of the reference-composition salinity scale. *Deep-Sea Research Part I: Oceanographic Research Papers*, 55(1):50–72.

Mills, S. J., Christy, A. G., Génin, J. M. R., Kameda, T., and Colombo, F. (2012). Nomenclature of the hydrotalcite supergroup: natural layered double hydroxides. *Mineralogical Magazine*, 76(5):1289–1336.

Mitsunobu, S., Takahashi, Y., Sakai, Y., and Inumaru, K. (2009). Interaction of synthetic sulfate green rust with antimony(V). *Environmental Science and Technology*, 43:318–323.

Miyata, S. (1983). Anion-exchange properties of hydrotalcite-like compounds. *Clays and Clay Minerals*, 31(4):305–311.

Miyata, S. and Okada, A. (1977). Synthesis of Hydrotalcite-like compounds and their physico-chemical properties - the systems Mg^{2+}-Al^{3+}-$SO_4{}^{2-}$ and Mg^{2+}-Al^{3+}-$CrO_4{}^{2-}$. *Clays and Clay Minerals*, 25:14–18.

Moreno, H. A., Cocke, D. L., Gomes, J. A., Morkovsky, P., Parga, J., Peterson, E., and Garcia, C. (2007). Electrochemical generation of green rust using electrocoagulation. *ECS Transactions*, 3(18):67–78.

Myneni, S. C. B., Tokunaga, T. K., and Brown, G. E. J. (2008). Abiotic selenium redox transformations in the presence of Fe(II,III) oxides. *Science*, 1106(1997).

Neumann, T. (2012). 2 - Fundamentals of aquatic chemistry relevant to radionuclide behaviour in the environment. In Poinssot, C. and Geckeis, H., editors, *Radionuclide Behaviour in the Natural Environment: Science, Implications and Lessons for the Nuclear Industry*, pages 13–43. Woodhead Publishing.

Okamoto, K., Sasaki, T., Fujita, T., and Iyi, N. (2006). Preparation of highly oriented organic-LDH hybrid films by combining the decarbonation, anion-exchange, and delamination processes. *Journal of Materials Chemistry*, 16(17):1608–1616.

O'Loughlin, E. J. and Burris, D. R. (2004). Reduction of halogenated ethanes by green rust. *Environmental Toxicology and Chemistry*, 23(1):41–48.

O'Loughlin, E. J., Kelly, S. D., Cook, R. E., Csencsits, R., and Kemner, K. M. (2003a). Reduction of uranium(VI) by mixed ron(II)/iron(III) hydroxide (green rust): Formation of UO_2 nanoparticles. *Environmental Science and Technology*, 37(4):721–727.

O'Loughlin, E. J., Kelly, S. D., Kemner, K. M., Csencsits, R., and Cook, R. E. (2003b). Reduction of Ag^{I}, Au^{III}, Cu^{II}, and Hg^{II} by Fe^{II}/Fe^{III} hydroxysulfate green rust. *Chemosphere*, 53(5):437–446.

Olowe, A. A. (1988). *Corrosion aqueuse du fer en milieux sulfates : Mécanisme, cinétique et structures*. PhD thesis, Université Nancy 1.

Olowe, A. A., Bauer, P., Genin, J. M. R., and Guezennec, J. (1989). Mössbauer effect evidence of the existence of green rust 2 transient compound from bacterial corrosion in marine sediments. *Corrosion*, 45(3):229–235.

Olowe, A. A. and Génin, J. M. R. (1991). The mechanism of oxidation of ferrous hydroxide in sulphated aqueous media: Importance of the initial ratio of the reactants. *Corrosion Science*, 32(9):965–984.

Olowe, A. A., Marie, Y., Refait, P., and Génin, J. M. R. (1994). Mechanism of formation of delta FeOOH in a basic aqueous medium. *Hyperfine Interactions*, 93(1):1783–1788.

Ona-Nguema, G., Abdelmoula, M., Jorand, F., Benali, O., Géhin, A., Block, J. C., and Génin, J. M. R. (2002). Iron(II,III) hydroxycarbonate green rust formation and stabilization from lepidocrocite bioreduction. *Environmental Science and Technology*, 36:16–20.

Ookubo, A., Ooi, K., and Hayashi, H. (1993). Preparation and phosphate ion-exchange properties of a Hydrotalcite-like compound. *Langmuir*, 9(5):1418–1422.

Ossa, F. O., Hofmann, A., Spangenberg, J. E., Poulton, S. W., Stüeken, E. E., Schoenberg, R., Eickmann, B., Wille, M., Butler, M., and Bekker, A. (2019). Limited oxygen production in the Mesoarchean ocean. *Proceedings of the National Academy of Sciences of the United States of America*, 116(14):6647–6652.

Ounsy, M., Girardot, R., Saintin, K., and Viguier, G. (2013). Online data reduction for high throughput beamlines. In *International conference on accelerators and large experimental physics control systems*, page 217.

Palmer, S. J., Frost, R. L., and Nguyen, T. (2008). Thermal decomposition of hydrotalcite with molybdate and vanadate anions in the interlayer. *Journal of Thermal Analysis and Calorimetry*, 92(3):879–886.

Parkhurst, D. L. and Appelo, C. A. J. (2013). *Description of input and examples for PHREEQC version 3: a computer program for speciation, batch-reaction, one-dimensional transport, and inverse geochemical calculations*. US Geological Survey.

Parmar, N., Gorby, Y. A., Beveridge, T. J., and Ferris, F. G. (2001). Formation of green rust and immobilization of nickel in response to bacterial reduction of hydrous ferric oxide. *Geomicrobiology Journal*, 18(4):375–385.

Perez, J. P. H. (2019). *Green rust formation and reactivity with arsenic species*. PhD thesis, Freie Universität Berlin.

Perez, J. P. H., Freeman, H. M., Brown, A. P., Van Genuchten, C. M., Dideriksen, K., S'Ari, M., Tobler, D. J., and Benning, L. G. (2020). Direct visualization of arsenic binding on green rust sulfate. *Environmental Science and Technology*, 54(6):3297–3305.

Perez, J. P. H., Mangayayam, M. C., Rubio, S. N., Freeman, H. M., Tobler, D. J., and Benning, L. G. (2018). Intercalation of aromatic sulfonates in 'green rust' via ion exchange. *Energy Procedia*, 146:179–187.

Perez, J. P. H., Schiefler, A. A., Rubio, S. N., Reischer, M., Overheu, N. D., Benning, L. G., and Tobler, D. J. (2021). Arsenic removal from natural groundwater using 'green rust': Solid phase stability and contaminant fate. *Journal of Hazardous Materials*, 401:123327.

Plançon, A. (1981). Diffraction by layer structures containing different kinds of layers and stacking faults. *Journal of Applied Crystallography*, 14(5):300–304.

Plançon, A. (2002). CALCIPOW : a program for calculating the diffraction by disordered lamellar structures . *Journal of Applied Crystallography*, 35(3):377–377.

Plançon, A. and Drits, V. A. (2000). Phase analysis of clays using an expert system and calculation programs for X-ray diffraction by two- and three-component mixed-layer minerals. *Clays and Clay Minerals*, 48(1):57–62.

Poinssot, C., Baeyens, B., and Bradbury, M. H. (1999). Experimental and modelling studies of caesium sorption on illite. *Geochimica et Cosmochimica Acta*, 63(19-20):3217–3227.

Post, J. E. and Bish, D. L. (1989). Rietveld refinement of crystal structures using powder X-ray diffraction data. In Bish, D. L. and Post, J. E., editors, *Modern Powder Diffraction*, pages 277–308. Mineralogical Society of America.

Radha, A. V., Vishnu Kamath, P., and Shivakumara, C. (2005). Mechanism of the anion exchange reactions of the layered double hydroxides (LDHs) of Ca and Mg with Al. *Solid State Sciences*, 7(10):1180–1187.

Randall, S. R., Sherman, D. M., and Ragnarsdottir, K. V. (2001). Sorption of As(V) on green rust ($Fe_4(II)Fe_2(III)(OH)_{12}SO_4.3H_2O$) and lepidocrocite ($\gamma$-FeOOH): Surface complexes from EXAFS spectroscopy. *Geochimica et Cosmochimica Acta*, 65(7):1015–1023.

Refait, P., Abdelmoula, M., and Génin, J. M. R. (1998). Mechanisms of formation and structure of green rust one in aqueous corrosion of iron in the presence of chloride ions. *Corrosion Science*, 40(9):1547–1560.

Refait, P., Abdelmoula, M., Trolard, F., Génin, J. M. R., Ehrhardt, J. J. J., and Bourrié, G. (2001). Mössbauer and XAS study of a green rust mineral; the partial substitution of Fe^{2+} by Mg^{2+}. *American Mineralogist*, 86(5-6):731–739.

Refait, P., Benali, O., Abdelmoula, M., and Génin, J. M. R. (2003). Formation of 'ferric green rust' and/or ferrihydrite by fast oxidation of iron(II-III) hydroxychloride green rust. *Corrosion Science*, 45(11):2435–2449.

Refait, P., Drissi, S., Abdelmoula, M., and Génin, J. M. R. (2002). Synthesis and reactivity of Mg(II)-Fe(II)-Fe(III) hydroxycarbonates. *Hyperfine Interactions*, 139:651–655.

Refait, P., Drissi, S. H., Pytkiewicz, J., and Génin, J. M. R. (1997). The anionic species competition in iron aqueous corrosion: Role of various green rust compounds. *Corrosion Science*, 39(9):1699–1710.

Refait, P. and Génin, J. M. R. (1993). The oxidation of ferrous hydroxide in chloride-containing aqueous media and Pourbaix diagrams of green rust one. *Corrosion Science*, 34(5):797–819.

Refait, P. and Génin, J. M. R. (1997). The mechanisms of oxidation of ferrous hydroxychloride β-$Fe_2(OH)_3Cl$ in aqueous solution: The formation of akaganeite vs goethite. *Corrosion Science*, 39(3):539–553.

Refait, P., Reffass, M., Landoulsi, J., Sabot, R., and Jeannin, M. (2014). Role of nitrite species during the formation and transformation of the Fe(II-III) hydroxycarbonate green rust. *Colloids and Surfaces A: Physicochemical and Engineering Aspects*, 459:225–232.

Rennert, T., Eusterhues, K., De Andrade, V., and Totsche, K. U. (2012). Iron species in soils on a mofette site studied by Fe K-edge X-ray absorption near-edge spectroscopy. *Chemical Geology*, 332-333:116–123.

Rives, V. (2001). *Layered double hydroxides: Present and future*. Nova Science.

Rodriguez-Carvajal, J. (1990). FULLPROF: a program for Rietveld refinement and pattern matching analysis. In *Satellite meeting on powder diffraction of the XV congress of the IUCr*.

Rogers, C. M., Burke, I. T., Ahmed, I. A. M., and Shaw, S. (2014). Immobilization of chromate in hyperalkaline waste streams by green rusts and zero-valent iron. *Environmental Technology*, 3330(October 2015):1–6.

Roh, Y., Lee, S. Y., Elless, M. P., and Foss, J. E. (2000). Incorporation of radioactive contaminants into pyroaurite-like phases by electrochemical synthesis. *Clays and Clay Minerals*, 48(2):266–271.

Rounds, S. A. and Wilde, F. D. (2012). Chapter A6 - Section 6.6 - Alkalinity and acid neutralizing capacity. In *U.S. Geological Survey Techniques of Water-Resources Investigations, book 9*, pages 1–45. U.S. Geological Survey.

Ruby, C., Abdelmoula, M., Aissa, R., Medjahdi, G., Brunelli, M., and François, M. (2008). Aluminium substitution in iron(II-III)-layered double hydroxides: Formation and cationic order. *Journal of Solid State Chemistry*, 181(9):2285–2291.

Ruby, C., Abdelmoula, M., Naille, S., Renard, A., Khare, V., Ona-Nguema, G., Morin, G., and Génin, J. M. R. (2010a). Oxidation modes and thermodynamics of FeII-III oxyhydroxycarbonate green rust: Dissolution-precipitation versus in situ deprotonation. *Geochimica et Cosmochimica Acta*, 74(3):953–966.

Ruby, C., Usman, M., Naille, S., Hanna, K., Carteret, C., Mullet, M., François, M., and Abdelmoula, M. (2010b). Synthesis and transformation of iron-based layered double hydroxides. *Applied Clay Science*, 48(1-2):195–202.

Russell, M. (2018). Green rust: The simple organizing 'seed' of all life? *Life*, 8(3):35.

Scherrer, P. (1918). Bestimmung der größe und der inneren struktur von kolloidteilchen mittels röntgenstrahlen. *Nachrichten von der gesellschaft der wissenschaften zu göttingen, mathematisch-physikalische klasse*, pages 98–100.

Schikorr, G. (1933). Uber Eisen(lI)-hydroxyd und ein ferromagnetisches Eisen(ll)-hydroxyd. *Zeitschrift für anorganische und allgemeine Chemie*, 212(1):33–39.

Schmehl, W. R. and Jackson, M. L. (1955). Interstratification of layer silicates in two soil clays. *Clays and Clay Minerals*, 4(1):423–428.

Shannon, R. D. (1976). Revised effective ionic radii and systematic studies of interatomic distances in halides and chaleogenides. *Acta crystallographica Section A*, 32.

Shi, C., Beidaghi, M., Naguib, M., Mashtalir, O., Gogotsi, Y., and Billinge, S. J. L. (2014). Structure of Nanocrystalline Ti_3C_2 MXene Using Atomic Pair. *Physical Review Letters*, 112(12):125501.

Sihn, Y. and In-Ho, Y. (2020). Aqueous U(VI) removal by green rust and vivianite at phosphate-rich environment. *Membrane Water Treatment*, 11(3):207–215.

Simon, L., François, M., Refait, P., Renaudin, G., Lelaurain, M., and Génin, J. M. R. (2003). Structure of the Fe(II-III) layered double hydroxysulphate green rust two from Rietveld analysis. *Solid State Sciences*, 5(2):327–334.

Sparks, D. L. (2001). Elucidating the fundamental chemistry of soils: Past and recent achievements and future frontiers. *Geoderma*, 100(3-4):303–319.

Sposito, G. (1981a). Cation exchange in soils: an historical and theoretical perspective. *Chemistry in the soil environment*, 40:13–30.

Sposito, G. (1981b). *The thermodynamics of soil solution*. Oxford University Press.

Stampfl, P. P. (1969). Ein basisches Eisen-II-III-karbonat in Rost. *Corrosion Science*, 9(3):185–187.

Staunton, S. and Roubaud, M. (1997). Adsorption of ^{137}Cs on montmorillonite and illite: Effect of charge compensating cation, ionic strength, concentration of Cs, K and fulvic acid. *Clays and Clay Minerals*, 45(2):251–260.

Steefel, C. I., Carroll, S., Zhao, P., and Roberts, S. (2003). Cesium migration in Hanford sediment: a multisite cation exchange model based on laboratory transport experiments. *Journal of Contaminant Hydrology*, 67(1-4):219–246.

Stucki, J. W. (1980). The quantitative assay of minerals for Fe^{2+} and Fe^{3+} Using 1,10-Phenanthroline: II. A photochemical method. *Soil Science Society of America Journal*, 45(3):638–641.

Stucki, J. W. and Anderson, W. L. (1980). The quantitative assay of minerals for Fe(II) and Fe(III) using 1,10-Phenanthroline: I. Sources of variability. *Soil Science Society of America Journal*, 45(3):633–637.

Sumoondur, A., Shaw, S., Ahmed, I., and Benning, L. G. (2008). Green rust as a precursor for magnetite: an in situ synchrotron based study. *Mineralogical Magazine*, 72(1):201–204.

Tamaura, Y., Saturno, M., Yamada, K., and Katsura, T. (1984). Transformation of γ-FeO(OH) to Fe_3O_4 and green rust II in an aqueous solution. *Bulletin of the Chemical Society of Japan*, 57(9):2417–2421.

Tardy, Y. and Fritz, B. (1981). An ideal solid solution model for calculating solubility of clay minerals. *Clay Minerals*, 16(4):361–373.

Taviot-Guého, C., Feng, Y., Faour, A., and Leroux, F. (2010). Intercalation chemistry in a LDH system: anion exchange process and staging phenomenon investigated by means of time-resolved, in situ X-ray diffraction. *Dalton Transactions*, 39(26):5994–6005.

Taviot-Guého, C., Prévot, V., Forano, C., Renaudin, G., Mousty, C., and Leroux, F. (2018). Tailoring hybrid layered double hydroxides for the development of innovative applications. *Advanced Functional Materials*, 28(27):1703868.

Taylor, R. M. (1980). Formation and properties of Fe(II)-Fe(III) hydroxy-carbonate and its possible significance in soil formation. *Clay Minerals*, 15:369–382.

Thomas, A. N., Eiche, E., Göttlicher, J., Steininger, R., Benning, L. G., Freeman, H. M., Tobler, D. J., Mangayayam, M., Dideriksen, K., and Neumann, T. (2020). Effects of metal cation substitution on hexavalent chromium reduction by green rust. *Geochemical Transactions*, 21(2).

Tonkin, J. W., Balistrieri, L. S., and Murray, J. W. (2004). Modeling sorption of divalent metal cations on hydrous manganese oxide using the diffuse double layer model. *Applied Geochemistry*, 19(1):29–53.

Tournassat, C., Bizi, M., Braibant, G., and Crouzet, C. (2011). Influence of montmorillonite tactoid size on Na-Ca cation exchange reactions. *Journal of Colloid and Interface Science*, 364(2):443–454.

Tournassat, C., Bourg, I. C., Steefel, C. I., and Bergaya, F. (2015). Chapter 1 - Surface properties of clay minerals. In *Developments in Clay Science*, volume 6, pages 5–31. Elsevier B.V.

Tournassat, C., Gailhanou, H., Crouzet, C., Braibant, G., Gautier, A., and Gaucher, E. C. (2009). Cation exchange selectivity coefficient values on smectite and mixed-layer illite/smectite minerals. *Soil Science Society of America Journal*, 73(3):928–942.

Tournassat, C., Neaman, A., Villéras, F., Bosbach, D., and Charlet, L. (2003). Nanomorphology of montmorillonite particles: Estimation of the clay edge sorption site density by low-pressure gas adsorption and AFM observations. *American Mineralogist*, 88(11-12 PART 2):1989–1995.

Tremosa, J., Arcos, D., Bensenouci, F., Gaucher, E. C., Tournassat, C., and Hadi, J. (2012). Geochemical characterization and modelling of the Toarcian/Domerian porewater at the Tournemire underground research laboratory. *Applied Geochemistry*, 27(7):1417–1431.

Trolard, F. (2006). Fougerite: From field experiment to the homologation of the mineral. *Comptes Rendus Geoscience*, 338(16):1158–1166.

Trolard, F., Abdelmoula, M., Bourrié, G., Humbert, B., and Génin, J. M. R. (1996). Mise en évidence d'un constituant de type "rouilles vertes" dans les sols hydromorphes. Proposition de l'existence d'un nouveau minéral : la "fougérite". *Comptes rendus de l'Académie des sciences. Série 2. Sciences de la terre et des planètes*, 323(12):1015–1022.

Trolard, F. and Bourrié, G. (2008). Chapter 5 - Geochemistry of green rusts and fougerite: A reevaluation of Fe cycle in soils. In *Advances in Agronomy*, volume 99, pages 227–288. Academic Press.

Trolard, F., Bourrié, G., Abdelmoula, M., Refait, P., and Feder, F. (2007). Fougerite, a new mineral of the pyroaurite-iowaite group: Description and crystal structure. *Clays and Clay Minerals*, 55(3):323–334.

Usman, M., Byrne, J. M., Chaudhary, A., Orsetti, S., Hanna, K., Ruby, C., Kappler, A., and Haderlein, S. B. (2018). Magnetite and green rust: Synthesis, properties, and environmental applications of mixed-valent iron minerals. *Chemical Reviews*, 118:3251–3304.

Usman, M., Hanna, K., Abdelmoula, M., Zegeye, A., Faure, P., and Ruby, C. (2012). Formation of green rust via mineralogical transformation of ferric oxides (ferrihydrite, goethite and hematite). *Applied Clay Science*, 64:38–43.

Verburg, K. and Baveye, P. (1994). Hysteresis in the binary exchange of cations on 2:1 clay minerals: A critical review. *Clays and Clay Minerals*, 42(2):207–220.

Vodyanitskii, Y. N. and Shoba, S. A. (2015). Ephemeral Fe(II)/Fe(III) layered double hydroxides in hydromorphic soils: A review. *Eurasian Soil Science*, 48(3):240–249.

Vydra, F. and Přibil, R. (1959). Utilization of ternary and ion-association complexes in chemical analysis - I: Selective extraction and colorimetric determination of traces of iron as "ferroïn iodide". *Talanta*, 3(1):72–80.

Vydra, F. and Přibil, R. (1960). New redox systems - II: Oxidation of cobaltII with ironIII chloride in 1:10-phenanthroline solutions. *Talanta*, 5(1):44–52.

Vysostskii, G. N. (1905). Gley. *Eurasian Soil Science (Pochvovedenie)*, 4:291–327.

Vysostskii, G. N. (1999). On the 275th anniversary of the russian academy of sciences-gley. *Eurasian Soil Science*, 32(10):1063–1068.

Waasmaier, D. and Kirfel, A. (1995). New analytical scattering-factor functions for free atoms and ions. *Acta Crystallographica Section A*, 51(3):416–431.

Wang, Q. (2018). *Pre-combustion Carbon Dioxide Capture Materials*. Royal Society of Chemistry, London, UK.

Wang, Y., Morin, G., Ona-Nguema, G., Juillot, F., Guyot, F., Calas, G., and Brown, G. E. J. (2010). Evidence for different surface speciation of arsenite and arsenate on green rust: An EXAFS and XANES study. *Environmental Science and Technology*, 44:109–115.

Warren, B. E. (1941). X-Ray diffraction in random layer lattices. *Physical Review*, 59(9):693–698.

Weatherington-rice, J. and Bigham, J. M. (2006). Buried pre-Illinoian-age lacustrine deposits with "green rust" colors in Clermont county. *The Ohio journal of science*, 106(2):35–44.

Wechsler, B. A. B. A., Lindsley, D. H., and Prewitt, C. T. (1984). Crystal structure and cation distribution in titanomagnetites ($Fe_{3-x}Ti_xO_4$). *American Mineralogist*, 69(7-8):754–770.

Williams, A. G. B. and Scherer, M. M. (2001). Kinetics of Cr(VI) reduction by carbonate green rust. *Environmental Science and Technology*, 35(17):3488–3494.

Wu, Y., Yu, Y., Zhou, J. Z., Liu, J., Chi, Y., Xu, Z. P., and Qian, G. (2012). Effective removal of pyrophosphate by Ca-Fe-LDH and its mechanism. *Chemical Engineering Journal*, 179:72–79.

Yin, W., Strobel, B. W., and Hansen, Christian, H. B. (2017). Amino acid-assisted dehalogenation of carbon tetrachloride by green rust: Inhibition of chloroform production. *Environmental Science and Technology*, 51:3445–3452.

Yun, S. K. and Pinnavaia, T. J. (1995). Water content and particle texture of synthetic hydrotalcite-like layered double hydroxides. *Chemistry of Materials*, 7:348–354.

Zegeye, A., Bonneville, S., Benning, L. G., Sturm, A., Fowle, D. A., Jones, C., Canfield, D. E., Ruby, C., MacLean, L. C., Nomosatryo, S., Crowe, S. A., and Poulton, S. W. (2012). Green rust formation controls nutrient availability in a ferruginous water column. *Geology*, 40(7):599–602.

Zegeye, A., Ona-Nguema, G., Carteret, C., Huguet, L., Abdelmoula, M., and Jorand, F. (2005). Formation of hydroxysulphate green rust 2 as a single Iron(II-III) mineral in microbial culture. *Geomicrobiology Journal*, 22(7-8):389–399.

Zhang, P., Qian, G., Xu, Z. P., Shi, H., Ruan, X., Yang, J., and Frost, R. L. (2012). Effective adsorption of sodium dodecylsulfate (SDS) by hydrocalumite (CaAl-LDH-Cl) induced by self-dissolution and re-precipitation mechanism. *Journal of Colloid and Interface Science*, 367(1):264–271.

Zhao, J., Xiong, S., Ai, J., Wu, J., Huang, L.-Z., and Yin, W. (2021). Stabilized green rusts for aqueous Cr(VI) removal: Fast kinetics, high iron utilization rate and anti-acidification. *Chemosphere*, 262:127853.

Zhu, M., Farrow, C. L., Post, J. E., Livi, K. J. T., Billinge, S. J. L., Ginder-Vogel, M., and Sparks, D. L. (2012). Structural study of biotic and abiotic poorly-crystalline manganese oxides using atomic pair distribution function analysis. *Geochimica et Cosmochimica Acta*, 81:39–55.

APPENDIX A

LIST OF ABBREVIATIONS

AEC Anionic Exchange Capacity

CEC Cationic Exchange Capacity

DIC Dissolved Inorganic Carbon

DSC Differential Scanning Calorimetry

EDX Energy-dispersive X-ray spectroscopy

EPMA Electron Probe Micro-Analyzes

HPLC High-Performance Liquid Chromatography

IMA International Mineralogical Association

LDH Layered Double Hydroxide

PDF Pair Distribution Function

SSA Specific Surface Area

TEM Transmission Electronic Microscope

TGA Thermogravimetric Analysis

XRD X-ray Diffraction

APPENDIX B

INTERSTRATIFICATION MODELS

B.1 Experiment "$NaHCO_3$−XRD"

Table S1 – List of parameters to model XRD patterns of interstratified micro-Co-GR phase during "$NaHCO_3$-XRD" experiment with MLM2C code. This table is the same as Table V.1.

V/V_r	R	W_{Cl}	W_{CO_3}	P_{ClCl}	$P_{CO_3CO_3}$	c^* Gr-Cl (Å)	c^* Gr-CO_3 (Å)
0.0	1	1	0	1	-	7.957	-
2.6	1	1	0	1	-	7.957	-
3.8	1	0.890	0.110	0.993	0.943	7.957	7.585
6.0	1	0.715	0.285	0.985	0.962	7.952	7.585
7.2	1	0.520	0.480	0.963	0.960	7.945	7.585
8.1	1	0.340	0.660	0.945	0.972	7.910	7.585
8.9	1	0.260	0.740	0.940	0.979	7.900	7.585
12.3	1	0.140	0.860	0.910	0.985	7.900	7.585
18.7	1	0.080	0.920	0.890	0.990	7.900	7.585
20.4	1	0.070	0.930	0.890	0.992	7.900	7.585

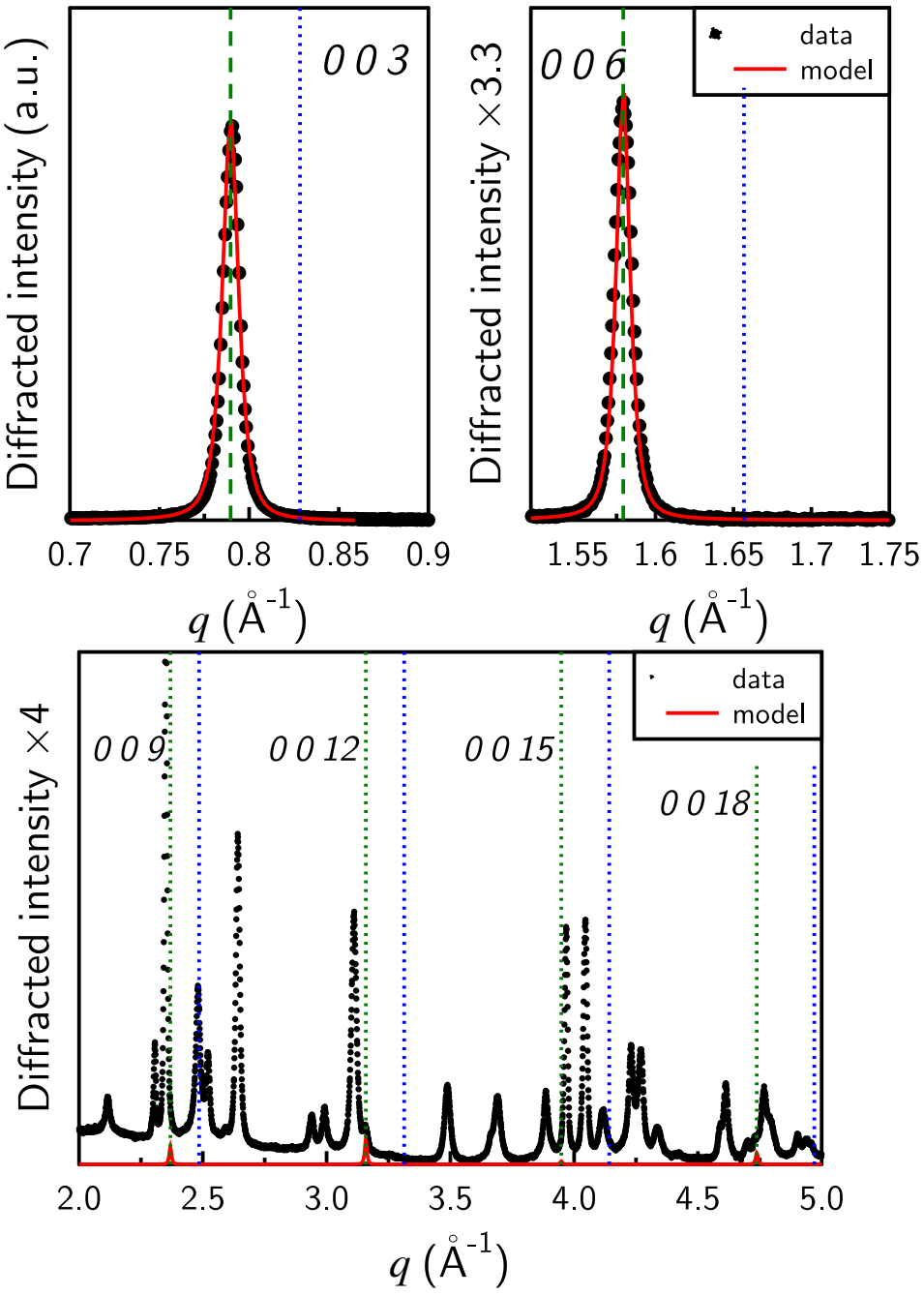

Figure S1 – Interstratification processes on micro-Co-GR sample during an exchange with C(IV) species at $V/V_r = 0$ (Solution concentration: 10 mmol·L^{-1} NaCl and 40 mmol·L^{-1} $NaHCO_3$). Green dashed line was the initial position of the *00l* reflections of micro-Co-GR(Cl) phase (for $V/V_r = 0$). Blue dashed line was the initial position of the *00l* reflections of micro-Co-GR(C(IV)) phase (for $V/V_r = 20.4$)).

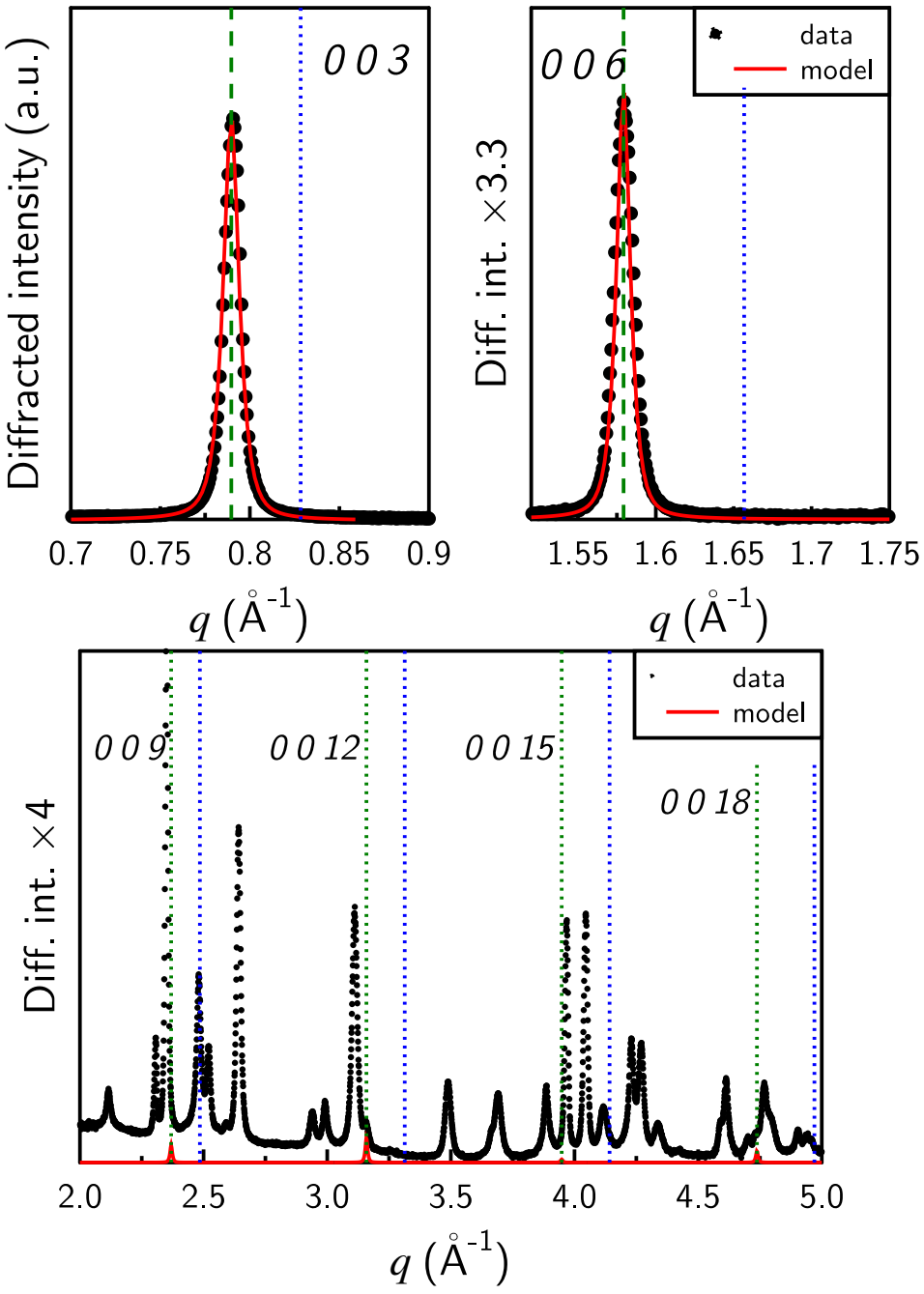

Figure S2 – Interstratification processes on micro-Co-GR sample during an exchange with C(IV) species at $V/V_r = 2.6$ (Solution concentration: 10 mmol·L^{-1} NaCl and 40 mmol·L^{-1} $NaHCO_3$). Green dashed line was the initial position of the *00l* reflections of micro-Co-GR(Cl) phase (for $V/V_r = 0$). Blue dashed line was the initial position of the *00l* reflections of micro-Co-GR(C(IV)) phase (for $V/V_r = 20.4$)).

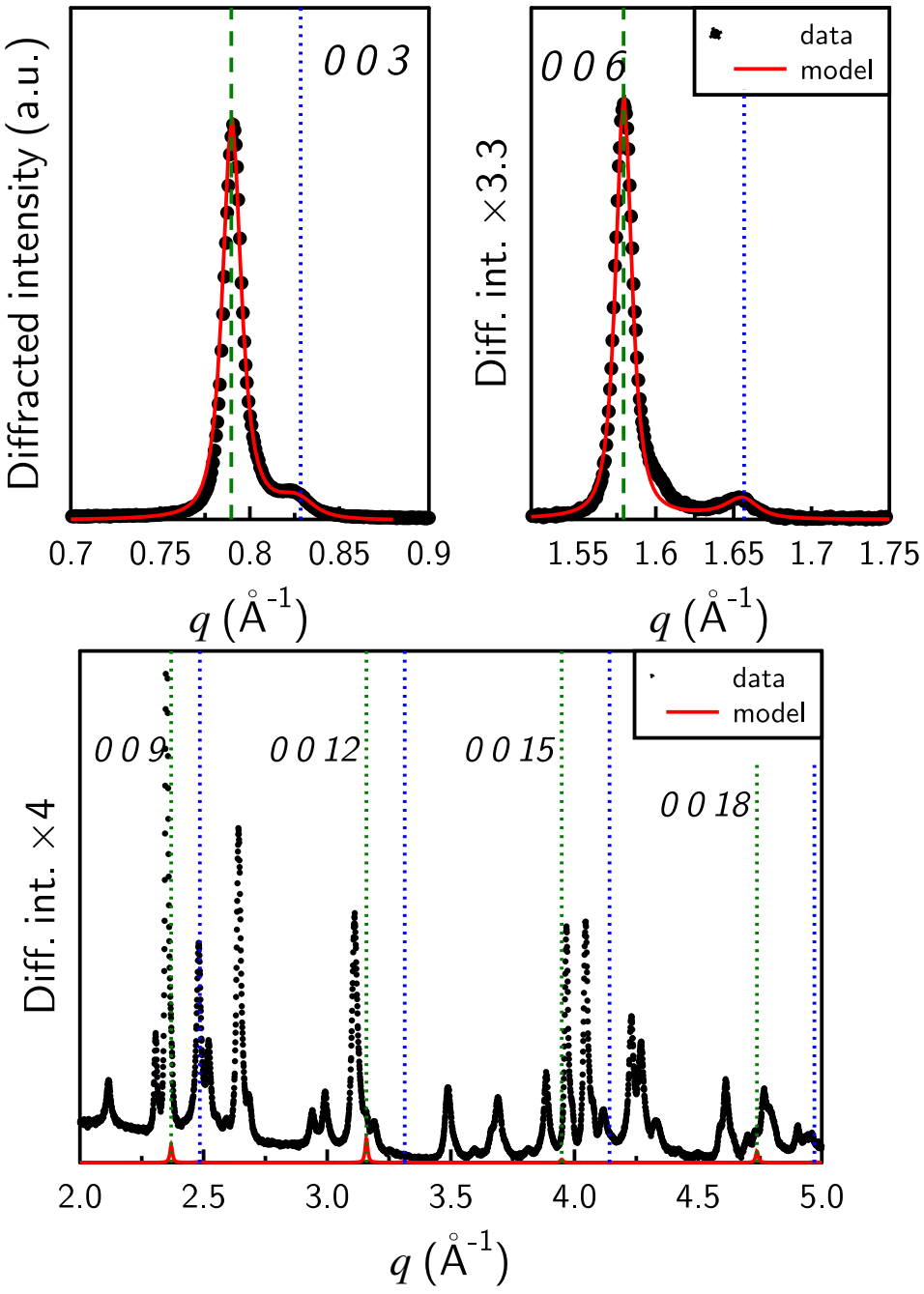

Figure S3 – Interstratification processes on micro-Co-GR sample during an exchange with C(IV) species at $V/V_r = 3.8$ (Solution concentration: 10 mmol·L^{-1} NaCl and 40 mmol·L^{-1} $NaHCO_3$). Green dashed line was the initial position of the *00l* reflections of micro-Co-GR(Cl) phase (for $V/V_r = 0$). Blue dashed line was the initial position of the *00l* reflections of micro-Co-GR(C(IV)) phase (for $V/V_r = 20.4$)).

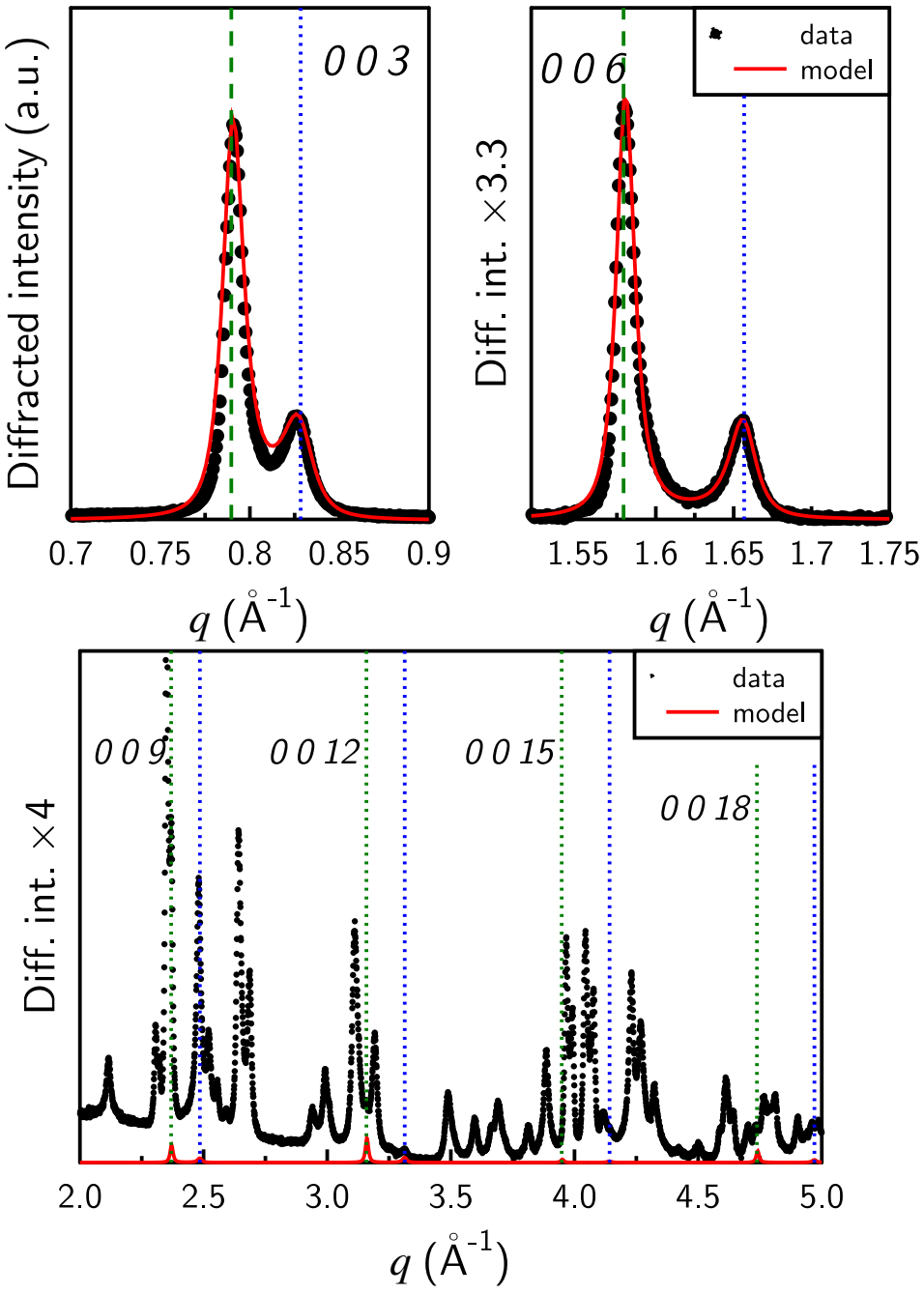

Figure S4 – Interstratification processes on micro-Co-GR sample during an exchange with C(IV) species at $V/V_r = 6.0$ (Solution concentration: 10 mmol·L^{-1} NaCl and 40 mmol·L^{-1} $NaHCO_3$). Green dashed line was the initial position of the *00l* reflections of micro-Co-GR(Cl) phase (for $V/V_r = 0$). Blue dashed line was the initial position of the *00l* reflections of micro-Co-GR(C(IV)) phase (for $V/V_r = 20.4$)).

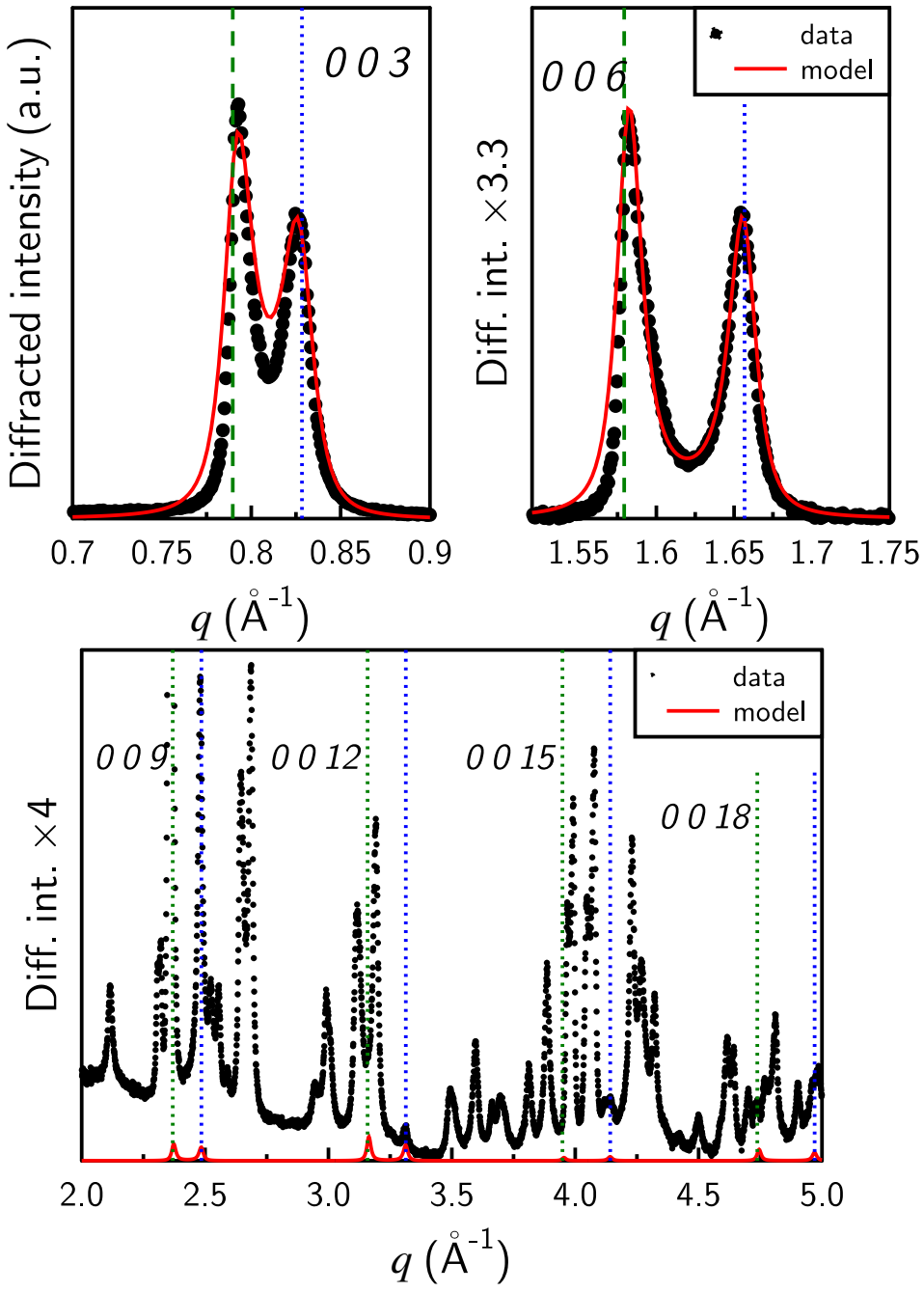

Figure S5 – Interstratification processes on micro-Co-GR sample during an exchange with C(IV) species at $V/V_r = 7.2$ (Solution concentration: 10 mmol·L^{-1} NaCl and 40 mmol·L^{-1} $NaHCO_3$). Green dashed line was the initial position of the *00l* reflections of micro-Co-GR(Cl) phase (for $V/V_r = 0$). Blue dashed line was the initial position of the *00l* reflections of micro-Co-GR(C(IV)) phase (for $V/V_r = 20.4$)).

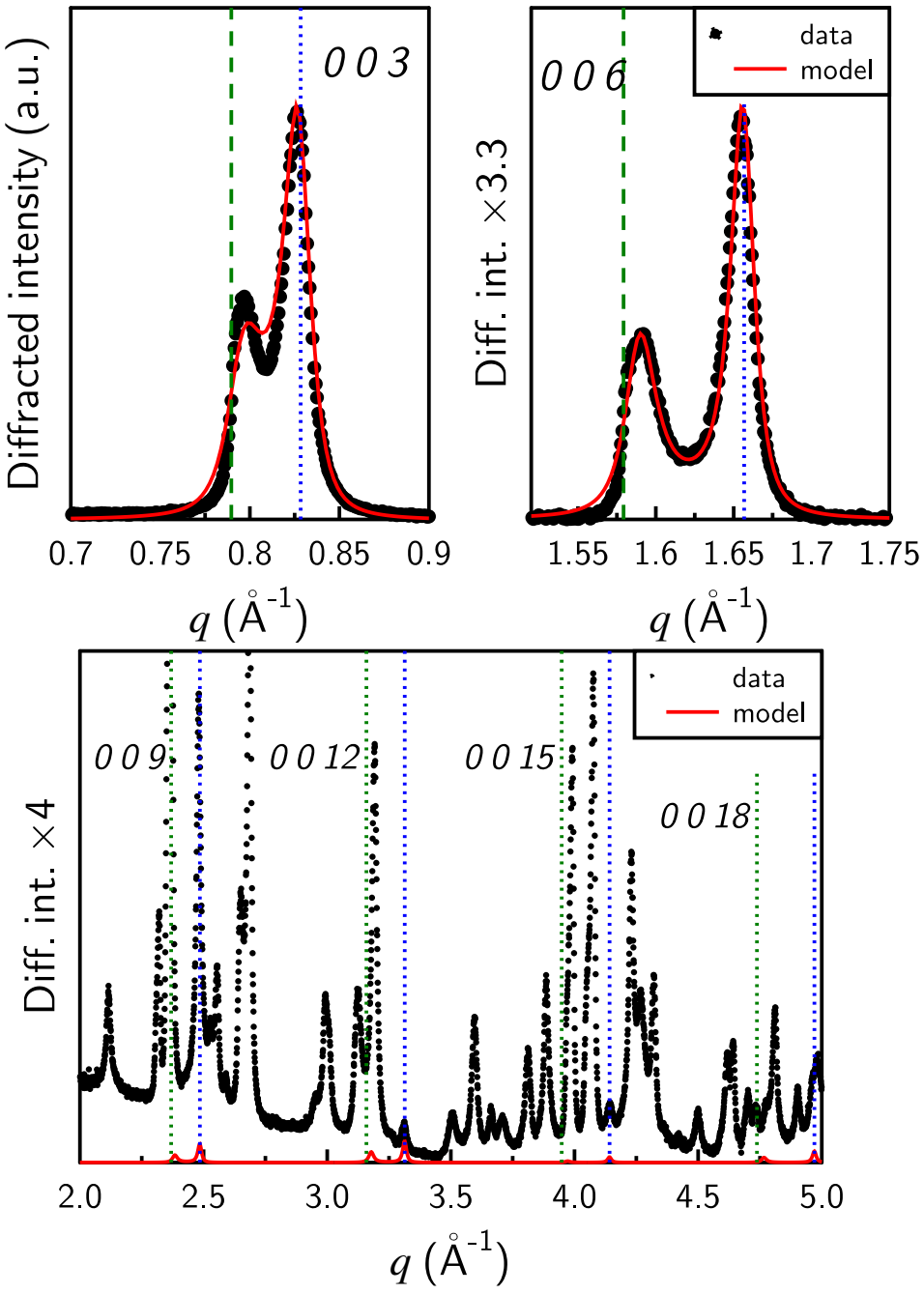

Figure S6 – Interstratification processes on micro-Co-GR sample during an exchange with C(IV) species at $V/V_r = 8.1$ (Solution concentration: 10 mmol·L^{-1} NaCl and 40 mmol·L^{-1} $NaHCO_3$). Green dashed line was the initial position of the *00l* reflections of micro-Co-GR(Cl) phase (for $V/V_r = 0$). Blue dashed line was the initial position of the *00l* reflections of micro-Co-GR(C(IV)) phase (for $V/V_r = 20.4$)).

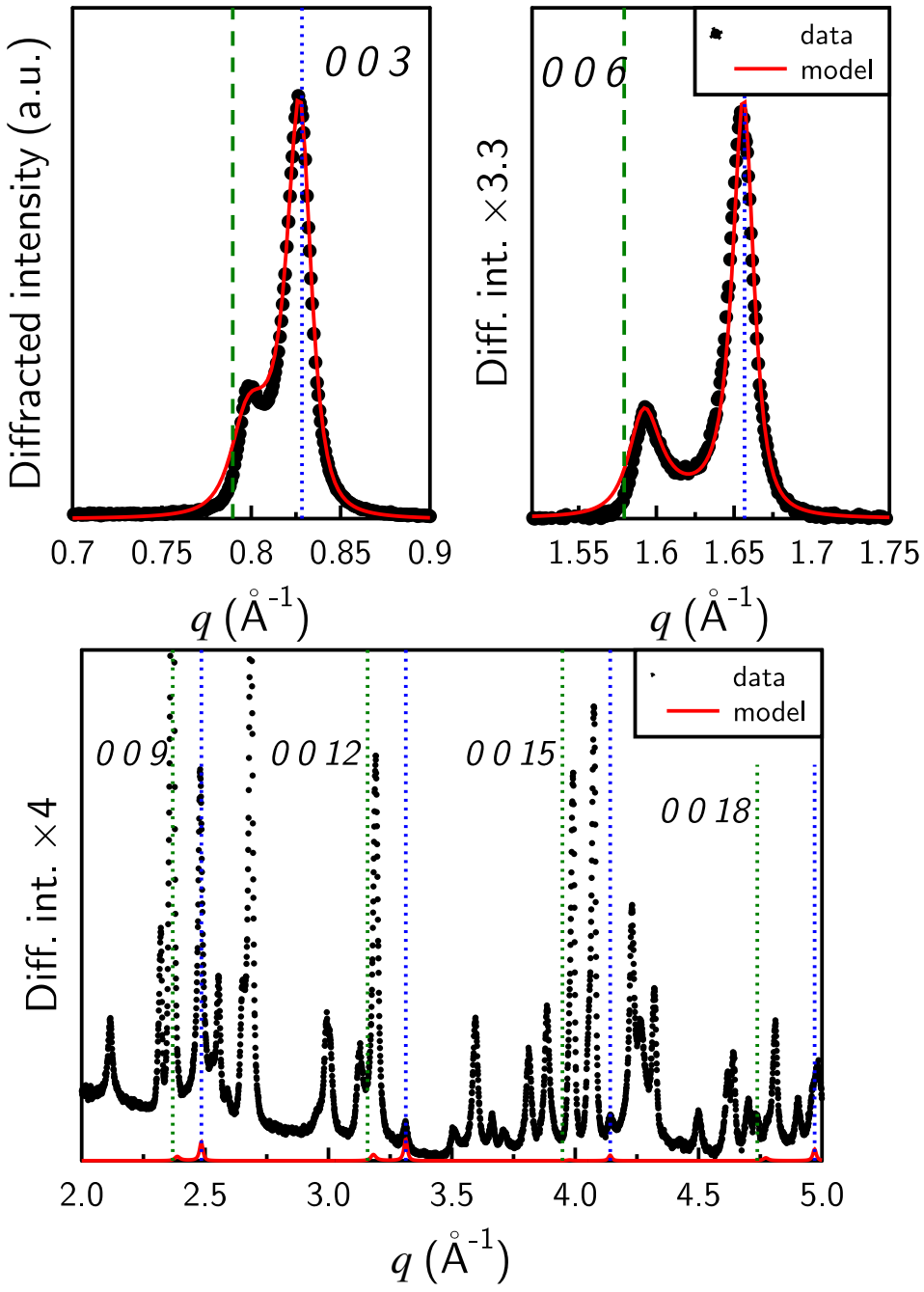

Figure S7 – Interstratification processes on micro-Co-GR sample during an exchange with C(IV) species at $V/V_r = 8.9$ (Solution concentration: 10 mmol·L^{-1} NaCl and 40 mmol·L^{-1} $NaHCO_3$). Green dashed line was the initial position of the *00l* reflections of micro-Co-GR(Cl) phase (for $V/V_r = 0$). Blue dashed line was the initial position of the *00l* reflections of micro-Co-GR(C(IV)) phase (for $V/V_r = 20.4$)).

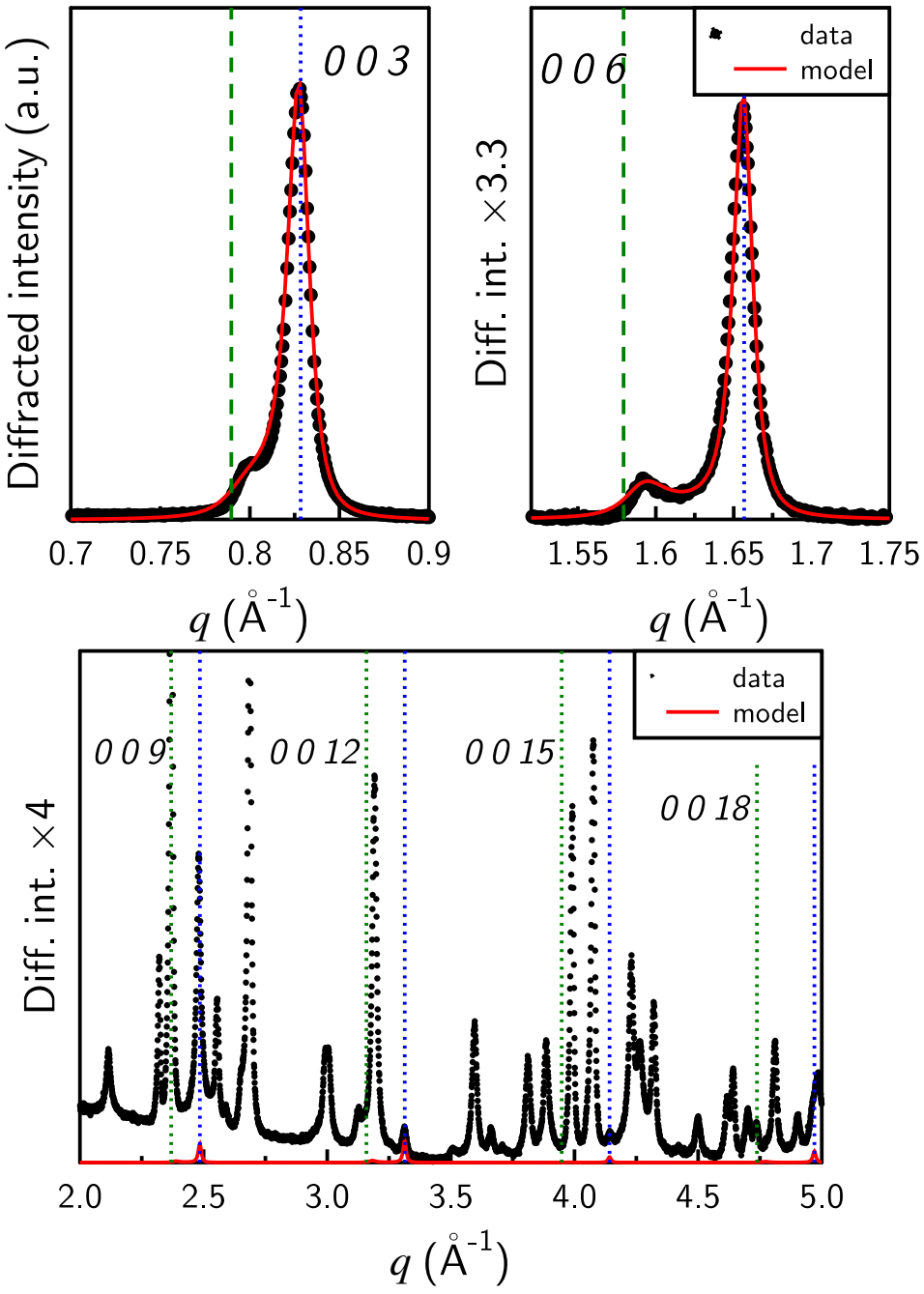

Figure S8 – Interstratification processes on micro-Co-GR sample during an exchange with C(IV) species at $V/V_r = 12.3$ (Solution concentration: 10 mmol·L^{-1} NaCl and 40 mmol·L^{-1} $NaHCO_3$). Green dashed line was the initial position of the *00l* reflections of micro-Co-GR(Cl) phase (for $V/V_r = 0$). Blue dashed line was the initial position of the *00l* reflections of micro-Co-GR(C(IV)) phase (for $V/V_r = 20.4$)).

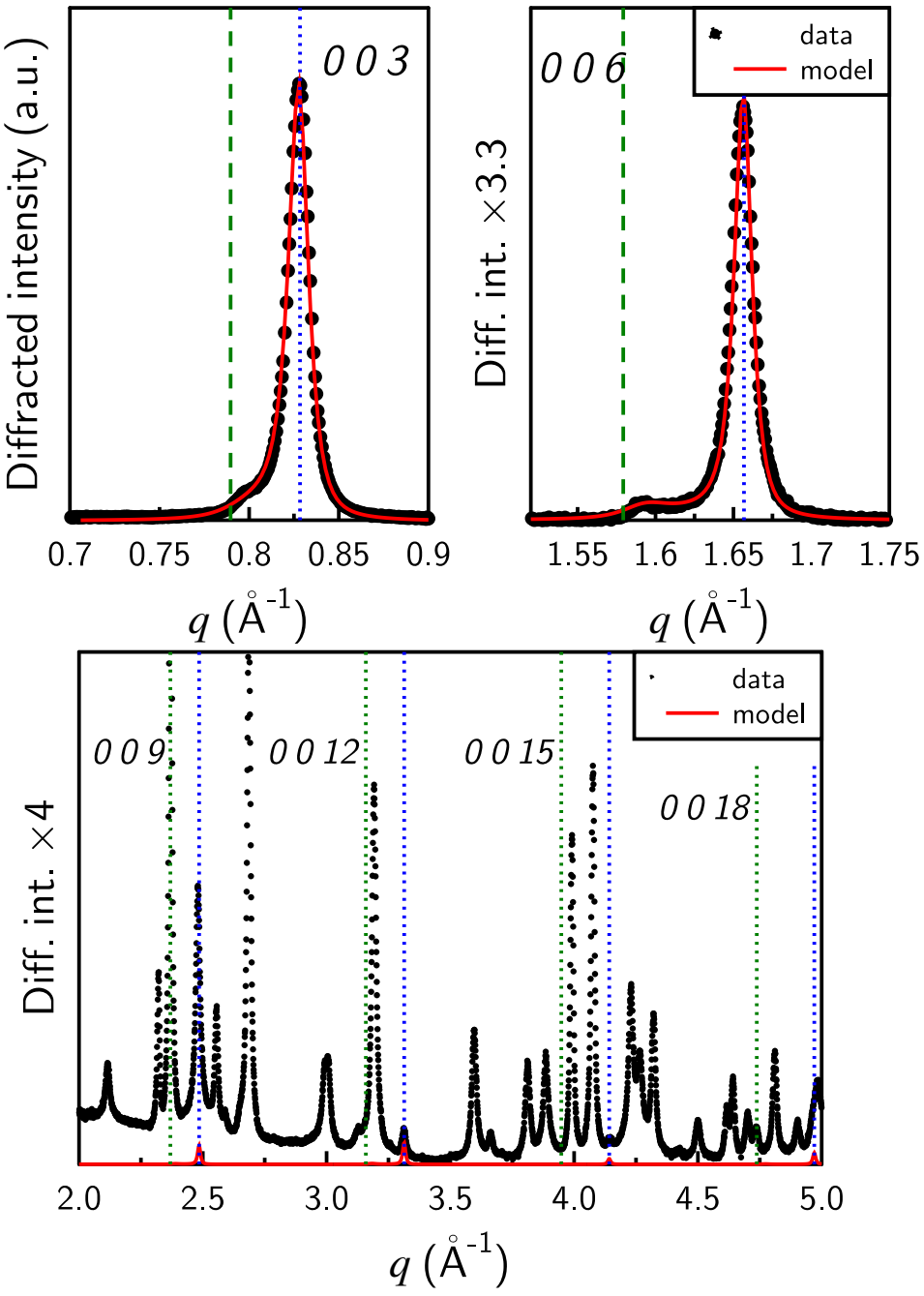

Figure S9 – Interstratification processes on micro-Co-GR sample during an exchange with C(IV) species at $V/V_r = 18.7$ (Solution concentration: 10 mmol·L^{-1} NaCl and 40 mmol·L^{-1} $NaHCO_3$). Green dashed line was the initial position of the *00l* reflections of micro-Co-GR(Cl) phase (for $V/V_r = 0$). Blue dashed line was the initial position of the *00l* reflections of micro-Co-GR(C(IV)) phase (for $V/V_r = 20.4$)).

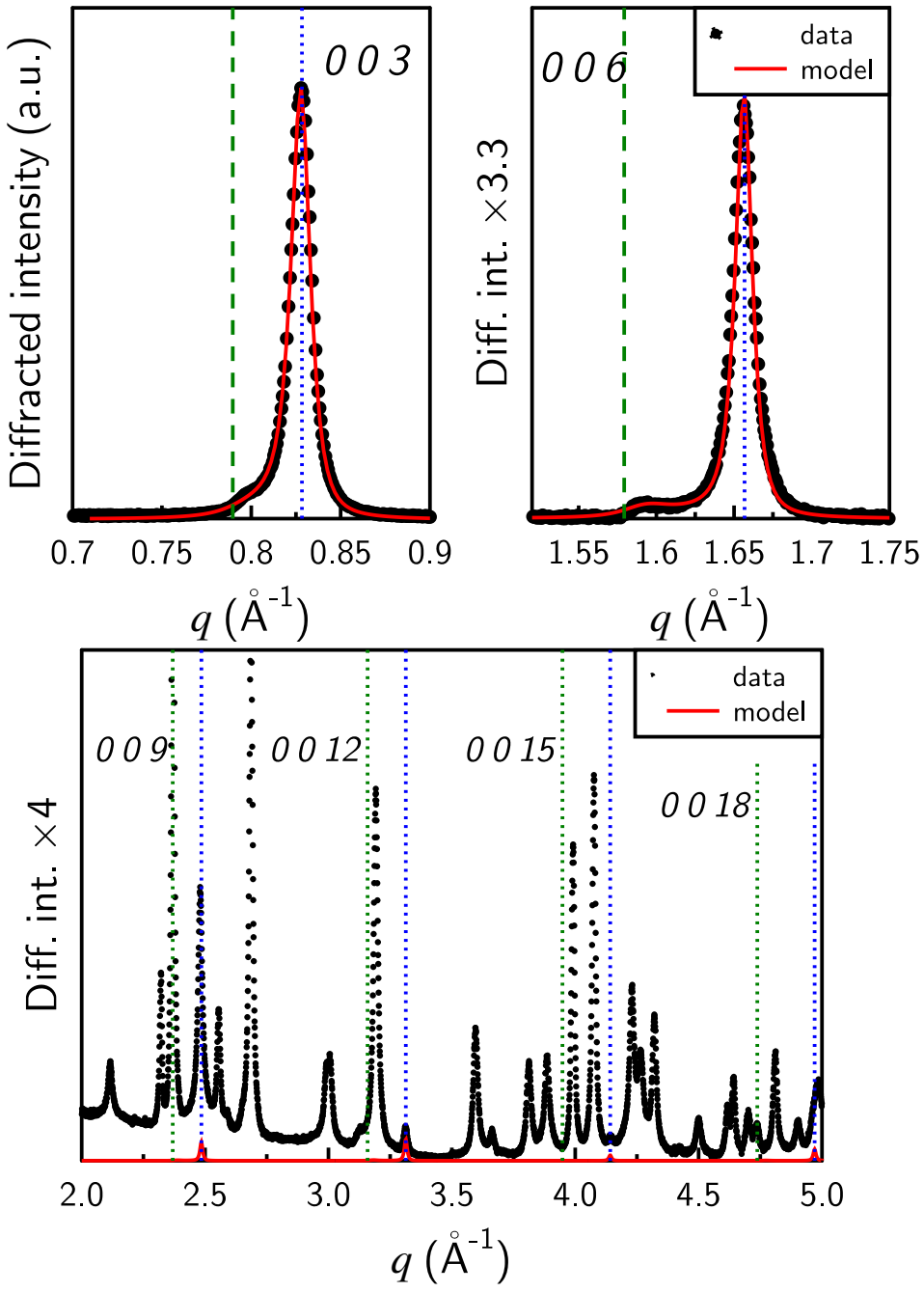

Figure S10 – Interstratification processes on micro-Co-GR sample during an exchange with C(IV) species at $V/V_r = 20.4$ (Solution concentration: 10 mmol·L^{-1} NaCl and 40 mmol·L^{-1} $NaHCO_3$). Green dashed line was the initial position of the *00l* reflections of micro-Co-GR(Cl) phase (for $V/V_r = 0$). Blue dashed line was the initial position of the *00l* reflections of micro-Co-GR(C(IV)) phase (for $V/V_r = 20.4$)).

B.2 Experiment "Na_2CO_3−XRD" - 2 layer interstratification model

Table S2 – List of parameters to model XRD patterns of interstratified micro-Co-GR phase with 2 layers, Gr-Cl and GR-CO_3, during "Na_2CO_3-XRD" experiment with MLM2C code. This table is the same as Table V.2.

V/V_r	R	W_{Cl}	W_{CO_3}	P_{ClCl}	$P_{CO_3CO_3}$	c^* Gr-Cl (Å)	c^* Gr-CO_3 (Å)	σ^*
0.0	1	1	0	1	-	7.95	-	0.65
1.3	1	0.94	0.06	0.997	0.953	7.965	7.52	0.80
3.8	1	0.86	0.14	0.992	0.951	7.965	7.58	0.80
6.8	1	0.57	0.43	0.965	0.954	7.975	7.61	0.80
7.7	1	0.455	0.545	0.964	0.970	7.98	7.62	1
8.9	1	0.26	0.74	0.95	0.982	7.97	7.63	0.75
13.2	1	0	1	-	1.000	-	7.62	0.70
16.6	1	0	1	-	1.000	-	7.61	0.7

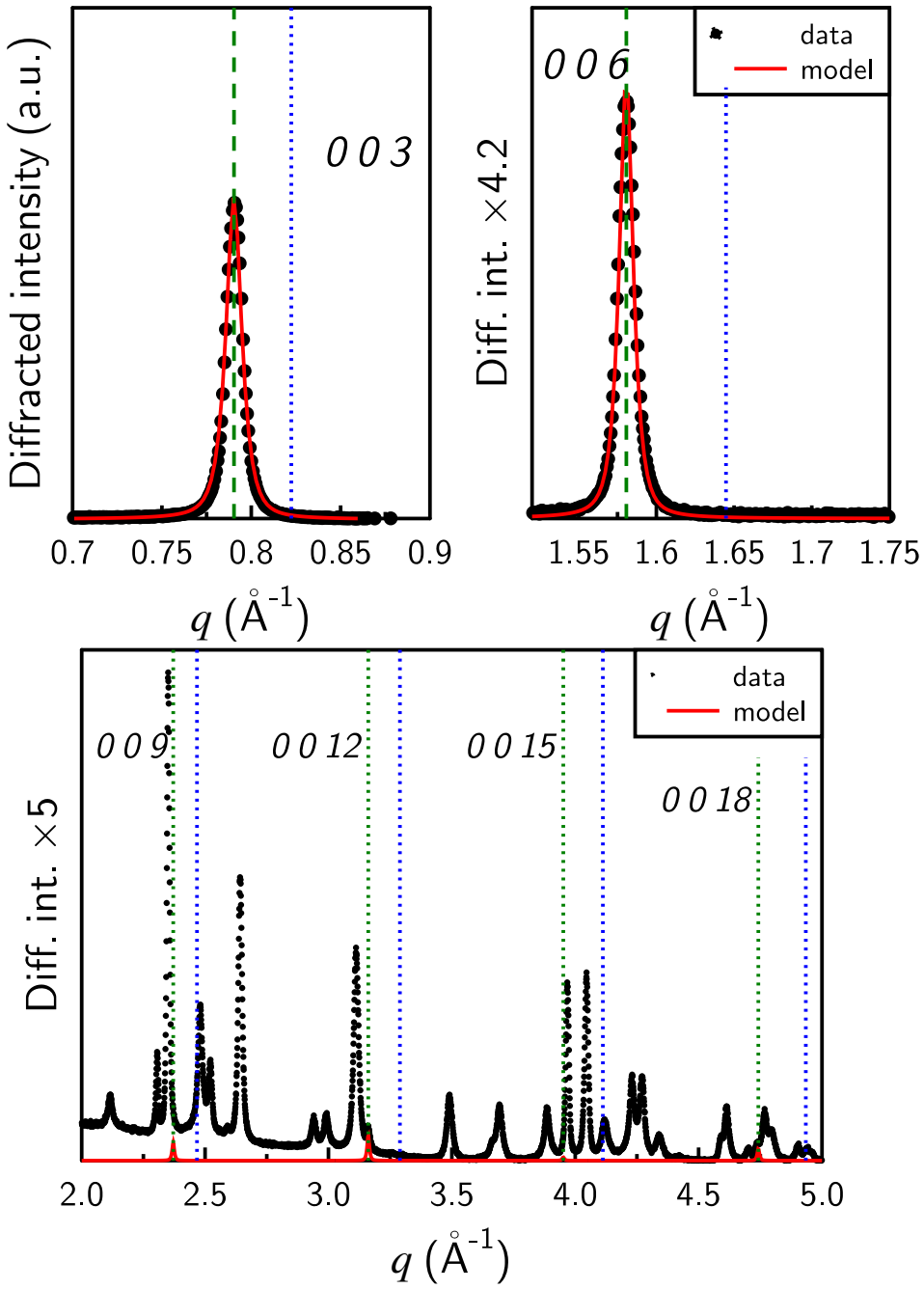

Figure S11 – Initial structure of micro-Co-GR(Cl) sample before an exchange with carbonate species. Green dashed line was the initial position of the *00l* reflections of micro-Co-GR(Cl) phase (for $V/V_r = 0$). Blue dashed line was the initial position of the *00l* reflections of micro-Co-GR(C(IV)) phase (for $V/V_r = 16.6$)).

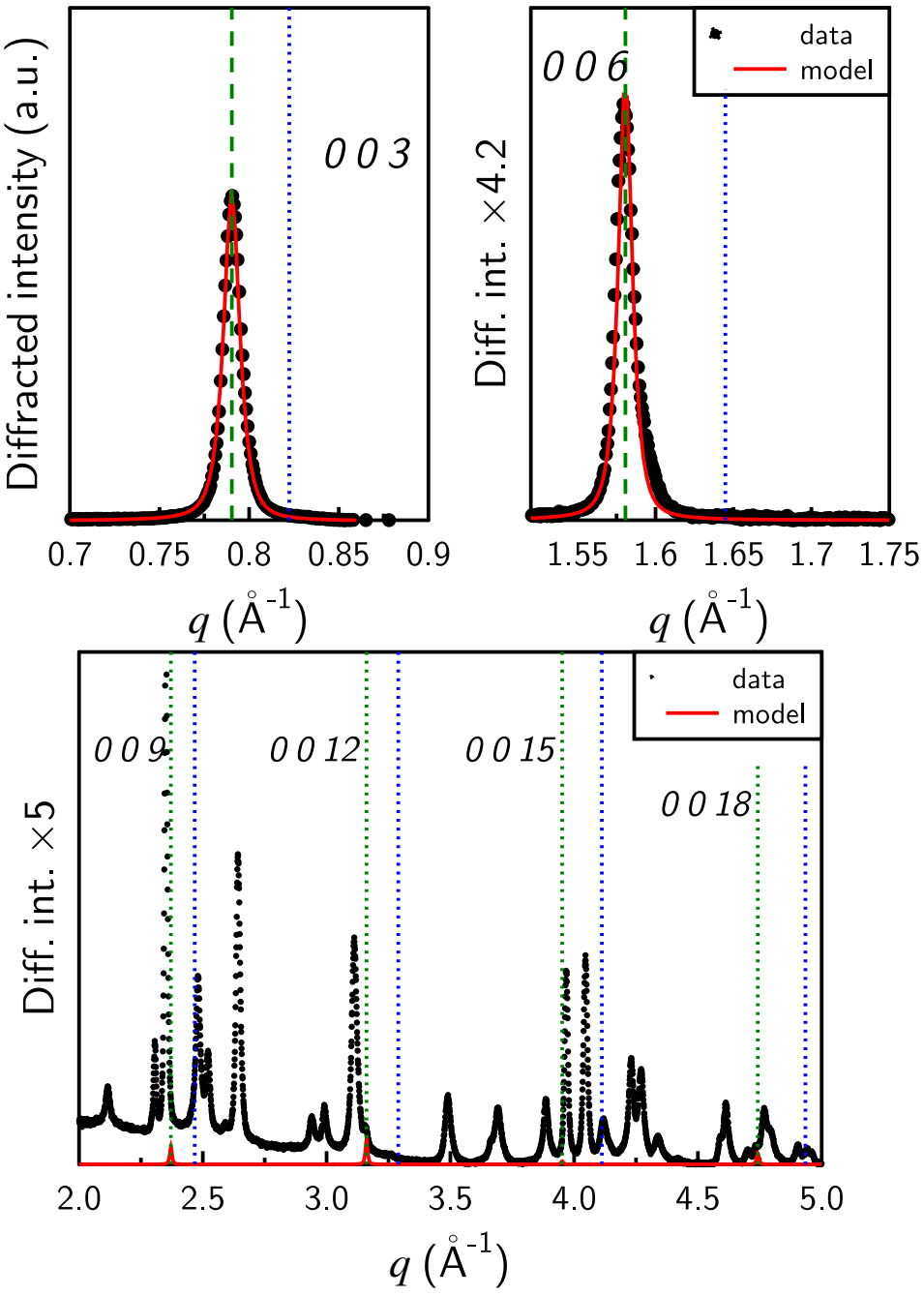

Figure S12 – Interstratification processes on micro-Co-GR sample with a interstratification of 2 layers during an exchange with carbonate species at $V/V_r = 0$ (Solution concentration: 40 mmol·L^{-1} NaCl and 10 mmol·L^{-1} Na_2CO_3). Green dashed line was the initial position of the *00l* reflections of micro-Co-GR(Cl) phase (for $V/V_r = 0$). Blue dashed line was the initial position of the *00l* reflections of micro-Co-GR(C(IV)) phase (for $V/V_r = 16.6$)).

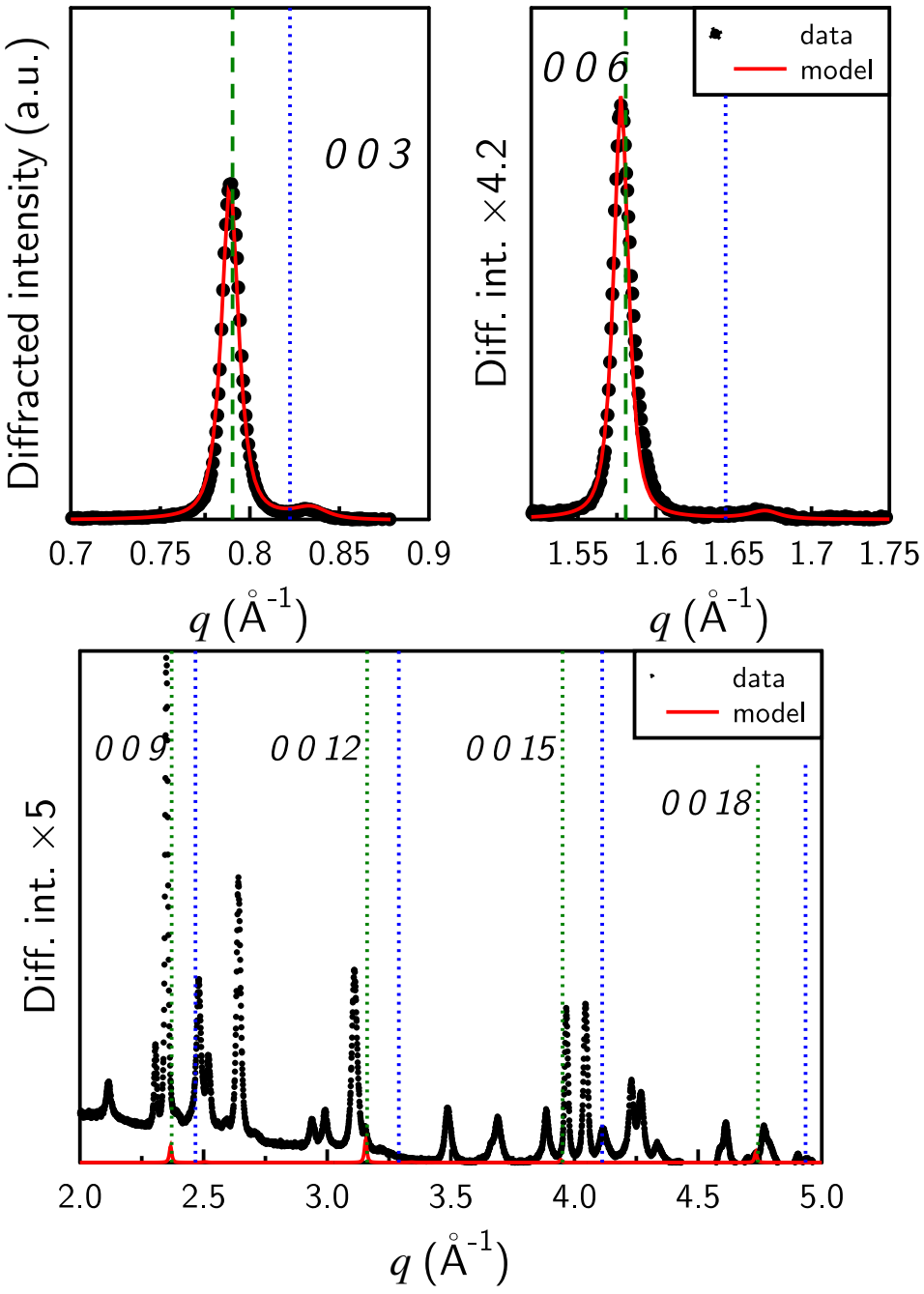

Figure S13 – Interstratification processes on micro-Co-GR sample with a interstratification of 2 layers during an exchange with carbonate species at $V/V_r = 1.3$ (Solution concentration: 40 mmol·L^{-1} NaCl and 10 mmol·L^{-1} Na_2CO_3). Green dashed line was the initial position of the *00l* reflections of micro-Co-GR(Cl) phase (for $V/V_r = 0$). Blue dashed line was the initial position of the *00l* reflections of micro-Co-GR(C(IV)) phase (for $V/V_r = 16.6$)).

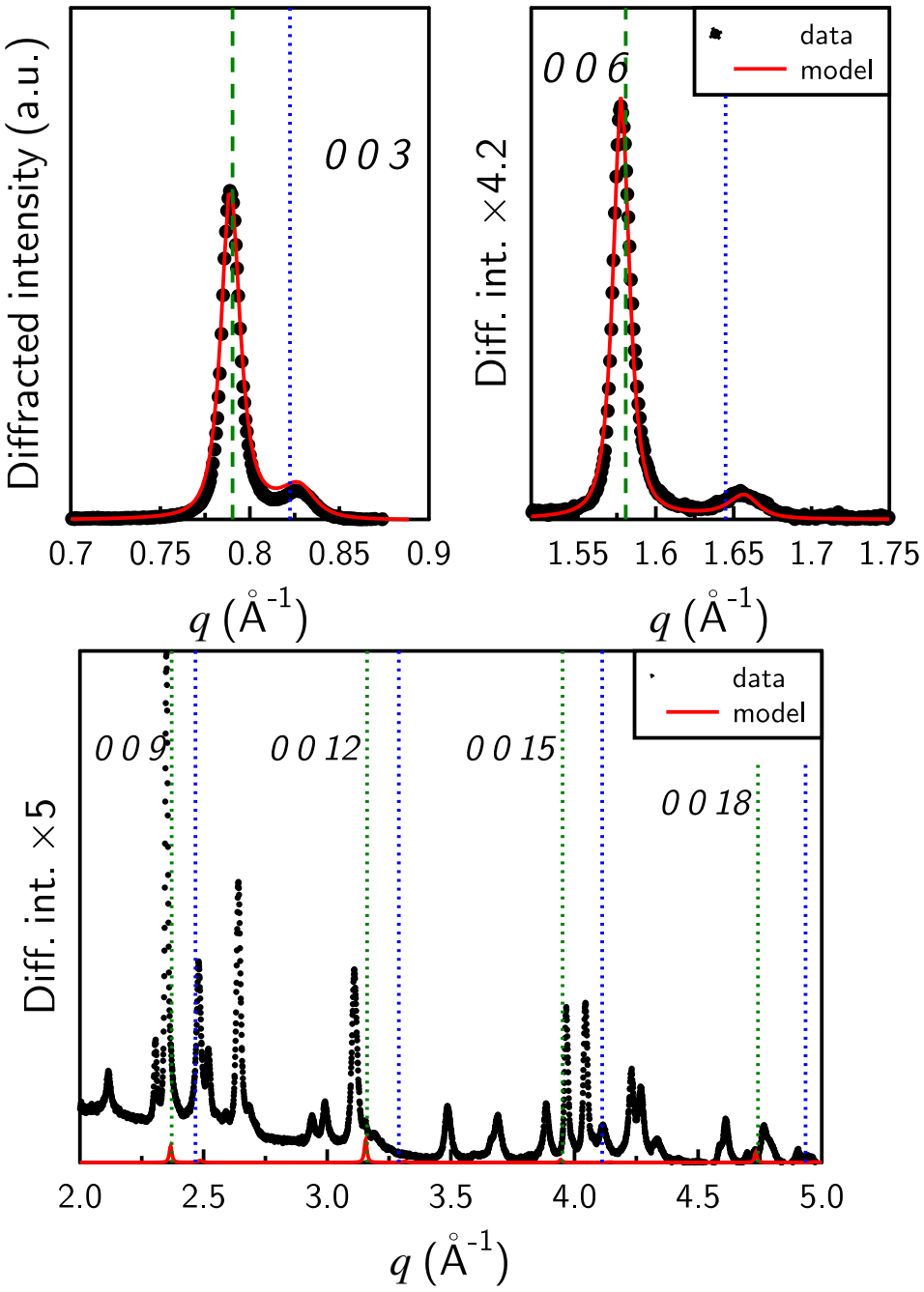

Figure S14 – Interstratification processes on micro-Co-GR sample with a interstratification of 2 layers during an exchange with carbonate species at $V/V_r = 3.8$ (Solution concentration: 40 mmol·L^{-1} NaCl and 10 mmol·L^{-1} Na_2CO_3). Green dashed line was the initial position of the *00l* reflections of micro-Co-GR(Cl) phase (for $V/V_r = 0$). Blue dashed line was the initial position of the *00l* reflections of micro-Co-GR(C(IV)) phase (for $V/V_r = 16.6$)).

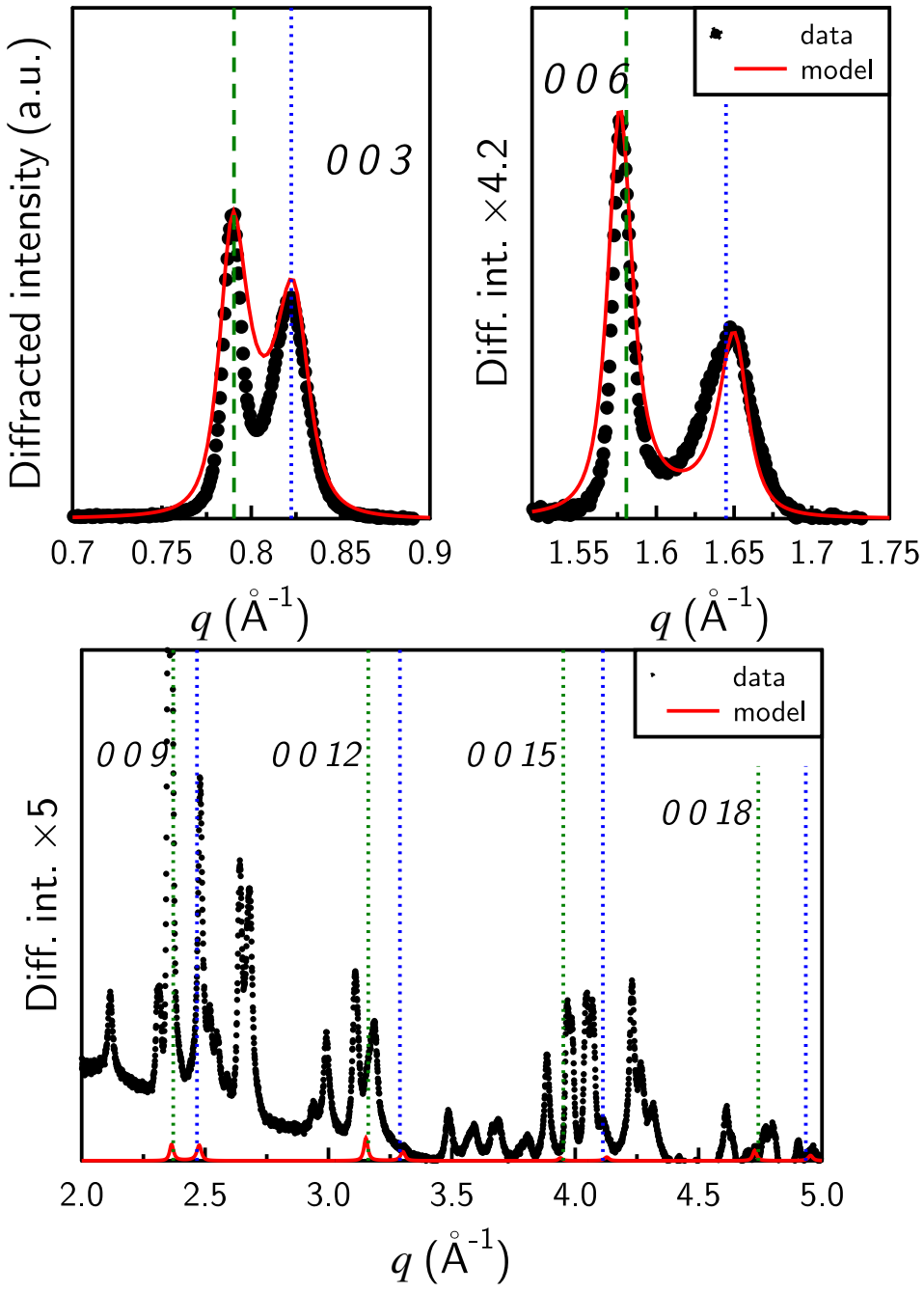

Figure S15 – Interstratification processes on micro-Co-GR sample with a interstratification of 2 layers during an exchange with carbonate species at $V/V_r = 6.8$ (Solution concentration: 40 mmol·L^{-1} NaCl and 10 mmol·L^{-1} Na_2CO_3). Green dashed line was the initial position of the *00l* reflections of micro-Co-GR(Cl) phase (for $V/V_r = 0$). Blue dashed line was the initial position of the *00l* reflections of micro-Co-GR(C(IV)) phase (for $V/V_r = 16.6$)).

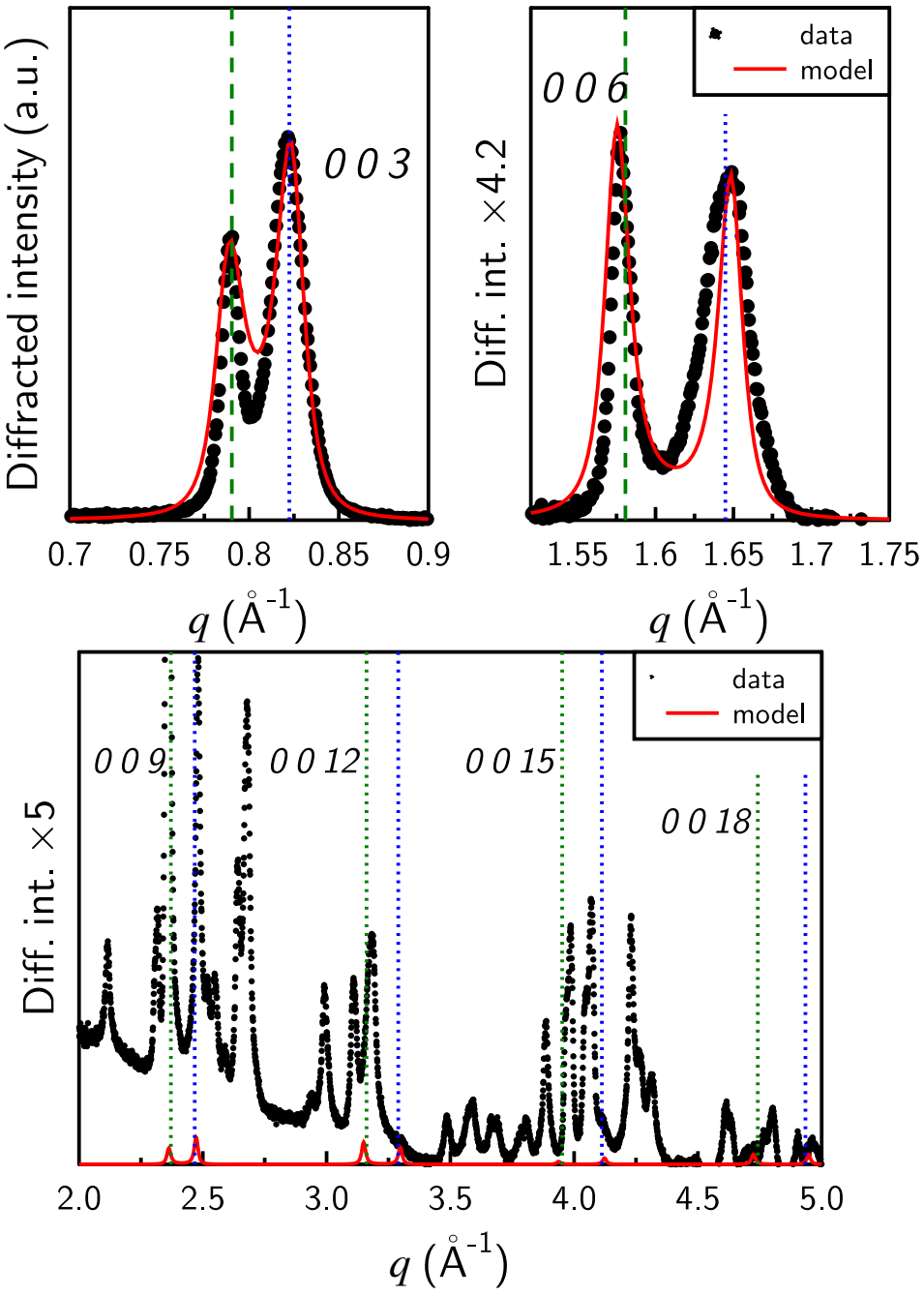

Figure S16 – Interstratification processes on micro-Co-GR sample with a interstratification of 2 layers during an exchange with carbonate species at $V/V_r = 7.7$ (Solution concentration: 40 mmol·L^{-1} NaCl and 10 mmol·L^{-1} Na_2CO_3). Green dashed line was the initial position of the *00l* reflections of micro-Co-GR(Cl) phase (for $V/V_r = 0$). Blue dashed line was the initial position of the *00l* reflections of micro-Co-GR(C(IV)) phase (for $V/V_r = 16.6$)).

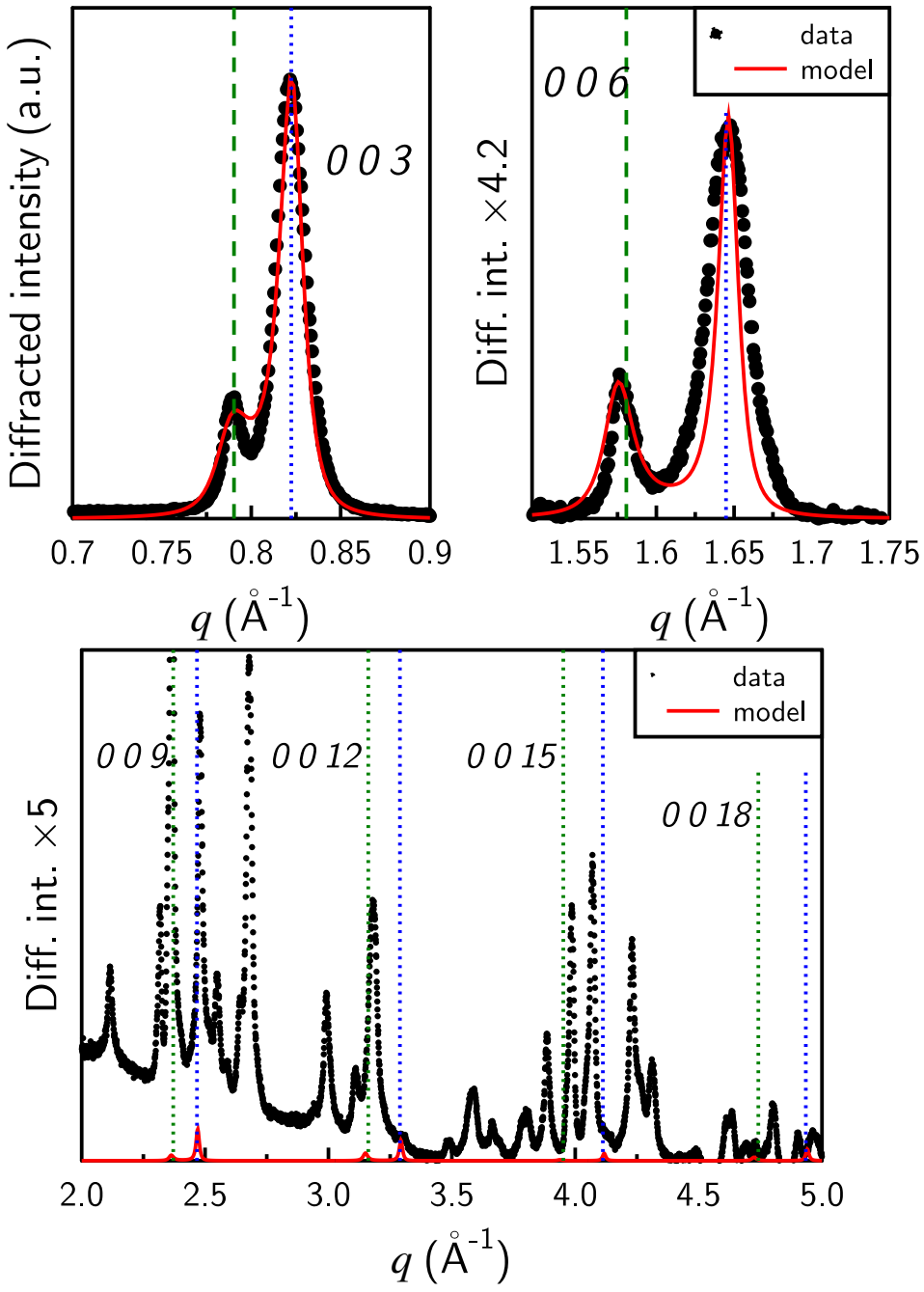

Figure S17 – Interstratification processes on micro-Co-GR sample with a interstratification of 2 layers during an exchange with carbonate species at $V/V_r = 8.9$ (Solution concentration: 40 mmol·L^{-1} NaCl and 10 mmol·L^{-1} Na_2CO_3). Green dashed line was the initial position of the *00l* reflections of micro-Co-GR(Cl) phase (for $V/V_r = 0$). Blue dashed line was the initial position of the *00l* reflections of micro-Co-GR(C(IV)) phase (for $V/V_r = 16.6$)).

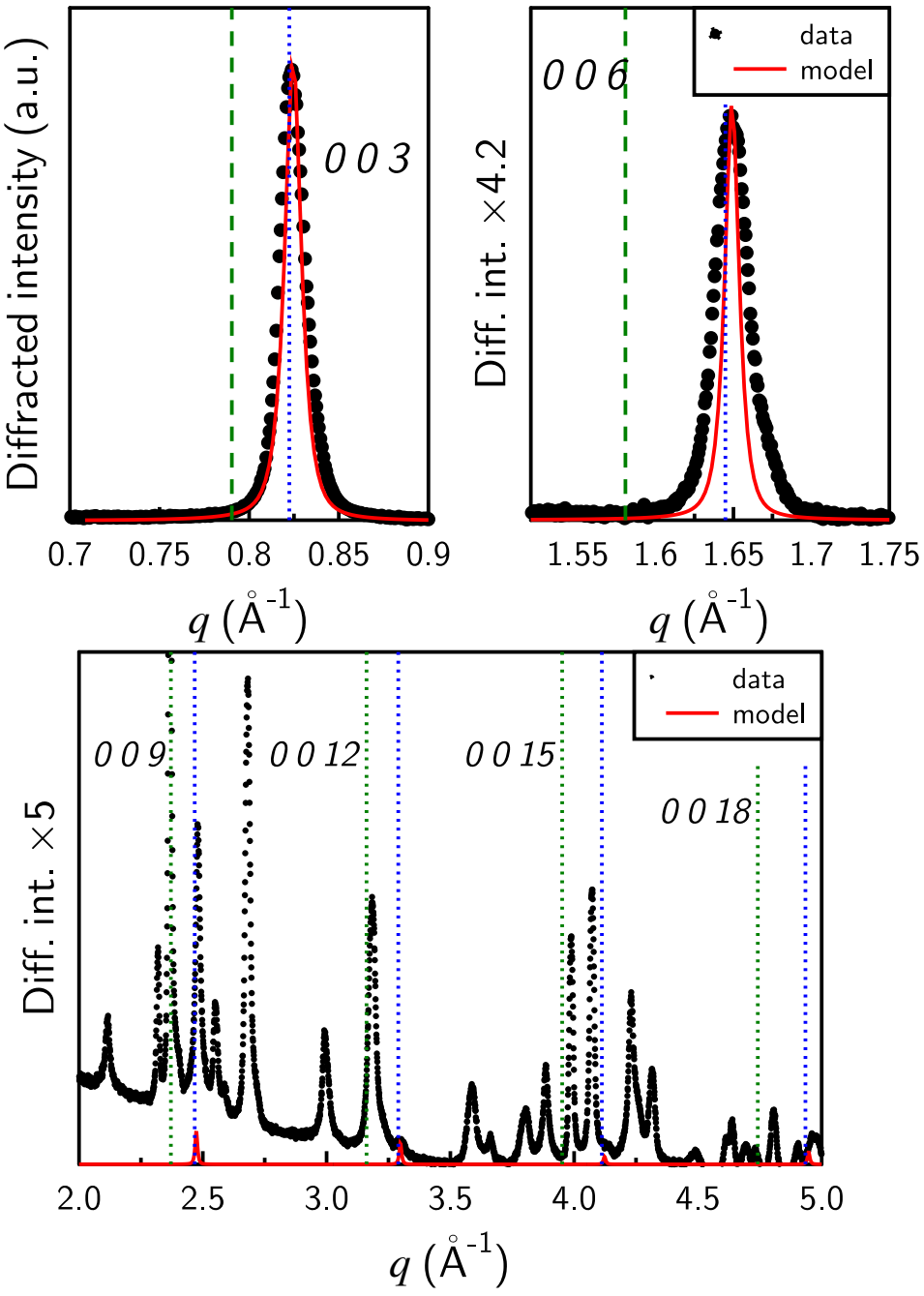

Figure S18 – Interstratification processes on micro-Co-GR sample with a interstratification of 2 layers during an exchange with carbonate species at $V/V_r = 13.2$ (Solution concentration: 40 mmol·L^{-1} NaCl and 10 mmol·L^{-1} Na_2CO_3). Green dashed line was the initial position of the *00l* reflections of micro-Co-GR(Cl) phase (for $V/V_r = 0$). Blue dashed line was the initial position of the *00l* reflections of micro-Co-GR(C(IV)) phase (for $V/V_r = 16.6$)).

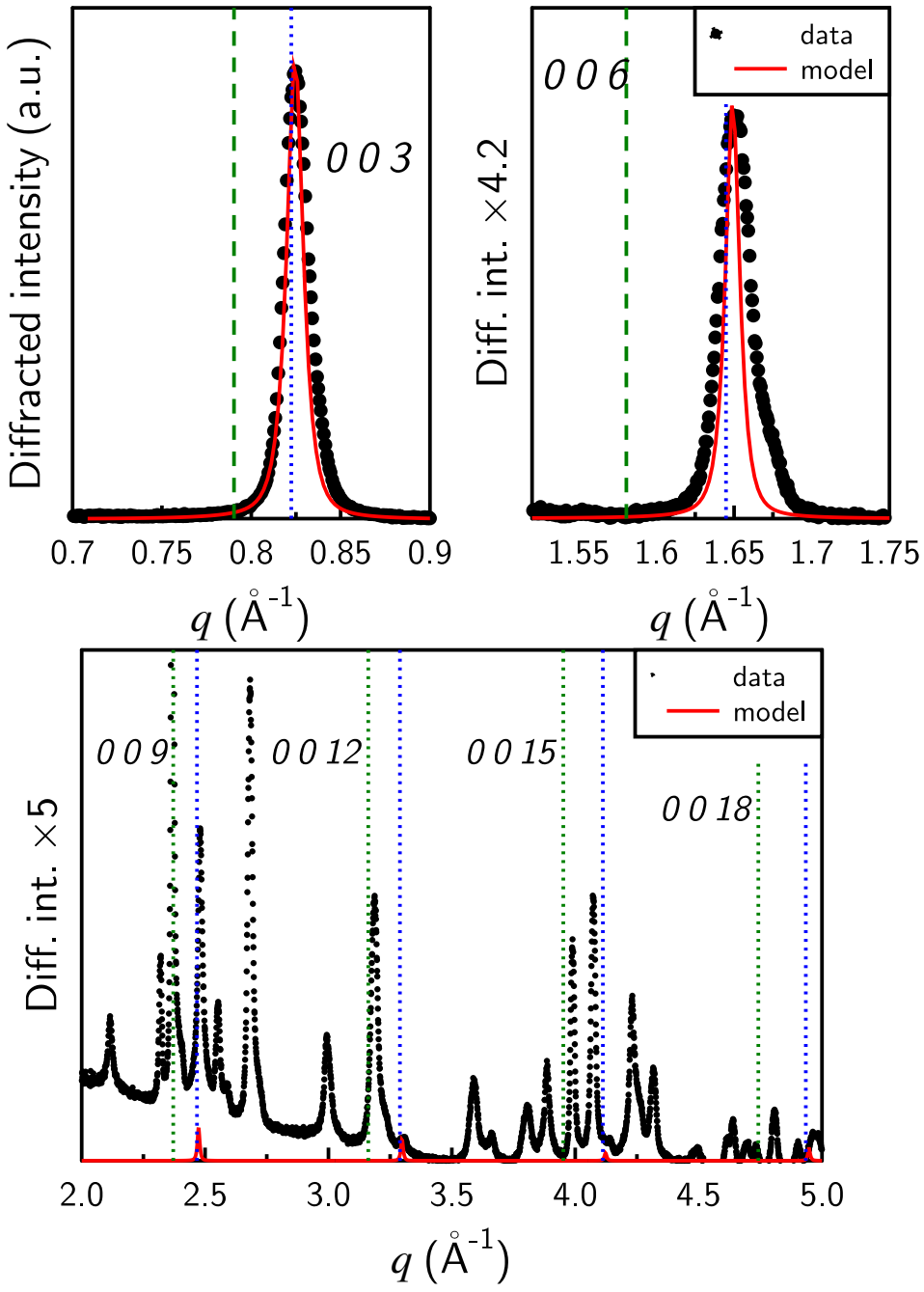

Figure S19 – Interstratification processes on micro-Co-GR sample with a interstratification of 2 layers during an exchange with carbonate species at $V/V_r = 16.6$ (Solution concentration: 40 mmol·L^{-1} NaCl and 10 mmol·L^{-1} Na_2CO_3). Green dashed line was the initial position of the *00l* reflections of micro-Co-GR(Cl) phase (for $V/V_r = 0$). Blue dashed line was the initial position of the *00l* reflections of micro-Co-GR(C(IV)) phase (for $V/V_r = 16.6$)).

B.3 Experiment "$NaHCO_3$−XRD" - 3 layer interstratification model

Table S3 – List of parameters to model XRD patterns of interstratified micro-Co-GR phase with 3 layers, Gr-Cl, GR-CO_3−1 and Gr-CO_3−2, during "Na_2CO_3-XRD" experiment with MLM2C code. This table is the same as Table V.3.

		Abundance			Gr-Cl			Gr-CO_3−1 & Gr-CO_3−2 interstratified				
Model	V/V_r	W_{Cl}	W_{CO_3-1}	W_{CO_3-2}	P_{ClCl}	c^* Gr-Cl	σ∗	$P_{CO_3CO_3-1}$	$P_{CO_3CO_3-2}$	c^* Gr-CO_3−1	c^* Gr-CO_3−2	σ*
2 layers	0.0	1	0	0	1	7.950	0.55	-	-	-	-	0.55
	1.3	0.94	0.06	0	0.997	7.950	0.65	0.953	-	7.520	-	0.65
	3.8	0.86	0.14	0	0.992	7.965	0.80	0.951	-	7.580	-	0.80
3 layers	6.8	0.68	0.21	0.11	1	7.970	1.20	0.890	0.796	7.700	7.470	0.1
	7.7	0.53	0.30	0.16	1	7.970	1.20	0.890	0.796	7.700	7.470	0.1
	8.9	0.26	0.50	0.24	1	7.970	1.20	0.890	0.766	7.700	7.470	0.1
	13.2	0.00	0.68	0.32	-	-	-	0.890	0.766	7.680	7.470	0.1
	16.6	0.00	0.68	0.32	-	-	-	0.890	0.766	7.670	7.470	0.1

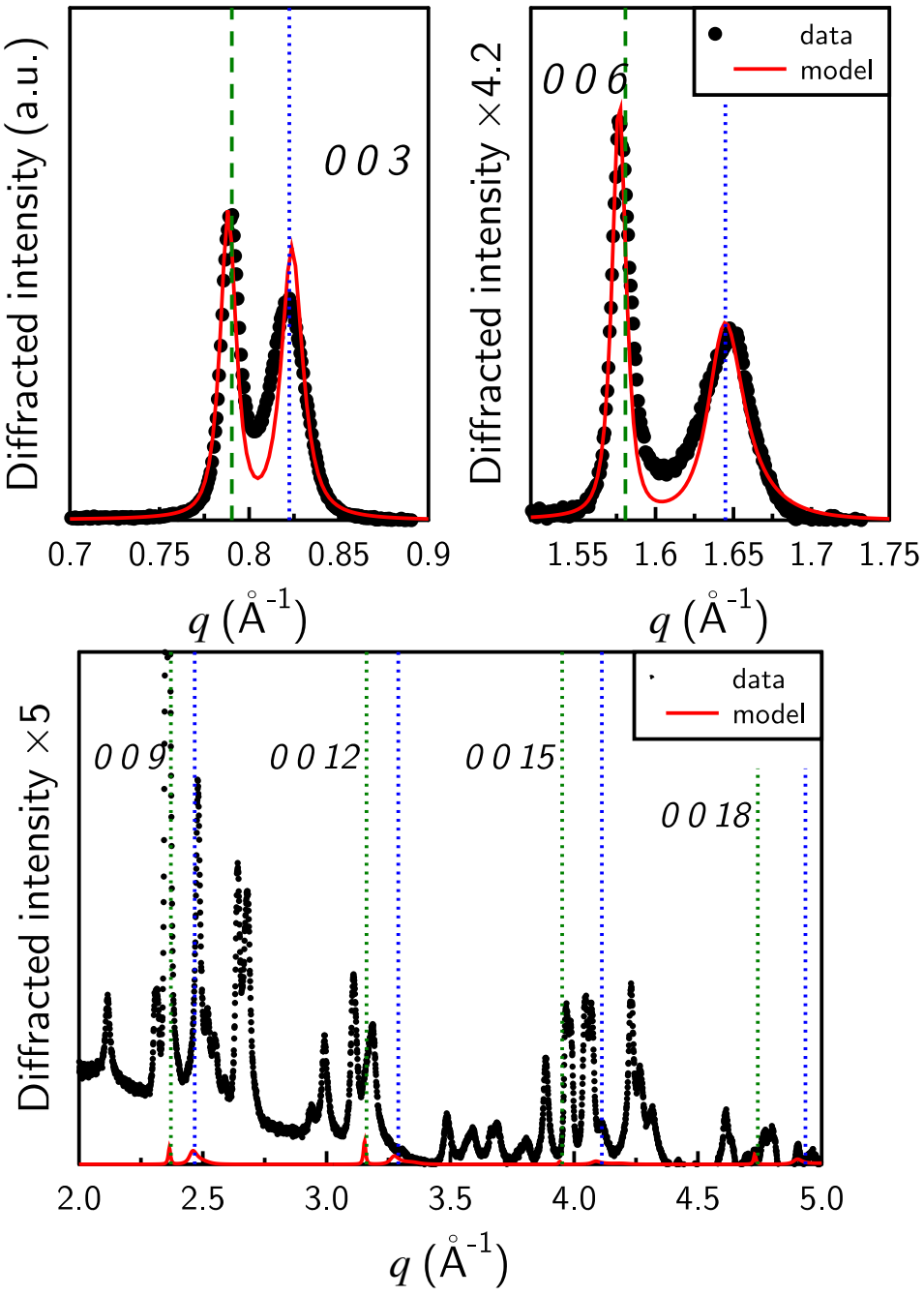

Figure S20 – Interstratification processes on micro-Co-GR sample with a interstratification of 3 layers during an exchange with carbonate species at $V/V_r = 6.8$ (Solution concentration: 40 mmol·L^{-1} NaCl and 10 mmol·L^{-1} Na_2CO_3). Green dashed line was the initial position of the *00l* reflections of micro-Co-GR(Cl) phase (for $V/V_r = 0$). Blue dashed line was the initial position of the *00l* reflections of micro-Co-GR(C(IV)) phase (for $V/V_r = 16.6$)).

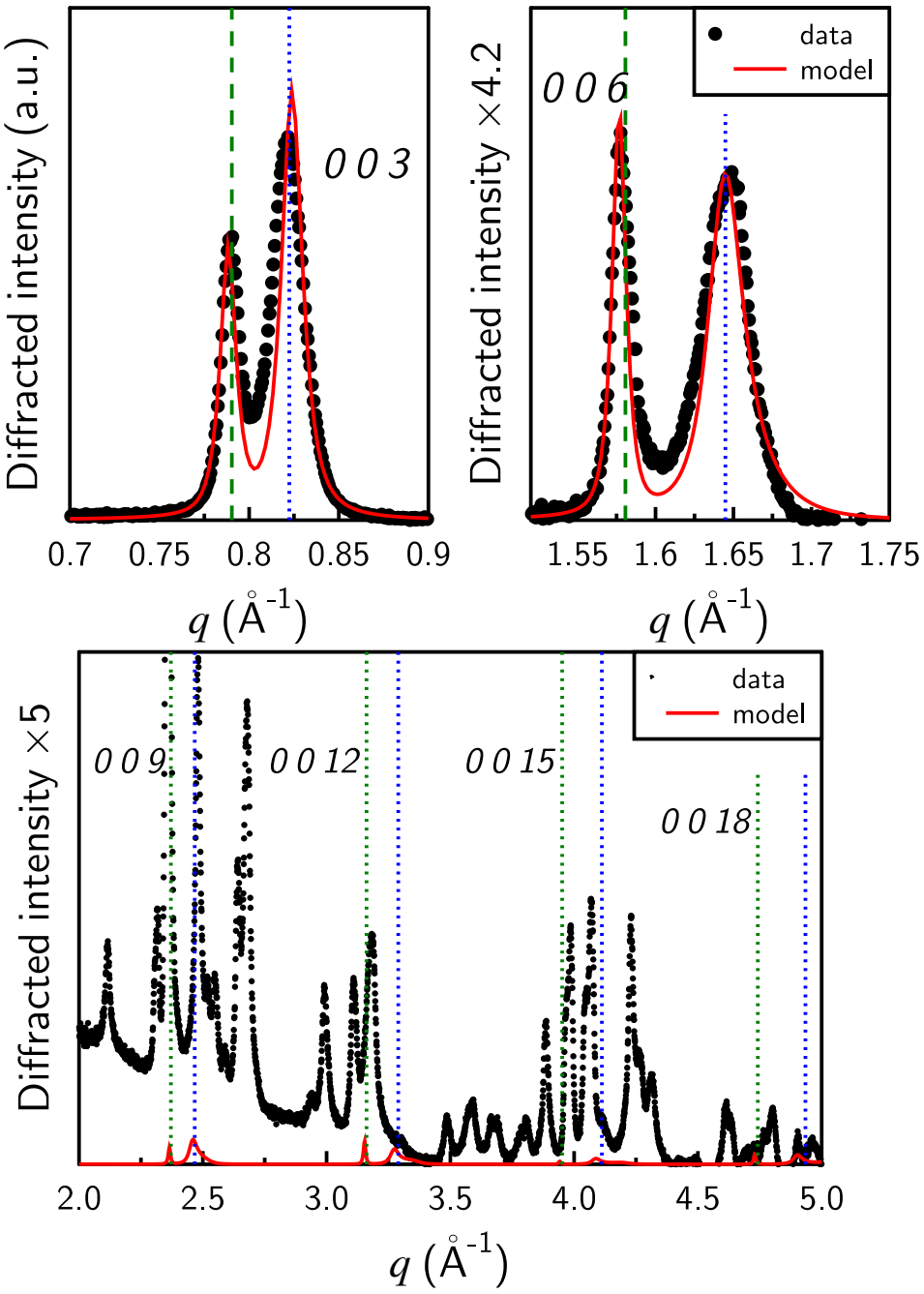

Figure S21 – Interstratification processes on micro-Co-GR sample with a interstratification of 3 layers during an exchange with carbonate species at $V/V_r = 7.7$ (Solution concentration: 40 mmol·L^{-1} NaCl and 10 mmol·L^{-1} Na_2CO_3). Green dashed line was the initial position of the *00l* reflections of micro-Co-GR(Cl) phase (for $V/V_r = 0$). Blue dashed line was the initial position of the *00l* reflections of micro-Co-GR(C(IV)) phase (for $V/V_r = 16.6$)).

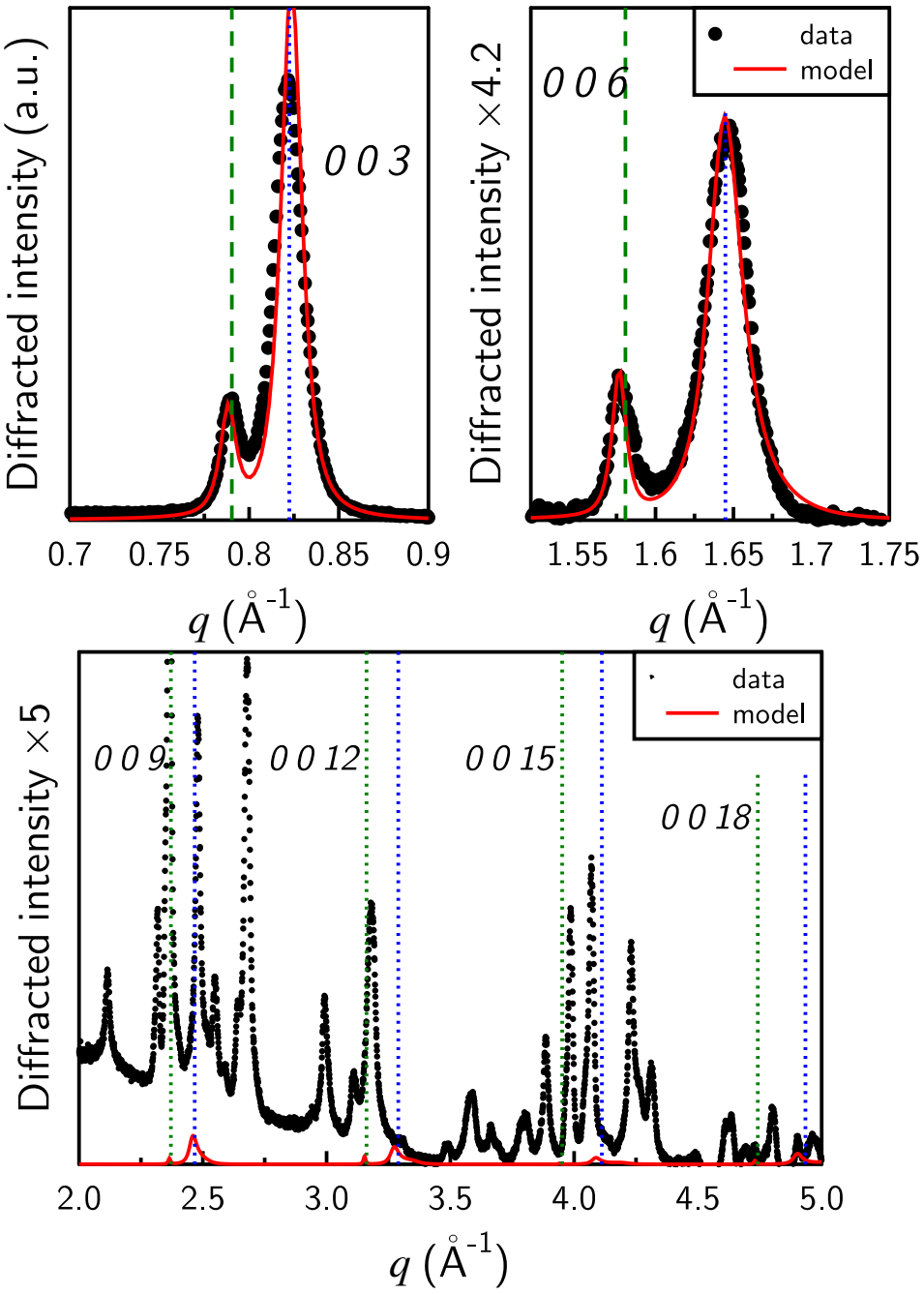

Figure S22 – Interstratification processes on micro-Co-GR sample with a interstratification of 3 layers during an exchange with carbonate species at $V/V_r = 8.9$ (Solution concentration: 40 mmol·L^{-1} NaCl and 10 mmol·L^{-1} Na_2CO_3). Green dashed line was the initial position of the *00l* reflections of micro-Co-GR(Cl) phase (for $V/V_r = 0$). Blue dashed line was the initial position of the *00l* reflections of micro-Co-GR(C(IV)) phase (for $V/V_r = 16.6$)).

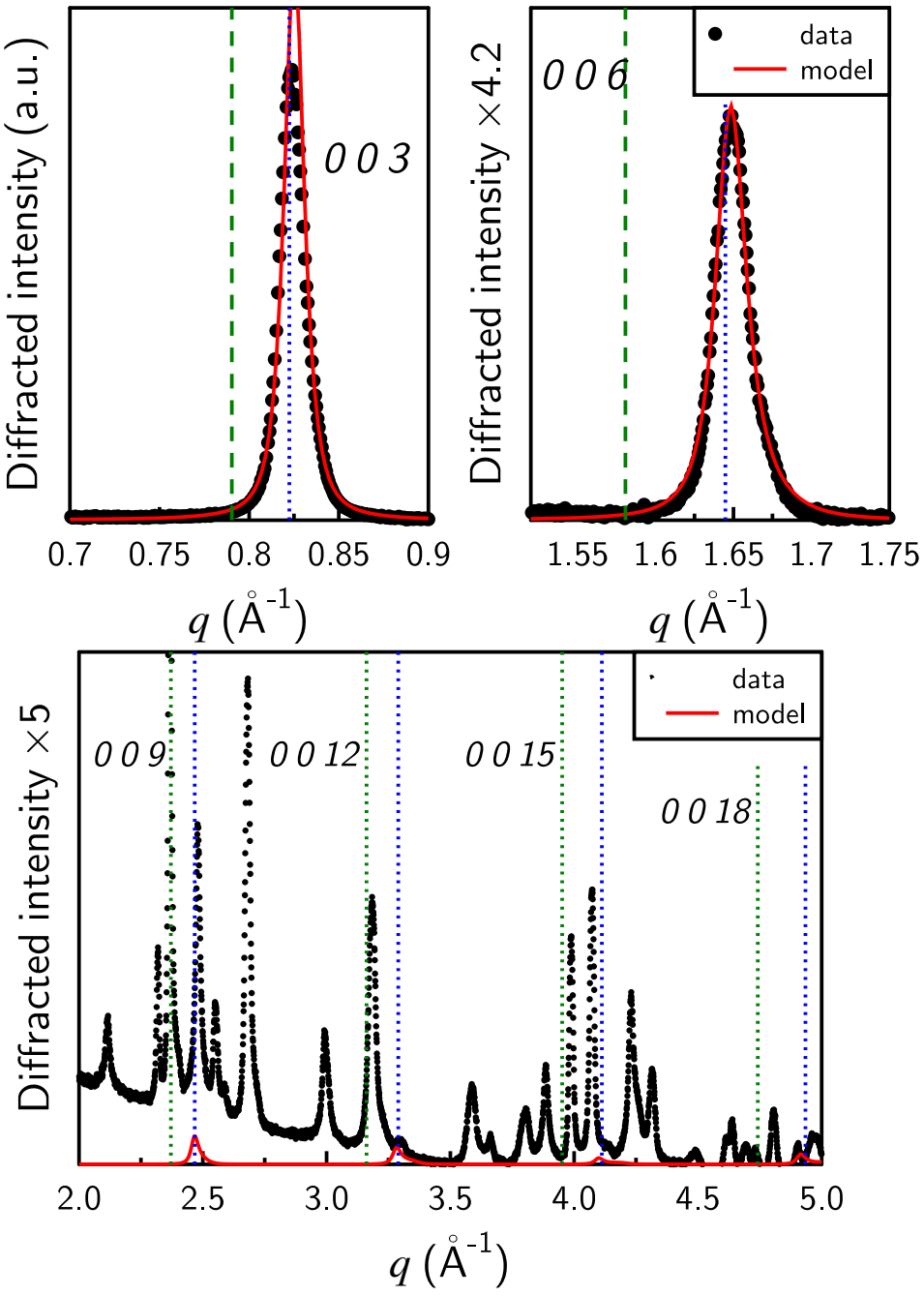

Figure S23 – Interstratification processes on micro-Co-GR sample with a interstratification of 3 layers during an exchange with carbonate species at $V/V_r = 13.2$ (Solution concentration: 40 mmol·L^{-1} NaCl and 10 mmol·L^{-1} Na_2CO_3). Green dashed line was the initial position of the *00l* reflections of micro-Co-GR(Cl) phase (for $V/V_r = 0$). Blue dashed line was the initial position of the *00l* reflections of micro-Co-GR(C(IV)) phase (for $V/V_r = 16.6$)).

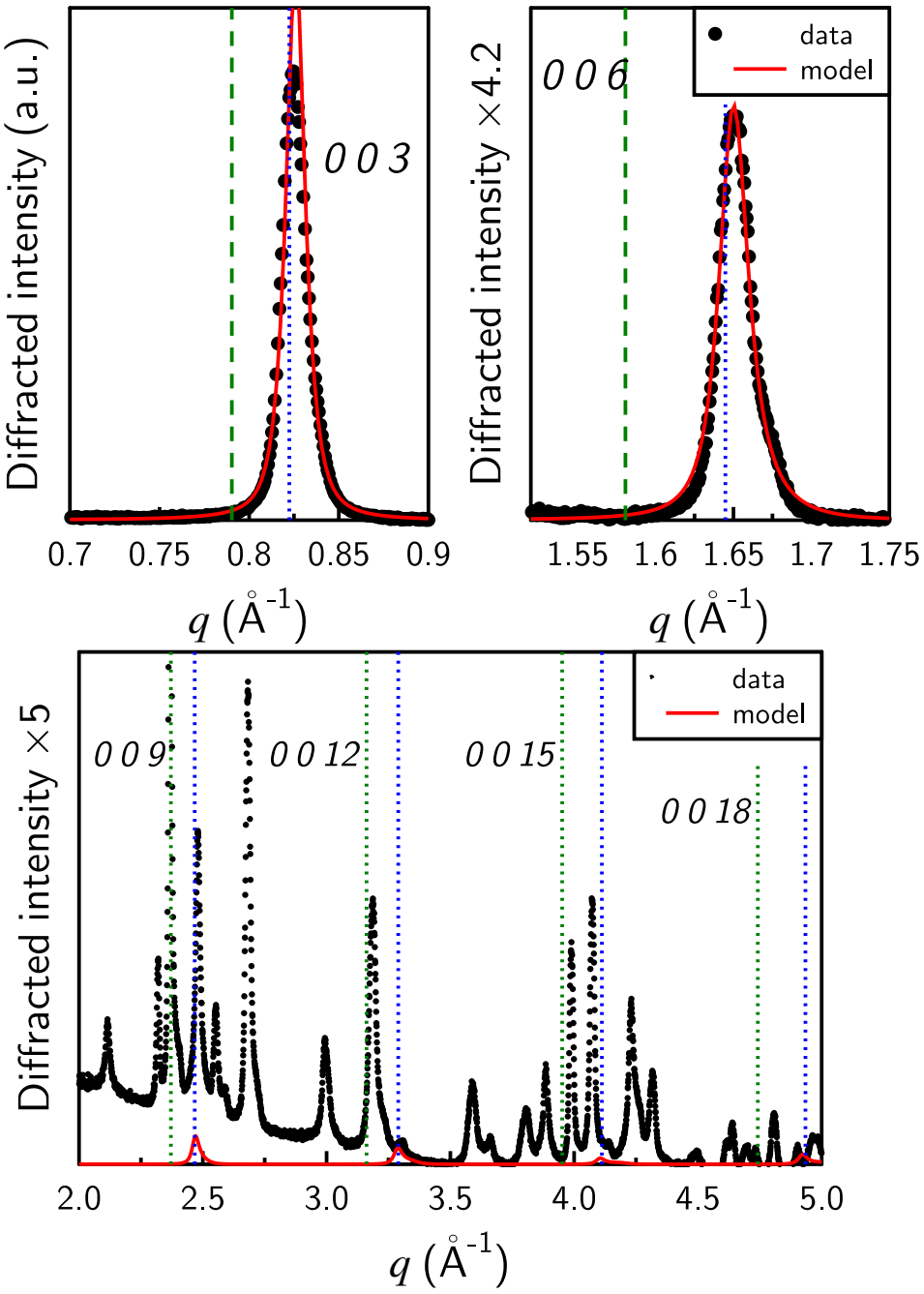

Figure S24 – Interstratification processes on micro-Co-GR sample with a interstratification of 3 layers during an exchange with carbonate species at $V/V_r = 16.6$ (Solution concentration: 40 mmol·L^{-1} NaCl and 10 mmol·L^{-1} Na_2CO_3). Green dashed line was the initial position of the *00l* reflections of micro-Co-GR(Cl) phase (for $V/V_r = 0$). Blue dashed line was the initial position of the *00l* reflections of micro-Co-GR(C(IV)) phase (for $V/V_r = 16.6$)).

APPENDIX C

BATCH EXCHANGE EXPERIMENTS

For every experiment, each stock and sampled solutions have been measured twice by HPLC for Cl^- and SO_4^{2-} concentrations. These two measurements were made in the same collection bottle. Some samples have four measurements because they were analyzed at two different dilutions and measured twice at each dilution. The mass of the solid sample is given as it was measured, so without any correction. Dissolved Inorganic Carbon (DIC) has been measured once by alkalinity except for stock solutions containing carbonate species that have been measured at the start and at the end of the experiments.

C.1 $Cl^- \leftrightharpoons SO_4^{2-}$ exchange

C.1.1 Protocol

Table S1 – Nomenclature and prepared concentrations of solutions used for batch experiments involving sulphate ions

Solution name	Concentration NaCl (mmol·L^{-1})	Concentration Na2SO4 (mmol·L^{-1})
Cl50	50	0
S25	0	25
S15	0	15
S5/Cl40	40	5
S2.5/Cl45	45	2.5
S1/Cl48	48	1
S0.5/Cl49	49	0.5

Table S2 – Protocol for the batch exchange experiments of micro-Co-GR (see Table S1 for nomenclature of solutions, AEC - anionic exchange capacity)

Protocol	Exp Micro S25	Exp Micro S5/Cl40	Exp Micro S2.5/Cl45	Exp Micro S1/Cl48	Exp Micro S0.5/Cl49
Equilibrium phase	200 mL Cl50				
Rinsing 1	30-40 mL Milli-Q Water Direct Filtration				
Exchange phase 1 - 1	200 mL S25	200 mL S5/Cl40	20 mL S2.5/Cl45	200 mL S1/Cl48	200 mL S0.5/Cl49
2	200 mL S25	201 mL S5/Cl40	40 mL S2.5/Cl45	200 mL S1/Cl48	200 mL S0.5/Cl49
3	200 mL S25	202 mL S5/Cl40	60 mL S2.5/Cl45	200 mL S1/Cl48	200 mL S0.5/Cl49
4	*End of this experiment*	203 mL S5/Cl40	100 mL S2.5/Cl45	200 mL S1/Cl48	200 mL S0.5/Cl49
5		204 mL S5/Cl40	200 mL S2.5/Cl45	200 mL S1/Cl48	200 mL S0.5/Cl49
6			200 mL S2.5/Cl45		
Rinsing 2	30-40 mL Milli-Q Water Direct Filtration				
Exchange phase 2 - 1		200 mL S25	200 mL S15	200 mL S25	200 mL S25
2			200 mL S15	200 mL S25	
Obtained parameters	Exchange stoichiometry + AEC	Surface equivalent fraction + Selectivity coefficents			

Table S3 – Protocol for the batch exchange experiments of nano-Co-GR (see Table S1 for nomenclature of solutions, AEC - anionic exchange capacity)

Protocol	Exp Nano S25	Exp Nano S5/Cl40	Exp Nano S2.5/Cl45
Equilibrium phase	200 mL Cl50		
Rinsing 1	30-40 mL Milli-Q Water Direct Filtration		
Exchange phase 1 - 1	200 mL S25	200 mL S5/Cl40	10 mL S2.5/Cl45
2	200 mL S25	200 mL S5/Cl40	10 mL S2.5/Cl45
3	200 mL S25	200 mL S5/Cl40	10 mL S2.5/Cl45
4	*End of this experiment*	200 mL S5/Cl40	15 mL S2.5/Cl45
5		200 mL S5/Cl40	20 mL S2.5/Cl45
6			20 mL S2.5/Cl45
Rinsing 2		30-40 mL Milli-Q Water Direct Filtration	
Exchange phase 2 - 1		200 mL S25	200 mL S15
2			200 mL S15
Obtained parameters	Exchange stoichiometry + AEC	Equivalent fraction + Selectivity coefficents	

C.1.2 Results

Table S4 – Measurements of batch experiment on micro-Co-GR sample with a solution containing 25 mmol·L^{-1} of Na_2SO_4 (Solution nomenclature in Table S1, Protocol in Table S2, Exp nb - Experiment number, Output conc. - Output concentration, <d.l. - inferior to detection limit, n.a. - not analyzed)

Exp nb	Type	Input solution	Masse (g) Initial	Final	Output conc. (mmol·L^{-1}) Cl^-	SO_4^{2-}
1	Micro-Co-GR sample		0.44			
	Stock solutions	Cl50			52.19	<d.l.
					52.06	<d.l.
		S25			<d.l.	26.61
					<d.l.	26.20
	Equilibrium phase	Cl50	200.01	195.67	53.38	<d.l.
					52.72	<d.l.
	Exchange phase 1-1	S25	200.01	n.a.	3.37	24.29
					3.39	24.51
	1-2	S25	200.05	197.34	0.08	26.05
					0.08	26.21
	1-3	S25	200.05	199.40	<d.l.	26.08
					<d.l.	26.31
2	Micro-Co-GR sample		0.5			
	Stock solutions	Cl50			52.19	<d.l.
					52.06	<d.l.
		S25			<d.l.	26.61
					<d.l.	26.20
					n.a.	25.47
	Equilibrium phase	Cl50	200.02	198.30	52.97	n.a.
	Exchange phase 1-1	S25	200.01	198.27	3.56	23.97
	1-2	S25	200.02	198.92	0.21	24.77
	1-3	S25	200.02	n.a.	0.07	25.38
3	Micro-Co-GR sample		0.49			
	Stock solutions	Cl50			51.77	0.02
					51.90	<d.l.
		S25			<d.l.	26.49
					<d.l.	25.76
	Equilibrium phase	Cl50	200.03	n.a.	52.97	0.03
					53.69	<d.l.
	Rinsing 1	Milli-Q water		38.77	2.68	<d.l.
					2.73	0.00
					2.76	0.03
					2.75	0.05
	Exchange phase 1-1	S25	200.01	197.30	3.84	23.29
					3.81	22.98
	1-2	S25	200.03	199.01	0.44	26.15
					0.43	25.70
	1-3	S25	200.01	198.90	0.04	26.20
					0.03	25.95

Table S5 – Measurements of batch experiment on micro-Co-GR sample with a solution containing 5 $mmol \cdot L^{-1}$ of Na_2SO_4 and 40 $mmol \cdot L^{-1}$ of NaCl (Solution nomenclature in Table S1, Protocol of Exp Micro S5/Cl40 in Table S2, Output conc. - Output concentration, <d.l. - inferior to detection limit, n.a. - not analyzed)

Type	Input solution	Masse (g) Initial	Final	Output conc. ($mmol \cdot L^{-1}$) Cl^-	SO_4^{2-}
Micro-Co-GR sample		0.4800			
Stock solutions	Cl50			51.77	0.02
				51.90	<d.l.
	S5/Cl40			41.84	5.22
				41.53	5.17
	S25			<d.l.	26.49
				<d.l.	25.76
Equilibrium phase	Cl50	200.05	197.4	53.77	0.02
				51.87	0.02
Rinsing 1	Milli-Q water		37.05	3.17	<d.l.
				3.13	<d.l.
				3.15	<d.l.
				3.09	<d.l.
Exchange phase 1-1	S5/Cl40	200.03	199.01	44.27	3.53
				44.42	3.53
1-2	S5/Cl40	200.02	n.a.	42.49	4.71
				42.43	4.69
1-3	S5/Cl40	200.06	199.59	41.89	5.12
				41.43	4.99
1-4	S5/Cl40	200.03	198.3	41.58	5.12
				41.03	5.00
1-5	S5/Cl40	200.04	199.2	41.35	5.13
				40.73	4.88
Rinsing 2	Milli-Q water		28.85	3.82	0.27
				3.83	0.27
Exchange phase 2-1	S25			3.74	0.26
				3.76	0.25
2-2	S25	200.02	n.a.	0.16	25.09
				0.12	24.05

Table S6 – Measurements of batch experiment on micro-Co-GR sample with a solution containing 2.5 mmol·L^{-1} of Na_2SO_4 and 45 mmol·L^{-1} of NaCl (Solution nomenclature in Table S1, Protocol of Exp Micro S2.5/Cl45 in Table S2, Output conc. - Output concentration, <d.l. - inferior to detection limit, >d.l. - superior to detection limit, n.a. - not analyzed)

Type	Input solution	Masse (g) Initial	Final	Output conc. (mmol·L^{-1}) Cl^-	SO_4^{2-}	
	Micro-Co-GR sample		0.74			
	Stock solutions	Cl50			51.59	<d.l.
					51.54	<d.l.
		S2.5/Cl45			>d.l.	2.35
					>d.l.	2.35
					44.58	2.41
					44.45	2.40
		S15			<d.l.	15.76
					<d.l.	15.76
	Equilibrium phase	Cl50	206.02	203.15	53.59	>d.l.
					53.65	>d.l.
	Rinsing 1	Milli-Q water	40.03	39.90	4.36	>d.l.
					4.35	>d.l.
					4.42	>d.l.
					4.43	>d.l.
	Exchange phase 1-1	S2.5/Cl45	20.03	19.68	>d.l.	0.44
					>d.l.	0.44
					43.21	0.41
					43.04	0.40
	1-2	S2.5/Cl45	40	39.06	>d.l.	0.92
					>d.l.	0.92
					47.30	0.97
					47.19	0.96
	1-3	S2.5/Cl45	50.04	50.02	>d.l.	1.29
					>d.l.	1.29
					47.42	1.35
					46.81	1.33
	1-4	S2.5/Cl45	100.02	99.72	>d.l.	1.71
					>d.l.	1.71
					45.66	1.74
					45.58	1.73
	1-5	S2.5/Cl45	200.06	199.31	>d.l.	2.04
					>d.l.	2.04
					42.50	1.97
					42.31	1.97
	1-6	S2.5/Cl45	200.02	200.01	>d.l.	2.15
					>d.l.	2.15
					44.84	2.20
					44.69	2.19
	Rinsing 2	Milli-Q water	40	38.33	4.07	0.13
					4.09	0.13
					4.05	0.12
					4.05	0.12
	Exchange phase 2-1	S15	200.07	199.27	2.08	>d.l.

					2.09	>d.l.
					2.08	14.58
					2.06	14.34
	2-2	S15	200.05	164.39	0.29	>d.l.
					0.29	>d.l.
					0.21	15.84
					0.20	15.90

Table S7 – Measurements of batch experiment on micro-Co-GR sample with a solution containing 1 mmol·L^{-1} of Na_2SO_4 and 48 mmol·L^{-1} of NaCl (Solution nomenclature in Table S1, Protocol of Exp Micro S1/Cl48 in Table S2, Output conc. - Output concentration, <d.l. - inferior to detection limit, >d.l. - superior to detection limit, n.a. - not analyzed)

Type	Input solution	Masse (g) Initial	Final	Output conc. (mmol·L^{-1}) Cl^-	SO_4^{2-}
	Micro-Co-GR sample		0.61		
Stock solutions	Cl50			52.37	0.02
				53.12	0.02
	S1/Cl48			50.00	1.06
				49.98	1.06
	S25			0.02	26.01
				0.01	26.45
Equilibrium phase	Cl50	200.01	197.72	54.33	<dl
				54.78	<d.l.
Rinsing 1	Milli-Q water		36.04	3.37	<d.l.
				3.37	<d.l.
				3.39	<d.l.
				3.34	<d.l.
Exchange phase 1-1	S1/Cl49	200.01	200.15	49.43	0.92
				49.87	0.92
1-2	S1/Cl49	200.01	199.15	49.68	1.03
				50.36	1.03
1-3	S1/Cl49	200.02	199.26	50.05	1.04
				50.24	1.05
1-4	S1/Cl49	200.04	200.85	50.22	1.05
				49.63	1.05
1-5	S1/Cl49	200.04	199.27	50.52	1.05
				49.60	1.05
Rinsing 2	Milli-Q water		41.49	3.34	0.04
				3.36	0.05
				3.32	0.05
				3.32	0.04
Exchange phase 2-1	S25	200.03	199.85	3.61	23.89
				3.62	23.93
2-2	S25	200.03	199.82	0.31	25.87
				0.31	25.82

Table S8 – Measurements of batch experiment on micro-Co-GR sample with a solution containing 0.5 mmol·L^{-1} of Na_2SO_4 and 49 mmol·L^{-1} of NaCl (Solution nomenclature in Table S1, Protocol of Exp Micro S0.5/Cl49 in Table S2, Output conc. - Output concentration, <d.l. - inferior to detection limit, >d.l. - superior to detection limit, n.a. - not analyzed)

Type	Input solution	Masse (g) Initial	Final	Output conc. (mmol·L^{-1}) Cl^-	SO_4^{2-}
Micro-Co-GR sample		0.5			
Stock solutions	Cl50			52.19	0.02
				52.08	0.03
	S0.5/Cl49			51.75	0.52
				51.47	0.50
				52.27	0.51
				50.67	0.49
	S25			<d.l.	26.31
				0.01	25.47
Equilibrium phase	Cl50	200.02	197.36	53.57	0.06
				53.75	<d.l.
Rinsing 1	Milli-Q water		37.23	3.22	<d.l.
				3.23	<d.l.
				1.01	<d.l.
				1.00	<d.l.
Exchange phase 1-1	S0.5/Cl49	200.03	199.07	50.27	0.42
				50.45	0.44
1-2	S0.5/Cl49	200.02	199.54	50.92	0.50
				50.71	0.51
1-3	S0.5/Cl49	200.02	199.16	50.74	0.52
				49.57	0.51
1-4	S0.5/Cl49	200	199.92	50.08	0.51
				46.95	0.53
1-5	S0.5/Cl49	200.03	198.99	50.48	0.52
				50.72	0.54
Rinsing 2	Milli-Q water		26.43	4.14	0.02
				4.15	0.02
				1.89	<d.l.
				1.89	<d.l.
Exchange phase 2-1	S25	200.02	197.25	1.08	24.01
				1.09	24.24

Table S9 – Measurements of batch experiment on nano-Co-GR sample with a solution containing 25 mmol·L^{-1} of Na_2SO_4 (Solution nomenclature in Table S1, Protocol in Table S2, Output conc. - Output concentration, <d.l. - inferior to detection limit, n.a. - not analyzed)

Type	Input solution	Masse (g) Initial	Final	Output conc. (mmol·L^{-1}) Cl^-	SO_4^{2-}
Nano-Co-GR sample		0.2100			
Stock solutions	Cl50			47.48	0.02
				47.72	0.02
	S25			<d.l.	23.68
				0.01	23.43
Equilibrium phase	Cl50	200.02	196.43	48.08	0.03
				48.94	0.02
Rinsing 1	Milli-Q water		37.11	2.68	0.00
				2.65	<d.l.
Exchange phase 1-1	S25	200.01	198.53	1.28	23.93
				1.28	24.08
1-2	S25	200	n.a.	0.17	22.10
				0.12	25.69
1-3	S25	200.05	n.a.	0.02	25.20
				0.02	23.04

Table S11 – Measurements of batch experiment on nano-Co-GR sample with a solution containing 2.5 mmol·L^{-1} of Na_2SO_4 and 45 mmol·L^{-1} of NaCl (Solution nomenclature in Table S1, Protocol of Exp Nano S2.5/Cl45 in Table S2, Output conc. - Output concentration, <d.l. - inferior to detection limit, >d.l. - superior to detection limit, n.a. - not analyzed)

Type	Input solution	Masse (g) Initial	Final	Output conc. (mmol·L^{-1}) Cl^-	SO_4^{2-}
Nano-Co-GR sample		0.2			
Stock solutions	Cl50			51.59	<d.l.
				51.54	<d.l.
	S2.5/Cl40			>d.l.	2.35
				>d.l.	2.35
				44.58	2.41
				44.45	2.40
	S15			0.03	15.76
				-0.02	15.76
Equilibrium phase	Cl50	203.76	194.42	52.27	<d.l.
				52.28	<d.l.
Rinsing 1	Milli-Q water	40.04	40	3.28	<d.l.
				3.27	<d.l.
				3.27	<d.l.
				3.23	<d.l.
Exchange phase 1-1	S2.5/Cl40	10.04	10.1	>d.l.	1.01
				>d.l.	1.01
				37.48	1.02
				37.43	1.06
1-2	S2.5/Cl40	10.16	10.04	>d.l.	1.46

				>d.l.	1.46
				45.87	1.50
				45.74	1.50
	1-3	S2.5/Cl40	10	10.03	>d.l.	1.44
					>d.l.	1.44
					47.35	1.49
					47.13	1.47
	1-4	S2.5/Cl40	15.03	14.65	>d.l.	1.70
					>d.l.	1.71
					46.17	1.79
					46.19	1.78
	1-5	S2.5/Cl40	20.02	20.08	>d.l.	1.90
					>d.l.	1.90
					45.21	1.95
					45.09	1.93
	1-6	S2.5/Cl40	20.03	19.58	>d.l.	1.93
					>d.l.	1.93
					45.82	1.99
					45.65	1.97
	Rinsing 2	Milli-Q water	40.11	39.76	2.55	0.11
					2.55	0.11
					2.50	0.10
					2.49	0.10
Exchange phase	2-1	S25	200.15	199.49	0.55	>d.l.
					0.55	>d.l.
					0.49	15.35
					0.49	15.33
	2-2	S25	200.02	167.31	0.18	>d.l.
					0.18	>d.l.
					0.09	15.93
					0.09	15.86

Table S10 – Measurements of batch experiment on nano-Co-GR sample with a solution containing 5 mmol·L^{-1} of Na_2SO_4 and 40 mmol·L^{-1} of NaCl (Solution nomenclature in Table S1, Protocol of Exp Nano S5/Cl40 in Table S2, Output conc. - Output concentration, <d.l. - inferior to detection limit, >d.l. - superior to detection limit, n.a. - not analyzed, ana. pb. - analytical problem: concentration of Cl^- < 0.1 mmol·L^{-1} were not reliable during the HPLC measurement of this experiment)

Type	Input solution	Masse (g) Initial	Final	Output conc. (mmol·L^{-1}) Cl^-	SO_4^{2-}
Nano-Co-GR sample		0.1900			
Stock solutions	Cl50			48.24	0.17
				47.45	0.11
	S5/Cl40			38.15	4.79
				38.01	4.88
	S25			<d.l.	26.57
				<d.l.	26.30
Equilibrium phase	Cl50	200.01	196.42	52.02	<d.l.
				52.57	<d.l.
Rinsing 1	Milli-Q water		44.65	2.24	<d.l.
				2.29	<d.l.
Exchange phase 1-1	S5/Cl40	200.04	198.9	42.47	4.55
				41.85	4.49
1-2	S5/Cl40	200	199.35	41.60	5.10
				41.65	5.12
1-3	S5/Cl40	200.01	195.03	41.27	5.14
				41.06	4.63
1-4	S5/Cl40	200.03	203.48?	39.90	4.99
				39.85	4.97
1-5	S5/Cl40	200	198.3	37.34	4.67
				37.68	4.79
Rinsing 2	Milli-Q water		36.64	2.35	0.23
				2.48	0.25
Exchange phase 2-1	S25	200.01	198.14	ana. pb.	25.00
				ana. pb.	24.59

C.2 Cl^- or $SO_4^{2-} \leftrightharpoons CO_3^{2-}$ exchange

C.2.1 Protocol

Table S12 – Nomenclature and prepared concentrations of solutions used for batch experiments involving carbonate species (Conc. - concentration)

Solution name	Conc. NaCl ($mmol \cdot L^{-1}$)	Conc. Na_2CO_3 ($mmol \cdot L^{-1}$)	Conc. $NaHCO_3$ ($mmol \cdot L^{-1}$)	Conc. Na_2SO_4 ($mmol \cdot L^{-1}$)
Cl50	50	0	0	0
C50	0	50	0	0
C25	0	25	0	0
C10/Cl30	30	10	0	0
C5/Cl40	40	5	0	0
HC50	0	0	50	0
HC10/Cl40	40	0	10	0
HC10/S10	0	0	10	10
HC10/S20	0	0	10	20

Table S13 – Protocols for the batch exchange experiments of micro-Co-GR with carbonate species (table 1/3, see Table S12 for nomenclature of solutions, AEC - anionic exchange capacity)

Protocol	Exp C50	Exp C25	Exp HC50
Equilibrium phase	200 mL Cl50		
Rinsing 1	30-40 mL Milli-Q Water Direct Filtration		
Exchange phase 1	200 mL C50	200 mL C25	200 mL HC50
2	200 mL C50	200 mL C25	200 mL HC50
3	200 mL C50	200 mL C25	200 mL HC50
4		200 mL C25	200 mL HC50
5		200 mL C25	
Obtained parameters	Exchange stoichiometry + AEC		

Table S14 – Protocols for the batch exchange experiments of micro-Co-GR with carbonate species (table 2/3, see Table S12 for nomenclature of solutions, AEC - anionic exchange capacity)

Protocol	Exp "$NaHCO_3$"	Exp "Na_2CO_3"-I	Exp "Na_2CO_3"-II
Equilibrium phase	200 mL Cl50		
Rinsing 1	30-40 mL Milli-Q Water Direct Filtration		
Exchange phase 1-1	30 mL HC10/Cl40	50 mL C10/Cl30	30 mL C5/Cl40
2	30 mL HC10/Cl40	50 mL C10/Cl30	30 mL C5/Cl40
3	30 mL HC10/Cl40	100 mL C10/Cl30	50 mL C5/Cl40
4	50 mL HC10/Cl40	100 mL C10/Cl30	50 mL C5/Cl40
5	50 mL HC10/Cl40	200 mL C10/Cl30	30 mL C10/C30
6	100 mL HC10/Cl40	200 mL C10/Cl30	50 mL C10/C30
7			50 mL C10/C30
Rinsing 2	30-40 mL Milli-Q Water Direct Filtration		
Exchange phase 2 - 1	200 mL HC50	200 mL C25	200 mL C25
2	200 mL HC50	200 mL C25	200 mL C25
Rinsing 2	30-40 mL Milli-Q Water Direct Filtration		
Exchange phase 2 - 1	30 mL HC10/S20		
2	50 mL HC10/S20		
3	100 mL HC10/S20		
4	200 mL HC10/S20		
Obtained parameters	Equivalent fraction + Selectivity coefficents (Exchange models)		

Table S15 – Protocols for the batch exchange experiments of micro-Co-GR with carbonate species (table 3/3, see Table S12 for nomenclature of solutions, AEC - anionic exchange capacity)

Protocol	Exp "$NaHCO_3$/Na_2CO_3"
Equilibrium phase	200 mL Cl50
Rinsing 1	30-40 mL Milli-Q Water Direct Filtration
Exchange phase 1 - 1	200 mL S25
2	200 mL S25
3	200 mL S25
Rinsing 2	30-40 mL Milli-Q Water Direct Filtration
Exchange phase 2 - 1	30 mL HC10/S10
2	30 mL HC10/S10
3	50 mL HC10/S10
4	50 mL HC10/S10
5	100 mL HC10/S10
6	100 mL HC10/S10
7	200 mL HC10/S10

C.2.2 Results

Table S16 – Measurements of batch experiment on micro-Co-GR sample with a solution containing 50 mmol·L^{-1} of Na_2CO_3 (Solution nomenclature in Table S12, Protocol in Table S13, Exp nb - Experiment number, Output conc. - Output concentration, DIC - Dissolved Inorganic Carbon, <d.l. - inferior to detection limit, n.a. - not analyzed)

Exp nb	Type	Input solution	Masse (g) Initial	Final	Output conc. (mmol·L^{-1}) Cl^-	DIC
1	Micro-Co-GR sample		0.5500			
	Stock solutions	Cl50			55.21	<d.l.
					55.10	
		C50			<d.l.	47.23
					<d.l.	47.48
	Equilibrium phase	Cl50	199.99	194.54	55.43	<d.l.
					55.42	
	Rinsing 1	Milli-Q water		29.53	7.13	<d.l.
					7.15	
	Exchange phase 1-1	C50	200.1	199.86	3.68	44.95
					3.66	
	2	C50	200.03	199.48	0.45	47.14
					0.45	
	3	C50	200.07	200.23	0.17	47.12
					0.16	
2	Micro-Co-GR sample		0.59			
	Stock solutions	Cl50			50.67	<d.l.
					50.56	
		C50			<d.l.	46.05
					<d.l.	46.14
	Equilibrium phase	Cl50	201.42	196.97	53.48	<d.l.
					53.39	
	Rinsing 1	Milli-Q water		19.98	10.29	<d.l.
					10.31	
	Exchange phase 1-1	C50	201.35	200.89	5.13	42.90
					5.11	
	2	C50	201.81	200.93	0.26	46.42
					0.26	
	3	C50	201.72	202.01	0.05	46.85
					0.05	

Table S17 – Measurements of batch experiment on micro-Co-GR sample with a solution containing 25 $mmol \cdot L^{-1}$ of Na_2CO_3 (Solution nomenclature in Table S12, Protocol in Table S13, Exp nb - Experiment number, Output conc. - Output concentration, DIC - Dissolved Inorganic Carbon, <d.l. - inferior to detection limit, n.a. - not analyzed)

Type	Input solution	Masse (g) Initial	Final	Output conc. ($mmol \cdot L^{-1}$) Cl^-	DIC
Micro-Co-GR sample		0.51			
Stock solutions	Cl50			52.07	<d.l.
				52.01	23.81
	C25			0.00	23.58
				0.00	
Equilibrium phase	Cl50	200.4	n.a.	54.81	<d.l.
				54.83	
Rinsing 1	Milli-Q water		22.08	9.63	<d.l.
				9.61	
Exchange phase 1-1	C25	200.07	199.75	3.77	21.59
				3.76	
2	C25	201.3	201.1	0.42	23.63
				0.42	
3	C25	200.2	199.85	0.12	23.49
				0.12	
4	C25	200.02	n.a.	0.04	23.82
				0.04	
5	C25	199.99	n.a.	0.04	23.74

Table S18 – Measurements of batch experiment on micro-Co-GR sample with a solution containing 50 $mmol \cdot L^{-1}$ of $NaHCO_3$ (Solution nomenclature in Table S12, Protocol in Table S13, Exp nb - Experiment number, Output conc. - Output concentration, DIC - Dissolved Inorganic Carbon, <d.l. - inferior to detection limit, n.a. - not analyzed)

Type	Input solution	Masse (g) Initial	Final	Output conc. ($mmol \cdot L^{-1}$) Cl^-	DIC
Micro-Co-GR sample		0.48			
Stock solutions	Cl50			51.35	<d.l.
				51.41	<d.l.
	HC50			<d.l.	49.72
				<d.l.	49.37
Equilibrium phase	Cl50	201	196	52.84	<d.l.
				53.00	
Rinsing 1	Milli-Q water		24.15	7.85	<d.l.
				7.85	
Exchange phase 1-1	HC50	199.88	n.a.	3.72	46.92
				3.70	
	HC50	200.17	n.a.	0.65	49.04
				0.65	
	HC50	200.14	n.a.	0.22	49.21
				0.22	
	HC50	199.73	n.a.	0.10	48.81
				0.10	

Table S19 – Measurements of batch experiment "$NaHCO_3$" on micro-Co-GR sample (Solution nomenclature in Table S1, Protocol in Table S2, Output conc. - Output concentration, <d.l. - inferior to detection limit, >d.l. - superior to detection limit, n.a. - not analyzed)

Type	Input solution	Masse (g) Initial	Final	Output conc. ($mmol \cdot L^{-1}$) Cl^-	DIC	SO_4^{2-}
Micro-Co-GR sample		0.4700				
Stock solutions	Cl50			51.34	<d.l.	<d.l.
				51.41		<d.l.
	HC10/Cl40			40.46	9.73	<d.l.
				40.33	9.71	<d.l.
	HC50			<d.l.	50.61	<d.l.
				<d.l.	50.51	<d.l.
	HC10/S20			<d.l.	10.29	21.10
				<d.l.	9.78	21.26
Equilibrium phase	Cl50	201.97	198.65	53.96	<d.l.	<d.l.
				53.96		<d.l.
Rinsing 1	Milli-Q water		27.61	6.34	<d.l.	<d.l.
				6.35		<d.l.
Exchange phase 1-1	HC10/Cl40	29.68	29.45	48.57	3.35	<d.l.
				48.71		<d.l.
2	HC10/Cl40	29.93	29.94	48.30	6.27	<d.l.
				48.41		<d.l.
3	HC10/Cl40	30.04	29.74	45.10	7.79	<d.l.
				45.04		<d.l.
4	HC10/Cl40	50.1	49.95	42.26	9.08	<d.l.
				42.23		<d.l.
5	HC10/Cl40	50.5	50.05	42.31	9.36	<d.l.
				42.38		<d.l.
6	HC10/Cl40	99.84	99.16	41.26	9.43	<d.l.
				41.28		<d.l.
Rinsing 2	Milli-Q water		29.38	4.41	1.95	<d.l.
				4.41		<d.l.
Exchange phase 2-1	HC50	204.62	201.82	0.19	47.36	<d.l.
				0.19		<d.l.
2	HC50	201.83	200.79	0.04	48.36	<d.l.
				0.04		<d.l.
Rinsing 3	Milli-Q water		28.09	0.02	7.16	<d.l.
				0.02		<d.l.
Exchange phase 3-1	HC10/S20	29.36	29.58	0.02	9.53	19.00
				0.03		18.81
2	HC10/S20	50.58	50.72	<d.l.	10.10	21.58
				<d.l.		21.39
3	HC10/S20	101.68	100.35	<d.l.	10.14	22.53
				<d.l.		22.57
4	HC10/S20	201.66	n.a.	<d.l.	10.13	21.62
				<d.l.		21.62

Table S20 – Measurements of batch experiment "Na_2CO_3-I" on micro-Co-GR sample (Solution nomenclature in Table S1, Protocol in Table S2, Output conc. - Output concentration, <d.l. - inferior to detection limit, >d.l. - superior to detection limit, n.a. - not analyzed)

Type	Input solution	Masse (g) Initial	Final	Output conc. ($mmol \cdot L^{-1}$) Cl^-	DIC
Micro-Co-GR sample		0.5000			
Stock solutions	Cl50			52.93	0.89
				52.73	
	C10/Cl30			32.69	9.48
				32.56	9.49
	C25			0.00	23.80
				0.00	23.69
Equilibrium phase	Cl50	200.34	197.47	54.56	1.91
				54.43	
Rinsing 1	Milli-Q water		27.80	6.97	1.58
				6.98	
Exchange phase 1-1	C10/Cl30	50.02	49.25	40.91	4.34
				40.94	
2	C10/Cl30	50.02	49.94	36.48	7.56
				36.37	
3	C10/Cl30	100.01	99.71	34.09	9.00
				34.12	
4	C10/Cl30	100.02	99.46	32.91	9.38
				32.95	
5	C10/Cl30	200	200.06	32.66	9.57
				32.47	
6	C10/Cl30	200.02	198.99	32.54	9.54
				32.42	
Rinsing 2	Milli-Q water		32.71	3.43	7.24
				3.44	
Exchange phase 2-1	C25	200.03	199.88	0.07	22.91
				0.07	
2	C25	200.03	199.7	0.06	23.79
				0.06	

Table S21 – Measurements of batch experiment "Na_2CO_3-II" on micro-Co-GR sample (Solution nomenclature in Table S1, Protocol in Table S2, Output conc. - Output concentration, <d.l. - inferior to detection limit, >d.l. - superior to detection limit, n.a. - not analyzed)

Type	Input solution	Masse (g) Initial	Final	Output conc. ($mmol \cdot L^{-1}$) Cl^-	DIC
Micro-Co-GR sample		0.55			
Stock solutions	Cl50			52.64	0.27
				52.64	
	C5/Cl40			41.81	4.67
				41.64	4.98
	C10/Cl30			31.80	9.55
				31.81	
	C25			<d.l.	23.88
				<d.l.	
Equilibrium phase	Cl50	200.63	197.23	53.91	2.41
				53.96	
Rinsing 1	Milli-Q water		26.22	6.74	10.62
				6.74	
Exchange phase 1-1	C5/Cl40	30.00	29.85	45.81	0.47
				45.59	
2	C5/Cl40	30.10	30.09	47.67	1.52
				47.54	
3	C5/Cl40	50.01	49.83	44.60	3.08
				44.49	
4	C5/Cl40	51.27		42.92	3.89
				42.98	
5	C10/Cl30	30.00	30.01	35.34	7.75
				35.24	
6	C10/Cl30	50.00	48.71	33.31	8.97
				33.12	
7	C10/Cl30	50.2	50.23	31.92	9.52
				31.81	
Rinsing 2	Milli-Q water		21.53	4.90	1.48
				4.90	
Exchange phase 2-1	C25	200.63	200.48	0.09	23.49
				0.09	
2	C25	201.68	202.85	0.04	24.15
				0.04	

Table S22 – Measurements of batch experiment "$NaHCO_3/Na_2SO_4$" on micro-Co-GR sample (Solution nomenclature in Table S1, Protocol in Table S2, Output conc. - Output concentration, <d.l. - inferior to detection limit, >d.l. - superior to detection limit, n.a. - not analyzed)

Type	Input solution	Masse (g) Initial	Final	Output conc. ($mmol \cdot L^{-1}$) Cl^-	DIC	SO_4^{2-}
Micro-Co-GR sample		0.5100				
Stock solutions	Cl50			52.30	<d.l.	<d.l.
				52.37		<d.l.
	S25			<d.l.		26.87
				<d.l.	0.37	26.89
	C10/S10			<d.l.	9.69	11.26
				<d.l.	9.62	11.17
Equilibrium phase	Cl50	235.74	232.77	54.31	0.04	<d.l.
				54.23		<d.l.
Rinsing 1	Milli-Q water		60.30	3.38	0.01	<d.l.
				3.37		<d.l.
Exchange phase 1-1	S25	203.9	203.55	4.21	0.20	24.20
				4.23		24.11
2	S25	202.03	201.85	0.47	0.26	26.90
				0.47		26.72
3	S25	202	199.88	0.10	2.43	27.01
				0.10		26.98
Rinsing 2	Milli-Q water		25.84	0.03	0.09	4.13
				0.03		4.13
Exchange phase 2-1	C10/S10	30.03	30.23	0.09	5.68	11.78
				0.09		11.78
2	C10/S10	29.98	29.99	0.06	7.90	13.07
				0.06		13.04
3	C10/S10	50	50.15	0.02	9.01	12.11
				0.02		12.09
4	C10/S10	50.02	49.91	0.01	9.20	11.98
				0.01		11.96
5	C10/S10	100	100.17	0.00	9.41	11.85
				0.00		11.82
6	C10/S10	100.01	99.14	0.00	9.35	11.50
				0.00		11.55
7	C10/S10	202.48	n.a.	0.01	9.54	11.82
				0.01		11.81

Myriam Agnel

Échanges anioniques binaires et ternaires pour le système chlore, sulfate et carbonate dans les rouilles vertes

Résumé:
La rouille verte est un hydroxyde double lamellaire Fe(II)/Fe(III). Les feuillets qui la composent sont chargés positivement en raison de la présence de fer trivalent. Cette charge est compensée par des anions situés dans l'espace interfoliaire. La rouille verte est un des rares matériaux inorganiques avec une grande capacité d'adsorption des anions. L'objectif de ce travail a été de comprendre les mécanismes et les équilibres thermodynamiques régissant les processus d'échange d'anions inorganiques (Cl^-, HCO_3^-/CO_3^{2-}, SO_4^{2-}) dans les environnements naturels, mais aussi artificiels, où peuvent se trouver les rouilles vertes. Les mécanismes d'échange ont pu être identifiés et quantifiés grâce à la combinaison de techniques d'analyse des matériaux, d'expériences en laboratoire, de mesures par diffraction des rayons X *in situ* et résolues dans le temps, et de modèles géochimiques. SO_4^{2-} remplace deux Cl^- par simple échange anionique sans dissolution/recristallisation des feuillets ou processus d'interstratification entre les feuillets. Deux Cl^- s'échangent pour un CO_3^{2-} via un processus d'interstratification des feuillets dont la charge est compensée soit par Cl^- soit par CO_3^{2-}. Pendant le processus d'échange, une précipitation de magnétite est observée. Des modèles thermodynamiques des échanges ioniques ont pu décrire les résultats expérimentaux et permettre de calculer des coefficients de sélectivité. Les paramètres de ces modèles ont dû être adaptés selon les anions considérés, le pH, la taille des cristaux ou leurs fautes d'empilement. Le travail effectué dans cette thèse aide à prédire le comportement des rouilles vertes vis-à-vis du cycle géochimique des anions dans les gleysols.

Mots-clés : Rouille verte, Fougérite, Échange anionique, Hydroxyde double lamellaire

Anion exchange in green rust: the chloride, sulphate and carbonate binary and ternary systems

Summary:
Green rust is a Fe(II)/Fe(III) layered double hydroxide. Its layers are positively charged because of the occurrence of mixed Fe^{2+}/Fe^{3+} valence states. The charge is compensated by exchangeable anions located in the interlayer space. Green rust is one of the few inorganic materials with large anion adsorption capacity. The objective of this work was to obtain a mechanistic understanding and a rigorous thermodynamic framework to predict anion exchange processes in natural and engineered environments in which green rust is present. Various methods were combined for analyzing solid components, laboratory experiments and synchrotron *in situ* and time resolved X-ray diffraction measurements with geochemical modeling to decipher and quantify the mechanism of anion exchange in green rust.The exchange between chloride, sulphate and carbonate species was studied more specifically. SO_4^{2-} replaced two Cl^- by a simple anion exchange mechanism without dissolution-recrystallization or interstratification processes. Two Cl^- were exchanged by CO_3^{2-} with interstratification processes and a partial precipitation of magnetite. Ion exchange models were suitable to model the exchange of those three anions on green rust. However, selectivity coefficients in these models had to be adapted depending on the anions considered, pH, crystal size, and the presence or not of staking faults. This multiscale characterization can serve as a starting point for the building of mechanistic geochemical models that allow predicting the role of green rust on the geochemical cycle of ions in gleysols.

Keywords : Green rust, Fougerite, Anion exchange, Layered double hydroxide

Institut des Sciences de la Terre,
1A rue de la Férollerie 45100 Orléans